The cooperative manipulation of rigid objects with industrial robots is a challenging configuration for the control. The object is connected to multiple robots and integrated into the kinematic structure, resulting in actuation redundancy. Inaccuracies of the robots and tolerances of the object lead to deviations of the grasp points at the object, that are amplified due to coupling effects. This consequently results in inadequate object positioning and causes internal tensioning of the overall structure. A recent example of this object integration is the PARAGRIP handling system that was investigated in this thesis.

Today's control and calibration approaches, however, do not target the identification of the uncertain grasp points. Accordingly, in this thesis a kinematic calibration procedure for the PARAGRIP robotic arms and a self-calibration procedure for the object integrative handling system were developed to identify the actual grasp points at the object.

The kinematic calibration was investigated for a mathematically efficient serial and a hybrid kinematics model, both including the compensation of gravitational effects. The limited absolute accuracy of the PARAGRIP arms could be improved significantly.
In the context of the kinematic calibration, a new stiffness modeling approach was implemented by extending the concept of Matrix Structure Analysis. The implemented modeling approach allows for the automatic calculation of arbitrary kinematic structures and the compensation of the gravitational deformations.
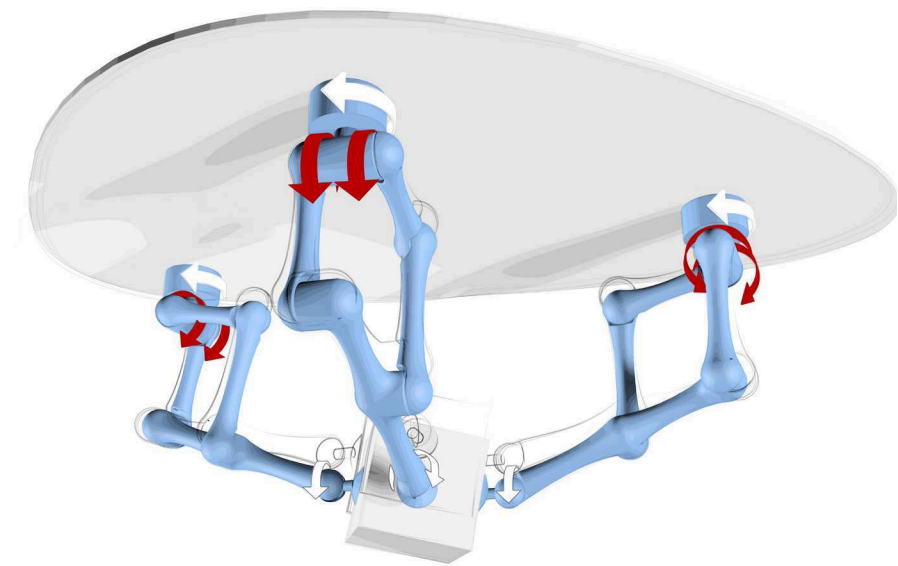Furthermore, a new self-calibration method for the object integrative handling system was developed based on the combination of direct and inverse kinematic calculations. The redundant sensor-information of the cooperating robots is evaluated to identify the actual grasp points at the integrated object.

The results show that the available redundant sensor information for object integrative robots or handling systems can be used to identify the grasp points at the object and compensate the internal inaccuracies automatically. This offers the opportunity to extend the capabilities of cooperating robots and allows for the reconfiguration and calibration without additional external metrology. The research and results described in this thesis yielded new findings for the PARAGRIP handling system, which can be generalized for every object integrative handling system with redundant actuation, in particular cooperating industrial robots.

9 783863 596316

Kinematic Accuracy and Self-Calibration of an
Object Integrative Handling System

Tim Detert

Tim Detert

Kinematic Accuracy and Self-Calibration of an Object Integrative Handling System

IGMR · Institut für Getriebetechnik, Maschinendynamik und Robotik

RWTH AACHEN UNIVERSITY

Edition Wissenschaft
Apprimus

Kinematic Accuracy and Self-Calibration
of an Object Integrative Handling System

Kinematische Genauigkeit und Selbstkalibrierung
eines Objekt-integrativen Handhabungssystems

Berichter:

Tim Detert:

Kinematic Accuracy and Self-Calibration of an Object Integrative Handling System

1. Auflage, 2018

Gedruckt auf holz- und säurefreiem Papier, 100% chlorfrei gebleicht.

Printed in Germany

D 82 (Diss. RWTH Aachen University, 2018)

Danksagung

Diese Dissertation ist im Rahmen meiner Tätigkeit als wissenschaftlicher Mitarbeiter am Institut für Getriebetechnik, Maschinendynamik und Robotik (IGMR) der RWTH Aachen University entstanden.

Ich danke meinem Doktorvater Professor Burkhard Corves und Professor Mathias Hüsing für die Möglichkeit zur Promotion und die Betreuung meiner Arbeit am Institut. Zusammen haben sie ein bereicherndes und angenehmes Arbeitsumfeld geschaffen, in dem sich hervorragend Forschen, Lehren und Arbeiten lässt. Vielen Dank auch an Professor Robert Schmitt und an Professor Kai-Uwe Schröder für anregende Gespräche und die Begleitung meiner Doktorprüfung.

Vielen Dank an alle Kollegen. Ihr habt das positive Arbeitsklima und die Zeit am Institut entscheidend geprägt. Ohne die tolle Atmosphäre, die vielen fachlichen Diskussionen, die gemeinsame Arbeit an verschiedensten Projekten und die Unterstützung für den Prüfstand, für die Datenverarbeitung und auch für organisatorische Belange wäre meine Dissertation in dieser Form nicht möglich gewesen. Die tägliche Zusammenarbeit, die gemeinsamen Pausen und auch die privaten Aktivitäten mit euch machen einfach Spaß.

Vielen Dank an „meine" Studenten. Mit euren Vorarbeiten und einiger Fleißarbeit habt ihr zum Fortschritt der Arbeit beigetragen.

Ganz besonders bedanke ich mich bei meinen Eltern und Geschwistern, die es mir mit ihrer Unterstützung und einem wunderbaren familiären Umfeld überhaupt erst ermöglicht haben, über das Studium hinaus bis zur Promotion erfolgreich zu sein.

Abschließend möchte ich mich bei meiner wunderbaren Frau Rike für den Rückhalt und das grenzenlose Verständnis in den besonders arbeitsreichen Phasen bedanken. Danke, ich freue mich auf unsere weitere gemeinsame Zukunft!

Abstract

The cooperative manipulation of rigid objects with industrial robots leads to redundant actuation, which is a challenging configuration for the control of cooperating robots. In such a configuration, the object is connected to multiple robots and integrated into the kinematic structure, resulting in actuation redundancy. Inaccuracies of the robots and tolerances of the object lead to deviations of the grasp points at the object that cannot be determined precisely. These deviations of the kinematics model from the real system are amplified due to coupling effects. This consequently results in inadequate object positioning and causes internal tensioning of the overall structure. A recent example of this object integration is the PARAGRIP handling system that was investigated in this thesis.

Today's control and calibration approaches, however, do not target the identification of the uncertain grasp points. Accordingly, in this thesis a kinematic calibration procedure for the PARAGRIP robotic arms and a self-calibration procedure for the object integrative handling system were developed to identify the actual grasp points at the object. The kinematic calibration was investigated for a mathematically efficient serial and a hybrid kinematics model, both including the compensation of gravitational effects. The choice of identification points and the optimization residual were investigated and the limited absolute accuracy of the PARAGRIP arms could be improved significantly based on the findings. In the context of the kinematic calibration, a new stiffness modeling approach was implemented by extending the concept of Matrix Structure Analysis. The implemented modeling approach allows for the automatic calculation of arbitrary kinematic structures and the compensation of the gravitational deformations. Furthermore, a new self-calibration method for the object integrative handling system was developed based on the combination of direct and inverse kinematic calculations. The redundant sensor-information of the cooperating robots is evaluated to identify the actual grasp points at the integrated object, to increase the system accuracy and to limit the impact of the coupling effects. The sensitivity and influencing factors of the method were investigated and verified in simulations.

The results show that the available redundant sensor information for object integrative robots or handling systems can be used to identify the grasp points at the object and compensate the internal inaccuracies automatically. The application of self-calibration to object integrative handling systems allows for an efficient and easy way of reconfiguration and calibration without additional external metrology. This offers the opportunity to extend the capabilities of cooperating robots and reduces the demand for complex robot control. The research and results described in this thesis yielded new findings for the PARAGRIP handling system, which can be generalized for every object integrative handling system with redundant actuation, in particular cooperating industrial robots.

Zusammenfassung

Die kooperierende Handhabung starrer Objekte mit Industrierobotern stellt, wegen der entstehenden Antriebsredundanz, eine herausfordernde Konfiguration für die Steuerung kooperierender Roboter dar. In einer solchen Konfiguration ist das Objekt mit mehreren Robotern verbunden und in die kinematische Struktur integriert, was zur Antriebsredundanz führt. Ungenauigkeiten der Roboter und Objekttoleranzen führen zu Abweichungen der Greifpunkte auf dem Objekt, die nicht präzise ermittelt werden können. Diese Abweichungen des kinematischen Modells vom realen System werden durch Kopplungseffekte verstärkt. Dies führt zu einer unzureichenden Positionierung des Objekts und verursacht innere Spannungen der Gesamtstruktur. Das in dieser Dissertation untersuchte PARAGRIP Handhabungssystem ist ein aktuelles Beispiel für diese Objektintegration.

Aktuell gibt es weder Steuerungs- noch Kalibrierungsansätze, die auf eine Identifikation der unbekannten Greifpunkte abzielen. In dieser Dissertation wurde ein Verfahren für die kinematische Kalibrierung der robotischen PARAGRIP Arme und ein Verfahren für die Selbstkalibrierung des objektintegrativen Handhabungssystems entwickelt, um die tatsächlichen Greifpunkte auf dem Objekt zu identifizieren. Die kinematische Kalibrierung wurde für ein mathematisch effizientes serielles und ein hybrides kinematisches Model untersucht und für beide Fälle um die Kompensation der Schwerkrafteinflüsse ergänzt. Verschiedene Messpunkte und das Optimierungsresiduum wurden untersucht und die eingeschränkte Absolutgenauigkeit der PARAGRIP Arme konnte basierend auf den Forschungsergebnissen signifikant gesteigert werden. Durch die Erweiterung der Matrix-Struktur-Analyse wurde ein neuer Ansatz zur Steifigkeitsmodellierung umgesetzt, der die automatische Berechnung beliebiger kinematischer Strukturen und die Kompensation der Verformungen durch die Schwerkraft für die kinematische Kalibrierung ermöglicht. Basierend auf der Kombination der direkten und inversen Kinematik wurde eine neue Methode zur Selbstkalibrierung des objektintegrativen Handhabungssystems entwickelt. Die redundanten Sensorinformationen der kooperierenden Roboter werden ausgewertet, um die tatsächlichen Greifpunkte am integrierten Objekt zu identifizieren, die Systemgenauigkeit zu erhöhen und so den Einfluss der Kopplungseffekte einzuschränken. Die implementierte Methode wurde simulativ verifiziert und die Sensitivitäten und die Einflussfaktoren wurden untersucht.

Die Ergebnisse zeigen, dass die verfügbaren redundanten Sensorinformationen von objektintegrativen Handhabungssystemen genutzt werden können, um die tatsächlichen Greifpunkte auf dem Objekt zu identifizieren und inhärente Ungenauigkeiten automatisch zu kompensieren. Die Anwendung der Selbstkalibrierung für objektintegrative Handhabungssysteme erlaubt eine einfache und effiziente Rekonfiguration und Kalibrierung ohne zusätzliche Messtechnik. Dies eröffnet die Möglichkeit die Fähigkeiten kooperierender Roboter zu erweitern und reduziert die Notwendigkeit komplexer Robotersteuerungen. Die neuen Erkenntnisse, die im Rahmen dieser Dissertation für das PARAGRIP Handhabungssystem erarbeitet wurden, können für jedes objektintegrative Handhabungssystem, insbesondere für kooperierende Industrieroboter, verallgemeinert werden.

Content

Variables, Abbreviations and Indices

Hereinafter the variables, abbreviations and indices (cursive sub- and superscripts) used in this thesis are listed. Scalar values and indices are represented by lower and upper cases, vectors by bold lower cases and matrices are represented by bold upper cases. Superscripts indicate the coordinate system of reference for all variables and vectors.

Latin Lower Case

a, b	sub-matrix pointer for rows	n	number of elements, cycles, …
$\boldsymbol{b}$	grasp point vector	p	parameter
b	width, component of $\boldsymbol{b}$	$\boldsymbol{p}$	parameter vector
c, d	sub-matrix pointer for columns	$\hat{\boldsymbol{p}}$	nominal parameter vector
d	diameter, distance	q	distributed gravitational load
$\boldsymbol{e}$	unit vector	$\boldsymbol{r}$	position vector
e, f	position functions	$\hat{\boldsymbol{r}}$	nominal position vector
$\boldsymbol{f}$	vector of generalized loads	$\bar{\boldsymbol{r}}$	average, measured position vector
g	gravitational constant	r	component of $\boldsymbol{r}$
h	height	t	thickness
j	number of rigid nodes	w	beam deflection
k	element of the stiffness matrix	w'	beam rotation
l	length, offset	x, y, z	translational coordinates
$\hat{l}$	nominal length	$\bar{x}, \bar{y}, \bar{z}$	average, measured coordinates
m	invariant coefficient	$\hat{x}, \hat{y}, \hat{z}$	nominal coordinates

Latin Upper Case

$\boldsymbol{0}$	zero matrix	M	uniaxial moment
A	cross-sectional area	$\mathcal{N}$	Gaussian normal distribution
$\boldsymbol{A}$	4x4 transformation matrix	O	Observability Index
AP	absolute accuracy	P	point
$\boldsymbol{AP}$	absolute accuracy vector	$\boldsymbol{R}$	rotational matrix (see below)
$\boldsymbol{C}$	compliance matrix	R	residual
E	Young's modulus	RP	position repeatability
F	uniaxial force	$\boldsymbol{S}$	skew-symmetric matrix
G	shear modulus	$\boldsymbol{T}$	rotational transformation matrix
$\boldsymbol{I}$	identity matrix	$\boldsymbol{U}, \boldsymbol{V}^*$	single value decomposition matrices
I	second moment of area	$\boldsymbol{V}$	cross product transf. matrix
$\boldsymbol{J}$	Jacobian matrix	$\boldsymbol{X}$	error propagation matrix
$\boldsymbol{K}$	stiffness matrix		

Greek Lower and Upper Case

α	wrist-joint angle	σ	singular value, standard deviation
$\hat{\alpha}$	nominal wrist-joint angle	φ	joint angle

$\bar{\alpha}$	measured wrist-joint angle	$\hat{\varphi}$	nominal joint angle
$\boldsymbol{\alpha}$	wrist-joint angle vector	$\boldsymbol{\varphi}$	joint angle vector
$\hat{\boldsymbol{\alpha}}$	nominal wrist-joint angle vector	$\hat{\boldsymbol{\varphi}}$	nominal joint angle vector
α, β, γ	rotational coordinates	ϑ	relative influence
$\hat{\alpha}, \hat{\beta}, \hat{\gamma}$	nominal rotational coordinates	χ	pose vector
$\bar{\alpha}, \bar{\beta}, \bar{\gamma}$	measured rotational coordinate	Δ	displacement, deviation
∂	partial derivative	$\boldsymbol{\Sigma}$	single value decomposition matrix

Indices and Coordinate Systems

0	global coordinate system	rel	relative
abs	absolute	sc	self-calibration
ax	axial	ser	serial
$axis$	joint A0, B0 axis	tor	torsional
e	load case	u	arbitrary body u
$grav$	gravitational	x, y, z	translational coordinates
hyb	hybrid	C	Cartesian
i	arm i, measurement i, joint i, …	H	intermediate coordinate system
j	Measurement pose j	O	point of origin, orientation
k, l	rigid node, link k	P	arbitrary point, position
l	link length	R, S, T	wrist-joint coordinate systems
lat	lateral	S	sample
m, n	link	$struct$	structure
mi	link m of arm i	T	torsion
$norm$	normal	TCP	Tool Center Point
obj	object	WJ	wrist-joint
p	p-norm dimension, parameter	α	wrist-joint angle
par	parallel	φ	joint angle
per	perpendicular	Θ	joint space
rad	radial	∞	maximum norm

Abbreviations

DBB	double-ball-bar	LED	Light Emitting Diode
CMM	coordinate measurement machine	MSA	Matrix Structure Analysis
DH	Denavit-Hartenberg	POE	product of exponentials formula
DHM	Denavit-Hartenberg-Modified	TCP	Tool Center Point
DOF	degrees of freedom	VJM	Virtual Joint Method
FEA	Finite Element Analysis		

Rotational Matrices

$$\boldsymbol{R}_x(\alpha) = \begin{pmatrix} 1 & 0 & 0 \\ 0 & \cos\alpha & -\sin\alpha \\ 0 & \sin\alpha & \cos\alpha \end{pmatrix} \qquad \boldsymbol{R}_y(\beta) = \begin{pmatrix} \cos\beta & 0 & \sin\beta \\ 0 & 1 & 0 \\ -\sin\beta & 0 & \cos\beta \end{pmatrix} \qquad \boldsymbol{R}_z(\gamma) = \begin{pmatrix} \cos\alpha & -\sin\alpha & 0 \\ \sin\alpha & \cos\alpha & 0 \\ 0 & 0 & 1 \end{pmatrix}$$

1 Introduction

Robotics and automation have significantly improved the production and assembly technology for mass production in the recent decades. Today, flexible production capabilities for small lot sizes and individualized products are needed. "Due to shorter product life cycles and rising demand for customization, flexibility and adaptability of assembly processes will become key elements for a sustainable success of industrial production in high-wage countries". This citation from Schmitt, Corves, Hüsing and others [SCH16, p. 878] expresses one central motivation for the research described in this thesis and performed within the Cluster of Excellence "Integrative Production Technology for High Wage Countries".

The increased flexibility and adaptability described can be gained by cooperation of stationary or mobile robotic systems, which find increasing application in industry for demanding handling tasks. Cooperating robots for example can be used to optimize complex tasks such as the multi-dimensional welding task shown in Figure 1-1a. Beyond that, cooperative manipulation enables many tasks that are difficult or impossible to execute by a single robot [CU16, p. 989]. These tasks for example include the manipulation of large payloads by load sharing as shown in Figure 1-1b or the manipulation of individualized or large-scale components without individual gripper technology or jigs as shown in Figure 1-1c.

a)   b)   c)
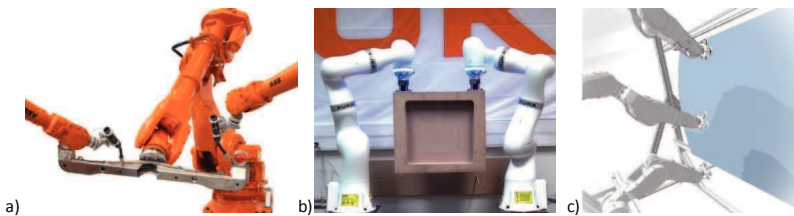
Figure 1-1: a) Cooperating industrial robots for welding [ABB17], b) load sharing cooperative manipulation with two force sensitive robots [KUK16], c) local shaping of an airplane structure [SCH16, p. 919]

One of the main challenges for such cooperating robots is the accurate synchronization within the system [SV12]. During the cooperation, and in particular the cooperative manipulation of rigid components, the handling object is connected to multiple robotic units and integrated into the kinematic structure. One recent example of this object integration is the PARARIP handling system shown in Figure 1-2, that will be investigated in this thesis. During object integration, the overall structure is actuated redundantly, which leads to coupling effects between the robots involved. Forces and torques are transmitted through the physically integrated object. Inaccuracies of the robots are amplified due to the coupling effects, which consequently results in inadequate object positioning. Furthermore, the redundant actuation can also cause tensioning and internal stresses of the structure.

Various approaches for the control of cooperating robots have been developed to cope with these challenges. The most common concept for robot manufacturers is the master-slave concept. It relies on the guidance of one robotic unit and the force control of the remaining robotic units.
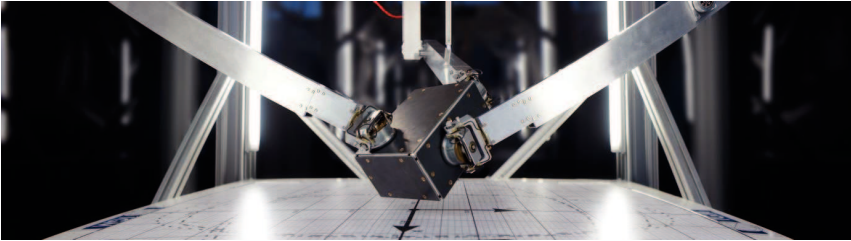
Figure 1-2: Object integrative handling system PARAGRIP (picture by Martin Riedel)

Recent research concentrates on the planning, programming and control of assembly opera-
tions for cooperating industrial robots (see for example [MSF16,MKA14,MME12]) and the
recently very successful dual arm robots (see for example [AK16,TMM14,KSS11]). These ap-
proaches, however, do not aim to improve the kinematic inaccuracies, causing the described
challenges of object integrative manipulation. This deficit is targeted in this thesis, by devel-
oping a calibration and a self-calibration approach for an object integrative handling sys-
tems, using the example of the PARAGRIP handling system.

The accuracy of a system of cooperating robots can for example be improved by the calibra-
tion of the robot base frames [WLY15,GDD14] or by external metrology for a common abso-
lute reference frame [NSG10,NSG12]. Furthermore, the actuation redundancy for object
integrative cooperating robots provides additional sensor information that can be used to
improve the accuracy of the overall system and limit the unfavorable coupling effects. This is
known as self-calibration. This field of research has not been addressed yet for object inte-
grative cooperating robots. Bennett and Hollerbach [BH91] as well as Bonitz and Hsia [BH97]
investigated the autonomous calibration of two linked serial arm manipulators connected
mechanically at their end-effectors. Their research is an early example of self-calibration for
systems, similar to the object integrative handling. The subsequent research, however, fo-
cused on the investigation of parallel robots with unaltered closed kinematic chains. The
self-calibration for the integration of an object and the identification of the according grasp
points have not been investigated yet.

In this thesis, the kinematic accuracy of an object integrative handling system is investigated
and a method of self-calibration, based on the redundant sensor information, is developed
to reduce the deficit found in the current state of research. The concept of self-calibration
allows for an efficient and easy way to reconfigure and calibrate cooperating object integra-
tive robots without additional external metrology. Such a concept offers the opportunity to
extend the capabilities of cooperating robots and reduces the demand for robot control by
autonomous calibration procedures using inherent sensor systems.

The investigation of self-calibration for the specific PARAGRIP prototype shown in this thesis
is a first step to investigate the capabilities of self-calibration for cooperating robots in gen-
eral.

2   Approach, Aims and Scope of the Thesis

As stated in the introduction, the object integrative cooperation of robotic units leads to a redundant actuator configuration. Limited robot accuracy and object tolerances reduce the overall system accuracy and introduce unintended internal tensioning to the coupled robots. The research approach described in the following targets this deficit to improve the kinematic inaccuracies of the system by combining classical methods of kinematic calibration and the evaluation of the available redundant sensor information by means of self-calibration.

Research Approach

The influencing factors that reduce the overall system accuracy for cooperating robot arms during object integration are shown in Figure 2-1. The inaccuracies and positioning errors of the robotic arms and object alter the overall kinematic structure with the integrated object. Specifically, the grasp points will be remote from the target position with the consequences described above.
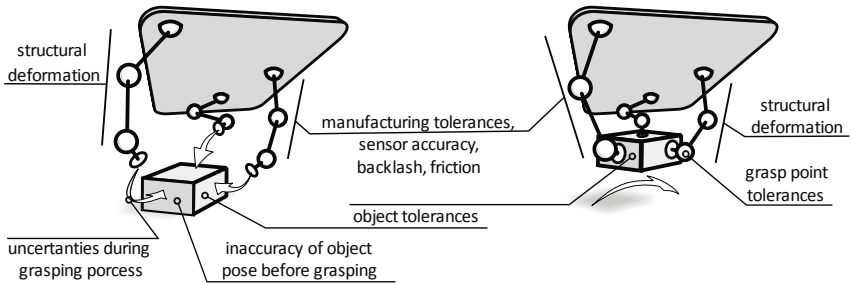
Figure 2-1: Accuracy influencing factors for object integrative handling with cooperating robots, shown for the PARAGRIP handling system

Manufacturing tolerances of the links and joints alter the kinematic structure and reduce the absolute accuracy of robotic arms. By identifying the real kinematic parameters and correcting the kinematic model, to some extent they can be compensated for. However, limited sensor accuracy in the drives, backlash in the gears and bearings, and friction limit the repeatability of every single robotic arm and cannot easily be compensated for. As robots and handling systems nevertheless have much better repeatability than accuracy, it is possible and advisable to improve the accuracy by calibration methods.

Structural deformations under load influence the accuracy of robots and handling systems. The gravitational loads due to the object payload and the self-weight of the robot deform the structure during the grasping and handling process. By modelling the stiffness properties and loads, these effects can be compensated for in the kinematic model by extending the kinematic parameter identification described above.

The remaining influencing factors (object pose, object tolerances and grasping uncertainties) shown in Figure 2-1 cannot be compensated for by classical calibration, gravitational compensation or external metrology. The pose of the handling object relative to the robots is

usually not known precisely before grasping and cannot always be captured accurately with acceptable effort. Dimensional tolerances of the object geometry, the residual of the partly compensated influencing factors (calibration and gravitational compensation) and unpredictable effects like friction and slip during grasping result in significant grasp point tolerances. Naturally, these tolerances are individual for every grasping process. For this reason, the concept of self-calibration for object integrative handling of cooperating robots is investigated. It allows for the compensation of aforementioned factors, without external metrology, by identifying the real grasp points after the object integration.

The general concept of self-calibration relies on the use of redundant sensor information, available within a kinematic structure. For cooperating articulated robots, this redundancy is easily achieved as soon as the object is integrated to the structure. As illustrated in Figure 2-2a, for example, 18 servo drives (red arrows) are available for a 6 degrees of freedom (DOF) motion, resulting in redundant information for up to 12 joint positions.

a)   b)
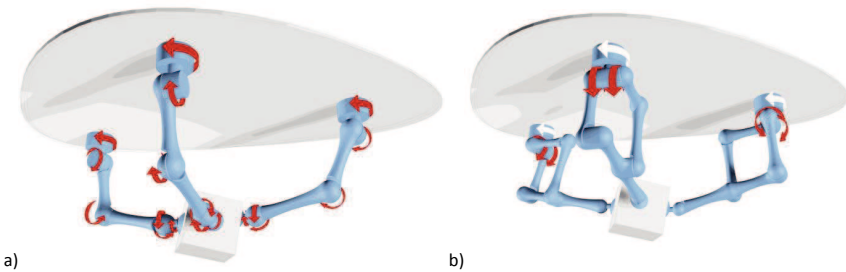
Figure 2-2: a) Cooperating 6 DOF robotic arms, b) object integration for the PARAGRIP handling system

For the PARAGRIP handling system, used for the self-calibration method and verification, the available sensor information is depicted in Figure 2-2b. The 6 main actuators driving the parallelograms (red arrow) are used to drive the kinematic structure with the integrated object. The additional actuators (white arrows) are set passive and can be used to gain the redundant position information. In this thesis, the details of this concept and its implementation are investigated by pursuing the following three aims.

Aims

The PARAGRIP handling concept offers advantages over classical cooperating industrial robots, like for example the reduced number of actuators and hybrid kinematics structure, as explained in detail in section 3. An improved understanding of the system properties will help future developments based on these advantages, and opportunities should find wider applications if transferred to collaborating robots in general.

Consequently, the first aim of the thesis is to gain a better understanding of the accuracy of the PARAGRIP and to develop, implement, and validate a kinematic calibration procedure.

The second aim is the compensation of gravitational effects within this kinematic calibration procedure, based on a new stiffness model that allows for the automatic calculation of the structural deformations for any position and load.

The third aim is the development, implementation, verification and validation of a self-calibration method for object integrative handling systems to identify the grasp points at the object and compensate the internal inaccuracies automatically.

The according research described in this thesis will yield new findings for the PARAGRIP handling system, which can be in the future generalized for every object integrative handling system with redundant actuation, in particular cooperating industrial robots.

Scope and Structure of the thesis

The PARAGRIP [Rie14] is a recent example of an object integrative handling system and the prototype will be used for the experimental verification of the developed methods. The handling concept, the robot prototype and its properties are described in section 3.

The kinematic accuracy and the identification of the kinematic parameters for a single arm of the handling system are investigated in section 4. Based on a state of research review, kinematic models and a suitable approach for the static calibration are investigated and validated for the prototype. Following on from the current state of research for different stiffness modeling approaches, an extended stiffness modeling method is developed and implemented based on the Matrix Structure Analysis in section 5. It is validated for the PARAGRIP prototype and extends the performance of the kinematic calibration. Based on current state of research approaches for self-calibration of parallel robots, a new method of self-calibration is developed and verified for the PARAGRIP handling system. It is described in section 6.

The main findings of the research performed are summarized and concluded in section 7. Finally, the results are discussed and an outlook to possible and advisable future investigations is given in section 8.

3 PARAGRIP Handling System

Riedel and others [Rie14,MRH13] developed a flexible and versatile handling concept, called PARAGRIP (Parallel Gripping) to address todays needs of customized production and to offer a flexible solution to component dependent individual handling tasks. The handling concept [MCR05] and its prototype are used as an exemplary application scenario for object integrative handling systems in this thesis. They are described briefly in this section.
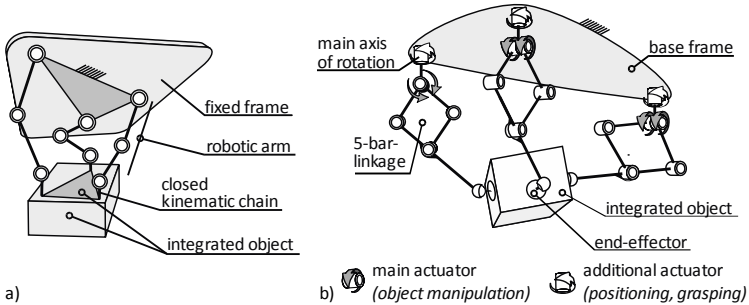
Figure 3-1: a) PARAGRIP handling concept, b) kinematic architecture (see [Rie14])

The handling concept is based on a reconfigurable architecture with a modular layout. Objects are handled with 6 DOF by forming a parallel kinematic structure including at least three robotic arms and integrating the object into the kinematic structure (see Figure 3-1a). The object integration is performed by grasping the object with the robotic arms. Here, grasping refers to all possible contact principles, for example form fit, force closure or even adhesive bonds realized by according end-effectors [Kur16]. The parallel kinematic robot structure is formed (and regenerated with every grasping process) by establishing the mechanical connection and closing the kinematic chains between the fixed frame and integrated object. Every robotic arm provides 3 actuated translational DOF to position the end-effector and 3 passive rotational DOF to allow for passive alignment of the orientation between robotic arm and object.

With this arm configuration, the 6 DOF object manipulation requires a minimum of 3 arms with 2 main actuators per arm and thus 6 main actuators in total. The robotic arms are realized as hybrid structure: The 2 main actuators drive a planar 5-bar linkage that is rotated around the main axis by an additional actuator (see Figure 3-1b). The additional actuator is compulsory for the spatial positioning of each single arm with its end-effector and the grasping procedure, but not necessarily needed for the multi-arm handling task with integrated object. This actuation redundancy provides additional sensor information, needed for the self-calibration.

The handling concept features high flexibility due to the reconfiguration of the kinematic structure. The system properties can be adapted to a given handling task, for example objects of different shapes, weight and size. The position of the end-effector on the object after grasping and the position of the arms on the base frame can be altered. Changes here

have great effect on the overall system performance: For example, the workspace, wrench and velocity capabilities, stiffness and accuracy can be influenced in a wide range. Additionally, the system can be reconfigured by scaling the quantity or changing the type of robotic arms used for object integration. By adding or removing supplementary arm-units, a wide range of objects with different sizes and weights can be handled. Actuation redundancy can improve the stiffness and payload properties and allow for the support of large and sensitive objects at many grasping points. The adaption of the kinematic parameters especially enables fast and easy reconfiguration by changing the contact point on the object with every grasping procedure. The system configuration can even be adapted or changed during object motion by dynamically re-grasping the object with additional arms. For details on the dynamic reconfiguration see [CMR11].
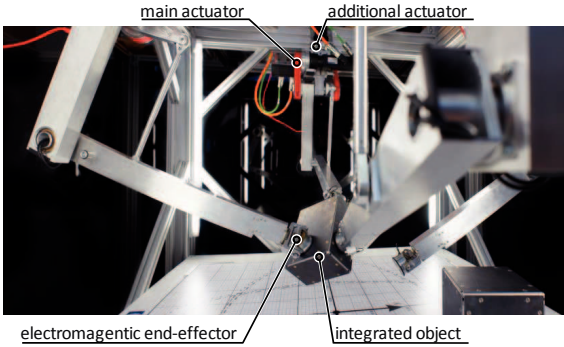
Figure 3-2: PARAGRIP prototype with 4 robotic arms (picture by Martin Riedel)

The PARAGRIP prototype shown in Figure 3-2 was implemented with four identical robotic arms. The main actuators are realized using standard servo drives in combination with form-fit traction belts, while the additional actuators are servo drives directly attached to the main axis of rotation. Two different types of end-effectors are implemented for the prototype: Electromagnetic end-effectors (see Figure 3-3a) were implemented originally due to the easy energy supply and control. Kurtenbach [Kur16] developed and realized vacuum end-effectors (see Figure 3-3b) to widen the range of objects that can be grasped.
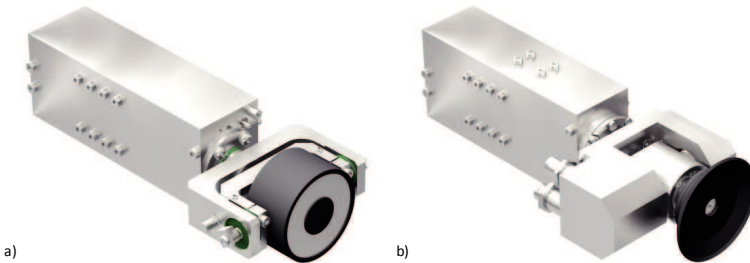
Figure 3-3: a) Electromagnetic, b) vacuum end-effector for the PARAGRIP handling system (see [Kur16])

Recent developments include the continuous extension of the modular handling concept, namely by the systematic analysis and development of different end-effectors by Kurtenbach [KHC15,Kur16] and the extension of the concept towards the handling and shaping of flexible components [ADI15,BDÜ17]. The improvement in the accuracy by self-calibration, kinematic calibration [DMH14] and stiffness modeling [DC16] is the focus of this thesis.

The kinematic calculations for the PARAGRIP were described by Riedel [Rie14] and will be applied and modified if applicable for the calibration purpose in this thesis. The definitions of variables, indices and coordinate systems are adopted as far as possible, to guarantee consistency in literature, calculations and software.

Nominal Serial Kinematics Model for the PARAGRIP Arm

Each PARAGRIP arm (see Figure 3-4) is composed of a planar 5-bar linkage (links 1-4 and joints A_0, A, B_0, B and C) that is rotated around the main axis (joint D_0). The superposition of the rotational motion along the fixed arm coordinate system $0Ai$ and the planar motion in the x-z-plane of the moving arm coordinate system Ai result in a spatial motion, suitable to position the end-effector. The differentiation between the different arms i is not considered in sections 4 and 5, as long as only a single arm is investigated.
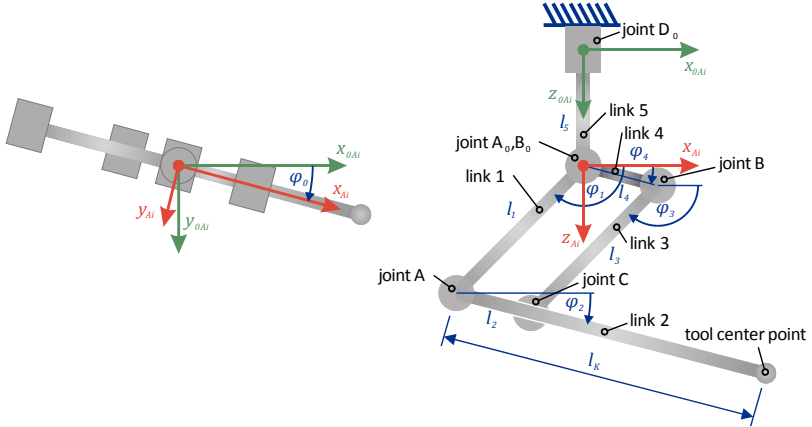
Figure 3-4: Coordinate systems and kinematic parameters for the PARAGRIP arm structure

For the ideal parallelogram composed of the links 1-4 with the nominal length $\hat{l}_1 = \hat{l}_3$ and $\hat{l}_2 = \hat{l}_4$, the nominal passive joint angles $\hat{\varphi}_2$ and $\hat{\varphi}_3$ are equal to the nominal joint angles $\hat{\varphi}_4$ and $\hat{\varphi}_1$:

$$\hat{\varphi}_2 = \hat{\varphi}_4 \tag{3.1}$$

$$\hat{\varphi}_3 = \hat{\varphi}_1 \tag{3.2}$$

The direct and inverse kinematics can be calculated analogously to a serial robotic arm. The according vector of nominal parameters $\hat{\boldsymbol{p}}_{ser}$ for the serial kinematics model is:

$$\hat{\boldsymbol{p}}_{ser} = (\hat{l}_1 \quad \hat{l}_k) \tag{3.3}$$

With the nominal link length $\hat{l}_1$ and $\hat{l}_k$ as shown in Figure 3-4.

The end-effector position is described using the position vector $\boldsymbol{r}_{TCP}$ of the tool center point (TCP, see Figure 3-5):

$$\boldsymbol{r}_{TCP} = \boldsymbol{r}(\hat{\boldsymbol{p}}_{ser}, \hat{\boldsymbol{\varphi}}) \tag{3.4}$$

$$^{0A}\boldsymbol{r}_{TCP} = \boldsymbol{R}_z(\hat{\varphi}_0) \cdot \begin{pmatrix} \hat{l}_1 \cdot cos(\hat{\varphi}_1) + \hat{l}_k \cdot cos(\hat{\varphi}_4) \\ 0 \\ \hat{l}_1 \cdot sin(\hat{\varphi}_1) + \hat{l}_k \cdot sin(\hat{\varphi}_4) \end{pmatrix} \tag{3.5}$$

With the nominal joint angle vector $\hat{\boldsymbol{\varphi}} = (\hat{\varphi}_0, \hat{\varphi}_1, \hat{\varphi}_4)$, the rotational matrix $\boldsymbol{R}_z$ and the nominal link length $\hat{l}_1$ and $\hat{l}_k$.

The inverse kinematic calculation for the PARAGRIP arm and handling system is described by Riedel [Rie14, p. 89–90].

Coordinate Systems and Wrist-Joint Angles for the End-Effector

The end-effectors shown in Figure 3-3 consist of three revolute joints used to provide the passive rotational DOF. The kinematic of the end-effector is expressed using the coordinate systems shown in Figure 3-5.
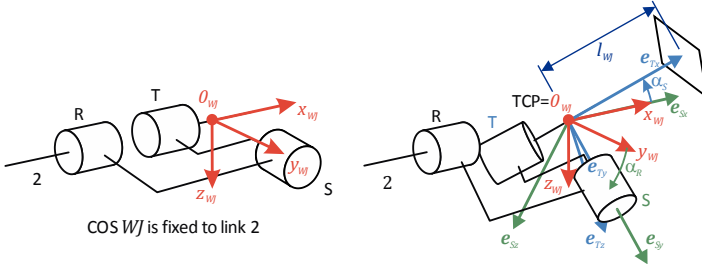
Figure 3-5: Coordinate System, joints and rotational angles for the PARAGRIP end-effector

The orientation of the consecutive axes R, S and T with respect to the fixed coordinate system WJ are expressed using the wrist-joint angles α_R and α_S. The rotation about axis T is not relevant for the kinematic calculation. The remaining distance from the TCP to the object surface is described by the wrist-joint offset l_{WJ} in direction of the unit vector $\boldsymbol{e}_{Tx}$ (see Figure 3-5).

4   Calibration by Kinematic Parameter Identification

The calibration of models and calculation procedures for robotic structures aims at the improvement of their quality and accuracy to describe the robotic structure and its behavior. In particular, the error of the end-effector poses with respect to a nominal pose or a reference trajectory is reduced. Deviations of the model parameters are reduced by identifying the actual parameters through the evaluation of external measurements and available information.

In principle, calibration can be applied to models of all complexities: To static, dynamic, rigid and flexible models including or excluding a variety of effects like friction, rigid body motion, backlash or the influence of the robot control system. Naturally, the effects taken into consideration and hence the complexity of the model limit the quality and accuracy that can be reached by calibration. At the same time, a higher model complexity increases the effort needed for a successful calibration and does not necessarily result in a better model quality after calibration. The identification of kinematic parameters, such as for example the length of the links, the offset of the driven joints from the encoder signal or the base position with respect to the global coordinate system, are referred to as kinematic calibration and will be detailed in the following sections. Roth and others [RMR87] classified this kinematic calibration as level 2 calibration, including the simpler level 1 (also called joint level) calibration, which is limited to the identification of the correct relationship of drive position transducer and the actual joint position. The more extensive calibration methods considering non-kinematic parameters like compliance, friction or dynamics are referred to as level 3 calibration. This classification into three levels is used widely, especially for articulated serial robots. Roth and others [RMR87] also state that kinematic calibration consists of the four sequential steps: Modeling, measurement, identification and compensation/correction. Elatta and others [EGZ04] give a comprehensive overview of the steps and different levels of calibration. An overview for the levels of calibration and sequential steps that are followed in this work is given in Figure 4-1.
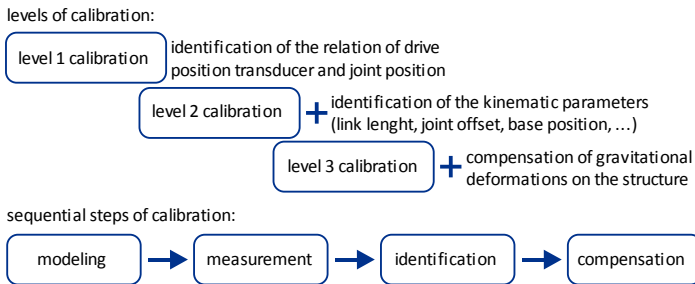

Figure 4-1: Levels and sequential steps of calibration

The model quality and accuracy that can be obtained by kinematic parameter identification does not solely depend on the approach chosen, but on the chosen measurement poses as well. An increased number of measurement poses enhances the reachable accuracy asymp-

totically to a certain limit value [DPM05]. An extensive expansion of the number of measured poses therefore is not productive. In fact, even more important than the number of poses is their sensitivity regarding the parameters of calibration. Appropriate methods to benchmark this sensitivity will be discussed in section 4.5, an overview is given by Sun and Hollerbach [SH08].

Kinematic calibration procedures are often classified by the type of robotic structure they are applied to, mainly distinguishing between parallel and serial manipulators but also hybrid structures. This is because the use of the direct or inverse kinematic calculations is not equally simple and meaningful for different structures. However, the methods, for example the use of external metrology, internal joint sensors or artificial motion restriction, in general can be used for different types of robotic structures.

In this work open loop, also called external calibration, and closed loop kinematic calibration are distinguished and considered. Similar and overlapping classifications are used in literature (for example [HW96,Mer06, p. 290,HLJ10]). To avoid confusions in the nomenclature, it should be noted that open and closed kinematic chains of a mechanism in literature often are named open and closed loops. In this thesis it is referred to open and closed loop for the classification of the calibration procedure only.

In open loop kinematic calibration external metrology is used to capture the position or pose of the end-effector or specific links. It is then compared to the prediction of the theoretical kinematic model to be calibrated. In closed loop kinematic calibration the residual between the theoretical kinematic model and the manipulators behavior is captured using redundancies and constraints in the system as detailed in section 6.1. In this section, the enhancement of the kinematic accuracy for a single arm of the handling system is performed with a level 2 open loop calibration. The extension to a level 3 calibration including the gravitational compensation for the structure is discussed in section 4.7. Details of the according stiffness modeling are given in section 5.

4.1   State of Research in Open Loop Calibration

Open loop kinematic calibration is characterized by using external metrology to precisely capture the end-effector pose or position of the manipulator. Even though open loop calibration is not restricted to open kinematic chains, it is well established and mainly applied for serial manipulators. In principle, the measurement of the end-effector pose can be performed with any metrology system with sufficient measurement accuracy. A good overview specifically for the commercially applied technologies is given by Nubiola and others [NSJ14]. The accuracy of the metrology system will influence the quality of the calibration and ideally it should be an order of magnitude better than the repeatability of the robotic structure. Examples are the laser interferometer used by Alici and Shirinzadeh [AS05], a laser tracker system used by Ying and others [YZR03], optical or mechanical coordinate measurement machines (CMM) used by Nefzi and others [NCH08] and Vischer and Clavel [VC00], visual

cameras used by Renaud and others [RVA06] or stereo vision systems used by Švaco and others [ŠŠŠ14].

The position and, if applicable, the orientation of the end-effector is captured for a set of robot poses. At the same time, the encoder signals for the drives are recorded for every measurement pose. Nubiola and others [NSJ14] compared the effectiveness of laser trackers and optical CMM including the optional measurement of the orientation. They conclude that both systems are equally effective and provide similar calibration results. The optical CMM can, however, be used much more efficiently, it is therefore used in this thesis (see section 4.3). The use of specific targets for the orientation measurement does not provide noticeably better results and in their conclusion is not beneficial for the calibration procedure, especially considering the high effort needed to design and calibrate the target itself.

For parameter identification, the theoretical end-effector position is calculated, using the direct kinematic model. The corrected kinematic parameters can be derived by numerical optimization to vary the kinematic parameters and minimize the deviation of the measured poses and the calculated theoretical poses. The numerical optimization can be implemented for example by means of the linear least square method used by Joubar and others [JZB15], the Levenberg–Marquardt method used by Ginani and Motta [GM11], the Kalman filter used by Park and others [PLC12], the singular value decomposition used by Agheli and Nategh [AN09] or artificial neural networks used by Wang and others [WBZ12].

The kinematic model is then corrected, using the best set of parameters from the optimization. To finally prove the success of the calibration, the absolute accuracy for the corrected kinematic model is measured.

There are two alternative approaches to the described open loop calibration procedure. The first approach is based on the independent analysis of each robot axis, called screw-axis measurements [HW96], rather than using the direct kinematics during identification. The parameters are based on an independent calculation for each joint and hence the relation between the identified parameters and the actual robot parameters are maintained more directly [GB93]. The joint axis direction and position are directly obtained from the measured movement of the following link by the so-called Circular Point Analysis [MRD91, p. 175–182]. The method is, however, strictly limited to serial robots with open chain kinematics.

The second approach is based on the direct error analysis to avoid limitations of the kinematic models. Tiang, Zeng and others [TZZ14,ZTL16] and Pastor and others [PKB13] proposed such an approach for serial robots: It is based on the error similarity analysis in the Cartesian workspace and relies on measured spatial data for the positioning error of the TCP. The error compensation is performed by modifying the target position coordinates, rather than the kinematic model. Gottlieb [Got14] proposed a parameter-free calibration of parallel structures. It is based on an error sample set in the configuration space and uses an interpolation of these correction factors. In contrast to the approach for serial robots, the error compensation is performed by modifying the drive positions and not the target positions in the Cartesian space.

In the following sections, a brief overview of the current state of research for open loop calibration for serial, parallel and hybrid structures is given to identify suitable approaches for the calibration of different handling systems.

4.1.1   Open Loop Calibration of Articulated Serial Robots

Open loop calibration has been established for serial robots, especially for the most popular articulated industrial robot since the 1980s [RMR87]. The principles have not changed even though the accuracy demands and the measurement technology have improved. The calculation of the direct kinematics is usually based on the Denavit-Hartenberg (DH) [DH55] model and parameters for serial structures. Numerical deficiencies for parallel consecutive joint axes, which cause redundant parameters and compromise the robustness of the calibration, led to new modeling approaches. Stone and Sanderson [SS88] suggested the S-Model to describe kinematics for the purpose of calibration. It is similar to the DH-notation, but does rely on additional parameters and transformations between coordinate systems. Zhuang and others [ZRH92] introduced the complete and parametrically continuous kinematic model that is based on singularity-free line parameters. Again, the approach is similar to the DH-notation and as compact, but specifically addressing the calibration. Hayati and Mirmirani [HM85] extended the DH-model by introducing an additional rotational parameter for nearly parallel axes (see Figure 4-2a). This approach is also known as Denavit-Hartenberg-Modified (DHM) and is commonly used for the calibration for serial [NB13,MdM01] as well as hybrid structures [AS05]. Schröder and others [SAG97] developed a systematic approach to set up DHM frames for arbitrary open kinematic chain structures. Okumura and Park [OP96] introduced the product of exponentials (POE) formula that is based on screw theory and avoids numerical singularities as found in DH-notation. It is robust against redundant parameters and as well widely used, for example by He and others [HLS14] and Chen and others [CWL14] for serial structures. Wu and others [YWL14] modified the POE formula by introducing a universal joint space description with independent kinematic parameters to simplify mathematical transformations needed in classical POE. Chen-Gang and others [CLC14] give a wide overview of kinematic calibration technologies of serial robots.
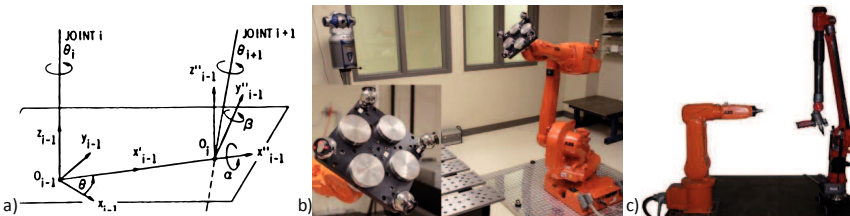

Figure 4-2:   Open loop calibration of articulated serial robots: a) DHM notation for near parallel revolute joints [HM85], b) experimental setup with a laser tracker [NB13], c) experimental setup with measurement arm [YWL14]

A selection of recent publications shows the range of accuracy improvement that can usually be achieved by open loop calibration for serial robots: Newman and others [NBH00], Wang and others [YWR06], Ginani and Motta [GM11], Švaco and others [ŠŠŠ14], Zeng and others [ZTL16], Lightcap and others [LHS08] and Nubiola and Bonev [NB13] provide recent measurement data for the open loop calibration for articulated serial robots. Details are not given here for the sake of compactness. The approaches differ from each other significantly with respect to the metrology system, the modeling and optimization approach and the number and characteristics of the considered poses. Therefore, this selection can only give an orientation to possible accuracies and not a comparative analysis of different approaches. Significant improvements of the accuracy can be achieved by open loop calibration. A remaining maximum position error of 0.7 mm and mean position error of 0.4 mm can be expected for a successful calibration of the kinematic model, at least when gravitational effects are considered. However, results with position errors two times as large can be observed for some approaches and set-ups as well. These values give a good orientation to assess the success of the calibration by kinematic parameter identification shown in this section.

4.1.2   Open Loop Calibration of Parallel Robots

While open loop calibration for serial robots is based on the calculation of the direct kinematics, this approach is rather challenging for parallel robots and rarely used. Everett and Lin [EL88,Eve89] extended the approach with additional constraints for every closed kinematic chain of the parallel robot. Masory and others [MWZ93,MJZ96] proposed a direct adaptation of the open loop principles used for serial robots. In more recent approaches the direct kinematics were applied to construct a compensation in Cartesian Space using neural networks [Yu08,GEF10]. However, the use of the direct kinematics is not common for the calibration of parallel robots, because it is not unique in most cases and often needs to be solved numerically, which is computationally intensive and not necessarily accurate.

The inverse kinematic calculations are less complex and are consequently commonly used for the open loop calibration of parallel structures. They can be solved separately for every kinematic chain of the parallel robot between end-effector and base. Each of these open chain calculations relates the end-effector pose to the position of the drives, similar to the inverse kinematics of a serial robot, and has an analytical solution in most cases. The fitness function in the optimization process is based on the residual of the position of the drives. The theoretical drive position for a measured end-effector pose is calculated and compared to the actual drive positions.

Wampler and others [WA92,WHA95] introduced the implicit loop formulation for serial and parallel robots as a unified approach. All constraints of the mechanism are treated by the same formulation of implicit loops, which includes closed kinematic chains of the mechanism and open chains with a measured end-effector position. For each implicit loop the sum of all displacements around the kinematic chains is claimed to be zero, taking into account kinematic and sensor parameters as well as measured and possibly unknown displacements. The

formulation of these implicit loops is analyzed statistically, based on the maximum-likelihood principle, to identify the parameters and achieve an estimation of the parameter and pose errors. Zuang and Yan [ZYM98] followed a similar formulation and advanced the approach to solve the system of equations. They introduced a cost function for the deviation and an identification Jacobian to determine the kinematic parameters from the linearized constraint equations. Another extension was proposed by Oliviers and Mayer [OM95]: The system of equations is solved using the singular value decomposition as a best approximation for a minimal least-square error. The implicit loop formulation and its adaptions describe the fundamental approach for the calibration of parallel robots and are widely used.

Based on the diversity in the possible formulations for the constraint equations, the according solving strategies, the types of available measurements and the kinematic structures, the variety of open loop calibration procedures is considerably higher than for the more standardized articulated serial robots. Majarena and others [MSS10], Last and others [LRH10, p. 93–106] and Hernández-Martínez and others [HLJ10] give an extensive overview regarding the different calibration methods and specific considerations for parallel manipulators.

A selection of publications indicate the range of accuracy improvement that can be achieved by open loop calibration for parallel robots: Bai and others [BMH16] (see Figure 4-3a), Zhang and others [ZDT16] (see Figure 4-3b), Traslosheros and others [TST13] (see Figure 4-3c), Chiang and others [CLH11], Ecorchard [Eco10], Rauf and others [RPR06], Meng and others [MTW03], Iuraşcu and Park [IP03] and Vischer and Clavel [VC00] provide experimental verifications for the open loop calibration for parallel robots.
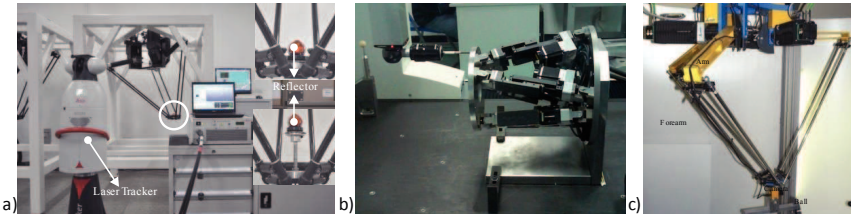
Figure 4-3: Open loop calibration of parallel robots: a) Delta robot with laser tracker [BMH16], b) Cutting machine with bridge type CMM [ZDT16], c) Delta robot with attached camera [TST13]

As the mechanisms investigated and their accuracy properties vary significantly, this selection only gives a rough orientation regarding possible accuracies and not a comparative analysis of different approaches. Remaining maximum position errors of about 0.2-1.7 mm and mean position errors of 0.05-1.6 mm were achieved. The improvement factor from the nominal to the calibrated model usually ranged between 2 and 15.

4.1.3   Open Loop Calibration of Hybrid Robotic Structures

To reduce the masses in movement and increase the performance of serial manipulators, a direct drive gear in a serial structure can be substituted by a closed kinematic chain, forming an overall hybrid structure. Examples are the investigated 3 DOF PARAGRIP arm structure

(see Figure 3-1b), 4 DOF industrial robots for palletizing, like the KR 40 PA [KUK17], as well as 6 DOF general purpose industrial robots, like the ABB IRB 2400 [ABB16]. Klimchik and others [KMA16,KMC16] showed that hybrid or quasi-serial industrial robots are preferable for large-scale tasks.

Neither the calibration approaches for serial nor for parallel robots can be directly applied to hybrid structures. The constraint equation for the closed kinematic chain needs to be considered to solve the kinematics of the driven link and the parameter redundancies induced by the closed kinematic chain need to be accounted for in the modeling approach. Common approaches for serial robots like the introduced DHM-notation can be adapted and applied for hybrid structures.
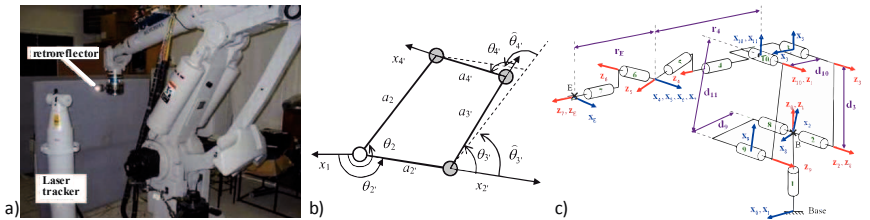
Ananthanarayanan and others [ASG92] fully described the kinematics of a general four-bar mechanism used as a manipulator, however, they did not apply a general calibration procedure, but individually identified the link length by measurements of the mechanically constrained mechanism. Schroer and others [SAL97] introduced a general formulation to solve the kinematic description of an actuated planar crank-slider mechanism and planar four-bar mechanisms for its passive joint values and integrate the solution to the kinematic description of the serial manipulator. Experiments showed a reduction of the mean positioning error from 0.65 mm to 0.34 mm, and to 0.18 mm considering elasticities as well. Alici and Shirinzade [AS05] (see Figure 4-4a) proposed a reduced modeling approach, neglecting most of the DH parameters of the passive joints. The accuracy was improved by a factor of 2.5, the remaining mean position error of 3.3 mm, however, seems to be comparatively insufficient, even though different experimental setups and measurement systems cannot be compared directly. Marie and Maurine [MM08] described a systematic analytical description of the geometrical and elastic error models for hybrid robot structures similar to Schroer and others [SAL97].

Figure 4-4: Open loop calibration of hybrid robots: a) experimental setup for calibration [AS05], b) degenerated parallelogram structure [TW12], c) structure of a palletizing robot [MM08]

To and Webb [TW12] (see Figure 4-4b) proposed a linearized approach for the analysis of a general serial manipulator with hybrid parallelogram structure. They applied Hayatis DHM-notation to describe the kinematics and analyzed the 4-bar linkage to describe the not ideal parallelogram. In contrast to Marie and Maurine [MM08] (see Figure 4-4c), they linearized the highly non-linear geometric terms and eliminated dependent parameters for their model. In comparison to the ideal model, the mean positioning error is reduced slightly. Taking

into account the compensation of gravitational effects as well, the consideration of the parallelogram did improve the calibration quality by a factor of 2, achieving a mean position error of 0.8 mm and 0.4 mm, respectively. Consequently, the hybrid kinematics model will be investigated and compared to the serial kinematics model for the PARAGRIP handling system.

4.2   Extended Kinematic Models for the PARAGRIP Arm

The kinematic model chosen for the kinematic calibration should be complete, minimal and consistent [Eco10, p. 39]. A complete model takes all error sources into account and hence, allows for their compensation after the calibration process. Naturally the number of identifiable error sources is limited by the calibration process itself, depending on the implemented method and measurement accuracy. Therefore, a careful consideration of the necessary parameters is needed. A complete model is minimal, if it does not contain redundant parameters that would hinder the unique parameter identification. This is particularly important for closed kinematic chains, were parameters are interrelated [EL88]. In a consistent model small variation of the mechanisms geometry results in accordingly small changes of the model parameters. An already introduced example to deal with the consistency of a model is the DHM notation by Hayati and Mirmirani [HM85] for consecutive parallel axis. Certainly, obtaining an according model to reach the optimal accuracy is not trivial, furthermore, the models are usually not generalizable and specific to the system under study [MSS10, p. 10273].

For the PARAGRIP arm different ways are possible to describe the kinematics. The most extensive one considering a complete DHM-notation leads to a set of 40 parameters: 6 parameters for the offset of the arm coordinate system $A0i$, 25 parameters for the joints (A_0, B_0, A, B, C), 4 parameters for the TCP and 5 additional MDH-parameters between joints A and C for the closed loop constraints. This parameter selection, however, is not minimal, as it contains redundancies. It is not complete, as a large set of parameters can be assumed to be negligible and not identifiable with the accuracy of standard external metrology. In a previous contribution different reduced models for the PARAGRIP arm were investigated [DMH14]. The considerations are continued in this section.

A serial and a hybrid model shown in Figure 4-5a and b are investigated and compared. The rotational axes of the planar linkage are assumed to be ideally parallel and coinciding for joints A_0 and B_0 (see Figure 3-4). Any displacement of the planar linkage perpendicular to the plane is expressed using the displacement Δy_{TCP} of the TCP.

The offset of the arm coordinate system is expressed using three translational and two rotational offsets $\Delta x, \Delta y, \Delta z, \Delta\alpha$ and $\Delta\beta$. The rotational offset around the z-axis is integrated into $\Delta\varphi_0$. For the more complex hybrid kinematics model, an additional parameter Δx_{axis} is introduced to account for offsets of coordinate system Ai with respect to the main axis of rotation (joint D_0) fixed to coordinate system $A0i$. The model parameters are listed in Table 4-1.
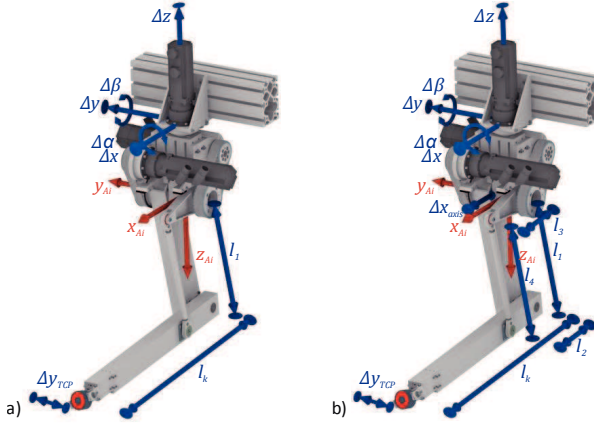
Figure 4-5: a) Serial, b) hybrid kinematics model of the PARAGRIP arm

model	model parameter	
serial kinematics	11	$\varphi_0, \varphi_1, \varphi_4, l_1, l_k, \Delta x, \Delta y, \Delta z, \Delta y_{TCP}, \Delta\alpha, \Delta\beta$
hybrid kinematics	15	$\varphi_0, \varphi_1, \varphi_4, l_1, l_2, l_3, l_4, l_k, \Delta x, \Delta y, \Delta z, \Delta y_{TCP}, \Delta\alpha, \Delta\beta, \Delta x_{axis}$

Table 4-1: Model parameters for the PARAGRIP arm serial and hybrid kinematics model

The parameter deviations $\Delta\varphi_i$ and Δl_i describe the deviation of the actual parameter values φ_i and l_i from their nominal values $\hat{\varphi}_i$ and $\hat{l}_i$:

$$\varphi_i = \hat{\varphi}_i + \Delta\varphi_i \tag{4.1}$$

$$l_i = \hat{l}_i + \Delta l_i \tag{4.2}$$

The displacement of the arm TCP position vector $\Delta\boldsymbol{r}$ in comparison to the nominal model can be calculated from the vector of parameter deviations $\Delta\boldsymbol{p}$ using the Jacobian matrix of parameters $\boldsymbol{J}_p$:

$$\Delta\boldsymbol{r} = \boldsymbol{J}_p \cdot \Delta\boldsymbol{p} \tag{4.3}$$

Serial Kinematics Arm Model

The parallelogram is assumed to be ideal for the serial kinematics model. The direct kinematic calculation introduced in equation (3.5) is extended to account for the introduced calibration parameters:

$$\boldsymbol{r}_{TCP} = \boldsymbol{r}(\hat{\boldsymbol{p}}_{ser}, \Delta\boldsymbol{p}_{ser}, \hat{\boldsymbol{\varphi}}) \tag{4.4}$$

With the nominal parameter vector $\hat{\boldsymbol{p}}_{ser}$ and the nominal joint angle vector $\hat{\boldsymbol{\varphi}}$.

$$^{0A}\boldsymbol{r}_{TCP} = \boldsymbol{R}_y(\Delta\beta) \cdot \boldsymbol{R}_x(\Delta\alpha) \cdot \boldsymbol{R}_z(\varphi_0) \cdot \begin{pmatrix} l_1 \cdot cos(\varphi_1) + l_k \cdot cos(\varphi_4) \\ \Delta y_{TCP} \\ l_1 \cdot sin(\varphi_1) + l_k \cdot sin(\varphi_4) \end{pmatrix} + \begin{pmatrix} \Delta x \\ \Delta y \\ \Delta z \end{pmatrix} \tag{4.5}$$

With the rotational matrices $\boldsymbol{R}_y$, $\boldsymbol{R}_x$ and $\boldsymbol{R}_z$.

The according vector of parameter deviations $\Delta \boldsymbol{p}_{ser}$ for the serial kinematics model is:

$$\Delta \boldsymbol{p}_{ser} = (\Delta \varphi_0 \ \ \Delta \varphi_1 \ \ \Delta \varphi_4 \ \ \Delta l_1 \ \ \Delta l_k \ \ \Delta x \ \ \Delta y \ \ \Delta z \ \ \Delta y_{TCP} \ \ \Delta \alpha \ \ \Delta \beta) \tag{4.6}$$

Hybrid Kinematics Arm Model

In the hybrid kinematics model the parallelogram is not considered ideal and the closed kinematic chain is accounted for explicitly. The redundancies occurring in the closed kinematic chains need to be analyzed to identify redundancies and guarantee completeness of the model. The identifiable parameters can be analyzed by calculation of the Jacobian matrices for the kinematic parameters of the linearized model [SK16, p. 118]. To and Webb [TW12] applied this general approach to a hybrid manipulator containing a parallelogram using the MDH-notation. Here the approach is applied in a similar way for the specific kinematic description of the PARAGRIP arm.

The vector of parameter deviations $\Delta \boldsymbol{p}$ is composed of the relevant kinematic parameters of the additional kinematic chain in the parallelogram. The parameter deviations $\Delta \varphi_1$ and Δl_1 of the serial link are not considered.

$$\Delta \boldsymbol{p} = (\Delta \varphi_2 \ \ \Delta \varphi_3 \ \ \Delta \varphi_4 \ \ \Delta l_2 \ \ \Delta l_3 \ \ \Delta l_4) \tag{4.7}$$

The Jacobian matrix of parameters $\boldsymbol{J}_p$ is composed of the Jacobian matrices $\boldsymbol{J}_{li}$ and $\boldsymbol{J}_{\varphi i}$ related to these parameters:

$$\boldsymbol{J}_p = (\boldsymbol{J}_{\varphi_2} \ \ \boldsymbol{J}_{\varphi_3} \ \ \boldsymbol{J}_{\varphi_4} \ \ \boldsymbol{J}_{l_2} \ \ \boldsymbol{J}_{l_3} \ \ \boldsymbol{J}_{l_4}) \tag{4.8}$$

The parallelogram forms a 4-bar linkage and is calculated using the vector sum to account for the position constraints:

$$\boldsymbol{l_1} + \boldsymbol{l_2} = \boldsymbol{l_3} + \boldsymbol{l_4} \tag{4.9}$$

This can be rewritten using the joint angles φ_i and link length l_i:

$$l_1 \cdot cos(\varphi_1) + l_2 \cdot cos(\varphi_2) = l_3 \cdot cos(\varphi_3) + l_4 \cdot cos(\varphi_4) \tag{4.10}$$

$$l_1 \cdot sin(\varphi_1) + l_2 \cdot sin(\varphi_2) = l_3 \cdot sin(\varphi_3) + l_4 \cdot sin(\varphi_4) \tag{4.11}$$

The passive joint angles φ_2 and φ_3 are unknown and need to be calculated from the kinematics of the deformed parallelogram. The implicit calculation of the position functions e and f needed for the direct kinematic calculation is given in Annex 9.1:

$$\varphi_2 = e(l_1, l_2, l_3, l_4, \varphi_1, \varphi_4) \tag{4.12}$$

$$\varphi_3 = f(l_1, l_2, l_3, l_4, \varphi_1, \varphi_4) \tag{4.13}$$

Considering small deviations $\Delta \varphi$ and Δl from the nominal values, the deviations $\Delta \varphi_2$ and $\Delta \varphi_3$ can be calculated from the linearization of equations (4.12) and (4.13):

$$\Delta \varphi_2 = \frac{\partial e}{\partial \varphi}\bigg|_{\Delta l=0} \cdot \Delta \varphi + \frac{\partial e}{\partial l}\bigg|_{\Delta \varphi=0} \cdot \Delta l \tag{4.14}$$

$$\Delta \varphi_3 = \frac{\partial f}{\partial \varphi}\bigg|_{\Delta l=0} \cdot \Delta \varphi + \frac{\partial f}{\partial l}\bigg|_{\Delta \varphi=0} \cdot \Delta l \tag{4.15}$$

Instead of deriving the linearization of the complex functions (4.12) and (4.13) directly, the linearization can be assembled from the derivatives of the ideal joint angles and the position constraints. The derivative of the ideal joint angles in equations (3.1) and (3.2) is:

$$\Delta\varphi_2 = \Delta\varphi_4 \tag{4.16}$$

$$\Delta\varphi_3 = \Delta\varphi_1 \tag{4.17}$$

Considering the parameter errors $l_i = \hat{l}_i + \Delta l_i$, the derivative of the position constraints in equations (4.10) and (4.11) is obtained:

$$\begin{aligned}(\hat{l}_1 + \Delta l_1)\cdot cos(\hat{\varphi}_1) + (\hat{l}_2 + \Delta l_2)\cdot cos(\hat{\varphi}_2 + \Delta\varphi_2) = \\ (\hat{l}_3 + \Delta l_3)\cdot cos(\hat{\varphi}_3 + \Delta\varphi_3) + (\hat{l}_4 + \Delta l_4)\cdot cos(\hat{\varphi}_4)\end{aligned} \tag{4.18}$$

$$\begin{aligned}(\hat{l}_1 + \Delta l_1)\cdot sin(\hat{\varphi}_1) + (\hat{l}_2 + \Delta l_2)\cdot sin(\hat{\varphi}_2 + \Delta\varphi_2) = \\ (\hat{l}_3 + \Delta l_3)\cdot sin(\hat{\varphi}_3 + \Delta\varphi_3) + (\hat{l}_4 + \Delta l_4)\cdot sin(\hat{\varphi}_4)\end{aligned} \tag{4.19}$$

Where $\hat{l}_3 = \hat{l}_1$, $\hat{l}_2 = \hat{l}_4$, $\hat{\varphi}_3 = \hat{\varphi}_1$ and $\hat{\varphi}_2 = \hat{\varphi}_4$.

By ignoring high-order terms and by linearization of the cosine and sine function (see Annex 9.2) $\Delta\varphi_2$ and $\Delta\varphi_3$ are obtained:

$$\Delta\varphi_2 = \underbrace{\frac{1}{\hat{l}_4}\cdot\frac{-cos(2\cdot\hat{\varphi}_1)}{sin(\hat{\varphi}_4 - s\hat{\varphi}_1)}}_{m_1}\cdot(\Delta l_3 - \Delta l_1) + \underbrace{\frac{1}{\hat{l}_4}\cdot\frac{-cos(\hat{\varphi}_1 + \hat{\varphi}_4)}{sin(\hat{\varphi}_4 - s\hat{\varphi}_1)}}_{m_2}(\Delta l_4 - \Delta l_2) \tag{4.20}$$

$$\Delta\varphi_3 = \underbrace{\frac{1}{\hat{l}_1}\cdot\frac{cos(\hat{\varphi}_1 + \hat{\varphi}_4)}{sin(\hat{\varphi}_1 - \hat{\varphi}_4)}}_{m_3}\cdot(\Delta l_3 - \Delta l_1) + \underbrace{\frac{1}{\hat{l}_1}\cdot\frac{-cos(2\cdot\hat{\varphi}_4)}{sin(\hat{\varphi}_1 - \hat{\varphi}_4)}}_{m_4}\cdot(\Delta l_4 - \Delta l_2) \tag{4.21}$$

Combining equations (4.16) and (4.17) (joint angles) with (4.20) and (4.21) (position constraints), the assembled linearization of the position functions is obtained:

$$\Delta\varphi_2 = \Delta\varphi_4 + m_1\cdot(\Delta l_3 - \Delta l_1) + m_2\cdot(\Delta l_4 - \Delta l_2) \tag{4.22}$$

$$\Delta\varphi_3 = \Delta\varphi_1 + m_3\cdot(\Delta l_3 - \Delta l_1) + m_4\cdot(\Delta l_4 - \Delta l_2) \tag{4.23}$$

The elements of the introduced Jacobian matrix of parameters J_p can be calculated analogously to the Jacobian matrices introduced for the MDH-notation in [HKG16, p. 119]:

$$J_{l_i} = \begin{pmatrix} e_{xi} \\ 0 \end{pmatrix} \tag{4.24}$$

e_{xi} is the unit vector of the x-axis for the according frame of joint i.

$$J_{\varphi_i} = \begin{pmatrix} e_{zi-1} \\ e_{zi-1} \times p_{zi-1} \end{pmatrix} \tag{4.25}$$

e_{zi-1} is the unit vector of the z-axis for the previous frame of joint i.

Here the formal DH-notation does not need to be fully applied. The position of the element coordinate systems introduced by [Rie14] largely corresponds to the according DH-notation as shown in Figure 4-6. Only the coordinate system $2'$ was added to comply with the DH-notation for the investigated kinematic chain. The z-axes according to DH-notation are not shown, they do not coincide with the general notation for the PARAGRIP arm as introduced by [Rie14] and as used in this thesis. The joint angles φ_i are proportional to the according DH joint angles θ_{ji} and the parameter deviations and Jacobian matrices are equivalent.
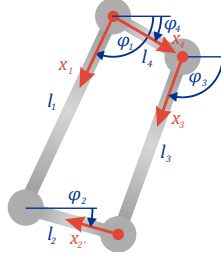
Figure 4-6: Coordinate systems for the PARAGRIP arm parallelogram

Equation (4.3) is extended by explicitly writing $\Delta \boldsymbol{p}$ from equation (4.7) and replacing $\Delta \varphi_2$ and $\Delta \varphi_3$ using equations (4.20) and (4.21):

$$\Delta \boldsymbol{r} = \underbrace{(\boldsymbol{J}_{\varphi_2} \quad \boldsymbol{J}_{\varphi_3} \quad \boldsymbol{J}_{\varphi_4} \quad \boldsymbol{J}_{l_2} \quad \boldsymbol{J}_{l_3} \quad \boldsymbol{J}_{l_4})}_{\boldsymbol{J}_p} \cdot \underbrace{\begin{pmatrix} \Delta \varphi_4 + m_1 \cdot (\Delta l_3 - \Delta l_1) + m_2 \cdot (\Delta l_4 - \Delta l_2) \\ \Delta \varphi_1 + m_3 \cdot (\Delta l_3 - \Delta l_1) + m_4 \cdot (\Delta l_4 - \Delta l_2) \\ \Delta \varphi_4 \\ \Delta l_2 \\ \Delta l_3 \\ \Delta l_4 \end{pmatrix}}_{\Delta \boldsymbol{p}} \tag{4.26}$$

By rearranging the resulting matrix equation, the new Jacobian matrices $\boldsymbol{J'}_{li}$ and $\boldsymbol{J'}_{\varphi i}$ are calculated for the corresponding parameters in equations (4.22) and expressed as a function of the original $\boldsymbol{J}_{li}$ and $\boldsymbol{J}_{\varphi i}$:

$$\Delta \boldsymbol{r} = (\boldsymbol{J'}_{\varphi_1} \; \boldsymbol{J'}_{\varphi_4} \; \boldsymbol{J'}_{l_1} \; \boldsymbol{J'}_{l_2} \; \boldsymbol{J'}_{l_3} \; \boldsymbol{J'}_{l_4}) \cdot \begin{pmatrix} \Delta \varphi_1 \\ \Delta \varphi_4 \\ \Delta l_1 \\ \Delta l_2 \\ \Delta l_3 \\ \Delta l_4 \end{pmatrix} \tag{4.27}$$

$$\boldsymbol{J'}_{\varphi_1} = \boldsymbol{J}_{\varphi_3} \tag{4.28}$$

$$\boldsymbol{J'}_{\varphi_4} = \boldsymbol{J}_{\varphi_2} \tag{4.29}$$

$$\boldsymbol{J'}_{l_1} = -m_1 \cdot \boldsymbol{J}_{\varphi_2} - m_3 \cdot \boldsymbol{J}_{\varphi_3} \tag{4.30}$$

$$\boldsymbol{J'}_{l_2} = -m_2 \cdot \boldsymbol{J}_{\varphi_2} - m_4 \cdot \boldsymbol{J}_{\varphi_3} + \boldsymbol{J}_{l_2} \tag{4.31}$$

$$\boldsymbol{J'}_{l_3} = m_1 \cdot \boldsymbol{J}_{\varphi_2} + m_3 \cdot \boldsymbol{J}_{\varphi_3} + \boldsymbol{J}_{l_3} \tag{4.32}$$

$$\boldsymbol{J'}_{l_4} = m_2 \cdot \boldsymbol{J}_{\varphi_2} + m_4 \cdot \boldsymbol{J}_{\varphi_3} + \boldsymbol{J}_{l_4} \tag{4.33}$$

Note that $\Delta \varphi_1$ and Δl_1 are now included in the vector of parameter deviations $\Delta \boldsymbol{p}$, even though they are not part of the originally investigated additional kinematic chain composed of link 4, link 3 and link 2.

As links 2 and 4 are designed to be parallel, it can be stated that $e_{x2'} = -e_{x4}$ for small deviations:

$$J_{l_2} = \begin{pmatrix} e_{x2'} \\ 0 \end{pmatrix} = -\begin{pmatrix} e_{x4} \\ 0 \end{pmatrix} = J_{l_4} \tag{4.34}$$

With equations (4.31) and (4.33), it can be seen that $J'_{l_2} = -J'_{l_4}$. Therefore, J'_{l_2} and J'_{l_4} are linearly dependent and hence Δl_2 and Δl_4 are redundant. It can be seen from equations (4.30) and (4.32) , that Δl_1 and Δl_3 are not redundant because J'_{l_1} and J'_{l_3} are linearly independent. This can be interpreted as follows: In the parallelogram of the PARAGRIP arm, the pair of link 2 and link 4 does only drive link 2, hence their ratio of length is decisive for the kinematic properties; theoretically their absolute length is irrelevant. Of course this only applies as long as the parameter deviations are small and the linearization can be assumed to be valid. This is different for the pair of link 1 and link 3: The absolute length of link 1 changes the properties of the main kinematic chain, namely the position of link 2 and the attached TCP.

Consequently, the parameter deviation Δl_4 is excluded from the parameter identification. Considering the 14 relevant parameters of the hybrid structure in Table 4-1 the vector of parameter deviations $\Delta \boldsymbol{p}_{hyb}$ for the hybrid kinematics model is:

$$\Delta \boldsymbol{p}_{hyb} = (\Delta \varphi_0 \ \ \Delta \varphi_1 \ \ \Delta \varphi_4 \ \ \Delta l_1 \ \ \Delta l_2 \ \ \Delta l_3 \ \ \Delta l_k \ \ \Delta x \ \ \Delta y \ \ \Delta z \ \ \Delta y_{TCP} \ \ \Delta \alpha \ \ \Delta \beta \ \ \Delta x_{axis}) \tag{4.35}$$

The according nominal vector of parameters $\widehat{\boldsymbol{p}}_{hyb}$ for the hybrid kinematics model is:

$$\widehat{\boldsymbol{p}}_{hyb} = (\hat{l}_1 \ \ \hat{l}_k \ \ \hat{l}_2 \ \ \hat{l}_3 \ \ \hat{l}_4) \tag{4.36}$$

The direct kinematics introduced in equation (3.5) is modified to account for the introduced calibration parameters:

$$\boldsymbol{r}_{TCP} = \boldsymbol{r}(\widehat{\boldsymbol{p}}_{hyb}, \Delta \boldsymbol{p}_{hyb}, \widehat{\boldsymbol{\varphi}}) \tag{4.37}$$

With the nominal joint angle vector $\widehat{\boldsymbol{\varphi}}$.

$$^{0A}\boldsymbol{r}_{TCP} = \boldsymbol{R}_y(\Delta\beta) \cdot \boldsymbol{R}_x(\Delta\alpha) \cdot \boldsymbol{R}_z(\varphi_0) \cdot \begin{pmatrix} l_1 \cdot cos(\varphi_1) + l_k \cdot cos(\varphi_2) + \Delta x_{axis} \\ \Delta y_{TCP} \\ l_1 \cdot sin(\varphi_1) + l_k \cdot sin(\varphi_2) \end{pmatrix} + \begin{pmatrix} \Delta x \\ \Delta y \\ \Delta z \end{pmatrix} \tag{4.38}$$

Note that φ_2 is calculated according to equation (4.12) using the actual parameters l_1, l_2, l_3, φ_1 and φ_4 and the nominal link length $\hat{l}_4$.

4.3   Measurement Procedure

The implemented measurement procedure is used to capture the end-effector position $\boldsymbol{r}_{TCP}$ and the actual drive positions $\boldsymbol{\varphi}$. The drive positions are captured from the drive encoders and the end-effector position is captured using an optical CMM as shown in Figure 4-7. The optical CMM records the position of infrared Light Emitting Diodes (LED) attached to moving objects or the hand-held SpaceProbe with probe tip. The pulsed signal of the LEDs is captured by three linear optical cameras and the position is processed by triangulation.
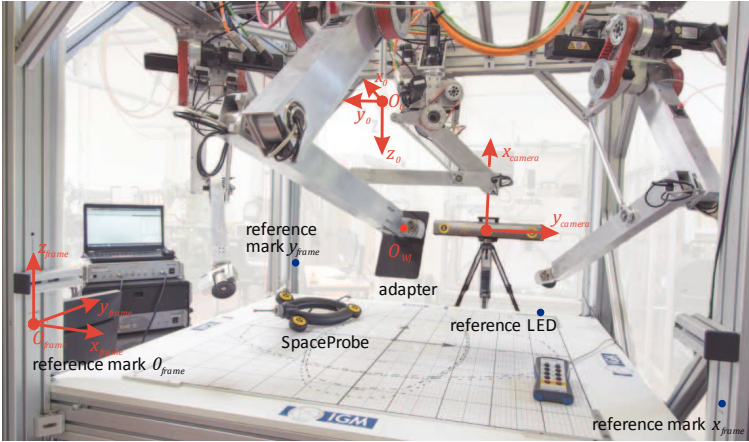
Figure 4-7: Coordinate systems and reference points for the Nikon K600 measurement system and the
           PARARGRIP handling system

The specified accuracies (see Table 4-2) are inhomogeneous because of the positioning of
the three linear cameras. The captured signal is less sensitive to changes close to the direction of sight z_{camera}.

	x_{camera}	y_{camera}	z_{camera}
SpaceProbe static accuracy (±2σ interval)	0.015 mm	0.015 mm	0.06 mm
single LED dynamic accuracy (±2σ interval)	0.025 mm	0.025 mm	0.09 mm
repeatability for the hand-held space probe (±4σ interval)	0.09 mm		

Table 4-2: Accuracy characteristics specified by the supplier [Met06] for the measurement distance of 3-4.5 m

All LED signals are captured for a time sequence of 1 second at 50 Hz measurement frequency and the position r is calculated as mean value $\bar{r}$ of the captured data to reduce the influence of measurement noise.

The captured positions are expressed in the camera coordinate system and transformed to
the global coordinate system 0 via the frame coordinate system. The reference marks are
captured with a hand-held SpaceProbe and used to define the transformation from the camera coordinate system to the frame coordinate system. This transformation is dependent on
the camera position and repeated for each measurement. The second transformation from
the frame to the global coordinate system is invariant and defined by the frame dimensions
and arm positions.

Figure 4-8 shows the frequency distribution for the continuously measured position of a
fixed reference LED on the frame to assess the accuracy of the aforementioned measurement and transformation procedure.

Four different measurements were performed at different times and from different camera positions. The first two measurements of the fixed reference LED were repeated for an unchanged camera position to evaluate the measurement drift. For all measurements, the position of the reference LED expressed in the global coordinate system 0 should ideally be identical. Measurement errors for the reference marks and the LED position superimpose and the maximum deviation is below 0.1 mm in y_0 and z_0-direction and 0.25 mm in the less accurate x_0 or z_{camera} direction (see Table 4-3). The measured position for the ^0x, ^0y and ^0z position of the reference LED drifted by 0.04 mm, 0.01 mm and 0.03 mm during the 3 h measurement 1 and the drift can be observed to be noticeably larger in the x_0 direction during the 7 h measurement 2. This behavior is not critical for a typical 1-2 hour lasting calibration measurement.
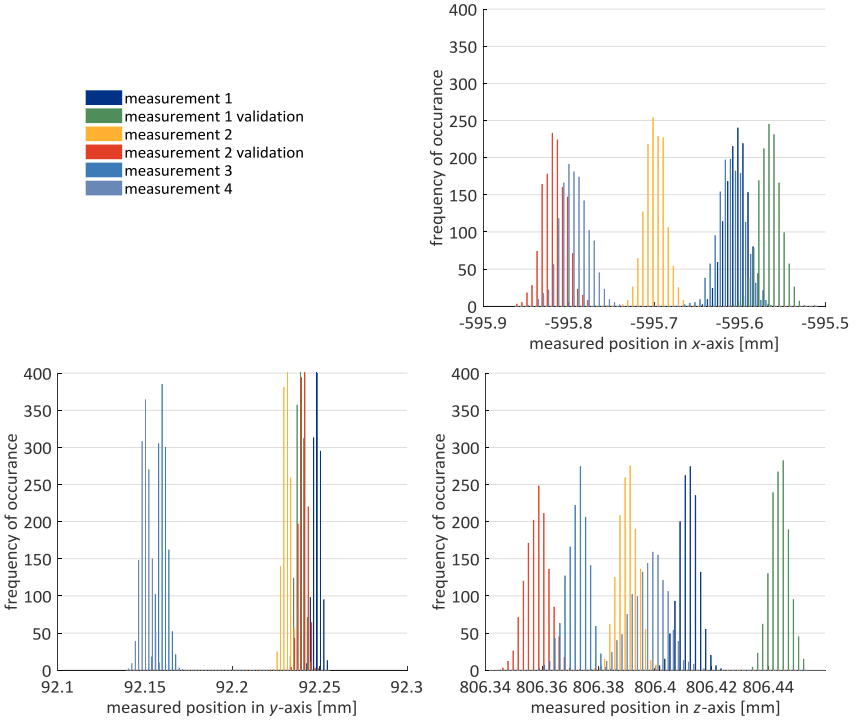

Figure 4-8:   Frequency distribution for the measured position of the reference LED (4 different measurements)

The measured frequency distribution for the static reference LED has a standard deviation σ of 0.014 mm, 0.002 mm and 0.004 mm for the ^0x, ^0y and ^0z position for a 27 s measurement with 1350 data points. This validates the specified static accuracy characteristics: Even though the static single LED accuracy is not specified and cannot be compared directly, the $\pm 2\sigma$ interval accuracy for the static SpaceProbe (with multiple LEDs) is 4 times as large as the measured σ.

	x_0-direction	y_0-direction	z_0-direction
standard deviation σ of the frequency distribution	0.014 mm	0.002 mm	0.004 mm
maximum deviation of the reference LED position within 4 measurements	0.253 mm	0.099 mm	0.086 mm
position drift for measurement 1 (3 h duration)	0.04 mm	0.01 mm	0.04 mm
position drift for measurement 2 (7 h duration)	0.12 mm	0.01 mm	0.04 mm

Table 4-3: Accuracy characteristics for the measurement procedure (measurement distance of 4 m)

Concluding, using the reference frame for an intermediate transformation results in a good alignment of the measurements. However, the coordinate transformations are rather sensitive to measurement errors of the reference point: Considering the maximum deviation of 0.25 mm, the comparison of absolute positions between measurements should be treated carefully. For the sake of completeness and with high relevance of the practical implications: The described measurement procedure is functional and accurate, it is, however, not necessarily robust. A variety of disturbances (for example air turbulences from the heating, limited and distracted visibility for the optical system or mechanical vibrations) need to be considered and were eliminated during many preliminary measurements.

The end-effector position r_{TCP} is defined by the mid-point of the spherical wrist-joint O_{WJ} (compare Figure 3-5) and cannot be captured directly. It is measured indirectly by capturing the position of three LEDs on an attached adapter (see Figure 4-9). The adapter is rotated with respect to the three wrist-joint axes of the fixed arm while capturing the LED positions that perform a spherical movement around O_{WJ}.
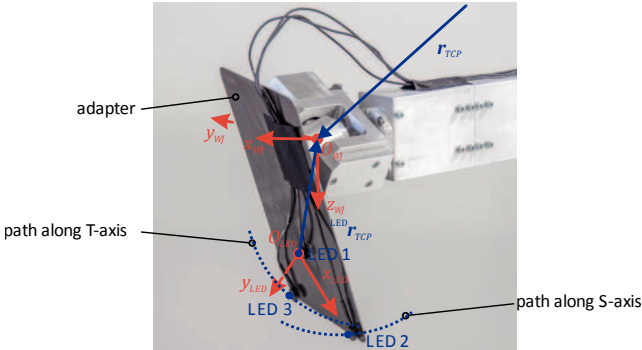

Figure 4-9: Reference LEDs on adapter plate to measure the end-effector position

The end-effector position $^{LED}r_{TCP}$ with respect to the measured LED coordinate system is identified by fitting each LED path to a sphere. This identification can be considered reliable and accurate, the mean deviation of path and sphere ranges between 0.05 mm and 0.08 mm for the performed measurements.

4.4   Absolute Accuracy and Repeatability

The accuracy of a robot or handling system is described by a variety of measures, for example the trajectory accuracy, the overshoot accuracy or even the stiffness of a structure. In this thesis, the repeatability and absolute accuracy for a static pose are used. Following the EN ISO 9283 standard [Eur98], the repeatability and absolute accuracy are defined for the position and orientation separately.

The absolute position accuracy AP_P is defined as the 2-norm of the deviation (measured over n cycles) of the target position and the average measured position in the given point:

$$AP_P = \sqrt{(\bar{x} - \hat{x})^2 + (\bar{y} - \hat{y})^2 + (\bar{z} - \hat{z})^2} \tag{4.39}$$

With the nominal coordinates of the target position $\hat{x}, \hat{y}, \hat{z}$ and the average measured position values $\bar{x}, \bar{y}, \bar{z}$ over n cycles:

$$\bar{x} = \frac{1}{n}\sum_{i=1}^{n} x_i, \quad \bar{y} = \frac{1}{n}\sum_{i=1}^{n} y_i, \quad \bar{z} = \frac{1}{n}\sum_{i=1}^{n} z_i \tag{4.40}$$

Where the coordinate values x_i, y_i, z_i are measured in cycle i out of n cycles.

The position repeatability RP_P is composed of the average deviation $|\Delta\bar{r}_{TCP}|$ and three times the corrected sample standard deviation σ_S:

$$RP_P = |\Delta\bar{r}_{TCP}| + 3 \cdot \sigma_S \tag{4.41}$$

With the average deviation $|\Delta\bar{r}_{TCP}|$, the deviation $|\Delta r_{TCP\,i}|$ for cycle i out of n cycles and the corrected sample standard deviation σ_S:

$$|\Delta\bar{r}_{TCP}| = \frac{1}{n}\sum_{i=1}^{n} |\Delta r_{TCP\,i}| \tag{4.42}$$

$$|\Delta r_{TCP\,i}| = \sqrt{(x_i - \bar{x})^2 + (y_i - \bar{y})^2 + (z_i - \bar{z})^2}$$

Where the coordinates x_i, y_i, z_i are measured in cycle i out of n cycles and $\bar{x}, \bar{y}, \bar{z}$ are the average values over n cycles. $\tag{4.43}$

$$\sigma_S = \sqrt{\frac{\sum_{i=1}^{n}(|\Delta r_{TCP\,i}| - |\Delta\bar{r}_{TCP}|)^2}{n - 1}} \tag{4.44}$$

This definition of the absolute position accuracy is widely accepted and often used for large sets of arbitrary points [NSJ14], a specific set of measurement- and verification points [ZTL16] or a constantly measured trajectory [KHO11].

Cheng and others [CZW11] use the more detailed ISO 302-2 standard for machine tools [Int14] that details different accuracy metrics for different directions of approach, reversal errors and so on. They apply it to the positioning accuracy of a 5 DOF parallel machine tool, where higher accuracies and more detailed specifications of the accuracy are demanded.

Santolaria and Ginés [SG13] analyzed the accuracy of a robot calibration based on the screw-axis measurements and Circular Point Analysis. The uncertainty in the identification of each single robot parameter can be calculated based on Monte-Carlo Analysis. Consequently, the method allows for an extensive assessment of the expected accuracy in the overall work-

space. Screw-axis measurements are, however, limited to serial kinematic chains and consequently a more general approach is followed in this thesis.

According to the standard EN ISO 9283 [Eur98] a set of 5 points, in the largest cubic or rectangular workspace possible, needs to be measured in 30 cycles. The points lie on a plane positioned diagonal in the rectangular workspace as shown in Figure 4-10, a definition widely used for industrial robots (see for example [KUK17]).
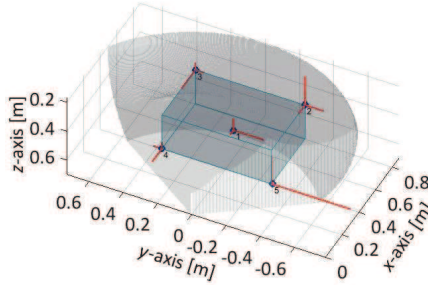

Figure 4-10: Reference points 1-5 on the diagonal plane for the rectangular workspace of the robotic arm and illustration of the deviation (red lines with 100x magnification) for nominal parameters for arm 1

The chosen rectangular workspace in Figure 4-10 does not represent the largest possible workspace for a PARAGRIP single arm. However, considering the object integration with multiple arms, it approximates the largest usable workspace of a single arm under the workspace restrictions imposed by the other arms in the chosen set up (see Figure 3-2).

Describing the accuracy and repeatability properties by such a reduced set of points (see Table 4-4) is sufficient: Comparative measurements for the chosen set-up have shown that referring to a point cloud within the rectangular or larger workspace resulted in similar mean and maximum accuracies. Consequently, the definition following the EN ISO 9283 standard gives a good representation for the accuracy behavior.

reference point	x_{0Ai}	y_{0Ai}	z_{0Ai}
1	500 mm	0 mm	506 mm
2	700 mm	-320 mm	366 mm
3	700 mm	320 mm	366 mm
4	300 mm	320 mm	600 mm
5	300 mm	-320 mm	600 mm

Table 4-4: Reference points position in the arm coordinate system $0Ai$

The absolute accuracy for the nominal parameters is shown in Figure 4-11 for a set of measurements. Slight variation of results can be explained by intermediate dismounting and mounting of the robotic system.
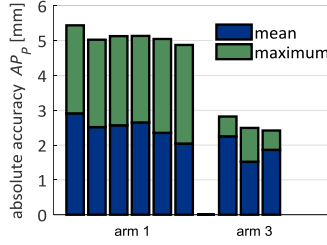
Figure 4-11: Mean and maximum absolute accuracy for arm 1 and arm 3

A typical set of deviations for the 5 reference points is given in Table 4-5 and illustrated in Figure 4-10. The poor maximum and mean absolute accuracy in combination with the good repeatability show a considerable potential for the calibration by kinematic parameter identification.

reference point	RP_P	AP_P	$x_i - \bar{x}$	$y_i - \bar{y}$	$z_i - \bar{z}$
1	0.086 mm	1.9840 mm	-0.3976 mm	-1.7616 mm	-0.8215 mm
2	0.057 mm	2.4152 mm	-0.8043 mm	-1.0958 mm	-1.9965 mm
3	0.040 mm	1.8107 mm	-1.6533 mm	-0.5235 mm	-0.5208 mm
4	0.065 mm	1.3404 mm	-1.1522 mm	0.5155 mm	-0.4509 mm
5	0.065 mm	5.0239 mm	0.3378 mm	-4.6059 mm	-1.9776 mm
mean	0.063 mm	2.5148 mm			

Table 4-5: Position repeatability and absolute position accuracy for the nominal parameters of arm 1 (measurement 2 in Figure 4-11)

4.5   Identification of the Kinematic Parameters

The actual kinematic parameters of the robotic arms are identified by evaluation of the measured end-effector positions $\bar{r}_{TCP\ i}$ and the captured drive positions $\boldsymbol{\varphi}_i$ for the identification points i. For the level 2 calibration, the nominal end-effector positions $\hat{r}_{TCP\ i}$ are calculated, using the direct kinematics model:

$$\hat{r}_{TCP\ i} = r(\hat{\boldsymbol{p}}, \Delta \boldsymbol{p}, \boldsymbol{\varphi}_i) = (\hat{x}_{TCP\ i} \quad \hat{y}_{TCP\ i} \quad \hat{z}_{TCP\ i})^T$$

With the vectors of parameters $\hat{\boldsymbol{p}}$ and parameter deviations $\Delta \boldsymbol{p}$ and the serial and hybrid direct kinematics model as introduced in equations (4.5) and (4.38)

(4.45)

Their deviations from the measured end-effector positions $\bar{r}_{TCP\ i}$ are calculated according to the absolute position accuracy AP introduced in equation (4.39):

$$AP_{Pi} = \sqrt{(\bar{x}_{TCP\ i} - \hat{x}_{TCP\ i})^2 + (\bar{y}_{TCP\ i} - \hat{y}_{TCP\ i})^2 + (\bar{z}_{TCP\ i} - \hat{z}_{TCP\ i})^2}$$

With the measured end-effector position values $\bar{x}_{TCP\ i}$, $\bar{y}_{TCP\ i}$ and $\bar{z}_{TCP\ i}$.

(4.46)

The deviations for all identification positions are expressed in the vector $\boldsymbol{AP}$. The parameter deviations $\Delta \boldsymbol{p}$ are derived by numerical optimization. The aim of the optimization is to minimize the overall deviation of all measurements, expressed by the residual R:

$$\min_{\Delta \boldsymbol{p} \in \mathbb{R}^n} R(\boldsymbol{AP}) = \min_{\Delta \boldsymbol{p} \in \mathbb{R}^n} R(\bar{r}_{TCP\ i}, \hat{r}_{TCP\ i}(\hat{\boldsymbol{p}}, \Delta \boldsymbol{p}, \boldsymbol{\varphi}_i))$$

(4.47)

The optimization is implemented using a combination of the genetic algorithm as described by Goldberg and Holland [GH88] and the Nelder-Mead simplex algorithm as described by Lagarias and others [LRW98]. After identifying a solution to the optimization problem using the genetic algorithm, this solution is refined by using the Nelder-Mead simplex algorithm with several recursive restarts. The according MATLAB® functions *ga* [Mat17a] and *fminsearch* [Mat17b] have proven to be stable and reliable for the parameter identification. A description of the initial implementation and first results for the kinematic parameter identification is given by Rodilla [Rod14 Dt].

Any numerical optimization algorithm evaluates a scalar value as final optimization criterion. Consequently, the deviation information given in $\boldsymbol{AP}$ needs to be consolidated in the single value residual R. In linear algebra, this operation is defined as a norm, a function, which assigns a positive scalar value to any non-zero vector. Examples are the Manhattan norm (sum of the absolute values), the well-known Euclidian norm or the maximum norm. They all derive from the general p-norm:

$$\|\boldsymbol{AP}\|_p = \left(\sum_{i=1}^{n} |AP_i|^p\right)^{1/p} \qquad\qquad (4.48)$$

The choice of the norm will influence the behavior and performance of the optimization and parameter identification. If choosing the Manhattan norm ($p = 1$), improvements of the deviation of any identification point would be treated equally without putting any weighting to the optimization. Already small deviations may be optimized on cost of a considerably large deviation at another identification point. The Euclidian or 2-norm ($p = 2$) is the usual choice in literature (see for example [JZB15,NB13,MSS10, 10283f]): All points are considered in every evaluation and particularly high deviations obtain a higher weight due to the quadratic relation. Because of this balanced behavior the according residual R_2 will be investigated for the calibration procedure:

$$R_2 = \|\boldsymbol{AP}\|_2 \qquad\qquad (4.49)$$

Norms of higher order increase this weighting factor up to the consideration of only the maximum deviation value for the maximum norm ($p = \infty$). If the maximum is considered, the deviation for a single point will be optimized, not considering the other deviations until they become larger than the original one. As a consequence all deviations are regarded and the residual is enveloping all point deviations with a priority on larger deviations. Because of this property, the residual R_∞ will be investigated and compared to the Euclidian norm:

$$R_\infty = \|\boldsymbol{AP}\|_\infty \qquad\qquad (4.50)$$

The calculation time of the chosen MATLAB® implementation is far better for the R_2 residual compared to the R_∞ residual. This may already give an indication of the overall performance of both alternative approaches.

The quality of the identified parameters can be assessed by checking the absolute accuracy after the compensation, as described in section 4.7. It should be noted that the unicity of the identified solution is not necessarily given. Independent from measurement noise and the

optimization performance, the mathematical problem may have multiple solutions, even for highly overdetermined problems after multiple measurements [Mer06, p. 297]. Practice, however, shows that good and reliable results can be achieved by the proposed calibration method.

The more detailed approach of evaluating the uncertainty of the parameter identification by Santolaria and Ginés [SG13] cannot be applied here as shown in section 4.4. A possible extension of the parameter identification is the application of the method of interval analysis as applied by Daney and others [DPN04,DAC06] for the kinematic calibration of a parallel platform. Using interval analysis, a confidence interval for each parameter can be calculated. An efficient implementation is, however, difficult to obtain and a specific problem formulation for the purpose of interval analysis is needed [Mer09]. This approach is hence not followed here, as it will not allow for an efficient use of the developed kinematic model. The classical verification of the calibration should be sufficient in this case.

Consideration of Gravitational Effects

The level 2 parameter identification as described above will be extended to a level 3 calibration by the compensation of gravitational deformations, as described later in section 5.5. The aim is to improve the accuracy under consideration of gravitational effects by identifying more precise kinematic parameters. For the level 3 calibration, the nominal end-effector positions $\hat{r}_{TCP\,i}$ for the positions i are calculated similar to equation (4.45), using the direct kinematics model and the displacement $\Delta r_{grav\,TCP}$ of the TCP due to gravitational effects:

$$\hat{r}_{TCP\,i} = r(\hat{p}, \Delta p, \varphi_i) + \Delta r_{grav\,TCP} = (\hat{x}_{TCP\,i} \quad \hat{y}_{TCP\,i} \quad \hat{z}_{TCP\,i})$$

With the vectors of nominal parameters $\hat{p}$, the parameter deviations Δp, the joint vector φ_i and the serial and hybrid kinematics model as introduced in equations (4.5) and (4.38).

(4.51)

Figure 4-12 shows the displacement of the TCP for a set of parameter identification points shown later in Figure 4-15. The displacement is considerably large and not homogeneous over the different points. Consider for example the identification points 8, 13 and 14: Because of their position at the border of the workspace in positive x-direction and the accordingly elongated arm position, the gravitational deformation does not only result in a large displacement in z-direction, but additionally in a considerable displacement in negative x-direction. Even the displacement in z-direction, the direction of the gravitational force, varies between 0.6 mm and 1.2 mm. Hence, the consideration of gravitational deformations can be expected to be significant for the parameter identification.
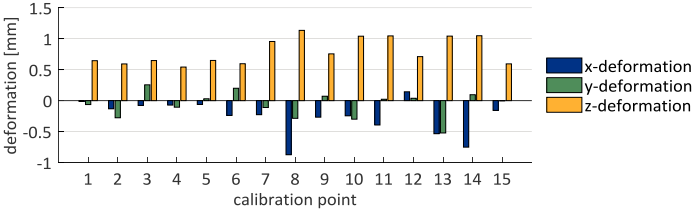
Figure 4-12: TCP displacement of the PARAGRIP arm due to gravitational effects for the 15 parameter identification points of the hybrid kinematics model at the workspace boundaries

The displacement of the TCP for the absolute accuracy reference points is shown in Figure 4-13. Even though the inhomogeneity is smaller for this set of points in the center of the workspace, the consideration of gravitational deformations of course needs to be considered for the absolute accuracy as well, after introducing it for the parameter identification. The nominal end-effector positions are calculated according to equation (4.51).
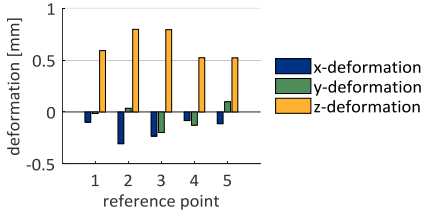
Figure 4-13: TCP displacement of the PARAGRIP arm due to gravitational effects for the absolute accuracy reference points

4.6   Choice of Identification Points

The parameter identification as described in section 4.5 can benefit significantly from the choice of the identification points i: Their quantity and in particular their positions are decisive for the quality of the calibration results.

The kinematic model used for the calibration (compare equation (4.45)) can be linearized at the nominal parameter values $\hat{\boldsymbol{p}}$:

$$\Delta \boldsymbol{r}_{TCP\,i} = \boldsymbol{X}_i \cdot \Delta \boldsymbol{p}$$

Where $\Delta \boldsymbol{r}_{TCP\,i}$ is the deviation of the measured position $\bar{\boldsymbol{r}}_{TCP\,i}$ and the calculated nominal position $\hat{\boldsymbol{r}}_{TCP\,i}$ for measurement point i. $\Delta \boldsymbol{p}$ is the parameter deviation. (4.52)

The matrix $\boldsymbol{X}_i$ is the Jacobian matrix of the direct kinematics equation in terms of the kinematic parameters, the so called error propagation matrix [BM91,SH08]:

$$\boldsymbol{X}_i(\hat{\boldsymbol{p}}, \Delta \boldsymbol{p}, \hat{\boldsymbol{\varphi}}_i,) = \left. \frac{\partial r_{TCP\,i}}{\partial \Delta p} \right|_{\Delta p = 0} \tag{4.53}$$

The dimension of the error propagation matrix X_i is $3 \times n_p$ for n_p parameters. The parameter identification is performed for n_i measurements and the overall error propagation matrix X is:

$$X = \left[X_1^T, \dots, X_{n_i}^T\right]^T \tag{4.54}$$

The calculation of the overall error propagation matrix X is implemented using the MATLAB® Symbolic Math Toolbox®. The deviation of all measurement positions can be calculated, if all parameters are linearly independent, as discussed in section 4.2:

$$\left[\Delta r_{TCP\,1}^T, \dots, \Delta r_{TCP\,n_i}^T\right]^T = X \cdot \Delta p \tag{4.55}$$

This equation, however, should not be used to derive the parameter deviation Δp, for example by using the Pseudo-Inverse matrix calculation, because higher order effects are not considered due to the linearization. It can, however, be used to analyze the observability of the parameters: Using the singular value decomposition [KL80], the overall error propagation matrix X can be expressed by multiplication of two orthogonal matrices U and V^* and the matrix Σ:

$$X = U \cdot \Sigma \cdot V^* \tag{4.56}$$

The matrix Σ contains the singular values σ_1 to σ_{n_p} for n_p independent parameters that are used for the calculation of the observability indices. Born and Menq [BM89,BM91] introduced the observability index O based on the multiplication of the non-zero singular values to select a set of measurement configurations with a minimal sensitivity to measurement noise and a maximum observability of the parameter errors:

$$O = \frac{\sqrt[n_p]{\sigma_1 \cdot \dots \cdot \sigma_{n_p}}}{\sqrt{n_p}} \tag{4.57}$$

High values of the observability index express a good observability of the parameter deviations and a low influence of measurement noise. Born and Menq [BM89,BM91] analyzed the significance of the index for many sets of identification positions. A higher observability index leads to better absolute accuracies and a lower variance of the results.

Based on this first proposition a set of observability indices have been proposed: Driels and Pathre [DP90] proposed the inverse of the condition number, Nahvi and Hollerbach [NH96] proposed an observability index based on the minimum singular value and developed the so called noise amplification index. Sun and Hollerbach [SH08] introduced an additional index based on the product of the reciprocal singular values. Joubair and Bonev [JB13,JTB16] compared the five different indices in simulations and measurements and concluded that the significance of the indices depends on the type of robot calibrated, but overall the first observability index as introduced in equation (4.57) seems to show the best performance. Accordingly, the identification points shown in Figure 4-14 are based on a numerical optimization with the reciprocal observability index as target value, using a fixed number of points and adjusting their position in the workspace.

This approach implicitly compares lengths and rotations with each other. As a consequence the formulation in equation (4.53) needs to be normalized to avoid the overestimation of either position or orientation deviations. In the following investigation for the PARAGRIP, 1 m is defined as characteristic length of a kinematic chain. When applying equation (4.53), the parameter deviation Δp is expressed in m and rad to normalize the formulation: A rotation of the kinematic chain by 0.001 rad due to a rotational parameter deviation results in a 0.001 m TCP displacement, considering the characteristic length of 1 m. Hence, it is equivalent to a translational parameter change of 0.001 m.
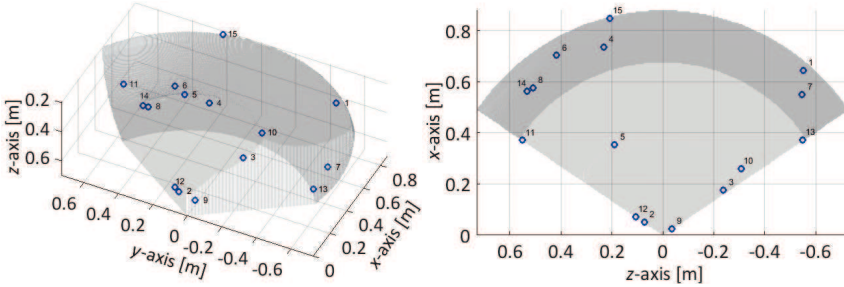
Figure 4-14: Identification points for the hybrid kinematics model based on the first observability index

The optimization of the set of identification points based on the observability indices results in identification points, close to the workspace boundaries (see for example [DPM05,AN09] and Figure 4-14), where the vicinity to singularities amplifies the transmission behavior. Therefore, an according set of manually chosen identification points is considered as well. The set of identification points chosen manually at the workspace boundaries is shown in Figure 4-15. The points are distributed nearly symmetric to the x-axis and evenly over the workspace. Agglomerations, that occur for the points optimized based on the observability index (for example points 12, 2 and 9 or points 14 and 8 in Figure 4-14), are avoided.
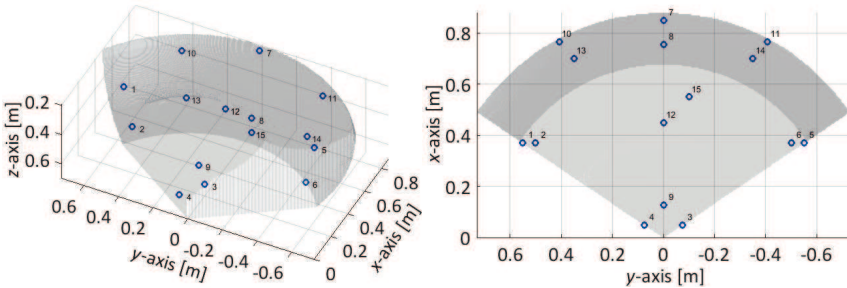

Figure 4-15: Identification points (1-12 for the serial and 1-15 for the hybrid kinematics model) according to the workspace boundary condition chosen

Horn and Notash [HN09] state, that no significantly better performance for a specific index can be observed, especially in comparison to a manually chosen set of identification points.

Both findings could be confirmed for the presented handling system and calibration proce-
dure: The first observability index showed the best performance in most cases, it did, how-
ever, not always outperform a set of manually chosen identification points at the workspace
boundaries [Rod14 Dt]. For this reason, the two different sets of identification points were
investigated further. It should be noted, that these sets outperform any calibration with
identification points in the rectangular workspace (see Figure 4-10). Even if the identification
points partly coincidence with the reference points, the achieved absolute position accuracy
is 25 % inferior.

The number of points chosen for the optimization should be sufficiently large to be able to
obtain a complete identification of the parameters. Clearly the number of data values (the
position of the end-effector for example contains 3 data values for the coordinates) needs to
exceed the number of parameters to be identified. Increasing the number of measurement
points reduces the influence of measurement noise, the effect, however, is limited. Exceed-
ing a certain number of identification points increases the calculation time without improv-
ing the calibration result [MSS10, p. 10282]. A selection of optimal identification points is
more efficient than increasing the numbof of points after a certain threshold [RFS09]. A reli-
able optimal number of measurement points has, however, not yet been found.

For the given handling system and calibration procedure, preliminary studies have confirmed
the existence of this threshold [DMH14]. Accordingly, 12 measurement points (36 data val-
ues) are chosen to identify the 11 parameters of the serial kinematics model and 15 meas-
urement points (45 data values) are chosen to identify the 14 parameters of the hybrid kin-
ematics model.

4.7   Kinematic Calibration Using the Extended Kinematic Models

Based on the introduced kinematic models, measurement procedure and parameter identi-
fication algorithm, the compensation of the modeling errors can be conducted. As a final
result, the end-effector positions can be calculated with a better accuracy based on equa-
tions (4.45) and (4.51).

A set of selected combination of arms, identification points and models is described in the
following sections, allowing for the most important conclusions and leading to the final
modeling approach. The first investigations regarding the different models, choice of identi-
fication points and different robot hardware, namely the type of end-effector, were per-
formed based on the maximum residual R_∞.

It can be observed, that the shown calibration approach is not fully robust for the maximum
residual R_∞. In Figure 4-16 the residual values and according mean deviations for all meas-
urements and optimizations are shown and analyzed in a box-plot, to illustrate the occur-
rence of measurement errors and outliers.

A confidence area (marked by the dashed lines in Figure 4-16) can be observed. It is charac-
terized by an acceptable mean absolute position accuracy AP_P, in comparison to the state of
research, and by low residuals that show a convincing relation to AP_P. The box-plots give a

good orientation of the confidence area: Upper outliers excluding the top 7 % of the measurements are marked red in the central plot in Figure 4-16. Results in the confidence area were used for the analysis below.
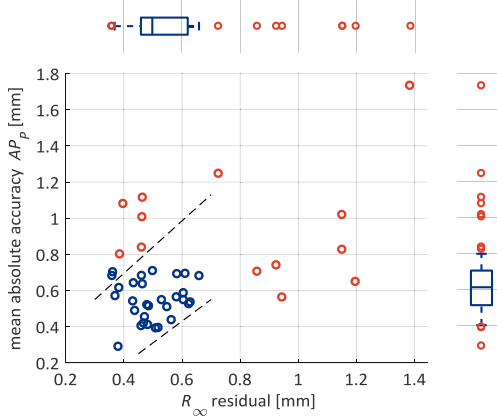

Figure 4-16: Distribution of residual values and mean absolute accuracy, box-plot with 0.6x interquartile range whiskers; outliers are marked red in the box-plot; upper outliers are marked red in the central plot

Results with low residual values but high mean absolute accuracy (points above the confidence area) in most cases resulted from the measurements based on observability index identification points. In most cases optimization results with a rather large residual above 0.7 mm should be rejected. However, in some cases the achieved absolute accuracy might still be acceptable. These observations indicate a limited robustness of this criterion and motivate to investigate the approach using the 2-norm residual as well. The findings for the maximum residual are compared to the results obtained with the 2-norm residual in a second step.

4.7.1   Calibration Using the Serial Kinematics Model

In a first approach, the calibration using the less complex serial kinematics model is evaluated. Figure 4-17 shows the relation of the R_∞ residual and absolute position accuracy AP_P as defined above for the serial kinematics model and the identification points at the workspace boundaries.

The relation of the optimization R_∞ residual and the mean absolute accuracy are shown in Figure 4-17 for the level 2 calibration (marker: o) of the serial kinematics model. The residual values range from 0.58 mm to 0.66 mm for different measurements and the according mean absolute accuracies range from 0.53 mm to 0.69 mm. The level 3 calibration with gravitational compensation (marker: ×) does improve the parameter identification results (mean absolute accuracies range from 0.39 mm to 0.52 mm) for the serial kinematics model. This is an improvement of 25-30 %. Note, that the level 2 and level 3 measurements linked by the dashed line rely on the same measurement data.
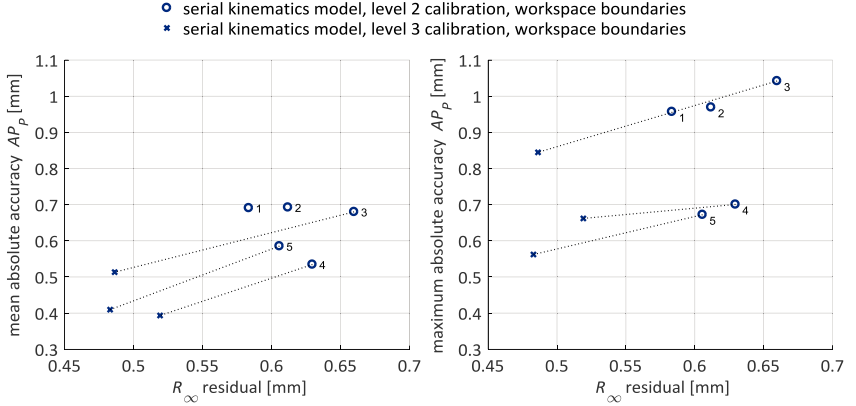
Figure 4-17: Relation of the R_∞ residual to the mean and the maximum absolute accuracy of arm 1, using the serial kinematics model and the identification points at the workspace boundaries

In the following sections the maximum absolute accuracy refers to the highest absolute accuracy value and defines the worst achieved accuracy. The maximum absolute accuracy shown in Figure 4-17 is not as good as expected in comparison to the mean absolute accuracy and the R_∞ residual. It ranges from 0.67 mm up to 1.04 mm for level 2 and is not convincing for measurements 1-3. The level 3 calibration has a less strong influence on the maximum absolute accuracy. Still improvements of 6-19 % were obtained, resulting in a value range from 0.56 mm up to 0.85 mm. Even though comparisons to the calibration results found in literature are difficult, the resulting accuracies are in a satisfying order of magnitude.

However, comparing measurements 1 and 2 with measurement 4 and 5, a significant variation of the achieved mean absolute accuracy can be observed, even though the R_∞ residual values are quite similar. Furthermore, the measurements 1-3 show a much inferior maximum accuracy for an identical calibration procedure and similar residuals if compared to measurement 4 and 5. This indicates a limited reliability for the parameter identification based on the serial kinematics model in combination with the R_∞ residual, which motivates further investigations of improved approaches.

4.7.2   Evaluation of Different Sets of Identification Points and Configurations

The approach using the serial kinematics model is followed to compare the choice of identifications points according to the observability index and the workspace boundaries with each other for different robot arms. The alternative end-effector configuration with electromagnetic end-effector (see section 3) is compared to the current version with vacuum suction end-effector. Finally, a brief comparison to the calibration using the hybrid kinematics model is made. Figure 4-18 shows the relation of the R_∞ residual and absolute position accuracy AP as defined above for the different combinations.
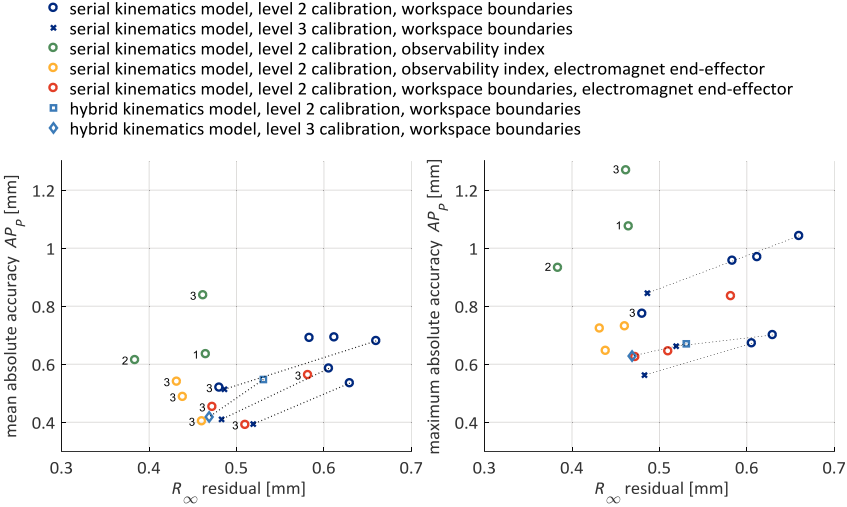
○ serial kinematics model, level 2 calibration, workspace boundaries
✱ serial kinematics model, level 3 calibration, workspace boundaries
○ serial kinematics model, level 2 calibration, observability index
○ serial kinematics model, level 2 calibration, observability index, electromagnet end-effector
○ serial kinematics model, level 2 calibration, workspace boundaries, electromagnet end-effector
▫ hybrid kinematics model, level 2 calibration, workspace boundaries
◇ hybrid kinematics model, level 3 calibration, workspace boundaries

Figure 4-18: Relation of the R_∞ residual to the mean and the maximum absolute accuracy. The measurements were performed on arm 1 if not labeled otherwise

The calibration based on the serial kinematics model and the identification points at the workspace boundaries (markers: ○, ✱) was already discussed above. In comparison, the calibration using the identification points based on the observability index (marker: ○) reaches better residual values, the average absolute accuracy reached is, however, inferior to the results for the identification points at the workspace boundaries. This might be due to a better distribution of the manually chosen points in the workspace, it is clearly an indication that the observability index is not necessarily an ideal criterion for the identification points. Note, that the measurements (marker: ○) were performed on 3 different arms. The parameter values for all arms are given in Table 9-3 in Annex 9.3.

For the alternative end-effector configuration with electromagnetic end-effector, a noticeably better mean and maximum accuracy can be obtained (markers: ○, ○), with the otherwise identical hardware. This might be explained by a less complex mechanical design of the alternative wrist-joints and shows the influence of the mechanical performance and repeatability to the identification process. For this set-up, the difference between the two sets of identification points is not evident.

Looking at the result for the hybrid kinematics model (markers: ▫, ◇) it can be seen, that the achieved absolute accuracies are similar to the best results achieved using the serial kinematics model (measurements 4 and 5 in Figure 4-17). This is, however, at the expense of a considerably longer computing time.

4.7.3   Comparison of the Serial and Hybrid Kinematics Model

Based on the identification points at the workspace boundaries, the serial and hybrid kinematics model are compared for the level 2 and level 3 calibration (see Figure 4-19) for robot

arm 1. The limited robustness for the R_∞ residual, leads to the comparative investigation of the often used R_2 residual. The computing time and convergence of the parameter identification is considerably better using R_2 in comparison to R_∞. Using the same abort criterion for the residual, the optimization terminates 7 times faster for the serial and 3 times faster for the hybrid kinematics model. Furthermore, using R_∞ the optimization should be iterated 10 times to achieve a reliable result, while a single execution is sufficient for the stable optimization based on the residual R_2.
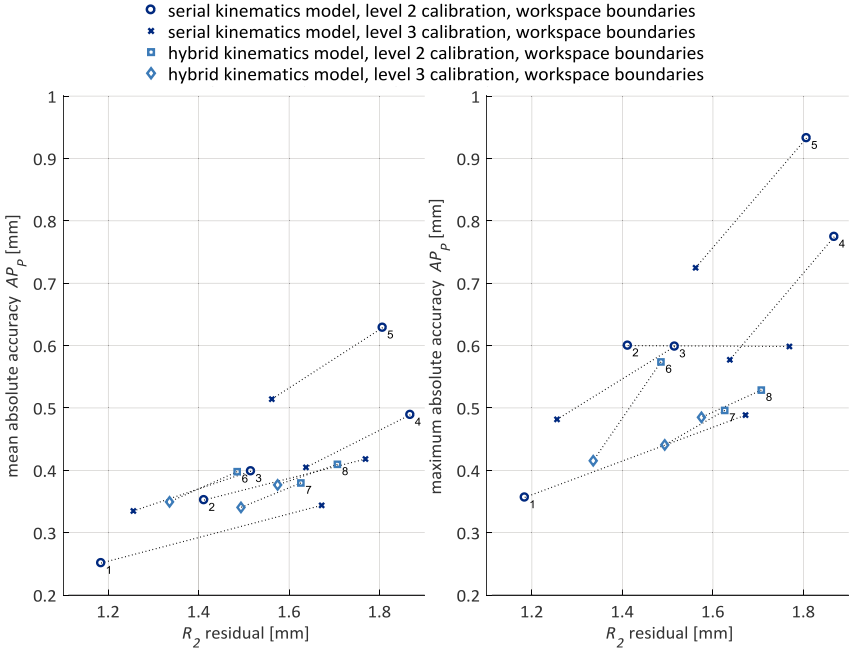
Figure 4-19: Relation of the R_2 residual to the mean and the maximum absolute accuracy of arm 1, using the serial and hybrid kinematics model and the identification points at the workspace boundaries

The calibration based on the serial kinematics model (markers: o, ×) results in mean absolute accuracies between 0.25 mm and 0.63 mm. The maximum absolute accuracy ranges from 0.36 mm to 0.93 mm. Again the results vary significantly and the very good measurement 1 is counteracted by the insufficient results of measurements 4 and 5. Furthermore, the level 3 calibration, including the compensation of gravitational effects, is inferior for measurements 1 and 2, which indicates, that the partly very good level 2 calibration results are based on coincidence rather than on reliable parameter identification.

The calibration results based on the hybrid kinematics model (markers: □, ◇) lie in a smaller bandwidth, between 0.34 mm to 0.41 mm mean absolute accuracy and 0.42 mm to 0.57 mm maximum absolute accuracy. The level 3 calibrations in comparison to the level 2 calibrations show an improvement of 10 % to 25 % for the absolute accuracy achieved. Even

though only a small set of measurements is shown here, the characteristics of the calibration procedure is reliable in other measurements as well (compare for example section 4.7.4). These results confirm the better performance using a kinematic model including the parallelogram, even though the difference to the serial kinematics model is not as significant as stated by To and Webb [TW12]. The achieved residual seems to be a good indication of the calibration quality. Outliers are, however, still not fully prohibited, but less often than for other calibration methods. The calculation time for the hybrid kinematics model is considerably longer than for the serial kinematics model, on a standard computer the parameter identification is performed within 7 minutes in comparison to a few seconds.

The deviations of the identified parameters from the nominal values are shown in Figure 4-20 for measurements 6-8. Analyzing their variation from each other will give a good insight into the robustness of the identification. The parameters $\Delta\varphi_0$, $\Delta\varphi_1$, $\Delta\varphi_4$, $\Delta\alpha$ and $\Delta\beta$ are identified without significant variation for both levels of calibration, an indication for a reliable identification.
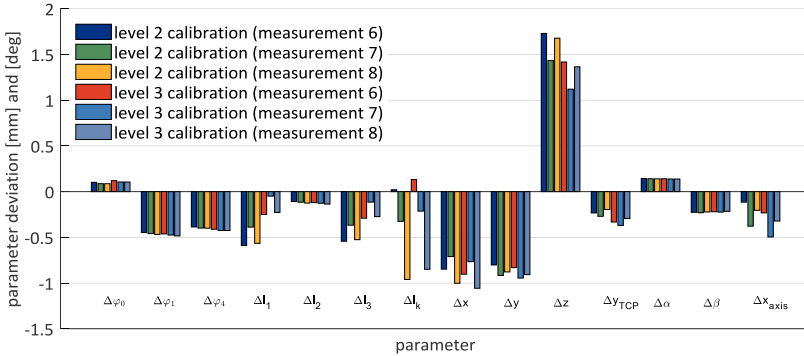
Figure 4-20: Deviation of the identified parameters from the nominal parameters for the level 2 and level 3 calibration of arm 1 using the hybrid kinematics model

The deviations Δl_1 and Δl_3 seem to correspond to each other. Even though they are not redundant as shown in section 4.2, they are closely related. Furthermore, they are negatively related to Δz, as they point to opposite directions for most of the identification positions (link 1 is vertical or nearly vertical in these situations). As expected, the parameter Δz is higher for the level 2 calibration, where the end-effector displacement in z-direction due to self-weight is not considered. The deviation Δl_2 is identified reliably, the values represent the properties of the redundant parameter l_4 as well.

The variation in Δx seems to counteract with the variation of Δx_{axis}. This seems feasible as the x_A-direction corresponds to the x_{A0}-direction for central positions of the arm and Δx_{axis} is rather small anyway. The parameters Δy and Δy_{TCP} vary slightly, without showing clear characteristics or dependencies.

The strong variations in the identified l_k can hardly be interpreted; in particular measurement 8 varies significantly from 6 and 7. The achieved absolute accuracy is, however, not

noticeably inferior. A counterpart or dependency cannot be easily observed for this parameter, even though it should have a strong and direct influence to the kinematic calculation. This effect could be related to the interpolation of O_{WJ} (see Figure 4-9).

Overall, the calibration based on the 2-norm residual R_2 shows a better performance and reliability of the calibration procedure. Concluding, the hybrid kinematics model and the 2-norm residual R_2 should preferably be used for the kinematic parameter identification and calibration of the system under investigation.

4.7.4   Calibration and Absolute Accuracy of the Handling System

Based on the results described above, the arms used for the object integrative handling tasks and the investigated self-calibration are calibrated using the hybrid kinematics model and 2-norm residual R_2. The calibration is performed as level 2 and level 3 calibrations with consideration of the gravitational effects. Due to a mechanical failure and unreproducible behavior, arm 3 could not be analyzed and the arms 1,2 and 4 were calibrated and used in the further investigations.

The achieved accuracies and residuals are shown in Figure 4-21. The calibration of arm 2 was particularly successful. The results for arm 4 are, however, not fully convincing, especially for the maximum deviation, but could not be improved with repetitive measurements. This might indicate a lower mechanical quality of the arm that was manufactured separately from arms 1-3.
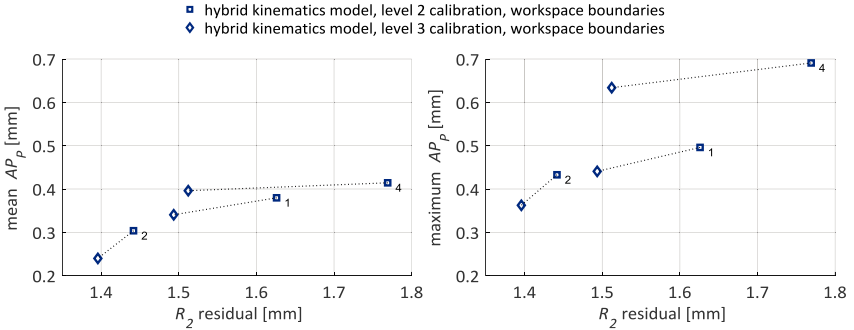
Figure 4-21: Optimization target value (norm deviation in mm) and absolute accuracy for the arms 1,2 and 4 for the 5 reference points on the workspace cube

The parameter deviations are shown in Figure 4-22 and Figure 4-23, the parameter values are given in Table 9-1 and Table 9-2 in Annex 9.3. They are within a reasonable range, even though Δl_k is comparably high for arm 4. As the results are consistent over different calibrations, it seems a feasible deviation of the parameter. The comparison of the level 2 and level 3 calibration shows the behavior discussed in section 4.7.3, for example the parameter Δz is noticeably higher if gravitational effects are not considered.
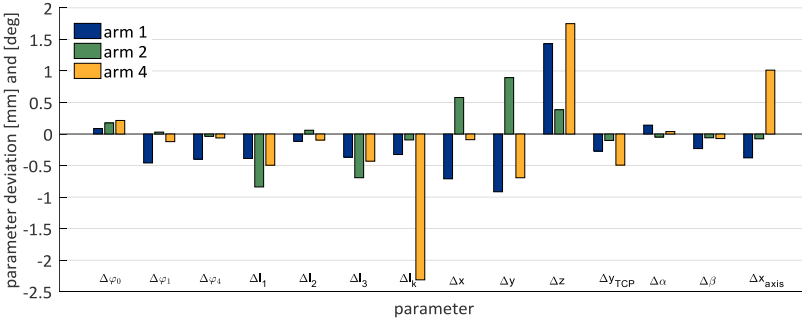
Figure 4-22: Deviation of the identified parameters from the nominal parameters for the level 2 calibration of arms 1, 2 and 4 using the hybrid kinematics model and 2-norm residual R_2
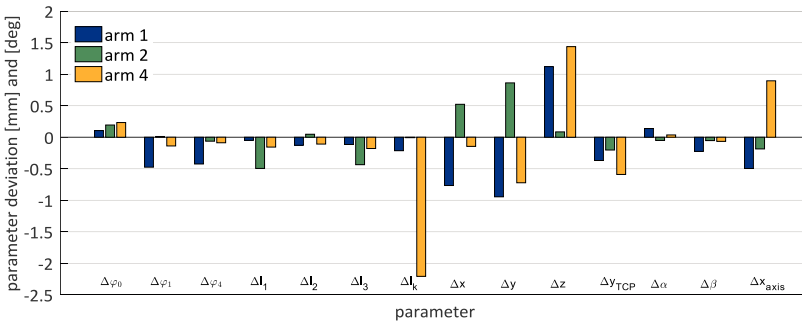

Figure 4-23: Deviation of the identified parameters from the nominal parameters for the level 3 calibration of arms 1, 2 and 4 using the hybrid kinematics model and 2-norm residual R_2

Finally, as an example, the achieved accuracy for arm 1 that was used for most of the investigations described above is shown in detail in Figure 4-24 and Table 4-6. The absolute accuracy values are reduced to a mean value of 0.34 mm and can hardly be recognized in the illustration, despite the used magnification.

reference point	AP_P	$x_i - \bar{x}$	$y_i - \bar{y}$	$z_i - \bar{z}$
1	0.41 mm	-0.32 mm	-0.09 mm	-0.25 mm
2	0.44 mm	-0.08 mm	0.40 mm	0.17 mm
3	0.23 mm	-0.21 mm	-0.07 mm	0.06 mm
4	0.31 mm	-0.07 mm	0.25 mm	-0.17 mm
5	0.31 mm	0.28 mm	0.01 mm	-0.12 mm
mean	0.34 mm			

Table 4-6: Absolute accuracy after level 3 calibration of arm 1 using the hybrid kinematics model
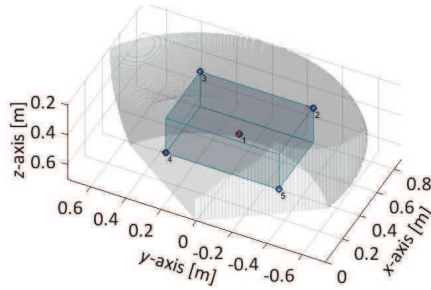
Figure 4-24: Illustration (red lines with 100x magnification) of the deviation for the identified parameters after level 3 calibration with the hybrid kinematics model and 2-norm residual R_2 for arm 1

4.8   Summary and Conclusion for the Calibration by Kinematic Parameter Identification

The investigation of the state of research in calibration by kinematic parameter identification shows the variety of approaches for different robotic structures. Based on this, the extended kinematic models for the PARAGRIP structure under investigations were developed, especially considering the necessary kinematic parameters for the identification and the avoidance of redundant parameters for the hybrid structure. A serial kinematics model with 11 parameters and a hybrid kinematics model with 14 parameters were investigated.

The measurement procedure was tested to be accurate and reliable, the overall set-up and approach is, however, not necessarily robust. This needs to be considered when analyzing the results. The widely used absolute position accuracy and repeatability allow for a comparison to published calibration results. The parameter identification itself is based on a numerical optimization of the remaining residual. The chosen residual and the identification points were investigated. The 2-norm residual for manually chosen identification points at the workspace boundaries performed best, using both the serial and the hybrid kinematics model.

The compensation of the kinematic models is convincing, especially for the hybrid kinematics model, even though the modeling and calculation are more complex and time consuming. It should, however, be noted, that the calibration performance differs for the different arms of the handling system. Using the simplified serial kinematics model results in a less accurate compensation and in particular in a less stable and reliable overall calibration procedure. In both cases, the introduced compensation of gravitational effects (see section 5 for details) can improve the results significantly. Based on this, the identified kinematic models will be used for the self-calibration in section 6.

5   Stiffness Modelling and Compensation of Gravitational Effects

The stiffness of a structure describes its resistance against mechanical deformation due to external or internal forces and moments. Process forces and the gravitational and inertial loads due to the payload and self-weight deform a robotic structure during operation. Consequently, high mechanical stiffness of a robotic structure in combination with high control stiffness allow for precise movements even for highly dynamic applications and heavy payloads in robotic applications. This led to a steady enhancement of the stiffness properties for classical industrial robots.

In contrast, new developments are compliant or soft robotic structures, with low mechanical stiffness (for example the BioRob [Tho12]), low control stiffness (for example the DLR Light Weight Robot [AEG08]) or bionic robots [RT15]. They are intended for use in human robot collaboration, the application of new control strategies and the utilization of new kinematics and principles of motion.

The ability to calculate the stiffness of a robotic structure with sufficient accuracy allows for the compensation of deformations and gravitational effects. It is crucial for the analysis and optimization of robotic structures. In this work, it is required for the compensation of gravitational effects during the kinematic calibration (level 3 calibration) and for future methods of self-calibration for cooperating robots and object integrative handling systems.

5.1   State of Research in Stiffness Modelling

The stiffness of a robotic structure relates the external load to the resulting deformation of the structure. It is usually defined by the Cartesian stiffness matrix $\boldsymbol{K}_c$ that links the displacement in translation and orientation to the external loads (forces and torques). In research and in industrial application, three main methods to derive the Cartesian stiffness matrix $\boldsymbol{K}_c$ of a mechanical structure can be distinguished: The Virtual Joint Method (VJM), the Finite Element Analysis (FEA) and the Matrix Structure Analysis (MSA). The principles of each method are explained in this section to derive a suitable approach for the PARAGRIP prototype and its use in the calibration procedures.

5.1.1   Virtual Joint Method

The VJM, also known as "lumped modeling", is based on the work of Salisbury [Sal80] for serial robotic structures and Gosselin [Gos90] for parallel manipulators and relies on the principle of virtual work. The stiffness of a structure is derived by reducing the compliance of every element in a structure to the compliance of the actuated joints by means of virtual compliant joints with equivalent stiffness. The approach extends the kinematic calculations for robotic manipulators by considering rigid elements and introducing compliant actuated joints. They are represented in the joint stiffness matrix $\boldsymbol{K}_\Theta$. Using the robotics Jacobian matrix $\boldsymbol{J}$, the Cartesian stiffness matrix $\boldsymbol{K}_c$ can be derived:

$$\boldsymbol{K}_c = \boldsymbol{J}^T \cdot \boldsymbol{K}_\Theta \cdot \boldsymbol{J} \tag{5.1}$$

The VJM allows for a simple modeling of stiffness properties and accurate results can be obtained with low computational effort, for example in comparison to FEA [EF99]. El-Khasawneh and others verified the VJM for the often investigated Stewart Hexapod platform by FEA simulation [EF99]. The main drawback of this method is that stiffness properties cannot be reduced to the actuated joints if the displacement due to external loads does not correspond to the compliance of an actuated joint. Furthermore, coupling effects cannot be modeled and are neglected [MGW07].

In recent works Pashkevich and others [PCW08] extended the VJM by using 6-dimensional virtual joints to account for cross coupling effects and the stiffness properties of all links. They extended the identification of the stiffness parameters used in the VJM by enhancing FEA identification algorithms [PKC09] as well as by considering non-linear properties [PKC11]. As the VJM maps the stiffness matrices between joint and Cartesian space using the Jacobian, the conventional formulation between joint and Cartesian space is only exactly valid for unloaded conditions, when the ideal Jacobian applies. The Conservative Congruence Transformation [Che00,HHK02,GL07] extends the conventional formulation by considering changes in the Jacobian due to deformation of the robotic system. Klimchick and others [KFC15] applied the extended VJM for the calibration of an articulated industrial robot. They give a detailed analysis of the identifiable parameters and feasible model reductions in the practical application. Examples of VJM representations from literature are shown in Figure 5-1.
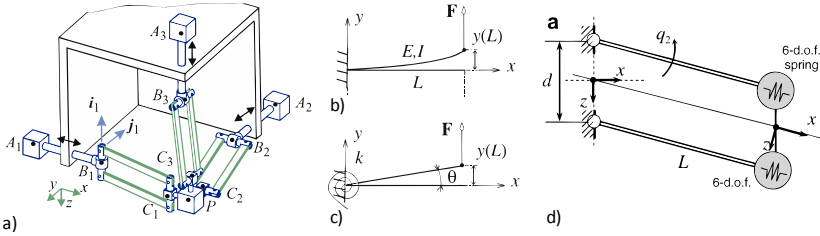
Figure 5-1: VJM representations: a) Orthoglide architecture [MGW07], b) flexible beam model [MGW07], c) virtual rigid beam [MGW07], d) lump stiffness model of the Delta robot parallelogram [PCW09]

Extended considerations are widely used in robotics to analyze and optimize stiffness properties, for example for a parameter identification method for a 6 DOF CBB industrial robot [KWD13]. Zhang and others [ZXM04] developed a 3PRS tripod based on global compliance indices and Pashkevich and other extended the VJM for over-constrained systems with parallelogram like a Delta Robot [PCW09]. Lian and others [LSS15,LSS16] introduced and validated a stiffness modeling approach based on the principle of virtual work for a parallel kinematic structure using the wrench and twist formulations from screw theory.

Considering the possible extensions of the VJM, it is suitable for the use in a kinematic calibration procedure. However, the MSA (see section 5.1.3) offers even more advantages and is preferred for the investigations in this thesis.

5.1.2   Finite Element Analysis

In the well-known FEA [RHA14,DTL12] the overall structure is sub-divided into a large number of finite elements that are connected to each other elastically. The solution to the resulting system of partial differential equations is approximated numerically. The FEA is the most accurate and reliable method as it allows for modeling joints, links and all elements with their real shape, dimensions, temperature influence, local effects like Hertz contacts, material properties and many more characteristics. Its accuracy is limited by the level of discretization, the quality of the used property data and of course by the effort needed to model different effects in detail. It requires, however, a high computational effort for the calculation of the system of equations and re-meshing the model in each configuration of the manipulator [NL07,PCM05].

a)   b)   0.24 bar   0.26 bar   0.32 bar
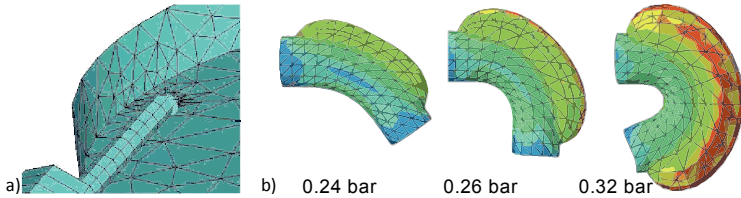
Figure 5-2:   Applications of FEA: a) model of a flexure hinge mechanism [YL08], b) simulation of a pneumatically actuated silicone module [EVL14]

Hence, the method is mainly used for final design considerations and stiffness analysis of complex systems, for example to analyze the behavior of flexure hinges in nano-positioning applications [YL08] (see Figure 5-2a), the analysis of soft materials like silicon actuators [EVL14] (see Figure 5-2b) or to investigate the dynamic system behavior [BPB12,Cam12]. Often the FEA is used to derive invariable stiffness properties of single components and for the use in other analysis methods like VJM and MSA [PCW08,KPC13]. Due to the complexity and computational effort the FEA will not be used for the stiffness modeling in the kinematic calibration procedure.

5.1.3   Matrix Structure Analysis

The MSA relies on the same ideas as the FEA [Kle15, p. 37–43], modeling the mechanical structure as a combination of compliant beam elements (see Figure 5-3a) connected by rigid nodes [Mar66,Arm91]. The stiffness properties of every beam element are represented as a 12×12 stiffness matrix. The Cartesian stiffness matrix K_{struct} of the whole structure is assembled considering the kinematic chains, specifically the connection of nodes. It links the displacement and external load for all elements of the structure.

The MSA as introduced originally is limited to beam elements and was extended by different researchers: Deblaise and others [DHM06] introduced the representation of kinematic relations and the effects of joint stiffness: Kinematic constraints (rigid body and joint movements) are introduced as additional boundary conditions to the system of linear equations. They are considered by solving the system of linear equations for the minimum potential

energy by the method of Lagrange multipliers. The stiffness of joints is accounted for by replacing the kinematic relations by a joint stiffness matrix. The approach was verified using FEA simulations and experimental results for a Delta structure.

Nagai and others [NL08] developed a systematic description based on MSA, where passive joints and rigid links are directly accounted for by using zero stiffness or zero compliance elements in the compliance or stiffness matrix of the according elements. The approach was verified by good agreement to FEA simulations. Taghvaeipour and others [TAL12] (see Figure 5-3b) propose a general formulation to calculate complex structures of flexible bodies connected by lower kinematic pairs based on screw theory and the concept of generalized springs. A flexible body connected to a kinematic pair results in 12 elastic DOF that are constrained in 5 DOF by a lower kinematic pair. Again, the resulting system of linear equations for the overall structure is solved for the minimum potential energy. Similar to Nagai and others [NL08], Cammarata [Cam12] introduced a method to determine the overall stiffness matrix of the structure based on the representation of pairs of flexible beams or rigid bodies connected by joints in a 12×12 stiffness matrix.
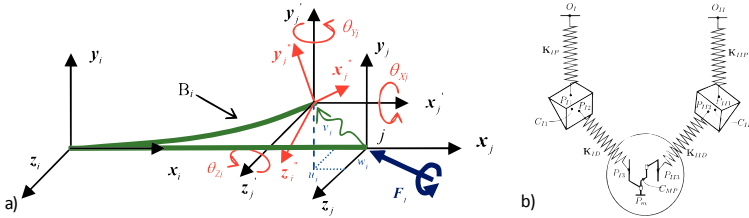
Figure 5-3: Modeling approaches of MSA: a) nodal wrench and displacement of a beam element [DHM06], b) elastostatic model of the McGill Schönflies motion generator [TAL12]

The MSA is used mainly for the stiffness analysis of parallel robotic structures, for example for Delta structures [CDM09,DHM06], the 6-RSS robot [GC08], a flexure-hinge 6-PSS structure [DDS05] or 6-UPS Hexapod [LWW02] and for electrodynamic analysis [BPC11]. The MSA is often verified by comparisons to FEA analysis, experimental validations are, however, difficult to obtain. Compared to the FEA, the MSA is less computational expensive and results in a good balance between computational costs and accuracy. In this thesis it is therefore applied for an extended stiffness modeling method that can be used in kinematic calibration procedures. It will be validated directly by measurements and indirectly by the use in the kinematic calibration, as already shown in section 4.7.

5.2   Implementation of the Stiffness Calculation Method

Based on the MSA, a method was implemented to model and analyze the stiffness proper-
ties of robotic structures and mechanisms, taking advantage of the good computational
speed and at the same time allowing for the consideration of complex elements in the mod-
el. The robotic structure is modeled as a combination of flexible elements connected by in-
finitesimal rigid nodes (see Figure 5-7, page 53). In comparison to the classical MSA, complex
links and flexible joints are taken into account. As joints are not considered rigid, the accord-
ing kinematic constraints are not taken into account by additional boundary conditions (rigid
body motions) for the linear system of equations. Instead, rotational and translational
movements, enabled by a joint, are considered by setting the according stiffness value to be
zero and rigid elements are set to a high numerical value (10^9 for the given implementation).
Force dependent non-linear elements, like rolling contact bearings, are considered by solving
the linear stiffness model with few iterations. A catalog of predefined elements is introduced
to allow for a fast and convenient automatic assembly of the stiffness model. An overview of
the new method is presented in [DC16].

The Cartesian stiffness matrix $^0\boldsymbol{K}_{struc\,0}$ of the structure relates the displacement (transla-
tion and orientation) of all nodes to the external loads:

$$^0\boldsymbol{f}_0 = \,^0\boldsymbol{K}_{struc\,0} \cdot \,^0\Delta\boldsymbol{\chi}_0 \tag{5.2}$$

Superscripts indicate the coordinate system of reference; the last subscript indicates the
point of reference for the equivalent load or displacement (see section 5.2.1).

The vector $^0\Delta\boldsymbol{\chi}_0$ represents the generalized pose (position and orientation) displacements
of all rigid nodes and the vector $^0\boldsymbol{f}_0$ represents the generalized external loads acting on the
rigid nodes. By solving the linear system of equations (5.2), the displacement of the structure
under external load can be derived.

5.2.1   Generalized Stiffness Matrices and Equivalent Displacements and Loads

All elements of the structure, loads and displacements are described by the linear system of
equations (5.2) and therefore need to be expressed in a common frame of reference. In this
approach, the element stiffness matrices, displacements and loads are generalized by calcu-
lating equivalent displacements and loads at the origin O_0 of the global coordinate system 0.
The concept of generalized springs was introduced by Lončarić [Lon87]. The application of
this general approach to the MSA is described in the following sections.

As a basis for the generalization, the movement of arbitrary rigid bodies, attached arbitrary
points and coordinate systems is introduced. For a point P on the rigid body u, the vector
$\boldsymbol{r}_{P,u}$ points from the origin O_u of the local coordinate system u to the point P (see Fig-
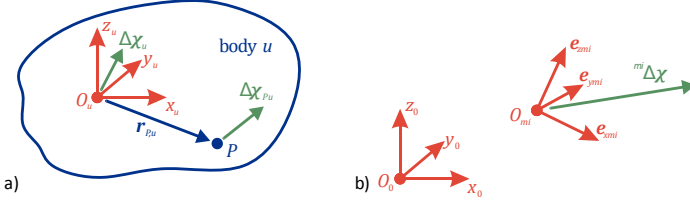ure 5-4a).

Figure 5-4: a) Rigid body motion for a point P, b) coordinate transformation

The displacement $\Delta\chi_{Pu}$ of point P on the rigid body u can be calculated from the equivalent displacement $\Delta\chi_u$ of the origin O_u of the rigid body:

$$\Delta\chi_{Pu} = V_{P,u} \cdot \Delta\chi_u \tag{5.3}$$

$$V_{P,u} = \begin{pmatrix} I_3 & -S_{r_{P,u}} \\ 0_3 & I_3 \end{pmatrix} \tag{5.4}$$

The matrix I_3 is the 3×3 identity matrix, 0_3 is the 3×3 zero matrix and $S_{r_{P,u}}$ is the 3×3 skew-symmetric matrix representing the cross product with the vector $r_{P,u}$ pointing from O_u to the point P:

$$S_{r_{P,u}} = \begin{pmatrix} 0 & -r_{P,u\,z} & r_{P,u\,y} \\ r_{P,u\,z} & 0 & -r_{P,u\,x} \\ -r_{P,u\,y} & r_{P,u\,x} & 0 \end{pmatrix} \tag{5.5}$$

$$r_{P,u} = \begin{pmatrix} r_{P,u\,x} \\ r_{P,u\,y} \\ r_{P,u\,z} \end{pmatrix} \tag{5.6}$$

The vectors and transformation matrix can be expressed in any coordinate system. The transposed transformation matrix $V_{P,u}^T$ is used to calculate a cut load f_P at point P on the rigid body u from an equivalent cut load f_u at the origin of the rigid body u:

$$f_P = V_{P,u}^T \cdot f_u \tag{5.7}$$

As simplification, the cut load f_P at point P on the rigid body u is expressed as f_P instead of f_{Pu}.

Next, the well-known coordinate transformation is introduced. A vector $^{mi}\Delta\chi$ is expressed in the local coordinate system mi and can be transformed to the global coordinate system 0 (see Figure 5-4b) using the rotation matrix $^0R_{mi}$:

$$^0\Delta\chi = \, ^0R_{mi} \cdot \, ^{mi}\Delta\chi \tag{5.8}$$

$$^0R_{mi} = \begin{pmatrix} ^0e_{x\,mi} & ^0e_{y\,mi} & ^0e_{z\,mi} & & 0_3 & \\ & 0_3 & & ^0e_{x\,mi} & ^0e_{y\,mi} & ^0e_{z\,mi} \end{pmatrix} \tag{5.9}$$

Where 0_3 is the 3×3 zero matrix and $^0e_{x\,mi}$, $^0e_{y\,mi}$ and $^0e_{z\,mi}$ are the unit vectors of the local coordinate system mi expressed in the global coordinate sytem 0.

The inverse operation can be calculated using $^{mi}R_0$ accordingly:

$$^{mi}R_0 = \left(\, ^0R_{mi} \right)^{-1} \tag{5.10}$$

$$^{mi}\Delta\chi = \, ^{mi}R_0 \cdot \, ^0\Delta\chi \tag{5.11}$$

The equivalent loads and displacements and consequently the generalized stiffness matrices can be derived with these transformations.

Equivalent Displacement

Instead of the rigid body u, now a rigid node k with an attached element mi as shown in Figure 5-5a is considered.
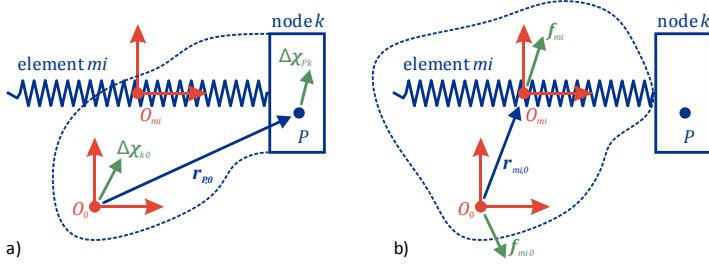

Figure 5-5: a) Equivalent displacement, b) equivalent load for the rigid node k and element mi

An imaginary extension of the rigid node k includes the origin O_0. Analogous to equation (5.3) the displacement $\Delta\chi_{Pk}$ of point P on k can be calculated from the equivalent displacement $\Delta\chi_{k\,0}$ at the origin O_0:

$$\Delta\chi_{Pk} = V_{P,0} \cdot \Delta\chi_{k\,0} \tag{5.12}$$

The origin O_0 is chosen as the generalized origin for all rigid nodes from now on. Note that now, the last index 0 expresses the coordinate system of equivalence for the equivalent displacement $\Delta\chi_{k\,0}$. The transformation matrix $V_{P,0}$ is formed from the vector $r_{P,0}$ pointing from O_0 to the point P. The displacement can then be transformed to the coordinate system mi, analogous to equation (5.11):

$$^{mi}\Delta\chi_{Pk} = {}^{mi}R_0 \cdot {}^0V_{P,0} \cdot {}^0\Delta\chi_{k\,0} \tag{5.13}$$

The transformation $^{mi}R_0 \cdot {}^0V_{P,0}$ derived from the concept of generalization is also known as the adjoint transformation, describing the relation of rigid body velocities [MLS94, p. 53–61] in mechanics. The equivalent displacement $^0\Delta\chi_{k\,0}$ can then directly be calculated from the displacement $^{mi}\Delta\chi_{Pk}$ of point P on k:

$$^0\Delta\chi_{k\,0} = {}^0V_{P,0}{}^{-1} \cdot {}^0R_{mi} \cdot {}^{mi}\Delta\chi_{Pk} \tag{5.14}$$

Equivalent Load

Analogous to equation (5.7), the transposed transformation matrix $V_{mi,0}{}^T$ is used to calculate the cut load f_{mi} at the point of origin O_{mi} (see Figure 5-5b) from the equivalent cut load $f_{mi\,0}$ at the origin O_0:

$$f_{mi} = V_{mi\,0}^T \cdot f_{mi\,0} \tag{5.15}$$

The transformation matrix $\boldsymbol{V}_{mi,0}$ is formed from the vector $\boldsymbol{r}_{mi,0}$ pointing from the origin O_0 to the origin O_{mi}. The cut load can then be transformed to the coordinate system mi:

$$^{mi}\boldsymbol{f}_{mi} = {}^{mi}\boldsymbol{R}_0 \cdot {}^0\boldsymbol{V}_{mi,0}^T \cdot {}^0\boldsymbol{f}_{mi\,0} \tag{5.16}$$

Vice versa the equivalent cut load $^0\boldsymbol{f}_{mi\,0}$ can be calculated from the cut load $^{mi}\boldsymbol{f}_{mi}$:

$$^0\boldsymbol{f}_{mi\,0} = {}^0\boldsymbol{V}_{mi,0}^{-T} \cdot {}^0\boldsymbol{R}_{mi} \cdot {}^{mi}\boldsymbol{f}_{mi} \tag{5.17}$$

Generalization of Stiffness Matrix
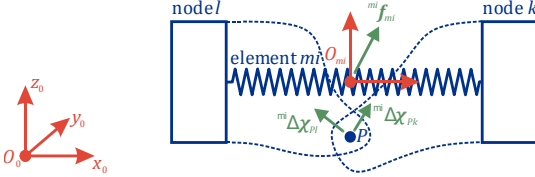
Figure 5-6:   Equivalent cut load and displacement for the generalized stiffness matrix

The local element stiffness matrix $^{mi}\boldsymbol{K}_{mi}$ links the relative (translational and rotational) displacement $^{mi}\Delta\boldsymbol{\chi}_{Pk} - {}^{mi}\Delta\boldsymbol{\chi}_{Pl}$ of a common point P on the two attached rigid nodes k and l to the cut load $^{mi}\boldsymbol{f}_{mi}$ in the element:

$$^{mi}\boldsymbol{f}_{mi} = {}^{mi}\boldsymbol{K}_{mi} \cdot \left({}^{mi}\Delta\boldsymbol{\chi}_{Pk} - {}^{mi}\Delta\boldsymbol{\chi}_{Pl}\right) \tag{5.18}$$

With (5.13) equation (5.18) can be expressed as follows:

$$^{mi}\boldsymbol{f}_{mi} = {}^{mi}\boldsymbol{K}_{mi} \cdot {}^{mi}\boldsymbol{R}_0 \cdot {}^0\boldsymbol{V}_{0,P} \cdot \left({}^0\Delta\boldsymbol{\chi}_{k\,0} - {}^0\Delta\boldsymbol{\chi}_{l\,0}\right) \tag{5.19}$$

By substituting equation (5.19) into (5.16), the generalized element stiffness matrices $^0\boldsymbol{K}_{mi\,0}$ can be derived:

$$^0\boldsymbol{f}_{mi\,0} = \underbrace{{}^0\boldsymbol{V}_{0,mi}^{-T} \cdot {}^0\boldsymbol{R}_{mi} \cdot {}^{mi}\boldsymbol{K}_{mi} \cdot {}^{mi}\boldsymbol{R}_0 \cdot {}^0\boldsymbol{V}_{0,P}}_{^0\boldsymbol{K}_{mi\,0}} \cdot \left({}^0\Delta\boldsymbol{\chi}_{k\,0} - {}^0\Delta\boldsymbol{\chi}_{l\,0}\right) \tag{5.20}$$

$$^0\boldsymbol{K}_{mi\,0} = {}^0\boldsymbol{V}_{0,mi}^{-T} \cdot {}^0\boldsymbol{R}_{mi} \cdot {}^{mi}\boldsymbol{K}_{mi} \cdot {}^{mi}\boldsymbol{R}_0 \cdot {}^0\boldsymbol{V}_{0,P} \tag{5.21}$$

The common point P of the two attached nodes and the origin O_{mi} of the elastic element coincide for the calculation of the element stiffness matrix and equation (5.21) can be simplified to:

$$^0\boldsymbol{K}_{mi\,0} = {}^0\boldsymbol{V}_{0,P}^{-T} \cdot {}^0\boldsymbol{R}_{mi} \cdot {}^{mi}\boldsymbol{K}_{mi} \cdot {}^{mi}\boldsymbol{R}_0 \cdot {}^0\boldsymbol{V}_{0,P} \tag{5.22}$$

With equation (5.22), now all element stiffness matrices $^{mi}\boldsymbol{K}_{mi}$ can be generalized to assemble the Cartesian stiffness matrix $^0\boldsymbol{K}_{struc\,0}$ from the generalized element stiffness matrices $^0\boldsymbol{K}_{mi\,0}$.

Example of a 1 Degree of Freedom Structure

The generalization of the element stiffness matrices is explained using the example of a 1 DOF structure with 3 elements, as shown in Figure 5-7. The orientations of link 1 and drive 2 are chosen to be aligned with the global coordinate system to simplify the resulting stiffness matrices and increase the traceability of the matrix operations. In this case, the rotation matrix R is a 6×6 identity matrix.
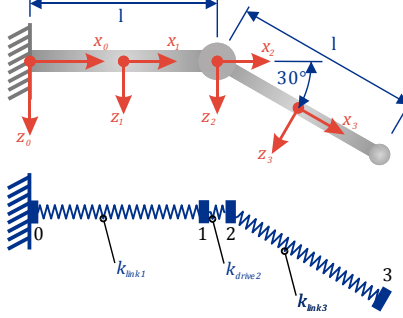

Figure 5-7: Stiffness model of a 1 DOF structure with 3 elements

The stiffness matrix $^1K_1$ for link 1 and the according transformation matrices $^0V_{10}$ and $^0R_1$ are given by:

$$^1K_1 = \begin{pmatrix} k_{1x} & 0 & 0 & 0 & 0 & 0 \\ 0 & k_{1y} & 0 & 0 & 0 & 0 \\ 0 & 0 & k_{1z} & 0 & 0 & 0 \\ 0 & 0 & 0 & k_{1\alpha} & 0 & 0 \\ 0 & 0 & 0 & 0 & k_{1\beta} & 0 \\ 0 & 0 & 0 & 0 & 0 & k_{1\gamma} \end{pmatrix}, \quad ^0V_{1,0} = \begin{pmatrix} 1 & 0 & 0 & 0 & 0 & 0 \\ 0 & 1 & 0 & 0 & 0 & \frac{l}{2} \\ 0 & 0 & 1 & 0 & -\frac{l}{2} & 0 \\ 0 & 0 & 0 & 1 & 0 & 0 \\ 0 & 0 & 0 & 0 & 1 & 0 \\ 0 & 0 & 0 & 0 & 0 & 1 \end{pmatrix}, \quad ^0R_1 = I_6 \tag{5.23}$$

Where I_6 is the 6×6 identity, k are scalar stiffness values for the different directions and l is the link length.

The local element stiffness matrices and according transformation matrices for all elements are listed in Annex 9.4. The generalized element stiffness matrices are calculated based on equation (5.22):

$$^0K_{10} = {}^0V_{1,0}^T \cdot {}^0R_1 \cdot {}^1K_1 \cdot {}^1R_0 \cdot {}^0V_{1,0} \tag{5.24}$$

$$^0K_{10} = \begin{pmatrix} k_{1x} & 0 & 0 & 0 & 0 & 0 \\ 0 & k_{1y} & 0 & 0 & 0 & \frac{l}{2} \cdot k_{1y} \\ 0 & 0 & k_{1z} & 0 & -\frac{l}{2} \cdot k_{1z} & 0 \\ 0 & 0 & 0 & k_{1\alpha} & 0 & 0 \\ 0 & 0 & -\frac{l}{2} \cdot k_{1z} & 0 & \frac{l^2}{4} \cdot k_{1z} + k_{1\beta} & 0 \\ 0 & \frac{l}{2} \cdot k_{1y} & 0 & 0 & 0 & \frac{l^2}{4} \cdot k_{1y} + k_{1\gamma} \end{pmatrix} \tag{5.25}$$

$$^0\mathbf{K}_{2\,0} = {}^0\mathbf{V}_{2,0}^T \cdot {}^0\mathbf{R}_2 \cdot {}^2\mathbf{K}_2 \cdot {}^2\mathbf{R}_0 \cdot {}^0\mathbf{V}_{2,0} \tag{5.26}$$

$$^0\mathbf{K}_{2\,0} = \begin{pmatrix} k_{2x} & 0 & 0 & 0 & 0 & 0 \\ 0 & k_{2y} & 0 & 0 & 0 & l \cdot k_{2y} \\ 0 & 0 & k_{2z} & 0 & -l \cdot k_{2z} & 0 \\ 0 & 0 & 0 & k_{2\alpha} & 0 & 0 \\ 0 & 0 & -l \cdot k_{2z} & 0 & l^2 \cdot k_{2z} & 0 \\ 0 & l \cdot k_{2y} & 0 & 0 & 0 & l^2 \cdot k_{2y} + k_{2\gamma} \end{pmatrix} \tag{5.27}$$

$$^0\mathbf{K}_{3\,0} = {}^0\mathbf{V}_{3,0}^T \cdot {}^0\mathbf{R}_3 \cdot {}^3\mathbf{K}_3 \cdot {}^3\mathbf{R}_0 \cdot {}^0\mathbf{V}_{3,0} \tag{5.28}$$

$$^0\mathbf{K}_{3\,0} = \begin{pmatrix} 0.25(3k_{3x} + k_{3z}) & 0 & 0.43(k_{3x} - k_{3z}) \\ 0 & k_{3y} & 0 \\ 0.43(k_{3x} - k_{3z}) & 0 & 0.25(k_{3x} + 3 \cdot k_{3z}) \\ 0 & -0.25 \cdot l \cdot k_{3y} & 0 \\ -0.43 \cdot l \cdot k_{3x} + 0.68 \cdot k_{3z} & 0 & -0.25 \cdot l \cdot k_{3x} + 1.18 \cdot k_{3z} \\ 0 & 1.43 \cdot lk_{3y} & 0 \end{pmatrix}$$

$$\cdots$$

$$\begin{pmatrix} 0 & -0.43 \cdot l \cdot k_{3x} + 0.68 \cdot k_{3z} & 0 \\ -0.25 \cdot l \cdot k_{3y} & 0 & 1.43 \cdot l \cdot k_{3y} \\ 0 & -0.25 \cdot l \cdot k_{3x} + 1.18 \cdot k_{3z} & 0 \\ 0.06 \cdot l^2 \cdot k_{3y} + k_{3\alpha} & 0 & -0.36 \cdot l^2 \cdot k_{3y} \\ 0 & 0.25 \cdot l^2 \cdot k_{3x} + 1.87 \cdot l^2 \cdot k_{3z} + k_{3\beta} & 0 \\ -0.36 \cdot l^2 \cdot k_{3y} & 0 & 2.05 \cdot l^2 \cdot k_{3y} + k_{3\gamma} \end{pmatrix} \tag{5.29}$$

Using the example of $^0\mathbf{K}_{3\,0}$, it is obvious that generalized element stiffness matrices become unintuitive and unclear even for simple examples, in this case because of the values for $sin(30°)$ and $cos(30°)$. Therefore, the implementation of an automatic algorithm is necessary to allow for convenient and clear stiffness modeling.

5.2.2   Assembly of the Stiffness Matrix of the Structure

The generalized Cartesian stiffness matrix of the structure $^0\mathbf{K}_{struc\,0}$ is assembled from the generalized element stiffness matrices $^0\mathbf{K}_{mi\,0}$ for element mi (for example link m of robot arm i). They link the equivalent relative (translational and rotational) displacement of two attached rigid nodes k and l to the equivalent cut load $^0\mathbf{f}_{mi\,0}$, both generalized to the origin O_0 of the global coordinate system 0:

$$^0\mathbf{f}_{mi\,0} = {}^0\mathbf{K}_{mi\,0} \cdot \left({}^0\Delta\boldsymbol{\chi}_{k\,0} - {}^0\Delta\boldsymbol{\chi}_{l\,0} \right) \tag{5.30}$$

The generalized Cartesian stiffness matrix of the whole structure $^0\mathbf{K}_{struc\,0}$ can be derived by superposition of all $^0\mathbf{K}_{mi\,0}$ at specific positions within $^0\mathbf{K}_{struc\,0}$. Let n be the number of elements in the structure and mi be the explicit index to identify each element of the structure.

Each element is attached to two rigid nodes k and l. With $k < l$ the according element stiffness matrix is notated as ${}^0\boldsymbol{K}_{mi\,kl\,0}$. Let j be the number of rigid nodes in the structure, including the fixed base $k = 0$. ${}^0\boldsymbol{K}_{struc\,0}$ is a $6(j-1) \times 6(j-1)$, zero matrix, filled up with the superposition of ${}^0\boldsymbol{K}_{mi\,kl\,0}$:

$$
{}^0\boldsymbol{K}_{struc}\,(6k-5:\,6k\,,6k-5:\,6k) = \sum_{mi=1}^{n} \left(+\ {}^0\boldsymbol{K}_{mi\,kl\,0}|k > 0\right)
$$

$$
{}^0\boldsymbol{K}_{struc}\,(6k-5:\,6k\,,6l-5:\,6l) = \sum_{mi=1}^{n} \left(-\ {}^0\boldsymbol{K}_{mi\,kl\,0}|k > 0\right)
$$

$$
{}^0\boldsymbol{K}_{struc}\,(6l-5:\,6l\,,6k-5:\,6k) = \sum_{mi=1}^{n} \left(-\ {}^0\boldsymbol{K}_{mi\,kl\,0}|k > 0\right) \tag{5.31}
$$

$$
{}^0\boldsymbol{K}_{struc}\,(6l-5:\,6l\,,6l-5:\,6l) = \sum_{mi=1}^{n} \left(+\ {}^0\boldsymbol{K}_{mi\,kl\,0}|l > 0\right)
$$

Where ${}^0K_{struc}(a:\,b\,,c:\,d)$ indicate the sub-matrix of ${}^0K_{struc}$ in the rows a to b and the columns c to d.

With the exception of the elements attached to the fixed base, that is $k = 0$, the generalized 6×6 element stiffness matrices are super-positioned 4 times with the stiffness matrix of the structure. This corresponds to the well-known 12×12 stiffness matrices used for the MSA of connected beam elements [Cam12,DHM06]. The first 6 rows and columns, representing the base $k = 0$ are deleted from the matrix to represent the fixed position and hence the displacement $\Delta\boldsymbol{\chi}_{0\,0} = 0$ of element 0. When establishing the 12×12 matrix for elements attached to 2 nodes, the concept of generalization is used implicitly. The off-diagonal 6×6 matrices do not only represent the stiffness properties of the structure but do also represent the equilibrium of forces and torques between both nodes. The same applies for the superposition of the generalized element stiffness matrices.

Example of a 1 Degree of Freedom Structure

The assembly of the generalized Cartesian stiffness matrix is explained for the example given above (see Figure 5-7). There are 3 elements and 4 nodes in the example structure (see Figure 5-7). Each element mi is attached to two rigid nodes k and l and the according element stiffness matrix is indexed ${}^0\boldsymbol{K}_{mi\,kl\,0}$. ${}^0\boldsymbol{K}_{struc\,0}$ is an 18×18 zero matrix, filled up with the superposition of ${}^0\boldsymbol{K}_{1\,01\,0}$, ${}^0\boldsymbol{K}_{2\,12\,0}$ and ${}^0\boldsymbol{K}_{3\,23\,0}$. Link 1 is attached to the nodes $k = 0$ and $l = 1$, the according sub-matrix is given by:

$$
{}^0\boldsymbol{K}_{struc}\,(1{:}6\,,1{:}6) = +\ {}^0\boldsymbol{K}_{1\,01\,0} \tag{5.32}
$$

Drive 2 is attached to the nodes $k = 1$ and $l = 2$, the according sub-matrices are given by:

$$
{}^0\boldsymbol{K}_{struc}\,(1{:}6\,,1{:}6) = +\ {}^0\boldsymbol{K}_{2\,12\,0}
$$

$$
{}^0\boldsymbol{K}_{struc}\,(1{:}6\,,7{:}12) = -\ {}^0\boldsymbol{K}_{2\,12\,0}
$$

$$
{}^0\boldsymbol{K}_{struc}\,(7{:}12\,,1{:}6) = -\ {}^0\boldsymbol{K}_{2\,12\,0} \tag{5.33}
$$

$$
{}^0\boldsymbol{K}_{struc}\,(7{:}12\,,7{:}12) = +\ {}^0\boldsymbol{K}_{2\,12\,0}
$$

For link 1 and drive 2, the generalized Cartesian stiffness matrix $^0\boldsymbol{K}_{struc\,0}$ is given by:

$$^0\boldsymbol{K}_{struc\,0} = \begin{pmatrix}
k_{1x}+k_{2x} & 0 & 0 & 0 & 0 & 0 & -k_{2x} & 0 & 0 & 0 & 0 & 0 \\
0 & k_{1y}+k_{2y} & 0 & 0 & 0 & \dfrac{lk_{1y}}{2}+lk_{2y} & 0 & -k_{2y} & 0 & 0 & 0 & -lk_{2y} \\
0 & 0 & k_{1z}+k_{2z} & 0 & -\dfrac{lk_{1z}}{2}-lk_{2z} & 0 & 0 & 0 & -k_{2z} & 0 & lk_{2z} & 0 \\
0 & 0 & 0 & k_{1\alpha}+k_{2\alpha} & 0 & 0 & 0 & 0 & 0 & -k_{2\alpha} & 0 & 0 \\
0 & 0 & -\dfrac{lk_{1z}}{2}-lk_{2z} & 0 & \dfrac{l^2k_{1z}}{4}+k_{1\beta}+l^2k_{2z} & 0 & 0 & 0 & lk_{2z} & 0 & -l^2k_{2z} & 0 \\
0 & \dfrac{lk_{1y}}{2}+lk_{2y} & 0 & 0 & 0 & \dfrac{l^2k_{1y}}{4}+k_{1\gamma}+l^2k_{2y}+k_{2\gamma} & 0 & -lk_{2y} & 0 & 0 & 0 & -l^2k_{2y}+k_{2\gamma} \\
-k_{2x} & 0 & 0 & 0 & 0 & 0 & k_{2x} & 0 & 0 & 0 & 0 & 0 \\
0 & -k_{2y} & 0 & 0 & 0 & -lk_{2y} & 0 & k_{2y} & 0 & 0 & 0 & lk_{2y} \\
0 & 0 & -k_{2z} & 0 & lk_{2z} & 0 & 0 & 0 & k_{2z} & 0 & -lk_{2z} & 0 \\
0 & 0 & 0 & -k_{2\alpha} & 0 & 0 & 0 & 0 & 0 & k_{2\alpha} & 0 & 0 \\
0 & 0 & lk_{2z} & 0 & -l^2k_{2z} & 0 & 0 & 0 & -lk_{2z} & 0 & l^2k_{2z} & 0 \\
0 & -lk_{2y} & 0 & 0 & 0 & -l^2k_{2y}+k_{2\gamma} & 0 & lk_{2y} & 0 & 0 & 0 & l^2k_{2y}+k_{2\gamma}
\end{pmatrix} \quad (5.34)$$

The generalized Cartesian stiffness matrix for all three links is not shown for the sake of clarity. The characteristics of the assembly can be fully observed for the example shown.
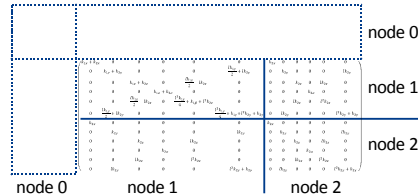
Figure 5-8: Representation of the nodes within the Cartesian stiffness matrix

As discussed for the generalized element stiffness matrices, the generalized Cartesian stiffness matrix for the overall structure shown in equation (5.34) is even less intuitive for simple examples, especially considering numerical values for the matrix entries. The implementation of the stiffness calculation method was therefore verified using MATLAB SimMechanics® and analytic calculations implemented for simple load cases. Using the same local element stiffness matrices, positions and orientations, all results could be validated up to the numerical accuracy for different structures, positions and load cases.

5.2.3 Calculation Sequence

Deriving the global stiffness matrix of the structure $^0K_{struc\,0}$ including non-linear elements and solving the linear system of equations (5.2) needs to be based on a deterministic algorithm, to be performed automatically with the necessary iterations. The developed sequence is shown in Figure 5-9 and described in this section. For each element, the following parameters need to be predefined:

- connecting rigid nodes,
- pose of the flexible element represented in the global coordinate system 0,
- element type (for example hollow rectangular Euler beam),
- element properties dependent on the element type (for example length, width, Young's modulus, etc. or identification number for bearings).
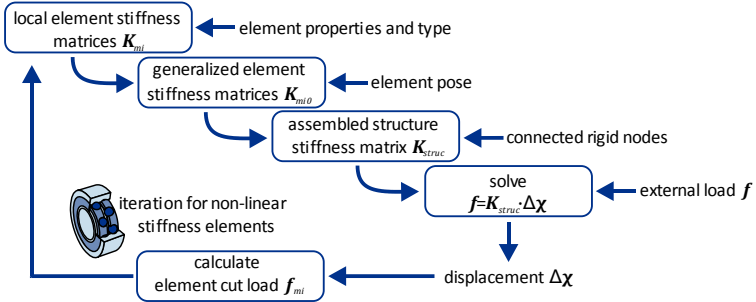
Figure 5-9: Sequence of the calculation procedure

By defining these parameters, the overall structure is fully described and the stiffness properties for the given pose can be calculated. For every type of element, for example a rectangular beam or a ball bearing, a specific calculation procedure is stored in a catalog. It allows for the determination of the local element stiffness matrix $^{mi}K_{mi}$ for every element mi, based on the element properties and pose as described in Annex 9.5 for the PARAGRIP prototype. The stiffness matrix for elements with force dependent stiffness properties (for example for ball-bearings) is calculated using a predefined unit force in the first iteration. The local element stiffness matrices are generalized depending on the pose of the element using equation (5.20). Following, the generalized stiffness matrix of the structure $^0K_{struc\,0}$ is as-

sembled from the element stiffness matrices $^0\boldsymbol{K}_{mi\,0}$ based on the connecting rigid nodes, using the superposition algorithm (5.31).

The resulting linear system of equations (5.2) needs to be solved to derive the displacement of the structure, represented by $^0\Delta\boldsymbol{\chi}_0$. In general, factorization methods are not efficient in solving linear system of equations with a large and sparse matrix like $^0\boldsymbol{K}_{struc\,0}$. Therefore, a set of numerical iterative solving methods to handle large, sparse input matrices has been tested with and without additional preconditioning. The tests have been run for different structures, poses and load cases. The best results regarding stability and convergence, number of iterations and computational time have been achieved using the generalized minimal residual method [SS86] without preconditioning and without inner restart of the iterations. A documentation of the implemented MATLAB® function *gmres* is given in [Mat16]. Especially for robot positions close to singularity, the condition of the sparse matrix becomes critical. Therefore, a verification of the numerical solution, for example by checking the residual of the linear system of equations, is crucial and implemented in the method. As shown in Figure 5-24 on page 75, the chosen critical residual of $8 \cdot 10^{-10}$ is not fulfilled for some calculation positions close to the workspace boundary. However, the residual is good for all positions with at least 2 mm distance from the workspace boundaries.

The previous steps are repeated iteratively, if the structure contains elements with a force dependent local stiffness matrix. The cut load $^{mi}\boldsymbol{f}_{mi}$, effective on the element mi with the attached rigid nodes k and l, is calculated from the local element stiffness matrix $^{mi}\boldsymbol{K}_{mi}$ as shown in equation (5.19) by:

$$^{mi}\boldsymbol{f}_{mi} = {}^{mi}\boldsymbol{K}_{mi} \cdot {}^{mi}\boldsymbol{R}_0 \cdot {}^0\boldsymbol{V}_{mi0} \cdot \left({}^0\Delta\boldsymbol{\chi}_{k\,0} - {}^0\Delta\boldsymbol{\chi}_{l\,0} \right) \tag{5.35}$$

The vectors $^0\Delta\boldsymbol{\chi}_{k\,0}$ and $^0\Delta\boldsymbol{\chi}_{l\,0}$ can be extracted from $^0\Delta\boldsymbol{\chi}_0$:

$$^0\Delta\boldsymbol{\chi}_{k\,0} = {}^0\Delta\boldsymbol{\chi}_0 \, (6k - 5 : 6k)$$

Where $^0\Delta\boldsymbol{\chi}_0 \, (c : d)$ indicate the sub-vector of $^0\Delta\boldsymbol{\chi}_{k\,0}$ in the columns c to d. $\tag{5.36}$

With the known load for every element, the force dependent stiffness matrices can be recalculated for the following iteration loop. Comparison with kinetostatic calculations and the analysis of multiple iteration steps show that two additional iterations are sufficiently accurate for low displacements in comparison to the dimensions of the given structure. As shown in Figure 5-10, the maximum divergence (for any direction of translation or rotation) to the previous iteration is about 0.1 % for the second iteration. The mean divergence is $3 \cdot 10^{-4}$ in this case. Both values decay down to magnitude 10^{-9} and 10^{-10}, respectively within 10 iterations.

The final result $^0\Delta\boldsymbol{\chi}_0$ represents the equivalent displacement of all rigid nodes at the point of origin O_0. To interpret this result, the displacement of a single node k, for example the TCP of the end-effector, is extracted from $^0\Delta\boldsymbol{\chi}_0$ and expressed in the local coordinate system k (with $^0\boldsymbol{V}_{k,0}$ formed from the vector pointing from O_0 to the point of origin O_k):

$$^k\Delta\boldsymbol{\chi}_k = {}^k\boldsymbol{R}_0 \cdot {}^0\boldsymbol{V}_{k,0} \cdot {}^0\Delta\boldsymbol{\chi}_{k\,0} \tag{5.37}$$
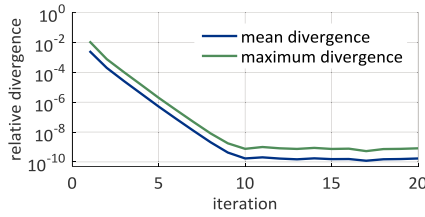
Figure 5-10: Relative divergence in the stiffness calculations from previous iterations (for 100 combinations of arbitrary load and pose of the PARAGRIP arm)

5.3   Stiffness Elements in the Model

As described above, a set of predefined elements is cataloged with the according calculation procedures for the local element stiffness matrix, to be able to automatize the calculation sequence for the stiffness model. Elements used for the PARAGRIP structure are shown in Figure 5-11 and described in this section.
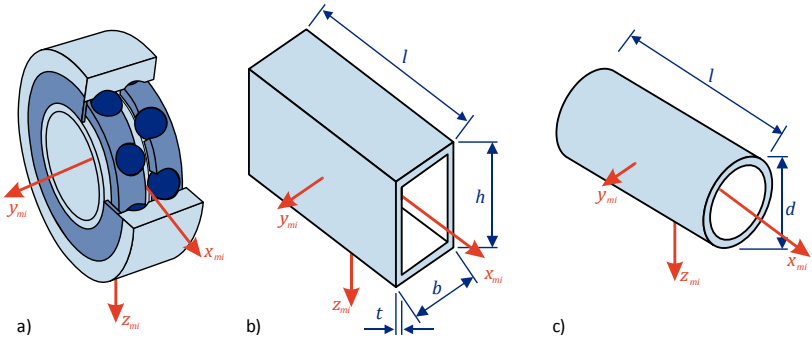
Figure 5-11: Coordinate systems and dimensions for a) ball-bearing, b) thin-walled rectangular profile and c) thin-walled round bar

5.3.1   Stiffness of Beam Elements

The compliance matrix of beam elements can be derived from Timoshenko's beam theory [Die05]. In comparison to the often used Euler-Bernoulli beam theory [DHM06], shear deformations are considered in Timoshenko's beam theory. They are relevant for slender beam elements with a small ratio between length l and wall thickness t. Slender beam elements do not apply for the PARAGRIP structure, but as they are typical for flexure hinges, Timoshenko's beam theory is used for the sake of universality.
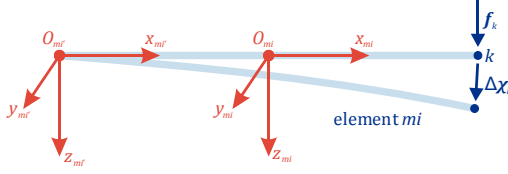
Figure 5-12: General beam element under load

Let the rigid node k be attached to beam m of arm i with a fixed coordinate system of reference frame $O_{mi'}$. The compliance matrix ${}^{mi'}C_{mi}$ links the displacement ${}^{mi'}\Delta\chi_k$ of the attached rigid node k to the external load ${}^{mi'}f_k$ on k:

$$ {}^{mi'}\Delta\chi_k = {}^{mi'}C_{mi} \cdot {}^{mi'}f_k \tag{5.38} $$

For the coordinate system mi' attached to the fixed base, the element compliance matrix is given by:

$$ {}^{mi'}C_{mi} = \frac{l}{E}
\begin{pmatrix}
\frac{1}{A} & 0 & 0 & 0 & 0 & 0 \\
0 & \frac{1}{3}\frac{l^2}{I_z}+\frac{E}{G \cdot A} & 0 & 0 & 0 & \frac{1}{2}\frac{l}{I_z} \\
0 & 0 & \frac{1}{3}\frac{l^2}{I_y}+\frac{E}{G \cdot A} & 0 & -\frac{1}{2}\frac{l}{I_y} & 0 \\
0 & 0 & 0 & \frac{E}{G \cdot I_T} & 0 & 0 \\
0 & 0 & -\frac{1}{2}\frac{l}{I_z} & 0 & \frac{1}{I_y} & 0 \\
0 & \frac{1}{2}\frac{l}{I_z} & 0 & 0 & 0 & \frac{1}{I_z}
\end{pmatrix} \tag{5.39} $$

E is the Young's modulus, G is the shear modulus and I_y, I_z and I_T represent the second moment of area.

Expressing the compliance matrix ${}^{mi'}C_{mi}$ and hence the displacement $\Delta\chi_k$, as well as the load f_k in the coordinate system mi in the center of the beam (see generalization of stiffness matrix in section 5.2.1) results in a diagonal matrix:

$$ {}^{mi}C_{mi} = \frac{l}{E}
\begin{pmatrix}
\frac{1}{A} & 0 & 0 & 0 & 0 & 0 \\
0 & \frac{1}{12}\frac{l^2}{I_z}+\frac{E}{G \cdot A} & 0 & 0 & 0 & 0 \\
0 & 0 & \frac{1}{12}\frac{l^2}{I_y}+\frac{E}{G \cdot A} & 0 & 0 & 0 \\
0 & 0 & 0 & \frac{E}{G \cdot I_T} & 0 & 0 \\
0 & 0 & 0 & 0 & \frac{1}{I_y} & 0 \\
0 & 0 & 0 & 0 & 0 & \frac{1}{I_z}
\end{pmatrix} \tag{5.40} $$

It should be stressed that cross coupling effects are still accounted for in this representation. Only by generalizing the compliance matrix to the so called center of stiffness [Lon87,Rob02], the matrix elements representing the cross-coupling effects are not repre-

sented explicitly by off-diagonal elements. The stiffness matrix $^{mi}\mathbf{K}_{mi}$ for beam elements can be derived by inversion of the compliance matrix $^{mi}\mathbf{C}_{mi}$:

$$^{mi}\mathbf{K}_{mi} = \left(^{mi}\mathbf{C}_{mi}\right)^{-1} \tag{5.41}$$

The second moments of area I_y and I_z can be calculated using classical beam theory [GWS14, p. 102–103] for the elastic elements of the structure. The torsion constant I_T is identical to the second moment of area I_x for circular shapes but cannot be calculated analytically for rectangular shapes as warping deformations on the front surface need to be considered. For many beam shapes approximate solutions are available [YB02, p. 401–425] and applied here for thin-walled rectangular profiles.

The second moments of area and cross section of a thin-walled round bar (see Figure 5-11c) are:

$$I_T = I_x = \frac{\pi}{32} \cdot \left(d^4 - d_{inner}^{\;4}\right) \tag{5.42}$$

$$I_z = I_y = \frac{\pi}{64} \cdot \left(d^4 - d_{inner}^{\;4}\right) \tag{5.43}$$

$$A = \frac{\pi}{4} \cdot \left(d^2 - d_{inner}^{\;2}\right) \tag{5.44}$$

With the inner diameter $d_{inner} = d - 2 \cdot t$ and t as wall thickness.

The torsion constant, second moments of area and cross section of a thin-walled rectangular profile (see Figure 5-11b) are:

$$I_Y = \frac{b \cdot h^3 - b_{inner} \cdot h_{inner}^{\;3}}{12} \tag{5.45}$$

$$I_Z = \frac{b^3 \cdot h - b_{inner}^{\;3} \cdot h_{inner}}{12} \tag{5.46}$$

With the inner width $b_{inner} = b - 2 \cdot t$ and inner height $h_{inner} = h - 2 \cdot t$.

$$I_T = \frac{4 \cdot A^2 \cdot h}{2 \cdot (b + h)} \tag{5.47}$$

$$A = 2 \cdot (b + h) \cdot t \tag{5.48}$$

5.3.2   Stiffness of Ball-Bearings

The stiffness properties of ball-bearings are non-linear and load dependent with cross coupling effects between radial displacement, axial displacement and torsion. Early studies investigated analytical and empirical approaches for the radial and axial stiffness properties [Pal46]. Current analytical approaches either aim at high computational speed by using a relatively simple model, for example Hertz's theory [BCB09], account for the cross-coupling effects of different loads [HSG00] or take into account dynamic effects [NRF13,LL05]. Even more complex approaches use finite element methods [GP12,DCG08] or neural networks [KHL06] to account for further characteristics like clearance, contact conditions and time dependent properties. The limiting assumptions in many of these stiffness models and comparisons of models and experimental data show that accurate stiffness properties of ball-

bearings are difficult to obtain: Many of the aforementioned methods are computationally expensive and require a large dataset.

Most manufacturers offer specific data for their roller-bearings (for example using the extensive calculation tool Bearinx® [Sch12]) to calculate the nonlinear displacement characteristics, taking into account the internal load distribution, the bearing deformations, the clearance and tolerances, pre-tensioning and a large set of further characteristics. To reduce the complexity of the overall stiffness model, characteristic curves for the axial and radial displacements Δ_{ax} and Δ_{rad} and the torsional displacement Δ_{tor} under different load conditions were generated in a previous work [Sei14 Dt] for a range of ball-bearings, as shown exemplarily in Figure 5-13 for the ball-bearing FAG 3807. The characteristic curves were calculated for a uniaxial load (F_{ax}, F_{rad} and M_{rad}) and for all possible load combinations and take into account the backlash of the bearing. The combined loads are scaled with respect to the maximum load considered. For example an axial load F_{ax} = 500 N (20 % of the 2500 N maximum force) was combined with a moment M_{rad} = 40 Nm (also 20 % of the 200 Nm maximum moment).
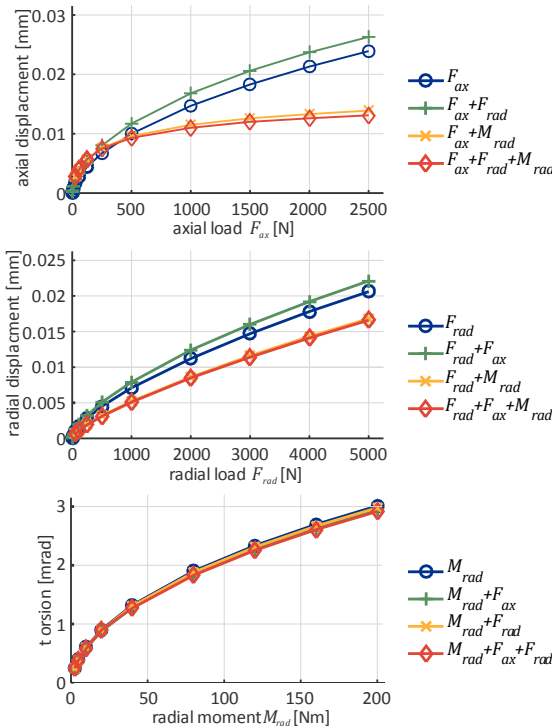
Figure 5-13: Characteristic curves for displacement and torsion for FAG 3807 ball-bearing under different load conditions

It is evident that combined loads influence the stiffness properties of the ball-bearings. The combined loads can be interpreted as pre-tensioning, increasing the stiffness of the bearing. The most obvious effect with an increased translational stiffness of up to 89 % (for the axial stiffness) results from an additional moment. This effect can be accounted for with a linear interpolation between the uniaxial characteristic curve and the curve for the combined load. For the combination of axial and radial load, the translational stiffness is reduced by up to 10 %, which is neglected to avoid the need of multi-dimensional characteristic data. For the torsional stiffness, the influence on combined loads is limited to a maximum of 3.5 % and is neglected as well. The stiffness matrix for the ball-bearings is derived by linear interpolation from the characteristic curves, neglecting cross-coupling effects:

$$
K_i = \begin{pmatrix}
k_{rad} & 0 & 0 & 0 & 0 & 0 \\
0 & k_{ax} & 0 & 0 & 0 & 0 \\
0 & 0 & k_{rad} & 0 & 0 & 0 \\
0 & 0 & 0 & k_{tor} & 0 & 0 \\
0 & 0 & 0 & 0 & 0 & 0 \\
0 & 0 & 0 & 0 & 0 & k_{tor}
\end{pmatrix}
\tag{5.49}
$$

$$
k_{rad} = \frac{F_{rad}}{\Delta_{rad}}, \quad k_{ax} = \frac{F_{ax}}{\Delta_{ax}}, \quad k_{tor} = \frac{M_{rad}}{\Delta_{rad}}
$$

The torsional stiffness is equal to zero for pivoting bearings that do not transmit any moments. The according coordinate system is shown in Figure 5-11a. The characteristic curves are defined for minimum loads of 1 N or 1 Nm up to a maximum load, specific for each bearing. For loads below the threshold, the stiffness properties are interpolated using the threshold value to account for backlash.

Considering the relatively low moments in the joints (see section 5.4.1) and the moderate contribution of the bearings to the overall compliance of the handling system (see section 5.4), these simplifications have minor influence on the calculated overall stiffness properties of the structure and allow for high computational speed.

5.3.3   Predefined Stiffness Elements

For complex structural components, like for example the vacuum gripper at the end-effector or the central connection to the frame, analytical approaches cannot be applied to calculate the stiffness properties accurately and with acceptable effort. In such cases the stiffness matrix can be derived from measurements or from FEA analysis by numerical processing of a set of deflection simulations [KPC13]. For the implementation the simplified predefined stiffness matrix is given by:

$$
K_i = \begin{pmatrix}
k_x & 0 & 0 & 0 & 0 & 0 \\
0 & k_y & 0 & 0 & 0 & 0 \\
0 & 0 & k_z & 0 & 0 & 0 \\
0 & 0 & 0 & k_\alpha & 0 & 0 \\
0 & 0 & 0 & 0 & k_\beta & 0 \\
0 & 0 & 0 & 0 & 0 & k_\gamma
\end{pmatrix}
\tag{5.50}
$$

It is defined by the single values for the diagonal entries (see annex 9.5 for examples); values that are not defined are interpreted to represent rigid properties.

5.3.4   Stiffness of the Vacuum End-Effector

The stiffness properties of the vacuum end-effector are mainly influenced by the soft rubber contact element and the bearings. They are dependent on the direction of load relative to the alignment of the wrist-joint axes R, S and T (Figure 5-14b).
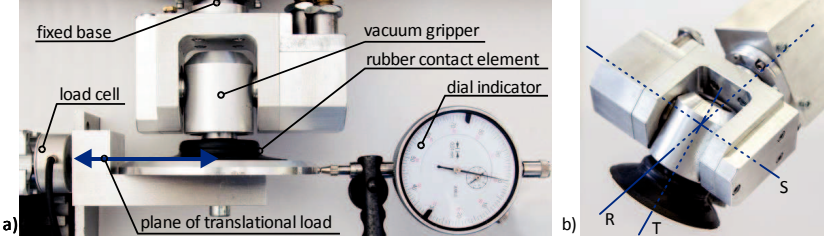

Figure 5-14: a) Experimental set-up for the determination of characteristic load-displacement curves of the vacuum end-effector (shown for the lateral displacement parallel to the S-axis), b) wrist-joint axes

The translational stiffness is determined by uniaxial measurements with the experimental set-up shown in Figure 5-14a. The vacuum end-effector is fixed in a base and normal and lateral forces are measured by a uniaxial load cell. The displacement is applied using a sliding carriage and measured using a dial indicator. The sliding carriage prohibits tilt within the measurement accuracy and ensures uniaxial loading conditions.

Characteristic curves for the normal displacement Δ_{norm} in direction of the T-axis, the lateral displacement parallel to the S-axis $\Delta_{lat\ par}$ and the lateral displacement perpendicular to the S-axis $\Delta_{lat\ per}$ were determined and are shown in Figure 5-15. For loads below a threshold of 2 N (absolute value), the stiffness properties are interpolated using the threshold value to avoid numerical instability.
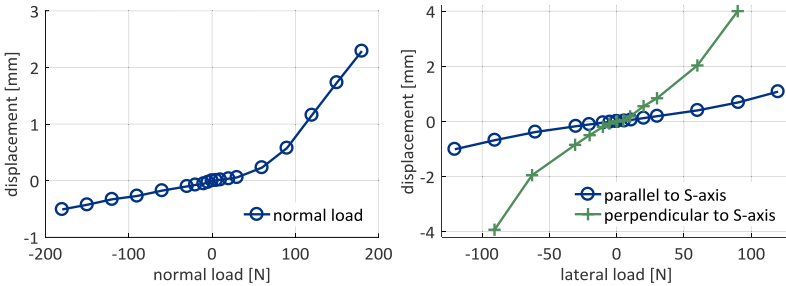
Figure 5-15: Characteristic curves for the displacement of the vacuum end-effector under normal and lateral load

The stiffness properties for the compression (negative normal load) and tension (positive normal load) differ from each other. For compression, the plastic contact surface of the rubber contact element is in direct contact to the surface of the grasped object. For tension, the contact is mainly established by the suction of the outer rubber ring, resulting in a lower stiffness. The stiffness properties for lateral load are determined for two different load cas-

es. For loads parallel to the S-axis (as shown in Figure 5-14) the stiffness is mainly determined by the lateral stiffness of the rubber contact element and the wrist-joint bearings. Loads perpendicular to the S-axis induce moments around the S-axis that are not supported by the kinematic structure. Therefore, the translational stiffness perpendicular to the S-axis is reduced due to the rotational compliance of the rubber contact element as shown in Figure 5-16.
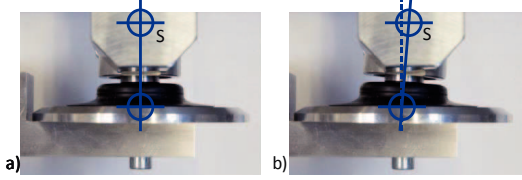
Figure 5-16: Deformation of the vacuum end-effector for a) no load, b) 150 N lateral load perpendicular to the S-axis of the wrist-joint

The stiffness matrix (5.51) for the vacuum end-effector is derived by linear interpolation of the characteristic curves:

$$
{}^{T}\boldsymbol{K}_{wrist\ joint} = \begin{pmatrix} k_{nom} & 0 & 0 & 0 & 0 & 0 \\ 0 & k_{lat\ par} & 0 & 0 & 0 & 0 \\ 0 & 0 & k_{lat\ per} & 0 & 0 & 0 \\ 0 & 0 & 0 & 0 & 0 & 0 \\ 0 & 0 & 0 & 0 & 0 & 0 \\ 0 & 0 & 0 & 0 & 0 & 0 \end{pmatrix}
\tag{5.51}
$$

$$
k_{norm} = \frac{F_{norm}}{\Delta_{norm}}, \quad k_{lat\ par} = \frac{F_{lat\ par}}{\Delta_{lat\ par}}, \quad k_{lat\ per} = \frac{F_{lat\ per}}{\Delta_{lat\ per}}
$$

The according coordinate system T is aligned with the gripped object and is shown in Figure 5-14b and Figure 3-5.

5.4   PARAGRIP Stiffness Model

The PARAGRIP arm structure (see Figure 5-17a) is modeled using the introduced stiffness calculation method based on the MSA. The links are represented by beam elements ($\boldsymbol{K}_{link\ 1}$, $\boldsymbol{K}_{link\ 2}$, $\boldsymbol{K}_{link\ k}$ and $\boldsymbol{K}_{link\ 3}$) and pre-defined stiffness elements from FEA ($\boldsymbol{K}_{link\ 4}$). The joints are represented by ball-bearings ($\boldsymbol{K}_{joint\ A0}$, $\boldsymbol{K}_{joint\ B0}$, $\boldsymbol{K}_{joint\ A}$, $\boldsymbol{K}_{joint\ B}$ and $\boldsymbol{K}_{joint\ C}$). The stiffness of the specific end-effector was measured and analyzed and is represented by a separate pre-defined stiffness element as introduced at the end of section 5.3. The drive stiffness ($\boldsymbol{K}_{drive\ 1}$ and $\boldsymbol{K}_{drive\ 4}$) including the belt gear and the connection to link 5 cannot be derived analytically or by FEA. Therefore, these stiffness parameters are identified by measurements and optimization, based on a set of simple load cases for the structure, as described in section 5.4.1. The same applies for the stiffness $\boldsymbol{K}_{link\ 5}$ and the drive stiffness $\boldsymbol{K}_{drive\ D0}$ of the main axis of rotation, which includes the internal bearings and the connection to the base. The analysis of the according complex assembly groups would be highly complicated.
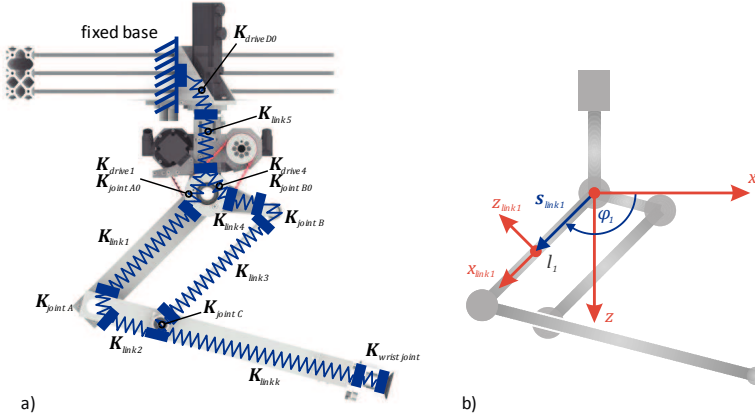
Figure 5-17: a) Structure of the PARAGRIP stiffness model, b) coordinate system for the stiffness element of link 1

Figure 5-17b shows the local coordinate system for the local element stiffness matrix $K_{link\,1}$, which is referred to for the generalization of the stiffness matrices (see 5.2.1). The connecting nodes, element types, properties and coordinate systems for all elements are given in Annex 9.5.

5.4.1   Identification of Parameters for the PARAGRIP Arm Stiffness Model

In case, the stiffness properties of structural elements cannot be calculated analytically or by FEA, they can be determined by measurements of the element or the complete structure. The parameter identification can either be based on a dynamic model (see for example [WWY10]) or on direct measurements of the stiffness properties of a single structural element or the complete structure (see for example [KFC15,DCC10,ZWZ05]), which is more efficient in most cases and used here. A set of 8 simple load cases, as shown in Figure 5-18 and detailed in Annex 9.6, is used to identify the parameters k_i for the stiffness matrices $K_{drive\,1}$, $K_{drive\,4}$, $K_{drive\,D_0}$ and $K_{link\,5}$. The load cases are chosen in a way as to allow for the most direct possible measurement of the properties. The measurements are performed with a dial indicator with a measurement resolution of 0.01 mm and repeated 3 times.
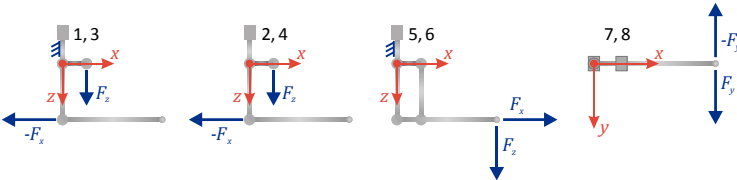
Figure 5-18: Positions of the PARAGRIP arm and direction of forces for the identification measurements of the stiffness model

The drive D_0 was fixed for load cases 1, 3, 5 and 6 using a rigid connection to directly attach link 5 to the base. The displacements of the rigid connection are below the measurement accuracy of 0.01 mm. This allows for the determination of $\boldsymbol{K}_{link\,5}$ from the measured displacements without fixation. The stiffness $\boldsymbol{K}_{drive\,D_0}$ can be derived when comparing the measured displacements for the fixed drive D_0 (load cases 1, 3, 5 and 6) to the unrestricted measurements (load cases 2, 4, 7 and 8). Furthermore, $\boldsymbol{K}_{drive\,1}$ and $\boldsymbol{K}_{drive\,4}$ can be derived from load cases 1-4, where the displacement of the drives in connection with the known displacement of link 1 and link 4, respectively, is measured. Link 3 was removed for the purpose of separately measuring the properties of drive 1 and drive 4, independent from the influences of the remaining structure. For all load cases, the drives were stopped with an activated safety brake when applicable or activated for a fixed position. The contouring error of the drive was validated to be zero and the results for stopped and activated motors did not differ from each other. The introduced PARAGRIP stiffness model is modified according to the missing link 3 and the fixation of drive D_0 for the given load cases to perform the parameter identification.

The stiffness parameters k_i can be identified by numerical optimization, minimizing the residual R between the measured displacement $\Delta \bar{\boldsymbol{r}}_{TCP\,e}$ and modeled nominal displacement $\Delta \hat{\boldsymbol{r}}_{TCP\,e}$ of the TCP for the given load cases e:

$$\min_{k_i \in \mathbb{R}^n} R(\Delta \bar{r}_{TCP\,e}, \Delta \hat{r}_{TCP\,e}) \tag{5.52}$$

It should be noted, that this residual R does not have the same central meaning as for the calibration and self-calibration and is only discussed briefly. It is calculated using the specific target function (5.55), to account for the absolute deviation $\Delta r_{abs\,e}$ and the relative deviation $\Delta r_{rel\,e}$:

$$\Delta r_{abs\,e} = |\Delta \hat{\boldsymbol{r}}_{TCP\,e} - \Delta \bar{\boldsymbol{r}}_{TCP\,e}| \tag{5.53}$$

$$\Delta r_{rel\,e} = \frac{|\Delta \hat{\boldsymbol{r}}_{TCP\,e} - \Delta \bar{\boldsymbol{r}}_{TCP\,e}|}{|\Delta \bar{\boldsymbol{r}}_{TCP\,e}|} \tag{5.54}$$

The measured displacements for the chosen load cases range from 0.11 mm to 2.82 mm. To account for this large range, the relative and the absolute deviations between model and measurement need to be considered for the calculation of Δr_e to achieve a well-adjusted significance to all load cases:

$$\Delta r_e = \begin{cases} \Delta r_{abs\,e} + \Delta r_{rel\,e} & |\Delta r_{abs\,e} > 0.03\;mm \\ 0.05 \cdot \Delta r_{abs\,e} & |\Delta r_{abs\,e} \leq 0.03\;mm \end{cases} \tag{5.55}$$

The relative deviation $\Delta r_{rel\,e}$ is only considered up to the threshold of 0.03 mm. It is not meaningful for small deviations close to the measurement accuracy. The optimization routine is quite sensitive to this threshold and the chosen threshold has shown the best results for the given measurement data (see Annex 9.7). The deviations $\Delta r_{abs\,e}$ and $\Delta r_{rel\,e}$ are in a similar order of magnitude for the given data and are not scaled or weighted. The weighting of the absolute deviation $\Delta r_{abs\,e}$ for values below the threshold is chosen to be 0.05, to prioritize the optimization of higher deviations that are not close to the measurement accuracy.

The residual R is calculated as the Euclidian norm of all deviations Δr_e for all load cases:

$$R = \sqrt{\sum_e \Delta r_e^2}$$
(5.56)

The optimization is implemented using the Nelder-Mead simplex algorithm as described by Lagarias and others [LRW98]. The according MATLAB® function *fminsearch* [Mat17b] has proven to be stable and reliable for the parameter identification. The optimization terminates with a final residual $R = 0.153$. The results are summarized in Table 5-1 and given in detail in Annex 9.7. The remaining deviations are higher than the theoretical measurement accuracy for some load cases. However, the verification of the model and identified parameters show good results (see section 5.4.2). Variations in the considered load cases and optimization routine do not change the verification results or model behavior significantly. The stiffness parameters applied for the model are listed in Annex 9.5. Preceding investigations of the measurements results are given in a previous work [Cab14 Dt].

	$\Delta r_{abs\,e}$	$\Delta r_{rel\,e}$
minimum deviation	0.0011 mm	0.0011
mean deviation	0.0299 mm	0.0545
maximum deviation	0.0660 mm	0.1667

Table 5-1: Deviation between modeled displacement and the parameter identification measurements

Joint Loads of the Handling System

To assess the value range for the characteristic curves for the ball-bearing stiffness and the vacuum end-effector stiffness, the joint loads of the handling system during normal operation were calculated and analyzed for a typical handling task of the prototype. During an example motion a 1 kg plate is moved with oscillating translational and rotational motions and a random spline in the whole PARAGRIP workspace. The dynamic loads are calculated considering the inertia of the object and the inertia of all arm components, as shown in [Rie14, p. 95–100]. This motion only exhibits 13-35 % of the maximum motor torque, dependent on the motor. Consequently, the resulting loads should be scaled to assess the maximum value range needed for the characteristic curves.

Based on the analysis, the bearing loads can be expected to be up to 400 N and 2 Nm, which is within the value range of the characteristics curves shown in Figure 5-13. The loads for the end-effector can be expected to be up to 50 N, again within the characteristics curves shown in Figure 5-15.

5.4.2   Validation of the Model

The PARAGRIP stiffness model is validated by measuring the translational displacement of the end-effector under static forces as introduced briefly in [DC16]. The forces are applied in the three coordinate directions of the arm using static weights and low-friction redirection of the load cable. The displacement is measured for arm 1 using an optical CMM with a minimum absolute accuracy of 0.15 mm (see section 4.3). 21 different measurements were per-

formed for representative positions of a single robotic arm as shown in Figure 5-19. They differ significantly from load cases used for the parameter identification and are listed in detail in Annex 9.8.
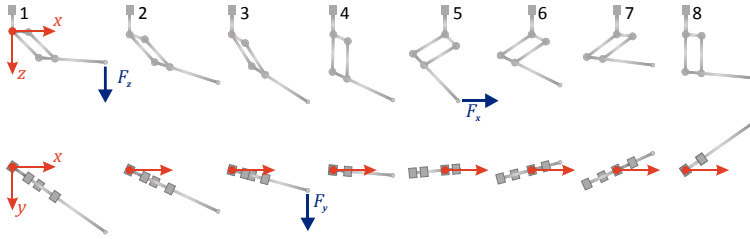

Figure 5-19: Positions of the PARAGRIP arm and direction of forces (indicated for exemplary positions) for the verification measurements of the stiffness model

Figure 5-20 to Figure 5-22 show the measured and calculated displacements for all load cases. The absolute accuracy of the CMM is indicated by error bars. Remaining friction in the load redirection and alignment deviations of the applied load are considered insignificant.
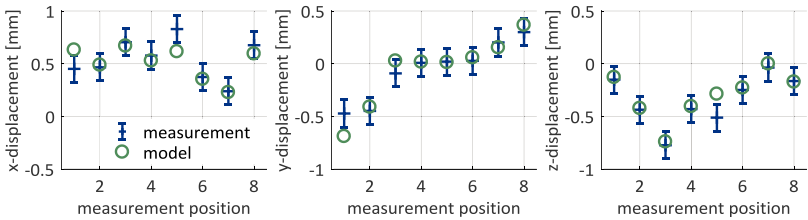
Figure 5-20: Measured and calculated end-effector displacement under uniaxial load in global x-direction
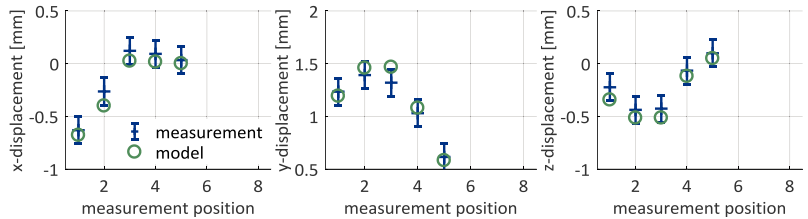
Figure 5-21: Measured and calculated end-effector displacement under uniaxial load in global y-direction
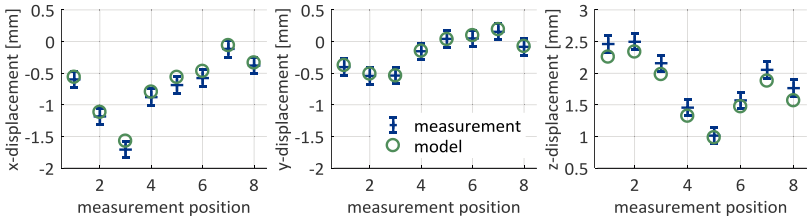
Figure 5-22: Measured and calculated end-effector displacement under uniaxial load in global z-direction

The calculated displacements are in good agreement with the measurements for all load cases. Measurements number 1 and 5 show increased deviations for uniaxial load in global x-direction, which may be a result of measurement errors. For the remaining load cases the deviations are summarized in Table 5-2. The maximum deviation between measurement and model is 0.22 mm for the norm of all directions. The average deviation is 0.13 mm for the norm of all directions, which is a 10 % deviation from the average measurement value. These results are in the same order of magnitude as the measurement accuracy and validate the stiffness model. Furthermore, they are in the same order of magnitude as the repeatability of the robotic arm and are hence considered sufficiently accurate.

	Δx	Δy	Δz	$|\Delta r|$
minimum deviation	0.01 mm	0.00 mm	0.01 mm	0.04 mm
mean deviation	0.07 mm	0.04 mm	0.09 mm	0.13 mm
maximum deviation	0.14 mm	0.15 mm	0.21 mm	0.22 mm

Table 5-2: Deviation between modeled displacement and the verification measurements for all load cases except 1 and 5

Concluding, the displacement in the direction of load as well as cross coupling effects can be calculated using the introduced model. Furthermore, the model and measurements show a similar agreement for both high and low loads within the range of expected loads on the PARAGRIP arms during handling. However, the remaining errors need to be considered, when applying the model to the methods of calibration and self-calibration, which might reach the limit of their possibility because of this constrained model quality.

5.4.3   Stiffness Influence Analysis

The PARAGRIP stiffness model allows for the assessment of the influence of different components on the overall compliance of the robotic arm and the handling system with integrated object, respectively. The analysis is based on the variation of the stiffness properties for each component or group of components i by the One-Factor-At-a-Time method. All components, except the components under investigation, are set to be ideally rigid in the model and the norm of the displacement $\Delta \chi_i$ at the end-effector or integrated object is calculated for the given load. The relative influence ϑ of each parameter p_i is calculated as follows:

$$\vartheta_{p_i} = \frac{|\Delta \chi_i|}{|\Delta \chi|}$$

(5.57)

With the displacement $\Delta \chi$ for the unmodified model without rigid elements.

The relative contribution to the elasticity of the structure is shown in Figure 5-23 as an average for 100 arbitrary load cases in the workspace.

The rotational compliance of the actuators (y-component of $k_{drive\ D0}$, $k_{drive\ 1}$ and $k_{drive\ 4}$: 41 %) and the compliance of the base frame attachment (x- and z-component of $k_{drive\ D0}$ and $k_{link\ 5}$: 25 %) are the main elasticity contributors for the single arm structure accounting for two thirds of the elasticity. However, the strong influence of the base frame attachment

is reduced to 12 % for the PARAGRIP structure with integrated object, as the loads introduce lower moments to the base frame attachment for this parallel kinematic configuration. The influence of the joints (9 % for the single arm and 21 % for the handling system) and links (12 % for the single arm and 29 % for the handling system) is significantly increased for the parallel kinematic configuration of the handling system, where relatively high link and joint forces occur [Rie14, p. 140].
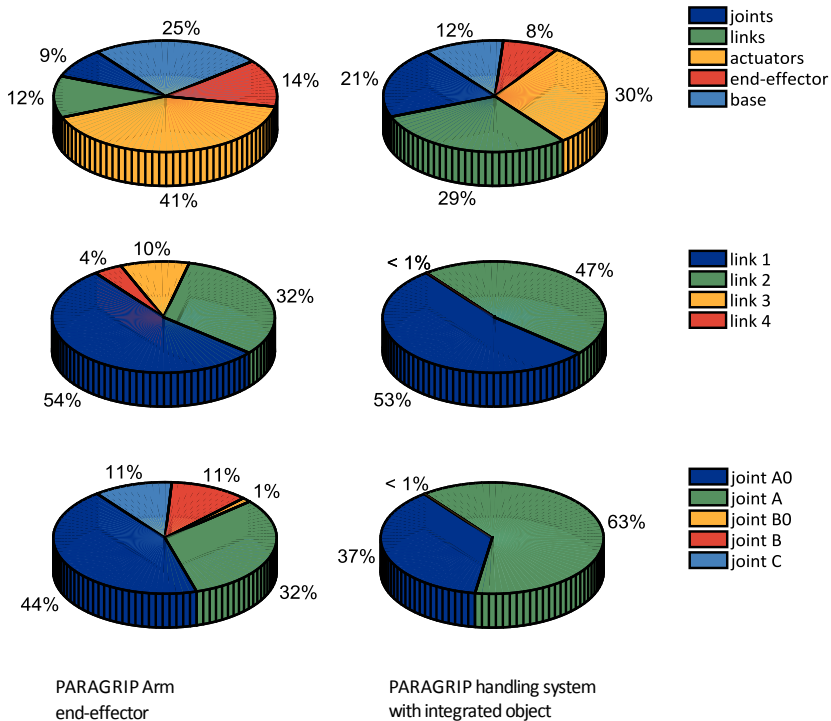

Figure 5-23: Elasticity contributors to absolute displacement at the TCP of the PARAGRIP arm and to the absolute displacement at the integrated handling object for the PARAGRIP handling system (average from 100 combinations of arbitrary load and static pose)

The detailed analysis of the links and joints shows the dominant influence of the main kinematic chain, composed of links 1 and 2 and the connected joints A0 and A. The influence of the second kinematic chain with links 3 and 4 and joints B0, B and C is low for the single arm and vanishes for the handling system with integrated object. As link 3 in the second kinematic chain only transmits unidirectional forces, all torques and transverse forces are supported by the main kinematic chain, which explains its main contribution to the elasticity of the system. These findings are in good agreement with the design considerations Riedel made for the synthesis and dimensioning of the structure based on joint loads and simplified beam models [Rie14, p. 140]. At the same time, the stiffness model allows for a more detailed

analysis of the overall joint influence that cannot be neglected for the given structure and is well balanced to the remaining elasticity contributors.

The end-effector has been observed to be rather soft in comparison to the joints and other elements: The translational stiffness values are approximately 2500 times lower for the end-effector, compared to the bearings in joint A0 (see section 5.3). However, end-effectors influence is not as high as one would expect based on this data. The end-effector is positioned close to the point of the application of force and does not support any moments, which reduces its deformations significantly. In summary, the stiffness properties of the base frame attachment, actuators, joints, links and end-effector are well balanced, for the parallel kinematic configuration of the PARAGRIP handling system.

5.5   Calculation of Gravitational Deformations

The pose dependent deformation of the structure due to the self-weight is investigated for the PARAGRIP arm to assess and compensate for its influence on the kinematic modeling and calibration. The self-weight can be approximated by introducing the masses of the joints as point forces and by substituting the distributed gravitational force of the links with an equivalent couple of force F_1, F_2 and moment M_1, M_2 at the connecting nodes of each beam element. The resulting load vector ${}^0\boldsymbol{f}_{grav\,0}$ after generalization is used as the according input to equation (5.2) to derive the generalized gravitational deformation ${}^0\Delta\boldsymbol{\chi}_{grav\,0}$. The resulting displacement ${}^{0A}\Delta\boldsymbol{r}_{grav\,TCP}$ of the TCP can be extracted as shown in equation (5.37). This approach is well known from FEA, where distributed loads are expressed by equivalent loads at the nodes of the finite elements based on the principle of virtual work [Kle15, p. 68–71].

The equivalent loads can be calculated for the different support configurations of the beam elements. Link 1 and link 4 have a fixed position and orientation defined by the actuator, hence, their rotation and deflection can be approximated by cantilever beams with a clamped and a free end. The same applies for link k that is fixed to joint C in position and orientation (see Figure 5-17). Link 2 and link 3 are supported by rotational joints at both ends, hence, their rotation and deflection can be approximated by simply supported beams (compare [Rie14, p. 139]).

Vertical Beam under Gravitational Load

The elongation Δl for cantilever and simply supported beams under uniform distributed load can be expressed by an equivalent point force F_2 at the free end of the beam [GWS14, p. 22–23]. For this trivial case, the force F_1 is calculated from the equilibrium of forces. The resulting equivalent loads are shown in Table 5-3.
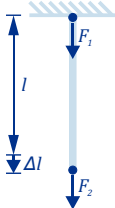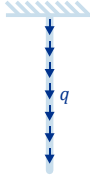
	point force at the nodes	uniformly distributed load
vertical beam		
elongation	$\Delta l = F_2 \cdot l \cdot \frac{1}{E \cdot A}$	$\Delta l = \frac{1}{2} \cdot q \cdot l^2 \cdot \frac{1}{E \cdot A}$
equivalent load	$F_1 = \frac{q \cdot l}{2}$ $F_2 = \frac{q \cdot l}{2}$ with $q = \frac{m \cdot g}{l}$	

Table 5-3: Substitution of the gravitational force for vertical beams

Horizontal Simply Supported Beam under Gravitational Load

The deflection w and rotation $w`$ at both ends of a beam define the state of the beam for the case of a uniformly distributed load and the case of equivalent loads. The equality of deflection $w$ and rotation $w`$ can therefore be used to calculate the equivalent loads, analogous to the principal of virtual work.
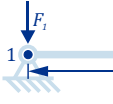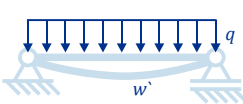
	point force at the nodes	point moment at the nodes	uniformly distributed load
simply supported beam			
rotation	$w`_1 = w`_2 = 0$	$w`_1 = \left(\frac{M_2}{6} - \frac{M_1}{3}\right) \cdot l \cdot E \cdot I$   $w`_2 = \left(\frac{M_1}{6} - \frac{M_2}{3}\right) \cdot l \cdot E \cdot I$	$w`_1 = \frac{1}{24} \cdot q \cdot l^3 \cdot E \cdot I$   $w`_2 = -\frac{1}{24} \cdot q \cdot l^3 \cdot E \cdot I$
deflection	$w_1 = w_2 = 0$	$w_1 = w_2 = 0$	$w_1 = w_2 = 0$
equivalent loads	$F_1 = \frac{q \cdot l}{2}$ $F_2 = \frac{q \cdot l}{2}$ with $q = \frac{m \cdot g}{l}$	$M_1 = -\frac{1}{12} \cdot q \cdot l^2$ $M_2 = \frac{1}{12} \cdot q \cdot l^2$ with $q = \frac{m \cdot g}{l}$	Young's modulus E second moment of area I

Table 5-4: Substitution of the gravitational force for a simply supported beam with an equivalent couple of force F_1, F_2 and moment M_1, M_2

For a horizontal simply supported beam, the deflection w is equal to zero for both connecting nodes in all load cases. The rotation $w`$ needs to be equivalent for the superposition of M_1 and M_2 and the effect of the gravitational force q [GWS14, p. 138–141]. With this substitution, the equivalent moments M_1 and M_2 can be calculated. F_1 and F_2 are calculated

from the equilibrium of forces. The resulting equivalent loads are shown in Table 5-4 and are identical to the results obtained from the principle of virtual work [Kle15, p. 69].
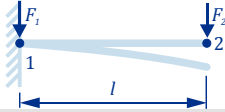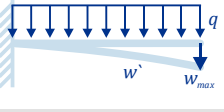
Horizontal Cantilever Beam under Gravitational Load

For a horizontal cantilever beam, the maximum deflection w_{max} at the free end of the beam (node 2) and the rotation $w`$ need to be equivalent for the superposition of F_2 and M_2 and the effect of the gravitational force q [GWS14, p. 138–141]. With this substitution, the equivalent force F_2 and the equivalent moment M_2 can be calculated. F_1 and M_1 are calculated from the equilibrium of forces and moments. The resulting equivalent loads are shown in Table 5-5 and are identical to the results obtained from the principle of virtual work [Kle15, p. 70].

	point force at the nodes	point moment at the nodes	uniformly distributed load
cantile-ver beam			
rotation	$w` = \frac{1}{2} \cdot F_2 \cdot l^2 \cdot E \cdot I$	$w` = -M_2 \cdot l \cdot E \cdot I$	$w` = \frac{1}{6} \cdot q \cdot l^3 \cdot E \cdot I$
deflec-tion	$w_{max} = \frac{1}{3} \cdot F_2 \cdot l^3 \cdot E \cdot I$	$w_{max} = -\frac{1}{2} \cdot M_2 \cdot l^2 \cdot E \cdot I$	$w_{max} = \frac{1}{8} \cdot q \cdot l^4 \cdot E \cdot I$
equiva-lent loads	$F_1 = \frac{q \cdot l}{2}$ $F_2 = \frac{q \cdot l}{2}$ with $q = \frac{m \cdot g}{l}$	$M_1 = -\frac{7}{12} \cdot q \cdot l^2$ $M_2 = \frac{1}{12} \cdot q \cdot l^2$ with $q = \frac{m \cdot g}{l}$	Young's modulus E second moment of area I

Table 5-5: Substitution of the gravitational force for a cantilever beam with an equivalent couple of force F_1, F_2 and moment M_1, M_2

Superposition of Horizontal and Vertical Load Case

The equilibrium forces are identical for horizontal and vertical load cases. However, the equivalent moments for the vertical load case are equal to zero. To calculate the effect of gravitational forces on the structure, both load cases are super-positioned, dependent on the position of the link. The resulting equivalent loads for link 1 (shown in Figure 5-17b) are shown in equations (5.58) to (5.61) and can be calculated analogous for the remaining links.

$$F_1 = \frac{1}{2} \cdot m_{link\,1} \cdot g \tag{5.58}$$

$$F_2 = \frac{1}{2} \cdot m_{link\,1} \cdot g \tag{5.59}$$

$$M_1 = cos(\varphi_1) \cdot \frac{-7}{12} \cdot m_{link\,1} \cdot g \cdot l_{link\,1} \tag{5.60}$$

$$M_2 = cos(\varphi_1) \cdot \frac{1}{12} \cdot m_{link\,1} \cdot g \cdot l_{link\,1} \tag{5.61}$$

Gravitational Effects on the PARAGRIP Structure

The gravitational effects on the PARAGRIP arm structure due to self-weight were investigated for the arm workspace to assess its influence to kinematic modeling. The TCP-displacement in vertical direction ranges between 0.15 mm and 1.28 mm and is highest for TCP-positions at elongated joint poses at the workspace boundaries, as shown in Figure 5-24. The sparse stiffness matrix tends to be ill-conditioned at the workspace boundaries (as explained in section 5.2.3) and calculation points violating the critical residual are not considered and marked accordingly in the figure. The horizontal TCP-displacement (2-norm of the x- and y-displacement) ranges from 0.01 mm up to 1.20 mm. However, the average horizontal displacement is 0.25 mm and is considerably lower than the 0.63 mm average vertical displacement. The displacements are inhomogeneous with respect to the full TCP-workspace, which clearly influences the accuracy of the kinematic calculations, as positioning errors due to the deformation under self-weight are not represented within the kinematic models. As shown in Figure 5-24, the displacements are relatively constant in the center of the workspace, especially for the displacement in the vertical z-direction. This limits the gravitation effect for most handling tasks.
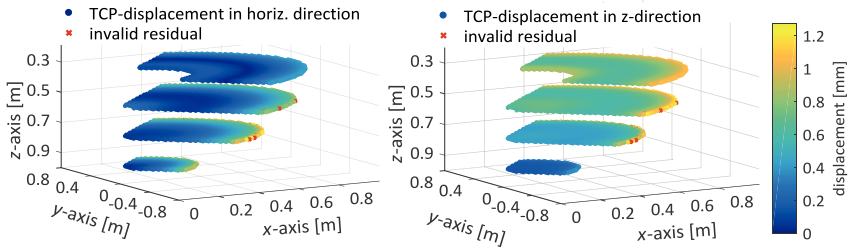
Figure 5-24: TCP-displacement of the PARAGRIP arm under its own weight for the horizontal (norm of x- and y-displacement) and vertical (z-displacement) direction in the arm workspace

However, the influence of the self-weight and its inhomogeneity is significant for the identification of the kinematic parameters (see section 4) and is implicitly represented in the quality of the kinematic calibration of the structure, which in large parts relies on measurements close to the workspace boundaries. Extending the procedure of kinematic parameter identification from level 2 to level 3 by gravitational compensation improves the gained absolute accuracy of a single arm by up to 25 % as described in section 4.7.

5.6   Summary and Conclusion for the Stiffness Modelling

The investigation of the state of research in stiffness modeling has shown that three main approaches, the Virtual Joint Method, the Finite Element Analysis and the Matrix Structure Analysis can be followed. The MSA was chosen as a basis for the extended stiffness modeling approach. It allows for the consideration of the stiffness for various elements, for example the integration of the nonlinear behavior of rolling contact elements based on characteristic curves. The local stiffness matrices were derived for generic beam elements, a set of ball-bearings, the end-effector and structural elements specific to the handling system. The individual stiffness properties were identified successfully by the analysis of simple load cases.

The calculation method is based on generalized stiffness matrices, which are expressed by means of equivalent displacements and loads. This unified approach allows for the implementation of a calculation sequence for the systematic assembly of the stiffness matrix of any structure. The stiffness modeling approach including the derived stiffness elements was validated for the investigated PARAGRIP handling system by measurements on an arbitrary trajectory in the workspace. It shows a good performance for both high and low loads, in particular considering cross coupling effects that are significant for the investigated structure.

The stiffness influence analysis showed a well-balanced distribution of the compliance between the joints, links, actuators, end-effector and base of the PARAGRIP arms. Furthermore, the mechanically dominant links 1 and 2 and the according joints are the main contributors for the structural stiffness and that the influence of the hybrid extension is low and even negligible after object integration.

Using the validated approach, the gravitational deformations of the structure were calculated for the kinematic calibration in section 4. A comprehensive stiffness analysis confirms the original design consideration for the handling system and shows well balanced properties. Based on this, the gravitational compensation is used for the level 3 calibration in section 4.

6   Self-Calibration for Object Integrative Handling Systems

Self-calibration can be applied for cooperating robots, or more specifically for object integrative handling systems, in order to compensate for influencing factors that cannot be compensated for by classical kinematic calibration (see section 2 and Figure 2-1). Beside others, the object pose and dimensional tolerances of the object geometry are usually not known precisely before grasping, as they vary with the grasping process. These factors induce a deviation of the actual grasp points from the nominal grasp points and consequently reduce the accuracy of the handling system.

Self-calibration allows for the identification of the real grasp points on the object without additional external metrology and will be applied to compensate for the mentioned influencing factors. It relies on the use of redundant sensor information, available within the kinematic structure and is a sub-category of the closed loop calibration explained in section 6.1.

The general considerations for calibration procedures, for example regarding the complexity, model quality, parameter identification and measurement poses, introduced in section 4, and the numerical optimization, introduced in section 4.1, apply for closed loop calibration just as they do for open loop calibration. As already mentioned many authors give an overview regarding (open and closed loop) calibration methods [MSS10,LRH10, p. 90–106,HLJ10,CLC14].

Closed loop calibration methods have been developed, applied and verified for articulated serial robots and various parallel and hybrid robots. Due to the existence of closed kinematic chains and the easy adaption of redundant sensors, most methods are applied for parallel structures. Up to now, closed loop calibration has, however, not been applied to object integrative handling systems and will therefore be investigated for this field of application. Based on the state of research described in the following section, a new approach of self-calibration is introduced in section 6.2 to identify the frequently changing parameters, namely grasp points, for cooperating robots. For the sake of compactness and to prove general feasibility of the approach, the investigations are limited to the PARAGRIP prototype and its specific kinematic configuration.

6.1   State of Research in Closed Loop Calibration

In closed loop kinematic calibration the residual between the theoretical kinematic model and the manipulator's behavior is calculated based on closed kinematic chains. It was first introduced by Bennett and Hollerbach [BH91] to eliminate the need of external metrology. They showed that consistency conditions in kinematic chain closure equations are adequate to calibrate a manipulator using the joint readings. Based on this, Wampler and others [WA92,WHA95] introduced the unified approach of implicit loop formulation that was already introduced in section 4.1.2.

Additional sensor information in each closed kinematic chain allow for the numerical optimization of the kinematic model and the according compensation of parameter deviations. For this, the number of internal sensors needs to exceed the number of DOF of the mechanism,

which is achieved by introducing the aforementioned closed kinematic chains. They can be introduced either by means of additional mechanical constraints, which reduces the number of DOF of the mechanism, as virtual closed kinematic chains with additional sensors or by analyzing existing closed kinematic chains with redundant sensors. These three approaches are explained in the following sections to give an overview of possible approaches and identify suitable approaches for the self-calibration of object integrative handling systems.

6.1.1   Constrained Closed Kinematic Chain Calibration

The closed kinematic chain calibration is based on the creation of mechanically constrained kinematic chains, resulting in sensor redundancy without the use of additional sensors. For a classical robot, the number of sensors is equal to the DOF of the structure. By mechanically limiting the mobility of the structure, the DOF of the system are reduced, while the number of available sensors in the drives remains constant. It is implemented either by restricting the movement of the end-effector in one or more directions of orientation or by fixing the mobility of one or more joints in the kinematic chains.

A part of the drives are used for the kinematically determined movement and the remaining drives are set passive to evaluate the sensor information. The redundant information allows for the establishment of a system of equations to determine the parameter deviations. The implementation of the mechanical constraints can be difficult because, depending on the mechanical constraint, a good force control is needed to avoid tensioning and deformations. Accordingly, there have been numerous simulative investigations of constrained close kinematic chain calibration and little experimental verifications as described in the following.

Depending on the design of the mechanical constraint, different conditions result from the remaining DOF and available sensor information, for example for the Stewart-Gough platform: Daney [Dan99] fixed two legs in their lengths and in their rotation relative to the base, resulting in 1 remaining rotational DOF and 3 redundant sensor information (see Figure 6-1a). Khalil and Besnard [KB99] investigated the fixation of one ball joint to the platform, resulting in 3 remaining rotational DOF and as well 3 redundant sensor information.

Rauf and Ryu [RR01] introduced a calibration technique for a 6 DOF Hexa-Slide manipulator by locking the platform with a ball joint, resulting in 3 rotational DOF. Chiu and Perng [CP04] limited the mobility of a hexapod manipulator to 4 DOF by adding a redundant spherical-prismatic leg with an additional sensor and setting 2 legs passive (see Figure 6-1b).

The aforementioned investigations have been performed in simulation only, showing the feasibility and some characteristics of different approaches. In general, the simulations show that the presented calibration is the most effective for large ranges of motion and can result in remaining parameter errors in the order of magnitude of the simulated measurement errors. They do, however, not state the reachable accuracy in experiments that is limited for example by the modeling quality.
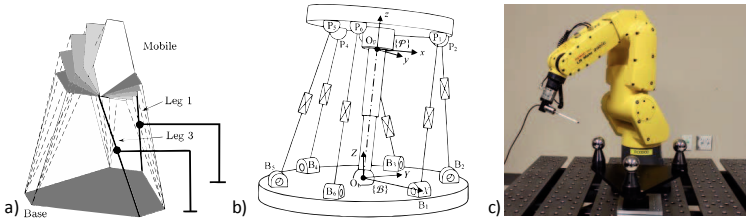
Figure 6-1: a) Rotational constraint for a hexapod by leg fixation [Dan99], b) mobility constraint for a hexapod manipulator [CP04], c) implementation of a distance and sphere constraint with precision touch probe [JB15]

Few recent publications show the actual range of accuracy improvement that can be achieved by closed loop calibration using constrained closed kinematic chains, albeit they additionally rely on added supporting sensors. Joubar and Bonev [JB15] implemented a spherical restriction for a serial manipulator by establishing contact between a high-precision probe-tip at the end-effector and a fixed sphere (see Figure 6-1c). A simulation study demonstrates the ability of the calibration approach, and the experimental verification shows that the robot's accuracy inside the target workspace is significantly improved by re-ducing the mean and maximum position errors from 0.698 mm to 0.086 mm and from 1.321 mm to 0.127 mm, respectively. A common approach known from machine-tool calibration is the use of a double ball-bar (DBB) measurement device to close the kinematic chain. The mechanical connection is established by two high-precision magnetic spheres, connected to each other with a high precision distance sensor. Ni and others [NZG16] used the DBB with a fixed sphere for a Delta robot, reducing the maximum and average position errors from 2.44 mm to 0.16 mm and from 2.20 mm to 0.15 mm.

Constrained calibration methods are less cost intensive compared to other methods, but are more difficult to implement because of the required mechanics and its control system. It should be noted that it is necessary to determine the algorithms and appropriate measuring points for each implementation of a mechanical constraint, making the approach hard to generalize. Furthermore, the limited available workspace usually results in less accurate re-sults compared to open loop calibration [GCH16]. Using mechanical constraints is not suita-ble for the self-calibration of cooperating robots, because of the implementation effort and the limited flexibility of the method.

6.1.2 Virtual Closed Kinematic Chain Calibration

The virtual closed kinematic chain calibration is based on closing the kinematic chains with a virtual linkage, usually a measurement device, adding virtual constraints to the system. The constraints are implemented by feeding back a measurement signal (for example a laser pro-jection on a plane) to the control and compensating any deviations during the movements of the kinematic chain. As described for closed kinematic chain calibration in section 6.1.1, the resulting redundancy is used to establish a system of equations and determine the parame-ter deviations.

Kim and others [KPL06] introduced a constraint plane to the end-effector of a Stewart-Gough platform. It is implemented using three digital distance indicators to control the movement of the manipulator in multiple parallel constrained planes. Abtahi and others [APA09] followed a similar approach by limiting the platform movements of a Hexaglide manipulator to rotations about a fixed point in space (see Figure 6-2a). Three dial indicators measuring a sphere at the manipulator platform were used to compensate for any position deviation. For both implementations, the drive sensor signals were only evaluated when the virtual constraints were satisfied. It should be noted, that the use of a probe-tip and DBB (see [JB15,NZG16] in section 6.1.1) could be classified as virtual closed kinematic chains without signal feedback to the control. The classifications are not necessarily unambiguous.

A common approach for the virtual closed kinematic chain calibration is the projection of a laser beam over, compared to the link length, large distances. The effect is an amplification of the orientation errors at the end-effector. Gatla and others [GLW07] used a laser attached to the end-effector of an industrial articulated robot. They evaluated the length of the laser beam that is projected on one or more fixed positions on a distant plane. The control feedback was realized using the signal of a vision camera to compensate for any deviations of the point of projection. Liu and others [LLN10] investigated the same approach for a Stewart-Gough platform in simulation (see Figure 6-2b), proving a significant improvement of the accuracy. Park and others [PLC12] measured the projection point of a laser module attached to the end-effector (see Figure 6-2c) and evaluated the deviations by means of Jacobian matrices obtained from differential kinematics to estimate the kinematic parameters. As no feedback to the control is implemented, the approach does not strictly follow the definition introduced above.
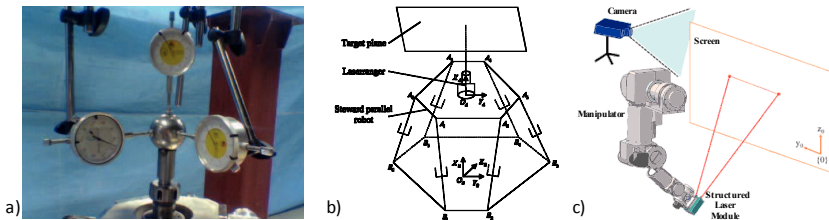
Figure 6-2: Virtual closed kinematic chains: a) virtual rotation constrained with three dial gauges [APA09], b) laser projection for a hexapod manipulator [LLN10], c) structured laser module and stationary camera [PLC12]

Ren and others [RFY13,RFS09] implemented an orientation constraint for a Stewart-Gough platform by leveling a biaxial inclinometer at the end-effector, to keep the two attitude angles constant. The method is verified and validated in simulation and by measurements.

Recent publications show the range of accuracy improvement that can be achieved by closed loop calibration using virtual closed kinematic chains: Gatla and others [GLW07] improved the mean and standard deviation of the radius of spread of the projected laser beam from 5.64 and 1.89 mm to 1.05 and 0.587 mm, respectively. Park and others [PLC12] reduced the

mean and maximum deviation of the projected laser points by a factor of 4 up to 10. Abthai and others [APA09] reduced the maximum positioning error from 3mm to 1mm and the average positioning error by more than 60 %. Using commercial inclinometers Rauf and others [RFS09] reduced the maximum position and orientation errors by 0.3 mm and 0.151 rad to less than 0.5 mm and 0.11 rad at the workspace boundaries. In comparison to other calibration, these improvements are small.

The virtual closed kinematic chain calibration usually relies on specific measurement equipment and algorithms for a specific robot. It can therefore hardly be generalized for an object integrative handling system, especially considering the changing object platform of the structure.

6.1.3   Redundant Sensor Calibration

The redundant sensor calibration is based on the evaluation of the position of passive joints in the kinematic structure using internal sensors. These additional sensors are either added to passive joints, added by means of additional passive kinematic chains or implemented by using encoders of existing redundant joint actuators, which are set passive for the calibration. Thus the number of the internal sensors exceeds the number of DOF of the structure. The redundant sensor calibration is also referred to as self-calibration. Both terms are used in this thesis.

The first approaches using redundant sensors for self-calibration were introduced in the 1990s based on the general considerations of Bennett and Hollerbach [BH91] (see section 6.1). Hollerbach and Lokhorst [HL95] calibrated a 6 DOF hand controller with two closed kinematic chains and resulting redundancy, by evaluating the distance equations of the attachment points between platform and kinematic chains. Nahvi and others [NHH94] presented a similar procedure for the self-calibration of a redundant parallel platform with 3 rotational DOF and 4 actuated linear joints. Wampler and others [WHA95] validated their implicit loop formulation (see section 4.1.2.) for the 6 DOF hand controller investigated by Hollerbach and Lokhorst [HL95]. Zhuang [Zhu97] introduced a self-calibration scheme for a Stewart-Gough platform with additional sensors located at the universal joints. The non-redundant and redundant direct and inverse kinematic calculations are compared or substituted into each other to calculate possible residuals for the parameter optimization.

Following these diverse approaches, an inhomogeneous variety of self-calibration methods have been proposed and investigated in the available literature. For example, the investigated structures, the type and degree of redundancy, the types of sensors or the implemented kinematic models differ from each other in all approaches. Only some are mentioned in this section to give an impression of different developments.

While most investigations were performed in simulation only, some publications show the range of accuracy improvement that can be achieved by self-calibration: Oiwa and Ikuma [OI14] equipped a 3 DOF parallel manipulator with a redundant passive chain including a displacement sensor to sequentially measure three directions of the platform. By optimizing

the kinematic model to minimize the length errors of the passive chain, the root mean square position error is reduced from 172 to 67 µm and the peak-to-peak error from 824 to 406 µm. Ecorchard [Eco10] compared different calibration and self-calibration approaches for a redundant 2 DOF scissor-kinematic used in a high precision machine tool, driven by 4 linear actuators. The deviation of the measured and calculated drive position for the redundant linear actuators is reduced from 0.414 mm and 0.641 mm to 0.14 mm and 0.07 mm, resulting in mean position deviation of 9 µm and maximum position deviation of 69 µm [Eco10, p. 73, 82-84]. Kurbanhusen and others [KYH08] investigated the self-calibration for a biologically inspired 7 DOF robotic arm with redundant cable actuation (see Figure 6-3a). The parameter identification is based on the differential change in the cable end-point distances and results in a reduction of the average deviation of the redundant cable length from 4.06 to 0.12 mm and from 1.4 mm to 0.33 mm for different joints.
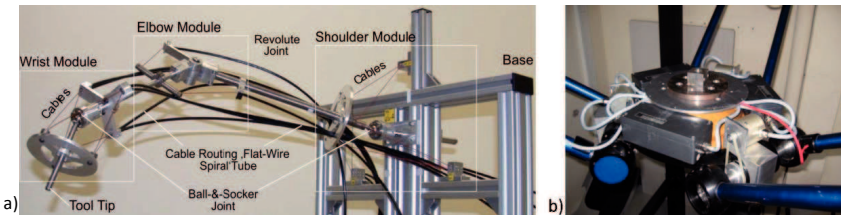
Figure 6-3: a) Biologically inspired 7 DOF cable-driven robotic arm [KYH08], b) experimental implementation of 3 redundant sensors on a Delta structure [EM05]

Ecorchard and Maurine [EM05] evaluated the passive joint angle between the platform and forearms of a Delta parallel robot using additional redundant sensors (see Figure 6-3b). The geometrical self-calibration with compensation of the non-geometrical gravity effects resulted in a reduction of the mean deviation of the passive joint angles from 1.63° to 0.24°.

Another field of application for self-calibration is cable driven robots, which are usually actuated redundantly. Borgstrom and others [BJB09] introduced the self-calibration for a 2 DOF system, showing a significant improvement of the accuracy. Sandretto and others [SDG13] compared two different approaches for a 6 DOF cable driven robot with 8 actuated cables. The mean relative position error is reduced significantly from 37 % to 0.3 % and the mean relative rotational error is reduced from 40.2 % to 1.9 %.

Alternative approaches for redundant sensor calibration rely on specific motion characteristics and alternative sensor systems, as shown for some examples: Joubar and other [JZB16] introduced a new approach for medical robots equipped with a force sensor at the end-effector. The gravitational force exerted from the tool to the sensor is evaluated as calibration information. The robot parameters are identified by minimizing the force and torque residuals, instead of minimizing the residuals of the end-effector pose, as done in conventional approaches. Müller and Ruggio [MR12] introduced a self-calibration method for a redundantly actuated 3 DOF planar parallel mechanism based on the motion reversal points of the actuators as kinematic calibration landmarks. Zhang and others [ZLD15] implemented an

online self-calibration for a serial robot using an inertial measurement unit. Du and Zhang [DZ13] and Jordt and others [JSS09] developed a self-calibration based on vision measurement with a camera attached to the end-effector.

The redundant sensor calibration is well suited for the self-calibration of object integrative handling systems, the accuracy improvements described in literature are convincing. The cooperation and physical link of multiple robotic arms result in a redundantly actuated structure and, by setting some actuators passive, the encoders can be evaluated to gain passive joint angles of the structure. This approach is therefore followed for the self-calibration of the PARAGRIP handling system. The self-calibration based on the combination of direct and inverse kinematic calculations by Zhuang [Zhu97] is adapted for the self-calibration of the object integrative handling system PARAGRIP as described in section 6.2.

6.2   Extended Kinematic Model for the PARAGRIP Handling System

The kinematic model for the self-calibration needs to represent the redundant sensor information and the real grasp points that will be identified. The available sensor information for the PARAGRIP handling system is illustrated in Figure 6-4. Note that the index i is used in the following sections to distinguish the different robotic arms. The 6 main actuators (joint angles φ_{1i} and φ_{4i}) are driving the kinematic structure with the integrated object. The additional actuators (joint angles φ_{0i}) are set passive and can be used to gain redundant position information. Additionally, the encoder signal for the wrist-joint angle α_{Ri} is available. The according actuator is used to align the end effector for the grasping process.

Figure 6-4: Available sensor information for the PARAGRIP handling system

The end-effector position of each arm in space is known by the measurement after the object integration. However, additional information is still needed to be able to calculate the unambiguous grasp point positions at the object: Three contact points with a fixed position relative to each other represent the measured end-effector positions of the PARAGRIP arms in space, illustrated by the triangles in Figure 6-5a. The motion of the object relative to these positions is, however, not fully restricted. The object can always rotate with respect to a fictive point in space, without violating the contact condition of any of the grasp points on the object surface as illustrated with the red triangle in Figure 6-5.
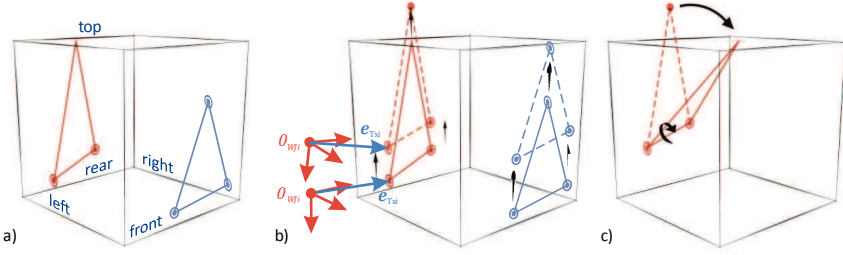
Figure 6-5: Ambiguity of the object position relative to 3 contact points with fixed distance (illustrated by the triangles)

This ambiguity can be resolved by using the additional sensor information for the wrist-joint angles α_{Ri}: The rotational motion of the cube can be observed by gaining additional information about the transformation between the coordinate systems WJ and T (see Figure 6-5b) and hence the orientation of the end effectors relative to the PARAGRIP arms. The wrist-joint angle α_R (see Figure 6-7b) contains partial information about this transformation and therefore will be evaluated in addition to the joint angles.

The contact surfaces top, rear and left for the configuration illustrated red in Figure 6-5 are perpendicular to each other, which allows for resolving the ambiguity as described above. If all 3 plane contact surfaces at the object have a common tangent as in the configuration illustrated blue, a sliding motion of the contact points along this tangent direction cannot be observed. According configurations are consequently not used for the self-calibration. These relationships have been proven analytically using a constrained screw theory method [HLZ09], as shown in a previous work [Rod16 Dt, p. 15–16].

6.2.1   Formulation of the Self-Calibration Problem

The aim of the self-calibration for object integrative cooperating robots and handling systems is the identification of the real grasp points at the object and finally the reduction of inaccuracies. The grasp points are represented by the grasp point vectors $\boldsymbol{b}_i$:

$$\boldsymbol{b}_i = \begin{pmatrix} b_{xi} \\ b_{yi} \\ b_{zi} \end{pmatrix} \tag{6.1}$$

The parameter vector for the self-calibration $\boldsymbol{p}_{sc}$ contains the two components of $\boldsymbol{b}_i$ that represent the grasp point position on the surface of the object for each arm i used. For the configuration shown in Figure 6-7, the parameter vector for the self-calibration $\boldsymbol{p}_{sc}$ is:

$$\boldsymbol{p}_{sc} = (b_{y1} \quad b_{z1} \quad b_{x2} \quad b_{y2} \quad b_{x3} \quad b_{z3}) \tag{6.2}$$

The third component is known from the object dimensions and the wrist-joint offset l_{WJ} perpendicular to the object surface. The nominal vectors of parameters $\hat{\boldsymbol{p}}_{hyb}$ and $\hat{\boldsymbol{p}}_{ser}$ and the according vectors of parameter deviations $\Delta\boldsymbol{p}_{ser}$ and $\Delta\boldsymbol{p}_{hyb}$ are extended accordingly by $\hat{l}_{WJ}$ and Δl_{WJ}. The deviation Δl_{WJi} was identified for each arm by external metrology, independently from the parameter identification. The formulation of the self-calibration problem

needs to allow for the evaluation of the residual between the actual joint angles φ_{1i}, φ_{4i}, φ_{0i} and α_{Ri} and the nominal joint angles $\hat{\varphi}_{1i}$, $\hat{\varphi}_{4i}$, $\hat{\varphi}_{0i}$ and $\hat{\alpha}_{Ri}$. The actual joint angles are the measured and corrected joint angles, based on the extended kinematic models introduced in section 4.2.

Zhuang [Zhu97] proposed the evaluation of the manipulators direct and inverse kinematic calculation with and without redundant sensing to gain the residual as a basis for self-calibration. By combination of different kinematic calculations, the residual is calculated by evaluating deviations of the manipulator poses or joint position values obtained in different ways. For example, the manipulator pose can be calculated using the passive joint positions and some of the actuated joint positions. This pose can be inserted into the inverse kinematics to calculate the theoretical position of all active joints. The so called first inverse measurement residual is now obtained by calculating the deviation between the measured and theoretical active joint positions. This approach is adapted in the following sections to develop a suitable formulation for the self-calibration of the PARAGRIP handling system. The deformation of the structure due to gravitational loads of the weight of the object, as illustrated in Figure 6-4, are not considered for this first approach. They could hardly be verified by simulation, but may be a valuable extension for future investigations.

Because the joint angles of the handling system can be observed and the object pose cannot, it is an obvious first step to start with the direct kinematic calculation.

6.2.2   Direct Kinematic Calculation

The direct kinematic calculation of the object pose is represented by the transformation matrix $^{0}\boldsymbol{A}_{Obj}$:

$$^{0}\boldsymbol{A}_{Obj} = \begin{pmatrix} ^{0}\boldsymbol{T}_{Obj} & ^{0}\boldsymbol{r}_{Obj} \\ 0\ 0\ 0 & 1 \end{pmatrix}$$

(6.3)

With the object position $^{0}\boldsymbol{r}_{Obj}$ and the rotational transformation matrix $^{0}\boldsymbol{T}_{Obj}$.
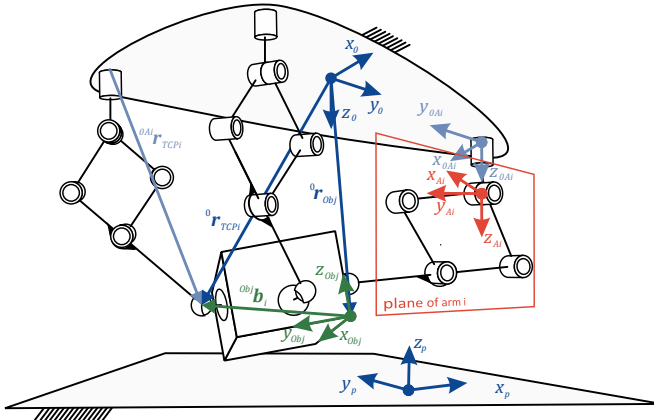
Figure 6-6: Global and local coordinate systems for the PARAGRIP handling system

The following calculations are based on the kinematic calculation originally formulated by Riedel [Rie14, p. 91–92]. The positions and coordinate systems used are shown in Figure 6-6. The object position $^0r_{Obj}$ can be calculated from one TCP position $^0r_{TCPi}$ and the known grasp points ^0b_i on the object:

$$^0r_{Obj} = {}^0r_{TCPi} - {}^0b_i = {}^0r_{TCPi} - {}^0T_{Obj} \cdot {}^{Obj}b_i \tag{6.4}$$

With the rotational transformation matrix $^0T_{Obj}$.

Using equation (6.4) the object position is obtained using three different TCP positions, one for each arm. This is problematic for the self-calibration, since the calculated object positions will deviate from each other due to tolerances and measurement errors. Therefore, the developed formulation is based on the object rotation only, expressed by the rotational transformation matrix $^0T_{Obj}$. It can be calculated using the intermediate coordinate system H in the plane of the grasp points (see Figure 6-7b):

$$^0T_{Obj} = {}^0T_H \cdot {}^HT_{Obj} \tag{6.5}$$

With the rotational transformation matrices ^0T_H and $^HT_{Obj}$.

The following calculations are formulated for the configuration shown in Figure 6-7b.
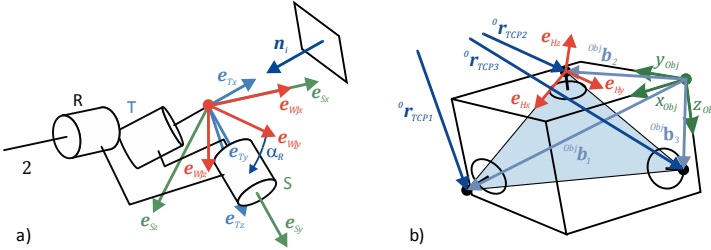
Figure 6-7: Coordinate system and position vectors for the integrated object, shown exemplarily for the arms 1, 2 and 3

The rotational transformation ^0T_H from the intermediate coordinate system to the global coordinate system can be obtained from the three TCP positions $^0r_{TCPi}$:

$$^0T_H = \left({}^0e_{Hx} \quad {}^0e_{Hy} \quad {}^0e_{Hz} \right) \tag{6.6}$$

With the unit vectors:

$$^0e_{Hx} = \frac{^0r_{TCP1} - {}^0r_{TCP2}}{|{}^0r_{TCP1} - {}^0r_{TCP2}|} \tag{6.7}$$

$$^0e_{Hz} = \frac{^0e_{Hx} \times \left({}^0r_{TCP3} - {}^0r_{TCP2} \right)}{|{}^0e_{Hx} \times \left({}^0r_{TCP3} - {}^0r_{TCP2} \right)|} \tag{6.8}$$

$$^0e_{Hy} = {}^0e_{Hz} \times {}^0e_{Hx} \tag{6.9}$$

The TCP position $^0\boldsymbol{r}_{TCPi}$ of each arm i is known from the serial and hybrid kinematics model (see equations (4.5) and (4.38)):

$$^0\boldsymbol{r}_{TCPi} = {}^0\boldsymbol{A}_{0Ai} \cdot {}^{0Ai}\boldsymbol{r}_{TCPi}(\widehat{\boldsymbol{p}}_i, \Delta\boldsymbol{p}_i, \boldsymbol{\varphi}_i) \tag{6.10}$$

With the known transformation matrix $^0\boldsymbol{A}_{0Ai}$, the nominal parameter vector $\widehat{\boldsymbol{p}}_{ser\,i}$ or $\widehat{\boldsymbol{p}}_{hyb\,i}$, the identified parameter deviations $\Delta\boldsymbol{p}_{ser\,i}$ or $\Delta\boldsymbol{p}_{hyb\,i}$ and the actual joint angle vector $\boldsymbol{\varphi}_i = (\varphi_{0i}, \varphi_{1i}, \varphi_{4i})$.

The rotational transformation $^H\boldsymbol{T}_{Obj}$ from the object coordinate system to the intermediate coordinate system can be obtained from the grasp point vectors $^{Obj}\boldsymbol{b}_i$ at the object:

$$^H\boldsymbol{T}_{Obj} = \begin{pmatrix} {}^{Obj}\boldsymbol{e}_{Hx} & {}^{Obj}\boldsymbol{e}_{Hy} & {}^{Obj}\boldsymbol{e}_{Hz} \end{pmatrix}^T \tag{6.11}$$

With the unit vectors:

$$^{Obj}\boldsymbol{e}_{Hx} = \frac{{}^{Obj}\boldsymbol{b}_1 - {}^{Obj}\boldsymbol{b}_2}{\left|{}^{Obj}\boldsymbol{b}_1 - {}^{Obj}\boldsymbol{b}_2\right|} \tag{6.12}$$

$$^{Obj}\boldsymbol{e}_{Hz} = \frac{{}^{Obj}\boldsymbol{e}_{Hx} \times \left({}^{Obj}\boldsymbol{b}_3 - {}^{Obj}\boldsymbol{b}_2\right)}{\left|{}^{Obj}\boldsymbol{e}_{Hx} \times \left({}^{Obj}\boldsymbol{b}_3 - {}^{Obj}\boldsymbol{b}_2\right)\right|} \tag{6.13}$$

$$^{Obj}\boldsymbol{e}_{Hy} = {}^{Obj}\boldsymbol{e}_{Hz} \times {}^{Obj}\boldsymbol{e}_{Hx} \tag{6.14}$$

The grasp point vectors $\boldsymbol{b}_i$ are given by equations (6.1) and (6.2). With this formulation, the direct kinematics problem for the handling system is solved using information for the 3 redundant joint angles φ_{0i} additional to the kinematically sufficient joint angles φ_{1i} and φ_{4i}. However, only relying on kinematically sufficient joint angles that fully describe the kinematic system with the integrated object would lead to a complex and computational intense calculation of the direct kinematics. Because of this, such an approach is not investigated.

6.2.3   Inverse Kinematic Calculation

After deriving the object orientation using the actual joint angles φ_{1i}, φ_{4i} and φ_{0i}, the inverse kinematic calculation of the nominal wrist-joint angles $\widehat{\alpha}_{Ri}$ is used to complete the formulation of the self-calibration problem. The nominal wrist-joint angles $\widehat{\alpha}_{Ri}$ are calculated based on the tilt between link 2 of arm i and the surface of the object (see Figure 6-7a):

$$\widehat{\alpha}_{Ri} = cos^{-1} \frac{{}^0\boldsymbol{e}_{WJy\,i} * {}^0\boldsymbol{e}_{Sy\,i}}{\left|{}^0\boldsymbol{e}_{WJy\,i}\right| \cdot \left|{}^0\boldsymbol{e}_{Sy\,i}\right|} \tag{6.15}$$

With the unit vectors $^0\boldsymbol{e}_{WJy\,i}$ and $^0\boldsymbol{e}_{Sy\,i}$ shown in Figure 6-7a and the $*$ operator for the scalar product of both vectors.

The unit vector $^0\boldsymbol{e}_{WJy\,i}$ of the wrist-joint coordinate system WJ in y-direction can be derived from the kinematic calculation of the arm (see equation (3.5)):

$$^{0Ai}\boldsymbol{e}_{WJy\,i} = \boldsymbol{R}_z(\varphi_{0i}) \cdot {}^{0Ai}\boldsymbol{e}_{A0y\,i} = \boldsymbol{R}_z(\varphi_{0i}) \cdot \begin{pmatrix} 0 \\ 1 \\ 0 \end{pmatrix} \tag{6.16}$$

$$^0\boldsymbol{e}_{WJy\,i} = {}^0\boldsymbol{A}_{0Ai} \cdot {}^{0Ai}\boldsymbol{e}_{WJy\,i} \tag{6.17}$$

With the transformation matrix $^0\boldsymbol{A}_{0Ai}$, the rotational matrix $\boldsymbol{R}_z$ and the actual joint angle φ_{0i}.

The unit vector $^0e_{Sy\,i}$ of the wrist-joint coordinate system S in y-direction can be derived from the vector ^0n_i normal to the surface of the object and the unit vector $^0e_{WJx\,i}$:

$$^0e_{Sy\,i} = \frac{^0n_i \times \,^0e_{WJx\,i}}{|\,^0n_i \times \,^0e_{WJx\,i}|} \tag{6.18}$$

$$^0n_i = \,^0T_{Obj} \cdot \,^{Obj}n_i \tag{6.19}$$

With the known rotational transformation matrix $^0T_{Obj}$ and normal vector $^{Obj}n_i$, shown in Figure 6-7a.

The unit vector $^0e_{WJx\,i}$ of the wrist-joint coordinate system WJ in x-direction can be derived similar to equation (6.16):

$$^{0Ai}e_{WJx\,i} = R_y(-\varphi_{2i}) \cdot R_z(\varphi_{0i}) \cdot \,^{0Ai}e_{A0x\,i} = R_y(-\varphi_{2i}) \cdot R_z(\varphi_{0i}) \cdot \begin{pmatrix} 1 \\ 0 \\ 0 \end{pmatrix} \tag{6.20}$$

$$^0e_{WJx\,i} = \,^0A_{0Ai} \cdot \,^{0Ai}e_{WJx\,i} \tag{6.21}$$

With the known transformation matrix $^0A_{0Ai}$ and the rotational matrices R_z and R_y for the actual joint angles φ_{0i} and φ_{2i}.

6.3   Identification of the Grasp points

With the calculations in sections 6.2.2 and 6.2.3, the object orientation and the nominal wrist-joint angles $\hat{\alpha}_{Ri}$ are expressed as a function of the measured joint angles φ_i, the parameter vector for the self-calibration p_{sc} and the identified kinematic parameters $\hat{p}_i$ and Δp_i of the i arms:

$$^0T_{Obj} = \,^0T_H \cdot \,^HT_{Obj} = \,^0T_{Obj}(\hat{p}_i, \Delta p_i, \varphi_i, p_{sc} \,\forall i) \tag{6.22}$$

$$\hat{\alpha}_{Ri} = \hat{\alpha}_{Ri}(\hat{p}_i, \Delta p_i, \varphi_i, p_{sc} \,\forall i) \tag{6.23}$$

$$\hat{\alpha}_R = \begin{pmatrix} \hat{\alpha}_{R1} \\ \hat{\alpha}_{R2} \\ \hat{\alpha}_{R3} \end{pmatrix} = \hat{\alpha}_R(\hat{p}_i, \Delta p_i, \varphi_i, p_{sc} \,\forall i) \tag{6.24}$$

The nominal wrist-joint angles $\hat{\alpha}_{Ri}$ are summarized in the vector $\hat{\alpha}_R$. Based on this formulation, the optimization problem and residual can be formulated. Practical implementations of the self-calibration have shown that the measurements of the wrist-joint angles α_{Ri} are not precise. Using a stepper motor and magnetic reference switch leads to a deviation $\Delta\alpha_{Ri}$ of the measured wrist-joint angles $\bar{\alpha}_{Ri}$ from the actual wrist-joint angles α_{Ri}:

$$\alpha_{Ri} = \bar{\alpha}_{Ri} + \Delta\alpha_{Ri} \tag{6.25}$$

$$\alpha_R = \begin{pmatrix} \alpha_{R1} \\ \alpha_{R2} \\ \alpha_{R3} \end{pmatrix} \tag{6.26}$$

The actual wrist-joint angles are summarized in the vector α_R. The deviation is constant during the measurement, but varies with each reference run. It needs to be identified by numerical optimization and the parameter vector p_{sc} therefore is not sufficient for the optimization.

The extended parameter vector $\boldsymbol{p}_{sc'}$ for the self-calibration is introduced accordingly:

$$\boldsymbol{p}_{sc'} = (b_{y1} \quad b_{z1} \quad b_{x2} \quad b_{y2} \quad b_{x3} \quad b_{z3} \quad \Delta\alpha_{R1} \quad \Delta\alpha_{R2} \quad \Delta\alpha_{R3}) \tag{6.27}$$

The parameter vector $\boldsymbol{p}_{sc'}$ is derived by numerical optimization. The aim of the optimization is to minimize the overall deviation of all measurements, expressed by the residual R:

$$\min_{\boldsymbol{p}_{sc'}\in\mathbb{R}^n} R = \min_{\boldsymbol{p}_{sc'}\in\mathbb{R}^n} R(\widehat{\boldsymbol{p}}_i, \Delta\boldsymbol{p}_i, \boldsymbol{\varphi}_i, \boldsymbol{\alpha}_R, \boldsymbol{p}_{sc}, \forall i) \tag{6.28}$$

The well-balanced Euclidian norm is used to calculate the residual R_α of the nominal wrist-joint angles $\widehat{\alpha}_{Ri}$ from the actual wrist-joint angles α_{Ri}:

$$R_\alpha = \|\widehat{\boldsymbol{\alpha}}_R - \boldsymbol{\alpha}_R\|_2 \tag{6.29}$$

Because of a position ambiguity, the above formulation of the optimization problem for the self-calibration is not yet sufficient to find a unique solution to the optimization problem. The orientation of the object ${}^0\boldsymbol{T}_{Obj}$ is calculated using the intermediate coordinate system H in the plane of the grasp points (see Figure 6-7b). The orientation of the plane is described in the global coordinate system with ${}^0\boldsymbol{T}_H$ and in the object coordinate system with ${}^H\boldsymbol{T}_{Obj}$. There are an infinite number of planes for ${}^H\boldsymbol{T}_{Obj}$ that are parallel to the plane for ${}^0\boldsymbol{T}_H$. With the above formulation, the optimization algorithm will find linearly dependent combinations of suitable grasp points by variation of the parameter vector $\boldsymbol{p}_{sc}$, and not converge to a solution.

This ambiguity can be eliminated by introducing a distance constraint to the optimization residual. The distance between two grasp points must be identical, no matter, if it is calculated using TCP positions ${}^0\boldsymbol{r}_{TCPi}$ or the grasp point vectors ${}^{Obj}\boldsymbol{b}_i$. Only one combination of suitable grasp points will fulfill this condition and the residual R_{TCP} is introduced:

$$R_{TCP} = \Delta d_{21} + \Delta d_{23} + \Delta d_{13} \tag{6.30}$$

$$\Delta d_{21} = \left| \left\| {}^0\boldsymbol{r}_{TCP2} - {}^0\boldsymbol{r}_{TCP1} \right\|_2 - \left\| {}^{Obj}\boldsymbol{b}_2 - {}^{Obj}\boldsymbol{b}_1 \right\|_2 \right| \tag{6.31}$$

$$\Delta d_{23} = \left| \left\| {}^0\boldsymbol{r}_{TCP2} - {}^0\boldsymbol{r}_{TCP3} \right\|_2 - \left\| {}^{Obj}\boldsymbol{b}_2 - {}^{Obj}\boldsymbol{b}_3 \right\|_2 \right| \tag{6.32}$$

$$\Delta d_{13} = \left| \left\| {}^0\boldsymbol{r}_{TCP1} - {}^0\boldsymbol{r}_{TCP3} \right\|_2 - \left\| {}^{Obj}\boldsymbol{b}_1 - {}^{Obj}\boldsymbol{b}_3 \right\|_2 \right| \tag{6.33}$$

With the deviation Δd_{ij} of the grasp point distances.

The residuals R_α and R_{TCP} are combined to the extended residual for the self-calibration R_{sc} and scaled to the same order of magnitude to achieve a balanced optimization behavior:

$$R_{sc} = \frac{R_\alpha}{9} + R_{TCP} \tag{6.34}$$

The scaling factor of 1/9 in equation (6.34) was determined empirically by the analysis of the order of magnitude of the residuals R_α and R_{TCP} in several preliminary simulations without scaling. The optimization formulated in equation (6.28) using the R_{sc} residual is implemented using the Nelder-Mead simplex algorithm as described by Lagarias and others [LRW98]. The according MATLAB® function *fminsearch* [Mat17b] has proven to be stable and reliable for this parameter identification with the nominal grasp points as starting values. The termination criterion for the optimization was evaluated experimentally. A relative change of the

residual R_{sc} of 10^{-6} is sufficient to identify the grasp points and a higher tolerance did not improve the results but led to a slightly increased calculation time. A description of a preliminary implementation for the PARAGRIP self-calibration is given by Rodilla [Rod16 Dt].

6.4   Choice of Object Poses for Identification

The results that can be achieved by the identification of the grasp points described in section 6.3 depend on the object poses j that are chosen for the identification measurement. The considerations and method regarding the choice of measurement points, their quantity and position are valid equivalent to the findings described in section 4.6. The according formulations and results for the self-calibration are summarized in this section. The kinematic equations for α_{Ri} (summarized in $\boldsymbol{\alpha}_R$) used for the self-calibration can be linearized around the nominal parameter values $\widehat{\boldsymbol{p}}_{sc}$:

$$\Delta\boldsymbol{\alpha}_{R\,j} = \boldsymbol{X}_j \cdot \Delta\boldsymbol{p}_{sc}$$

Where $\Delta\boldsymbol{\alpha}_{R\,j}$ is the deviation of the actual wrist-joint angles $\boldsymbol{\alpha}_{R\,j}$ and the calculated nominal wrist-joint angles $\widehat{\boldsymbol{\alpha}}_{R\,j}$ for measurement pose j. $\Delta\boldsymbol{p}_{sc}$ is the parameter deviation.   (6.35)

The error propagation matrix $\boldsymbol{X}_j$ for an object pose j is the Jacobian matrix of the kinematic equations for α_{Ri} (summarized in $\boldsymbol{\alpha}_R$):

$$\boldsymbol{X}_j\big(\widehat{\boldsymbol{p}}_{i\,j}, \Delta\boldsymbol{p}_{i\,j}, \boldsymbol{\varphi}_{i\,j}, \boldsymbol{p}_{sc}\,\forall i\big) = \left.\frac{\partial\boldsymbol{\alpha}_{R\,j}}{\partial\boldsymbol{p}_{sc}}\right|_{\boldsymbol{p}_{sc}=\widehat{\boldsymbol{p}}_{sc}}$$

(6.36)

With the nominal parameter vector for the self-calibration $\widehat{\boldsymbol{p}}_{sc}$.

The overall error propagation matrix $\boldsymbol{X}$ for n_j object poses j is:

$$\boldsymbol{X} = \left[\boldsymbol{X}_1^T, \dots, \boldsymbol{X}_{n_j}^T\right]^T$$

(6.37)

The need to scale parameters with different dimension or units against each other does not apply for this error propagation matrix of self-calibration. The parameter vector $\boldsymbol{p}_{sc}$ and the variable vectors $\boldsymbol{\alpha}_{R\,j}$ are homogeneous. The observability index O introduced in section 4.6 is calculated based on the singular values σ_1 to σ_{n_P} for n_p parameters resulting from the singular value decomposition of $\boldsymbol{X}$:

$$O = \frac{\sqrt[n_p]{\sigma_1 \cdot \dots \cdot \sigma_{n_p}}}{\sqrt{n_p}}$$

(6.38)

High values of this observability index express a good observability of the parameter deviations and a low influence of measurement noise. The set of identification poses shown in Figure 6-8a is based on a numerical optimization with the negative observability index as target value, using a fixed number of 12 poses, hence 36 data values for the 9 parameters, and adjusting their position and orientation in the workspace. The shown envelope of the workspace represents the possible positions with no object rotation. The optimized poses are close to the workspace boundaries and concentrated in two areas of the workspace.
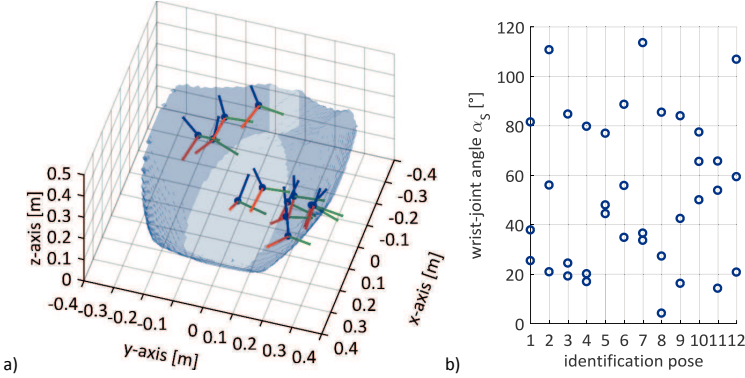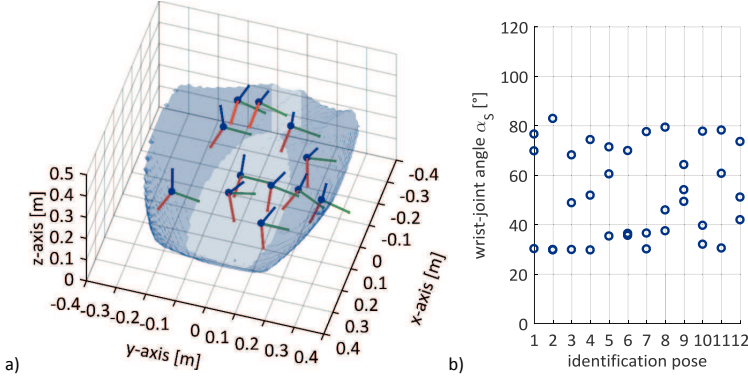
Figure 6-8: a) Optimized identification poses for the self-calibration based on the observability index, b) wrist-joint angles α_S for the identification poses

The identification of the grasp points and the introduced choice of object poses are based on the observation of the wrist-joint angles α_{Ri}. The observability of α_{Ri} might, however, be limited for specific configurations of the wrist-joint. The passive rotations of the axis R and the rotation of the axis T are kinematically identical in case of a singularity with collinear axes R and T, the wrist-joint angle α_S is zero in this case (see Figure 6-7a and [Rie14, p. 191]). A rotation of R, that can be observed, can be replaced or partly replaced by a rotation of T that cannot be observed.

Even though this relation is considered implicitly in the derivation of the error propagation matrix as can be seen in Figure 6-8b, this singularity should be avoided explicitly during the optimization of the identification poses. When considering geometric tolerances and the compliance of the structure, the described singularity effects may occur already in the vicinity of a singularity. Because of this, the optimization target value is improved by a scaling factor based on the minimum wrist-joint angle α_S for all arms and poses. It rises linearly from 1.0 for 20° to 2.0 for 30° and higher values. This additional condition does not deteriorate the observability index achieved in the optimization, the identification poses are, however, distributed more evenly over the workspace, as shown in Figure 6-9a. The resulting wrist-joint angles α_S are shown in Figure 6-9b. The minimum values are significantly higher in this case for most identification poses in comparison to the optimization without additional α_S condition.

Figure 6-9: a) Optimized identification poses for the self-calibration based on the observability index with additional condition for the wrist-joint angle α_S, b) wrist-joint angles α_S for the identification poses

A manually chosen set of identification poses is investigated for comparison. It is shown in Figure 6-10. The identification poses are chosen with an even distribution in the workspace and minimum wrist-joint angle α_S of 20° for all poses. Manually choosing these poses for the handling system with integrated object is more challenging than choosing the positions for a single PARAGRIP arm, because the orientation and position have to be considered and the workspace boundaries are less obvious. The selected set may therefore be not as good as the optimized ones. It will be used for the performance comparison.
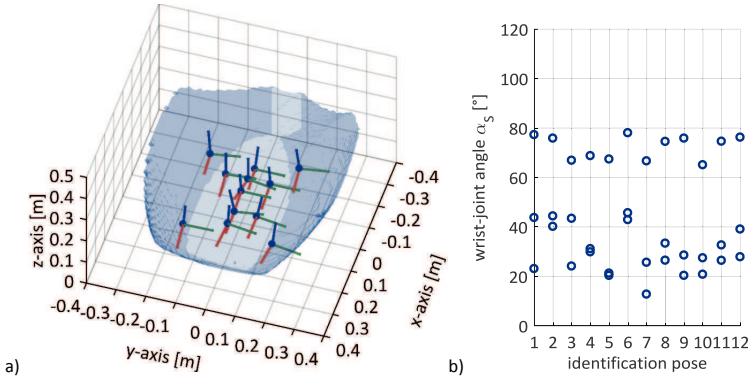
Figure 6-10: a) Manually chosen identification poses for the self-calibration with even distribution in the workspace and minimum wrist-joint angle α_S of 20°, b) wrist-joint angles α_S for the identification poses

6.5   Absolute Accuracy for Position and Orientation

In addition to the absolute position accuracy AP_P (see equation (4.39) and section 4.4), the absolute orientation accuracy is defined following the EN ISO 9283 standard [Eur98]. The absolute orientation accuracy is defined as the deviation (measured over n cycles) of the 3 orientation coordinates for each pose:

$$AP_\alpha = (\bar{\alpha} - \hat{\alpha}) \tag{6.39}$$

$$AP_\beta = (\bar{\beta} - \hat{\beta}) \tag{6.40}$$

$$AP_\gamma = (\bar{\gamma} - \hat{\gamma}) \tag{6.41}$$

The nominal orientation coordinates $\hat{\alpha}, \hat{\beta}, \hat{\gamma}$ are dependent on the rotational convention chosen, which is the Euler z, y', x'' convention in this case. The measured orientation coordinates $\bar{\alpha}, \bar{\beta}, \bar{\gamma}$ are averaged over n cycles:

$$\bar{\alpha} = \frac{1}{n}\sum_{i=1}^{n} \alpha_i, \quad \bar{y} = \frac{1}{n}\sum_{i=1}^{n} y_i, \quad \bar{z} = \frac{1}{n}\sum_{i=1}^{n} z_i \tag{6.42}$$

Where the orientation angles x_i, y_i, z_i are measured in cycle i out of n cycles.

The mean absolute orientation accuracy AP_O and the maximum absolute orientation accuracy $AP_{O\ max}$ are introduced for a more compact representation of the simulation results:

$$AP_O = \frac{1}{3}\big(|AP_\alpha| + |AP_\beta| + |AP_\gamma|\big) \tag{6.43}$$

$$AP_{O\ max} = max\big(|AP_\alpha|, |AP_\beta|, |AP_\gamma|\big) \tag{6.44}$$

The chosen rectangular workspace for the set of 5 reference poses is shown in Figure 6-11. It is dependent on the grasping position and on the integrated object and can therefore only be an example for the chosen configuration.
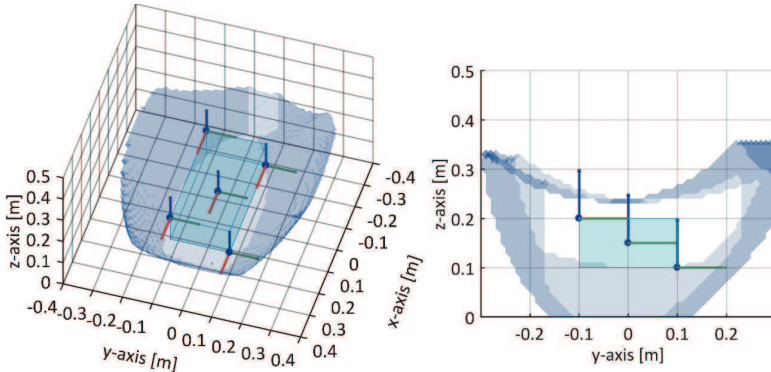
Figure 6-11: Reference points for the chosen rectangular workspace of the handling system

6.6   Verification of the Identification Procedure

The extended kinematic model for the self-calibration and the identification procedure introduced above are verified by simulation to judge the feasibility of the approach and the influencing factors. The influence of the inherent system inaccuracies is represented by repeating a set of simulated self-calibration with randomly distributed values of the different relevant variables.

6.6.1   Simulation of the Inherent System Inaccuracies

The Gaussian normal distribution can be used to represent coincidental tolerances for sufficiently large lots [Kle11, p. 153] and is commonly used to evaluate calibration processes (see for example [JZB15,RFY13,LLN10]).

Physical quantities used in the identification procedure, for example the translational coordinate x, are represented by a random value based on the normal distributed white Gaussian noise with the mean value equal to the nominal value $\hat{x}$ and the standard deviation σ_x:

$$x \sim \mathcal{N}(\hat{x}, \sigma_x^2)$$ (6.45)

This approach can be used to verify the identification procedure and estimate the calibration performance. However, dependent on the basic assumptions and considered effects in the simulation model and the measurement accuracy, experimental results for real structures often differ noticeably from achieved simulation results (see for example [RFS09,EM05]). This should be considered in the analysis of the results. The effects that have been considered for the simulation and the representative normal distributions are detailed in the following sections.

Grasp Point Tolerances

The deviations of the grasp points from their nominal position are based on the inaccuracy of the object before grasping, the object tolerances and uncertainties during the grasping process. These uncertainties include the sliding and pushing of the object due to the reciprocal impacts of the cooperating arms or, for example, changing friction during the passive alignment of the end-effector. The resulting grasp point deviations of this complex grasping procedure could not be described mathematically with acceptable effort due to the large number of effects and parameters to be considered. It can, however, be shown, that the inaccuracy of the object before grasping and the object tolerances can be represented by a Gaussian normal distribution. Preliminary investigations of the grasp point tolerances were performed in a previous work [Guo15 Dt].

Consequently, the grasp point deviation is simulated based on the measured deviation of a set of grasp points after real grasping processes. The actual grasp point positions have been measured in different experiments with a high resolution 3D-scan. The grasp point deviations in a single direction have been evaluated in specific experiments with video camera observations. The measurement of the 3D-scan ($\sigma_{\boldsymbol{p}_{sc}}$ = 6.3 mm) differs significantly from the experimental estimation for the 1-dimensional grasping processes ($\sigma_{\boldsymbol{p}_{sc}}$ = 0.5). Based on this

data, the grasp point deviation is estimated with a standard deviation $\sigma_{\boldsymbol{p}_{sc}}$ = 3 mm. This estimation is not critical for the verification, since only the pose to be identified is given as simulation input. The quality of the identification ultimately depends on the remaining deviation of the identified and actual grasp points. The vector for the self-calibration $\boldsymbol{p}_{sc}$ (see equation (6.2)) is represented by a normally distributed random value with the standard deviation $\sigma_{\boldsymbol{p}_{sc}}$:

$$\boldsymbol{p}_{sc} \sim \mathcal{N}\left(\hat{\boldsymbol{p}}_{sc}, \sigma_{\boldsymbol{p}_{sc}}^2\right) \tag{6.46}$$

This will result in an average absolute grasp point deviation of 2.4 mm ($0.7981 \cdot \sigma_{\boldsymbol{p}_{sc}}$).

Wrist-Joint Angle Deviations

The deviation $\Delta\alpha_{Ri}$ of the measured wrist-joint angles from the actual wrist-joint angles (see equation (6.25)) is simulated similar to the grasp point tolerances. The standard deviation $\sigma_{\Delta\alpha_{Ri}}$ = 0.48° was evaluated based on a set of high resolution 3D-scans after the reference procedure of the wrist-joint. The actual wrist-joint angles α_{Ri} are represented by a normally distributed random value with the standard deviation $\sigma_{\Delta\alpha_{Ri}}$:

$$\alpha_{Ri} \sim \mathcal{N}\left(\hat{\alpha}_{Ri}, \sigma_{\Delta\alpha_{Ri}}^2\right) \tag{6.47}$$

This will result in an average absolute wrist-joint angle deviation of 0.38° ($0.7981 \cdot \sigma_{\Delta\alpha_{Ri}}$:).

Tolerances of the Encoder Readings

The tolerances of the encoder readings for the joint angles $\boldsymbol{\varphi}_i$ and the wrist-joint angle $\boldsymbol{\alpha}_R$ are represented by Gaussian white noise:

$$\boldsymbol{\varphi}_i \sim \mathcal{N}\left(\hat{\boldsymbol{\varphi}}_i, \sigma_{\boldsymbol{\varphi}_i}^2\right) \tag{6.48}$$

$$\boldsymbol{\alpha}_R \sim \mathcal{N}\left(\hat{\boldsymbol{\alpha}}_R, \sigma_{\boldsymbol{\alpha}_R}^2\right) \tag{6.49}$$

The according standard deviations have been chosen to be equal to the nominal sensor resolution and are listed in Table 6-1. Practical comparisons of the desired and measured encoder position have shown control deviations in this order of magnitude or less.

joint angle	φ_{0i}	φ_{1i}	φ_{4i}	α_{Ri}
standard deviation	$\sigma_{\varphi_{0i}}$ = 0.003°	$\sigma_{\varphi_{1i}}$ = 0.002°	$\sigma_{\varphi_{4i}}$ = 0.002°	$\sigma_{\alpha_{Ri}}$ = 0.02°

Table 6-1: Standard deviation for the absolute accuracy after calibration and for the nominal model

Arm Position Accuracy

The accuracy of the TCP position of the robotic arms is relevant for the resulting joint angle readings during the self-calibration procedure and for the resulting pose of the integrated object. It is limited by the manufacturing tolerances and effects like backlash and friction and can be improved only up to some extent by calibration as shown in section 4. The position accuracy of different arms after the calibration was analyzed for 25 measurements for the different calibration models and for 50 measurements for the nominal model. An example of the resulting frequency distribution is given in Figure 6-12. The assumption of a normal distribution cannot be justified based on the limited set of available measurements but it is

considered sufficient for the verification. The mean value of the deviations is not significant for the simulation and will not be considered. The standard deviation does, however, vary noticeably for different directions.
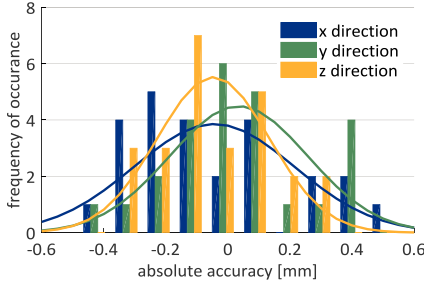
Figure 6-12: Frequency distribution for the absolute accuracy after hybrid kinematics model level 3 calibration

A comparison of the standard deviations for the different calibration models and the nominal model is given in Table 6-2. The accuracy of the different models is in a rather narrow range, compared to the nominal model. Therefore, the simulations are performed using the level 2 calibration with the serial kinematics model, representing the most conservative accuracy for the robotic arm and allowing for the best calculation speed.

standard deviation $\sigma_{r_{TCPi}}$	x_{A0}-direction	y_{A0}-direction	z_{A0}-direction
serial kinematics model, level 2	0.3029 mm	0.2364 mm	0.1853 mm
serial kinematics model, level 3	0.2928 mm	0.2234 mm	0.1962 mm
hybrid kinematics model, level 2	0.2882 mm	0.2486 mm	0.1664 mm
hybrid kinematics model, level 3	0.2587 mm	0.2222 mm	0.1282 mm
nominal model	1.9927 mm	2.1669 mm	1.7519 mm

Table 6-2: Standard deviation for the absolute accuracy after calibration and for the nominal model

The TCP position ${}^{0}\boldsymbol{r}_{TCPi}$ of each arm i (see equation (6.10)) is represented by a normally distributed random value with an individual standard deviation $\sigma_{r_{TCPi}}$ for each translational direction in the arm coordinate system $0A$:

$$
{}^{0A}\boldsymbol{r}_{TCPi} \sim \mathcal{N}\left({}^{0A}\hat{\boldsymbol{r}}_{TCPi}, \sigma_{r_{TCPi}}^2\right) \tag{6.50}
$$

6.6.2   Influence of the Simulated Tolerances and Deviations

The simulations have been implemented based on the tolerances and deviations introduced above. The manually selected set of identification poses is used for the investigation of the general areas of sensitivity described in this section. The deviation of the grasp points $\boldsymbol{b}_i$ and wrist-joint angles $\boldsymbol{\alpha}_R$ are used as simulation input and the remaining deviations after the self-calibration serve as a measure for the self-calibration performance.

The sensitivity of the procedure has been tested using the One-Factor-At-a-Time method. The tolerance of the encoder readings (joint angle noise) and the arm position accuracy has been simulated with increasing values starting from zero, while the remaining simulation

parameters were unchanged. The joint angle noise did not influence the simulated self-calibration performance, even for simulated measurement noise with 2.5 times higher standard deviations. It does not seem to be a critical influencing factor for the investigated handling system and the remaining analysis is focused on the effect of the arm position accuracy.

Figure 6-13a and b show the remaining grasp point deviation and the deviation of the wrist-joint angle α_R after the simulated self-calibration for a range of the arm absolute accuracy from 0 to 2.4 mm (average for all directions). The remaining deviations increase with higher values for the arm absolute accuracies and are more scattered, especially for mean arm accuracies above 0.8 mm. Outliers that perform inferior in comparison to most of the similar simulations can be observed, therefore any self-calibration should be executed multiple times, if possible, to achieve robust results.
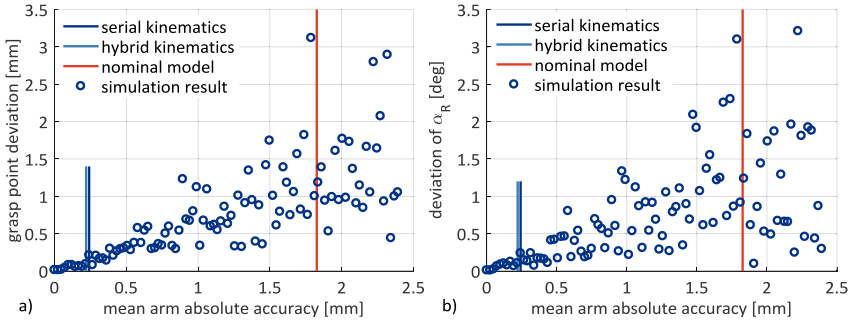
Figure 6-13: a) Mean grasp point deviation, b) mean deviation of wrist-joint angle α_R after the simulated self-calibration for a range of absolute accuracies of the robotic arm

The arm absolute accuracy is illustrated as vertical lines in Figure 6-13 for the nominal arm model and after calibration. The average absolute deviations that remain after self-calibration for the grasp points and the wrist-joint angle α_R are about 0.15 mm and 0.15° for the accuracies that can be achieved by kinematic calibration of the arms. This is a good improvement of the grasp point deviations in comparison to the average deviations of 2.4 mm used as input for the simulations. The improvement is smaller for the deviation of the wrist-joint angle α_R with an average initial deviation of 0.38°. This is no drawback, because the grasp point deviation is the critical quantity for the calibration performance. Furthermore, the balance between both deviations could be adjusted by the scaling factor for the residual introduced in equation (6.34).

Based on this simulation, it can be concluded that a successful identification of the grasp points would not be possible with the nominal kinematics models of the robotic arms. The remaining grasp point deviation between 0.5 mm and 2 mm would lead to an unacceptable accuracy of the handling system with integrated object. As a result, the modeling quality of the kinematic model used is crucial for the successful self-calibration. Its influence will be investigated in more detail in the next set of simulations by analyzing the resulting object accuracy.

The object pose can be calculated based on the direct kinematic calculation with the actual grasp points, the calibrated kinematic model and the theoretical joint angles. The actual grasp points are known, they were generated in equation (6.46) as simulation input. The theoretical joint angles are calculated based on the inverse kinematics model using the identified grasp points and nominal object position. The limited arm accuracy is effective in this simulation in two ways. First the performance of the grasp point identification is influenced because the joint angles are measured via the robotic arms. Secondly the resulting object pose is directly affected by the limited arm position accuracy. Accordingly, the TCP position $^0r_{TCPi}$ of each arm i is simulated for both calculations individually.

The resulting object pose accuracy is shown in Figure 6-14 for the simulated self-calibration for a range of the arm absolute accuracy from 0 to 0.6 mm (average for all directions). The behavior observed is similar to the behavior observed for the grasp-point identification. For the accuracies of the calibrated arms, the object pose accuracy ranges from 0.2 mm to 0.4 mm and from 0.06° to 0.15°. The achieved object position and orientation accuracy scatter noticeably for values above about 0.3 mm arm absolute accuracy. This again indicates a better possible performance of the self-calibration for a good arm absolute accuracy. A more detailed analysis of the accuracy distribution is given below.
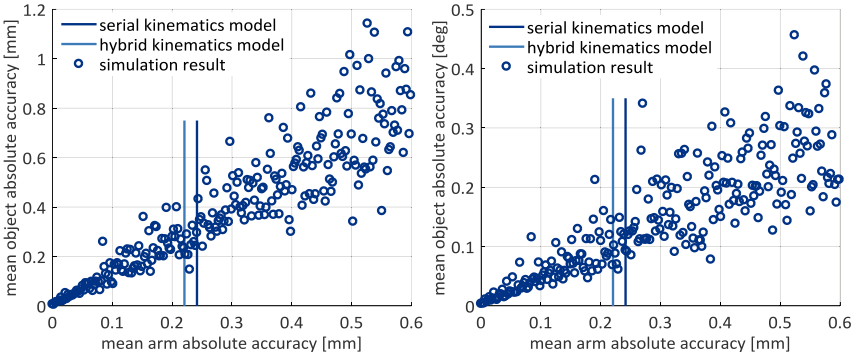
Figure 6-14: Object absolute accuracy after the simulated self-calibration for a range of absolute accuracies of the robotic arm

The resulting position accuracy of the object is approximately between factor 1 and 2 higher than the arm position accuracy. With this, the needed arm position accuracy for a desired accuracy of the object integrative handling system can be estimated. However, the relation of the remaining grasp point deviation and the resulting object pose accuracy (see Figure 6-15) is not strictly linear but varies significantly in-between repeated simulations. Drawing a conclusion about the resulting object pose accuracy is, hence, not possible based on the remaining grasp point deviation for a single simulation or measurement result. It can only serve as estimation for the overall performance.
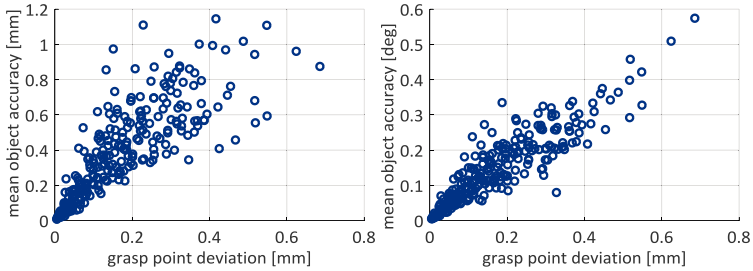
Figure 6-15: Relation of the remaining grasp point deviation and object pose accuracy after the simulated self-calibration for a range of absolute accuracies of the robotic arm

6.6.3   Accuracy Enhancement by Different Sets of Identification Poses

Following the above observations, the performance of the different sets of identification poses is analyzed based on a new set of simulations. The simulated self-calibration is implemented as described above using the mean arm absolute accuracy for the level 2 serial kinematics model (see Table 6-2). The results are compared to the nominal kinematics model and a level 2 model before self-calibration. The simulation of the nominal kinematics model is implemented by deriving the theoretical joint angles from the nominal inverse kinematics model using the nominal grasp points and object position. The resulting object pose is calculated based on the direct kinematic calculation with the actual grasp points, the calibrated kinematic model and the theoretical joint angles. The simulation for the level 2 serial kinematics model without self-calibration is implemented with the same direct kinematics. The theoretical joint angles are calculated using the level 2 serial kinematics model.

The object pose accuracy is evaluated for the 5 reference poses introduced in section 6.5. The distribution of the resulting mean absolute position accuracies are shown in the box-plots in Figure 6-16, the mean absolute orientation accuracies are shown in the box-plots Figure 6-17. Possible outliers outside the 1.5 time interquartile range are marked red. The average mean and maximum accuracy values are listed in Table 6-3.

The results for the nominal model and the level 2 model without self-calibration mainly depend on the simulated grasp point deviations. Because of the insufficient approximation of this simulation input, the resulting accuracies cannot be used for a quantitative evaluation but the qualitative improvement by self-calibration can be investigated. The object pose accuracy was measured for a set of example trajectories based on the level 2 model without self-calibration. The average absolute accuracy of 2.790 mm and 0.564° is in the same order of magnitude as the simulation results, the simulation, however, seems to overestimate the orientation error. A deeper discussion of these discrepancies is not purposeful, as the boundary conditions and object poses differ for the measurements and the simulation. The results give a first indication that the experimental validation of the developed self-calibration process needs to be performed extensively in the future.
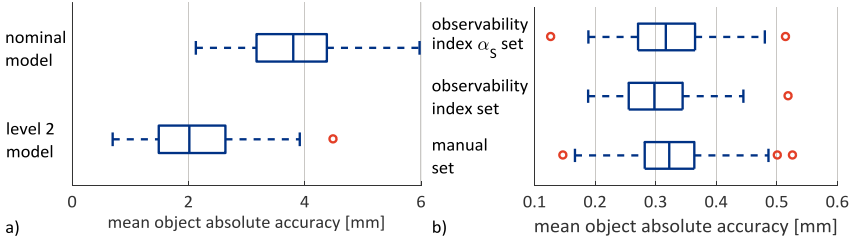
Figure 6-16: Distribution of the simulated mean object absolute position accuracy, box-plot with 1.5x interquartile range whiskers and possible outliers marked red
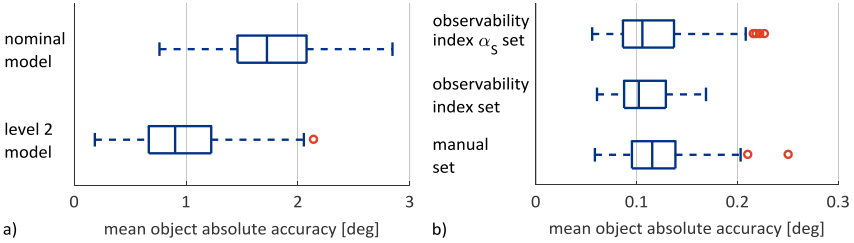
Figure 6-17: Distribution of the simulated mean object absolute orientation accuracy, box-plot with 1.5x interquartile range whiskers and possible outliers marked red

The self-calibration can be verified successfully based on the simulations, by comparing the simulated position accuracies before (see Figure 6-16a) and after self-calibration (see Figure 6-16b). The shown mean object absolute accuracy refers to the mean accuracy value for the 5 reference poses. The shown median and the average (see Table 6-3) of the mean absolute position accuracy are improved by a factor of 7 in comparison to the level 2 serial kinematics model without self-calibration.

The maximum object absolute accuracy listed in Table 6-3 refers to the maximum accuracy value for any of the 5 reference poses. The maximum of the absolute position accuracy is improved by a factor of 5. The accuracy does not only improve on average, the difference between the 5 reference points is reduced as well, which shows a more evenly distributed accuracy after self-calibration. The improvements for both, the average and maximum accuracy, are even better for the orientation accuracy shown in Figure 6-17.

The performance of the different sets of identification points is similar to each other: The distribution characteristics (median, average, quartiles, and whiskers) of the simulated accuracies for the manually chosen distribution and the optimized set with α_S condition vary by only a few percent, which is no significant difference. The performance is slightly superior for the set optimized only based on the observability index. The average mean accuracy is about 7 % better and the results are scattered in a smaller value range. The maximum accuracy values are about 3 % better, again with slightly better results for the orientation.

Overall, the performance of the self-calibration does not seem to be very sensitive to the exact choice of the identification sets, when comparing different optimized sets. This result

is similar to the findings from the kinematic arm calibration. The observability index gives a good orientation for a good set of identification poses, it is, however, not primarily critical to achieve an optimal parameter identification.

average value and	measured examples	nominal model	level 2 model	manual distribution	observability index	observability index α_S
mean absolute accuracy AP_P	2.790 mm	3.800 mm	2.108 mm	0.326 mm	0.301 mm	0.318 mm
maximum absolute accuracy AP_P	3.984 mm	5.418 mm	2.289 mm	0.484 mm	0.462 mm	0.472 mm
mean absolute accuracy AP_O	0.564°	1.764°	0.952 °	0.121°	0.108°	0.117°
maximum absolute accuracy $AP_{O\ max}$	1.815°	4.219°	1.646 °	0.308°	0.288°	0.293°
residual R_{SC}	-	-	-	0.1388	0.1505	0.1036

Table 6-3: Simulated average object accuracies for the 5 reference points for the nominal model and after self-calibration with different sets of identification poses

The verification results prove a successful implementation of the developed approach and give a good estimation of possible improvements of the absolute accuracy for object integrative handling concepts. Detailed experimental investigations can lead to an even better understanding of the performance of the self-calibration in future. It can, however, be expected to be individual and dependent on the kinematic structure of the cooperating robots and the integrated object.

6.7   Validation of the Self-Calibration Process

The developed and implemented self-calibration process needs to be validated by measurements. As discussed above, simulation and measurement results often vary significantly from each other. For this reason, first investigations for a validation of the process are described in this section.

The measurement object is integrated to the kinematic structure and moved to the identification poses. The joint angles φ_{1i} and φ_{4i} in the parallelogram are actuated, while the joint angles φ_{0i} and wrist-joint angles α_{Ri} align passively during the measurement motion. All joint angles are recorded and evaluated according to the self-calibration procedure.

During the measurement motion, significant restrictions of the prototype can be observed that limit the measurement quality: The wrist-joint axis R is actuated by a stepper motor with encoder and gearbox during the initial grasping process before setting it passive for the alignment. The gearbox and stepper motor induce inhomogeneous back-driving torques that hinder an optimal passive alignment and slip-stick effects occur, resulting in a discontinuous passive alignment. Furthermore, the friction in the passive joints D$_{0i}$ (joint angles φ_{0i}) is not identical for all arms, due to wear. The low stiffness of the vacuum end-effector leads to structural deformations close to the grasp point that change the kinematics. These effects cause different states of internal tensioning and deformation, limit the kinematic definite-

ness and consequently limit the passive alignment. As the loads due to friction are unknown, they cannot be compensated for easily using the developed stiffness model, without for example additional force sensors.

The passive alignment for the first measurement pose is shown in Figure 6-18. Starting from the initial pose in Figure 6-18a, the object is moved to the alignment poses. The 5-bar linkages (actuation of φ_{1i} and φ_{4i}) are moved to a new position and the passive angles φ_{0i} and α_{Ri} align because of the force transmission trough the integrated object. The resulting object pose is unique in the kinematic calculation, the passive alignment, however, does not necessarily result in this theoretical object pose (see Figure 6-18d), due to the limiting factors mentioned before.
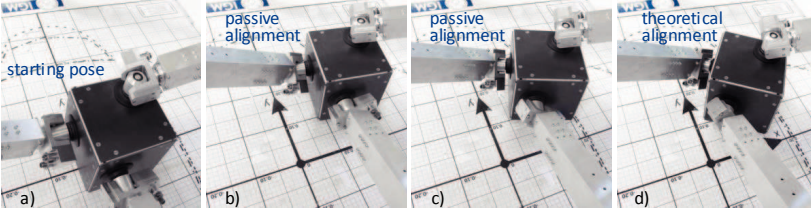
Figure 6-18: Starting pose, alternative passive alignments and theoretical alignment during self-calibration

The passive alignment for an exemplary pose (see Figure 6-18b and c) stops with an object rotation, smaller than the theoretical pose in Figure 6-18d. Furthermore, the alignment varies significantly between measurements. In these different alignment poses the relation of φ_{0i} and α_{Ri} is still valid although it is subject to tolerances. This means an alignment to the necessary pose might not necessarily be needed for a successful self-calibration. However, the induced measurement errors remain.

In a first validation approach the grasp points were measured manually and compared to the self-calibration results for three measurements to judge the feasibility of the validation using the existing PARAGRIP prototype. The average optimization residual R_{SC} was 2.9 for the measured data sets. These results are inferior to the simulation results by a factor of 20-30. Furthermore, the identified deviations $\Delta\alpha_{Ri}$ of the measured wrist-joint angles range from 2.3° to 8.3°. These values are outside the measured range with the standard deviation $\sigma_{\Delta\alpha_{Ri}} = 0.48°$. Finally, the identified grasp points do not represent the real grasp points or even show a clear improvement in comparison to the nominal grasp points. These results show, that the parameter identification was not successful and that the introduced self-calibration procedure cannot be validated with the current set up of the prototype.

The necessary modifications of the prototype and future investigations are discussed in sections 6.8 and 8.

6.8   Summary and Conclusion for the Self-Calibration

The investigation of the state of research for closed loop calibration methods has shown a broad range of approaches that are usually specific for the structure under investigation. Based on this, a self-calibration method for the object integrative handling system PARAGRIP was developed based on the combination of direct and inverse kinematic calculations and the evaluation of redundant sensor information.

The specific kinematic considerations, in particular the available sensor information for the kinematic modeling and the ambiguity of the object position relative to the robotic arms of the handling system were discussed. A formulation of the self-calibration problem and an extended kinematic model were formulated based on these considerations. It is based on the redundant direct kinematic calculation using the measured information for the actuated joint angles and the redundant inverse kinematic calculation, additionally using a measured wrist-joint angle for each arm. The identification of the grasp points at the object is based on a numerical optimization of the remaining residual that represents the deviation of measured and theoretical wrist-joint angles.

The self-calibration procedure was verified in a simulation approach. The simulation input was mainly obtained from various accuracy measurements and the kinematic calibration. The self-calibration could be verified successfully and the arm position accuracy was identified as the main influencing factor for the self-calibration performance. Similar to the results for the arm calibration, the choice of measurement poses is not very critical for the success of the self-calibration. The simulation results must be interpreted carefully. Often inferior results are obtained from measurements and practical implementations of the calibration or self-calibration processes.

The experimental validation of the self-calibration procedure showed significant drawbacks of the available prototype and was not concluded successfully. Inhomogeneous back-driving torques and friction in combination with the low stiffness of the vacuum end-effectors lead to a discontinuous and incomplete passive alignment of the integrated object.

For future investigations and a final validation of the self-calibration major modifications of the prototype are needed: The stepper motors need to be replaced by low friction encoders and the joint bearings need to be maintained or replaced. These modifications are not within the scope of this thesis and remain for further research. Furthermore, the transfer function between the actuated joints and the passive joints for the alignment is not considered explicitly in the selection of identification poses. Considering this relation could be a possible improvement for the practical implementation of the self-calibration procedure.

7 Summary and Conclusion

The first aim of this thesis was the implementation of a calibration procedure together with the accuracy assessment for the PARAGRIP handling system. The kinematic calibration was implemented and investigated for two new kinematic models: The mathematically efficient serial and the more computational intensive hybrid kinematics model. The limited absolute accuracy of the PARAGRIP arms could be improved significantly by parameter identification for both models and the hybrid kinematics model showed a more robust and reliable behavior in the calibration process. However, the difference was not as significant as expected based on current opinion in the research.

The experimental comparison of sets of different identification points showed similar results for both approaches, for the manual selection at the workspace boundaries and the observability index based optimization. This was not obvious beforehand based on research to date. In this context, the comparison of the 2-norm residual and the maximum residual showed significantly better behavior of the former, which justifies its widespread use.

The second aim of this thesis was the compensation of gravitational effects within the calibration procedure based on the automatic calculation of the structural deformations. A new stiffness modeling approach was implemented, based on the extension of the Matrix Structure Analysis. The stiffness model can be assembled and calculated automatically for arbitrary kinematic structures with various, linear or non-linear, elements from a catalog. The experimental validation for the PARAGRIP prototype was successful. The model and validation showed a well-balanced distribution of the compliance of all components, significant cross-coupling effects, and inhomogeneous stiffness properties within the workspace that can now be quantified based on the model.

The compensation of the gravitational deformations of the structure led to a significant improvement of the parameter identification for the arms. This shows the importance of stiffness modeling for the calibration processes.

The third aim of this thesis was to investigate self-calibration for object integrative handling systems to identify the grasp points at the object and compensate the internal inaccuracies automatically. A new self-calibration method was developed based on the combination of direct and inverse kinematic calculation. It incorporates specific considerations for the object position ambiguity when passive rotational alignment without redundant sensor information is used for the object integration. The verification of the implemented method showed a strong influence of the arm position accuracy on the performance of the grasp point identification in simulation. A correlation between the grasp point deviation and the object accuracy was for example shown. Similar to the results for the arm calibration, the choice of measurement poses is not very critical for the self-calibration procedure.

In summary, all research aims were achieved, only the validation of the self-calibration procedure was not concluded successfully: Significant drawbacks in the available prototype have hindered a sufficient passive alignment of the integrated object. This emphasizes the importance of an extensive experimental validation in the future.

8   Discussion and Outlook

Based on the presented research results, further investigations are needed to extend the results and transfer them to future applications.

The kinematic parameter identification for the PARAGRIP arm showed new results for the modeling of this specific structure. For future applications and transferal to industrial applications for example, the reliability of the measurement and identification procedure need to be improved. The changing conditions during the experiments and the long (and in some aspects unnecessary) complex data processing of the chosen implementation are examples of possible sources of error. Many of these problems are solved for industrial applications, where standardized procedures are available. Therefore, using the developed models and insights gained for similar kinematics may be suitable in such procedures and will aid any future investigations for the object integrative handling system PARAGRIP.

The introduced stiffness model could be extended with additional elements to broaden the possible applications. Few stiffness elements that go beyond the scope of this thesis are implemented currently, though others are both possible and useful, in particular standard elements like bearings or motors. Integrating existing stiffness data for such elements, for example provided by manufacturers, would be a worthwhile extension of the method.

The implementation of a non-linear modeling behavior may be worth future investigations as well. Even though the non-linear stiffness behavior of the elements is considered, this is not the case for the changing kinematics of the deformed structure. This is a valid simplification for the small deformations considered in this thesis. For highly deformable structures and in soft robotics, the combination of the kinematic calculations and the stiffness model could be a suitable approach, despite the increased complexity of these calculations.

Furthermore, the implemented stiffness models needs to be tested in a broader range of applications and structures to give a better understanding of the performance of the model, to identify possible weaknesses and necessary extensions.

Of course, most considerations regarding possible further research concern the self-calibration for object integrative handling systems and cooperating robots. The research is at an early stage and many improvements are still necessary. Some of these considerations are summarized in the following paragraphs.

The validation of the self-calibration procedure introduced in this thesis is a first point for future investigation. The according modifications of the prototype are necessary to conclude the validation as shown here, but also tests on other robots, possibly reliable and precise industrial robots with appropriate sensors would be possible. Experimental validations and extensive measurements are needed to quantify the performance of the self-calibration and gain reliable data for the reachable accuracies. As discussed before, significant deviations in the experimental results and the simulations can be expected. Such investigations should include different objects and contact surface configurations as well. The sensitivity of the self-calibration to the object's shape and to changing grasp point configurations is highly relevant for any practical implementation.

The self-calibration as introduced in this thesis relies on the evaluation of redundant sensor data. Consequently, extending the available sensor information for the PARAGRIP prototype will be beneficial for the self-calibration process. All wrist-joints of the robotic arms could be equipped with sensors, even though the practical implementation of the prototype may be difficult. A more realistic extension is the use of an additional robotic arm. This would introduce an additional grasp point that needs to be identified, but it solves the ambiguity of the object position discussed for the current implementation. 4 contact points with fixed position relative to each other cannot be placed arbitrarily on the objects surface.

The self-calibration offers the opportunity to be applied to all kinds of cooperating robotic systems. As shown in Figure 8-1a, a lot of redundant sensor information is available for 3 cooperating 6DOF articulated robots and such configurations could of course be scaled by using more or different robotic structures. A framework to identify the ideal set of active and passive joints for a given configuration would permit a flexible and versatile use of cooperating robots. The application for cooperating mobile robotic units and the extension of the identified parameters, for example to the relative base frame positions, are imaginable and could lead to highly flexible assembly systems.
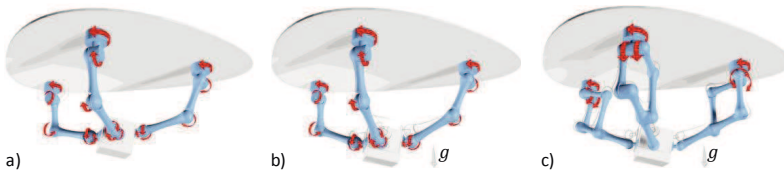
Figure 8-1:   Alternative and extended approaches for the self-calibration of cooperating robots

Another possible extension of the self-calibration and a new field of research is the evaluation of redundant force and torque information, rather than the evaluation of redundant position information alone. As illustrated in Figure 8-1b and c, the cooperating robots could be actuated deliberately in a redundant mode. The evaluation of the measured motor torques would allow for a self-calibration method based on kinematic calculations and on the implemented stiffness model. Tensioning of the structure would become a source of information, rather than an undesired source of error. Gravitational effects, the mass distribution of the object and changing loads when lifting the object could be considered as soon as actuation forces and torques are evaluated.

Another extension that should be mentioned is the use of continuous measurement data and the consideration of the systems dynamics: A much larger amount of data, and therefore a potentially better self-calibration performance, would be opposed to increasingly complex modeling, data acquisition and data analysis.

The self-calibration of object integrative handling systems is clearly a promising approach towards further developments in robotics, offering both a variety of interesting applications and possibilities for future research…

9 Annex

9.1 Calculation of the General 4-bar Linkage

The passive joint angle φ_2 can be calculated from the kinematics of the deformed parallelogram. Resolving equations (4.10) and (4.11) into l_3:

$$l_3\,cos(\varphi_3) = l_1\,cos(\varphi_1) + l_2\,cos(\varphi_2) - l_4cos(\varphi_4) \tag{9.1}$$

$$l_3\,sin(\varphi_3) = l_1\,sin(\varphi_1) + l_2\,sin(\varphi_2) - l_4sin(\varphi_4) \tag{9.2}$$

Square both equations and add them up to eliminate φ_3 using the Pythagorean trigonometric identity $sin^2(\varphi_1) + cos^2(\varphi_1) = 1$:

$$l_3{}^2 = l_2{}^2 + 2l_2\,cos(\varphi_2)\,(l_1\,cos(\varphi_1) - l_4cos(\varphi_4)) + (l_1\,cos(\varphi_1) - l_4cos(\varphi_4))^2$$
$$+ 2l_2\,sin(\varphi_2)\,(l_1\,sin(\varphi_1) - l_4sin(\varphi_4)) + (l_1\,sin(\varphi_1) - l_4sin(\varphi_4))^2 \tag{9.3}$$

Bring equation (9.3) into the form:

$$A\,cos(\varphi_2) + B\,sin(\varphi_2) = C \tag{9.4}$$

With:

$$A = 2l_2(l_1\,cos(\varphi_1) - l_4cos(\varphi_4)) \tag{9.5}$$

$$B = 2l_2(l_1\,sin(\varphi_1) - l_4sin(\varphi_4)) \tag{9.6}$$

$$C = l_3{}^2 - l_2{}^2 - l_1{}^2 - l_4{}^2 + 2l_1l_4\,cos(\varphi_1 - \varphi_4) \tag{9.7}$$

Equation (9.14) is resolved into $A\,cos(\varphi_2)$, square both sides and use the Pythagorean trigonometric identity:

$$A^2(1 - sin^2(\varphi_1)) = C^2 - 2CB\,sin(\varphi_2) + B^2\,sin(\varphi_2) \tag{9.8}$$

Using the quadratic formula results in:

$$sin(\varphi_2)_{1,2} = \frac{CB \pm A\sqrt{A^2 + B^2 - C^2}}{A^2 + B^2} \tag{9.9}$$

$$cos(\varphi_2)_{1,2} = \frac{AC \mp B\sqrt{A^2 + B^2 - C^2}}{A^2 + B^2} \tag{9.10}$$

By evaluating (9.9) and (9.10) the passive joint angle φ_2 can be calculated nonambiguous in the correct quadrant.

9.2 Linearization of the Position Constraints

The variables $\hat{l}_3$, $\hat{l}_2$, $\hat{\varphi}_3$ and $\hat{\varphi}_2$ are eliminated in equations (4.18) and (4.19) and the abbreviations $c\varphi_i = cos(\varphi_i)$ and $s\varphi_i = sin(\varphi_i)$ are introduced:

$$(\hat{l}_1 + \Delta l_1)\,c\,\hat{\varphi}_1 + (\hat{l}_4 + \Delta l_2)\,c(\hat{\varphi}_4 + \Delta\varphi_2) = (\hat{l}_1 + \Delta l_3)c(\hat{\varphi}_1 + \Delta\varphi_3) + (\hat{l}_4 + \Delta l_4)\,c\,\hat{\varphi}_4 \tag{9.11}$$

$$(\hat{l}_1 + \Delta l_1)\,s\,\hat{\varphi}_1 + (\hat{l}_4 + \Delta l_2)\,s(\hat{\varphi}_4 + \Delta\varphi_2) = (\hat{l}_1 + \Delta l_3)s(\hat{\varphi}_1 + \Delta\varphi_3) + (\hat{l}_4 + \Delta l_4)s\hat{\varphi}_4 \tag{9.12}$$

The cosine and sine function can be linearized using the Taylor expansion [Dah08, p. 20–21] as follows:

$$c(\hat{\varphi}_i + \Delta\varphi_i) = c\,\hat{\varphi}_i - s\hat{\varphi}_i\Delta\varphi_i \tag{9.13}$$

$$s(\hat{\varphi}_i + \Delta\varphi_i) = s\,\hat{\varphi}_i - c\hat{\varphi}_i\Delta\varphi_i \tag{9.14}$$

With these equations (9.11) and (9.12) are linearized:

$$\left(\hat{l}_1+\Delta l_1\right)c\,\hat{\varphi}_1+\left(\hat{l}_4+\Delta l_2\right)(c\,\hat{\varphi}_4-s\hat{\varphi}_4\Delta\varphi_2)=\left(\hat{l}_1+\Delta l_3\right)(c\,\hat{\varphi}_1-s\hat{\varphi}_1\Delta\varphi_3)+\left(\hat{l}_4+\Delta l_4\right)c\hat{\varphi}_4$$
$$\left(\hat{l}_1+\Delta l_1\right)s\,\hat{\varphi}_1+\left(\hat{l}_4+\Delta l_2\right)(s\,\hat{\varphi}_4-c\hat{\varphi}_4\Delta\varphi_2)=\left(\hat{l}_1+\Delta l_3\right)(s\,\hat{\varphi}_1-c\hat{\varphi}_1\Delta\varphi_3)+\left(\hat{l}_4+\Delta l_4\right)s\hat{\varphi}_4$$

(9.15)

Ignoring higher order terms leads to:

$$\left(\hat{l}_1+\Delta l_1\right)c\,\hat{\varphi}_1+\left(\hat{l}_4+\Delta l_2\right)c\,\hat{\varphi}_4-s\hat{\varphi}_4\Delta\varphi_2\hat{l}_4-s\hat{\varphi}_4\Delta\varphi_2\Delta l_2=$$
$$c\hat{\varphi}_1\left(\hat{l}_1+\Delta l_3\right)-s\hat{\varphi}_1\Delta\varphi_3\hat{l}_1-s\hat{\varphi}_1\Delta\varphi_3\Delta l_3+\left(\hat{l}_4+\Delta l_4\right)c\hat{\varphi}_4$$

(9.16)

$$\left(\hat{l}_1+\Delta l_1\right)s\,\hat{\varphi}_1+\left(\hat{l}_4+\Delta l_2\right)s\,\hat{\varphi}_4-c\hat{\varphi}_4\Delta\varphi_2\hat{l}_4-c\hat{\varphi}_4\Delta\varphi_2\Delta l_2=$$
$$s\hat{\varphi}_1\left(\hat{l}_1+\Delta l_3\right)-c\hat{\varphi}_1\Delta\varphi_3\hat{l}_1-c\hat{\varphi}_1\Delta\varphi_3\Delta l_3+\left(\hat{l}_4+\Delta l_4\right)s\hat{\varphi}_4$$

(9.17)

Isolating $\Delta\varphi_2$ in both equations and simplifying them:

$$\Delta\varphi_2=\frac{\Delta l_3c\hat{\varphi}_1-s\hat{\varphi}_1\Delta\varphi_3\hat{l}_1+\Delta l_4c\hat{\varphi}_4-\Delta l_1\,c\,\hat{\varphi}_1-\Delta l_2\,c\,\hat{\varphi}_4}{-s\hat{\varphi}_4\hat{l}_4}$$

(9.18)

$$\Delta\varphi_2=\frac{\Delta l_3s\hat{\varphi}_1-c\hat{\varphi}_1\Delta\varphi_3\hat{l}_1+\Delta l_4s\hat{\varphi}_4-\Delta l_1\,s\,\hat{\varphi}_1-\Delta l_2\,s\,\hat{\varphi}_4}{-c\hat{\varphi}_4\hat{l}_4}$$

(9.19)

Elimination of $\Delta\varphi_2$ and isolation of $\Delta\varphi_3$ from the remaining equation:

$$\frac{(\Delta l_3-\Delta l_1)c\hat{\varphi}_1+(\Delta l_4-\Delta l_2)\,c\,\hat{\varphi}_4-s\hat{\varphi}_1\Delta\varphi_3\hat{l}_1}{-s\hat{\varphi}_4}=\frac{(\Delta l_3-\Delta l_1)\,s\,\hat{\varphi}_1+(\Delta l_4-\Delta l_2)\,s\,\hat{\varphi}_4-c\hat{\varphi}_1\Delta\varphi_3\hat{l}_1}{-c\hat{\varphi}_4}$$

(9.20)

$$\left(\frac{s\hat{\varphi}_1\hat{l}_1}{s\hat{\varphi}_4}-\frac{c\hat{\varphi}_1\hat{l}_1}{c\hat{\varphi}_4}\right)\Delta\varphi_3=\frac{(\Delta l_3-\Delta l_1)\,s\,\hat{\varphi}_1+(\Delta l_4-\Delta l_2)\,s\,\hat{\varphi}_4}{-c\hat{\varphi}_4}-\frac{(\Delta l_3-\Delta l_1)c\hat{\varphi}_1+(\Delta l_4-\Delta l_2)\,c\,\hat{\varphi}_4}{-s\hat{\varphi}_4}$$

(9.21)

$$\frac{\hat{l}_1s(\hat{\varphi}_1-\hat{\varphi}_4)}{s\hat{\varphi}_4c\hat{\varphi}_4}\Delta\varphi_3=(\Delta l_3-\Delta l_1)\left(\frac{c\hat{\varphi}_1}{s\hat{\varphi}_4}-\frac{s\hat{\varphi}_1}{c\hat{\varphi}_4}\right)+(\Delta l_4-\Delta l_2)\left(\frac{c\,\hat{\varphi}_4}{s\hat{\varphi}_4}-\frac{s\,\hat{\varphi}_4}{c\hat{\varphi}_4}\right)$$

(9.22)

$$\Delta\varphi_3=(\Delta l_3-\Delta l_1)\frac{c\hat{\varphi}_1c\hat{\varphi}_4-s\hat{\varphi}_1\,s\hat{\varphi}_4}{\hat{l}_1s(\hat{\varphi}_1-\hat{\varphi}_4)}+(\Delta l_4-\Delta l_2)\frac{c\hat{\varphi}_4c\hat{\varphi}_4-s\hat{\varphi}_4s\hat{\varphi}_4}{\hat{l}_1s(\hat{\varphi}_1-\hat{\varphi}_4)}$$

(9.23)

$$\Delta\varphi_3=(\Delta l_3-\Delta l_1)\frac{c(\hat{\varphi}_1+\hat{\varphi}_4)}{\hat{l}_1s(\hat{\varphi}_1-\hat{\varphi}_4)}-(\Delta l_2-\Delta l_4)\frac{c(2\hat{\varphi}_4)}{\hat{l}_1s(\hat{\varphi}_1-\hat{\varphi}_4)}$$

(9.24)

Analogous, $\Delta\varphi_3$ is eliminated in equations (9.16) and (9.17) and the equations are simplified:

$$\Delta\varphi_3=\frac{(\Delta l_3-\Delta l_1)c\hat{\varphi}_1+(\Delta l_4-\Delta l_2)c\hat{\varphi}_4+s\hat{\varphi}_4\Delta\varphi_2\hat{l}_4}{s\hat{\varphi}_1\hat{l}_1}$$

(9.25)

$$\Delta\varphi_3=\frac{(\Delta l_3-\Delta l_1)s\hat{\varphi}_1+(\Delta l_4-\Delta l_2)s\hat{\varphi}_4+c\hat{\varphi}_4\Delta\varphi_2\hat{l}_4}{c\hat{\varphi}_1\hat{l}_1}$$

(9.26)

Analogous, $\Delta\varphi_3$ is eliminated and $\Delta\varphi_2$ is isolated from the remaining equations:

$$\left(\frac{s\hat{\varphi}_4\hat{l}_4}{s\hat{\varphi}_1}-\frac{c\hat{\varphi}_4\hat{l}_4}{c\hat{\varphi}_1}\right)\Delta\varphi_2=\frac{(\Delta l_3-\Delta l_1)s\hat{\varphi}_1+(\Delta l_4-\Delta l_2)s\hat{\varphi}_4}{c\hat{\varphi}_1}-\frac{(\Delta l_3-\Delta l_1)c\hat{\varphi}_1+(\Delta l_4-\Delta l_2)c\hat{\varphi}_4}{s\hat{\varphi}_1}$$

(9.27)

$$\Delta\varphi_2=\frac{(\Delta l_3-\Delta l_1)s\hat{\varphi}_1s\hat{\varphi}_1+(\Delta l_4-\Delta l_2)s\hat{\varphi}_1s\hat{\varphi}_4}{\hat{l}_4s(\hat{\varphi}_4-s\hat{\varphi}_1)}-\frac{(\Delta l_3-\Delta l_1)c\hat{\varphi}_1c\hat{\varphi}_1+(\Delta l_4-\Delta l_2)c\hat{\varphi}_1c\hat{\varphi}_4}{\hat{l}_4s(\hat{\varphi}_4-s\hat{\varphi}_1)}$$

(9.28)

$$\Delta\varphi_2=(\Delta l_3-\Delta l_1)\frac{-c(2\hat{\varphi}_1)}{\hat{l}_4s(\hat{\varphi}_4-s\hat{\varphi}_1)}+(\Delta l_4-\Delta l_2)\frac{-c(\hat{\varphi}_1+\hat{\varphi}_4)}{\hat{l}_4s(\hat{\varphi}_4-s\hat{\varphi}_1)}$$

(9.29)

9.3   Kinematic Parameters after Level 2 and Level 3 Calibration

parameter	$\Delta\varphi_0$	$\Delta\varphi_1$	$\Delta\varphi_4$	Δy_{TCP}	Δx_{axis}	l_1	l_2
nominal	0.000°	0.000°	0.000°	0.000 mm	0.000 mm	350.000 mm	150.000 mm
arm 1	0.087°	-0.459°	-0.399°	-0.270 mm	-0.378 mm	349.612 mm	149.884 mm
arm 2	0.175°	0.031°	-0.036°	-0.102 mm	-0.076 mm	349.161 mm	150.060 mm
arm 4	0.215°	-0.121°	0.062°	-0.493 mm	1.013 mm	349.505 mm	149.904 mm
parameter	$\Delta\alpha$	$\Delta\beta$	Δx	Δy	Δz	l_3	l_k
nominal	0.000°	0.000°	0.000 mm	0.000 mm	0.000 mm	350.000 mm	629.300 mm
arm 1	0.141°	-0.231°	-0.710 mm	-0.916 mm	1.433 mm	349.633 mm	628.975 mm
arm 2	-0.048°	-0.060°	0.579 mm	0.894 mm	0.385 mm	349.307 mm	629.206 mm
arm 4	0.039°	-0.072°	-0.090 mm	-0.694 mm	1.750 mm	349.570 mm	626.988 mm

Table 9-1: Kinematic Parameters after level 2 calibration for the hybrid kinematics model

parameter	$\Delta\varphi_0$	$\Delta\varphi_1$	$\Delta\varphi_4$	Δy_{TCP}	Δx_{axis}	l_1	l_2
nominal	0.000°	0.000°	0.000°	0.000 mm	0.000 mm	350.000 mm	150.000 mm
arm 1	0.106°	-0.475°	-0.424°	-0.369 mm	-0.496 mm	349.950 mm	149.873 mm
arm 2	0.194°	0.012°	-0.063°	-0.203 mm	-0.185 mm	349.505 mm	150.048 mm
arm 4	0.233°	-0.138°	-0.088°	-1.434 mm	0.896 mm	349.844 mm	149.892 mm
parameter	$\Delta\alpha$	$\Delta\beta$	Δx	Δy	Δz	l_3	l_k
nominal	0.000°	0.000°	0.000 mm	0.000 mm	0.000 mm	350.000 mm	629.300 mm
arm 1	0.139°	-0.224°	-0.766 mm	-0.945 mm	1.120 mm	349.885 mm	629.087 mm
arm 2	-0.050°	-0.053°	0.523 mm	0.863 mm	0.085 mm	349.565 mm	629.293 mm
arm 4	0.037°	-0.065°	-0.145 mm	-0.722 mm	1.107 mm	349.821 mm	627.093 mm

Table 9-2: Kinematic Parameters after level 3 calibration for the hybrid kinematics model

parameter	$\Delta\varphi_0$	$\Delta\varphi_1$	$\Delta\varphi_4$	Δy_{TCP}		l_1	l_2
nominal	0.000°	0.000°	0.000°	0.000 mm		350.000 mm	629.300 mm
arm 1	0.059°	-0.165°	-0.223°	-0.248 mm		348.894 mm	630.200 mm
arm 2	0.158°	0.150°	0.126°	-0.164 mm		348.936 mm	629.492 mm
arm 3	0.183°	0.123°	0.173°	-0.06 mm		349.139 mm	629.422 mm
arm 4	0.173°	0.044°	-0.030°	-0.549 mm		348.892 mm	628.390 mm
parameter	$\Delta\alpha$	$\Delta\beta$	Δx	Δy	Δz		
nominal	0.000°	0.000°	0.000 mm	0.000 mm	0.000 mm		
arm 1	0.154°	-0.126°	-1.615 mm	-0.752 mm	1.083 mm		
arm 2	-0.041°	0.004°	0.178 mm	0.914 mm	0.295 mm		
arm 3	0.013°	-0.025°	0.122 mm	-0.497 mm	-0.412 mm		
arm 4	0.042°	-0.078°	0.500 mm	-0.264 mm	1.623 mm		

Table 9-3: Kinematic Parameters after level 2 calibration for the serial kinematics model

9.4   Stiffness and Transformation Matrices for the Example Structure

$$
{}^1K_1 = \begin{pmatrix} k_{1x} & 0 & 0 & 0 & 0 & 0 \\ 0 & k_{1y} & 0 & 0 & 0 & 0 \\ 0 & 0 & k_{1z} & 0 & 0 & 0 \\ 0 & 0 & 0 & k_{1\alpha} & 0 & 0 \\ 0 & 0 & 0 & 0 & k_{1\beta} & 0 \\ 0 & 0 & 0 & 0 & 0 & k_{1\gamma} \end{pmatrix}, \quad {}^0V_{1,0} = \begin{pmatrix} 1 & 0 & 0 & 0 & 0 & 0 \\ 0 & 1 & 0 & 0 & 0 & \frac{l}{2} \\ 0 & 0 & 1 & 0 & -\frac{l}{2} & 0 \\ 0 & 0 & 0 & 1 & 0 & 0 \\ 0 & 0 & 0 & 0 & 1 & 0 \\ 0 & 0 & 0 & 0 & 0 & 1 \end{pmatrix}, \quad {}^0R_1 = I_6 \qquad (9.30)
$$

$$
{}^2K_2 = \begin{pmatrix} k_{2x} & 0 & 0 & 0 & 0 & 0 \\ 0 & k_{2y} & 0 & 0 & 0 & 0 \\ 0 & 0 & k_{2z} & 0 & 0 & 0 \\ 0 & 0 & 0 & k_{2\alpha} & 0 & 0 \\ 0 & 0 & 0 & 0 & 0 & 0 \\ 0 & 0 & 0 & 0 & 0 & k_{2\gamma} \end{pmatrix}, \quad {}^0V_{2,0} = \begin{pmatrix} 1 & 0 & 0 & 0 & 0 & 0 \\ 0 & 1 & 0 & 0 & 0 & l \\ 0 & 0 & 1 & 0 & -l & 0 \\ 0 & 0 & 0 & 1 & 0 & 0 \\ 0 & 0 & 0 & 0 & 1 & 0 \\ 0 & 0 & 0 & 0 & 0 & 1 \end{pmatrix}, \quad {}^0R_2 = I_6 \qquad (9.31)
$$

$$
{}^3K_3 = \begin{pmatrix} k_{3x} & 0 & 0 & 0 & 0 & 0 \\ 0 & k_{3y} & 0 & 0 & 0 & 0 \\ 0 & 0 & k_{3z} & 0 & 0 & 0 \\ 0 & 0 & 0 & k_{3\alpha} & 0 & 0 \\ 0 & 0 & 0 & 0 & k_{3\beta} & 0 \\ 0 & 0 & 0 & 0 & 0 & k_{3\gamma} \end{pmatrix}, \quad {}^0R_3 = \begin{pmatrix} cos(30°) & 0 & -sin(30°) & 0 & 0 & 0 \\ 0 & 1 & 0 & 0 & 0 & 0 \\ sin(30°) & 0 & cos(30°) & 0 & 0 & 0 \\ 0 & 0 & 0 & 1 & 0 & 0 \\ 0 & 0 & 0 & 0 & 1 & 0 \\ 0 & 0 & 0 & 0 & 0 & 1 \end{pmatrix}
$$

$$(9.32)$$

$$
{}^0V_{3,0} = \begin{pmatrix} 1 & 0 & 0 & 0 & 0.25 \cdot l & 0 \\ 0 & 1 & 0 & 0 & 0 & \left(1 + \frac{cos(30°)}{2}\right)l \\ 0 & 0 & 1 & -0.25 \cdot l & -\left(1 + \frac{cos(30°)}{2}\right)l & 0 \\ 0 & 0 & 0 & 1 & 0 & 0 \\ 0 & 0 & 0 & 0 & 1 & 0 \\ 0 & 0 & 0 & 0 & 0 & 1 \end{pmatrix}
$$

9.5   Stiffness Elements of the PARAGRIP Structure
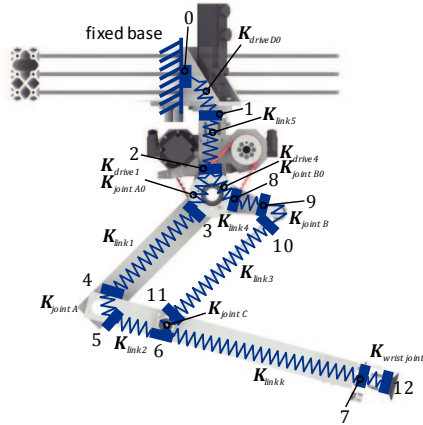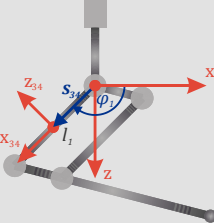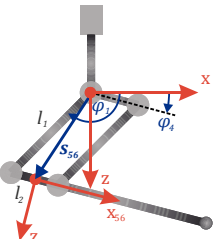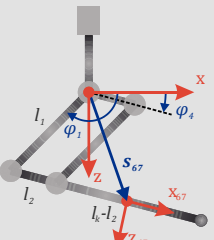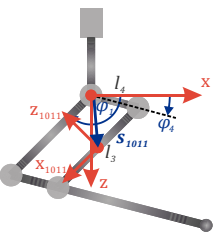
Figure 9-1: Structure of the PARAGRIP stiffness model with the connecting nodes

Table 9-4 lists the coordinate systems, properties and positions for all stiffness elements of the PARAGRIP structure. The coordinate systems and positions are indexed according to the connecting nodes shown in Figure 9-1.

element	coordinate system	properties	position and orientation
link 1		thin-walled rectangular beam connect nodes: 3 and 4 length l_1: 0.350 m width b: 0.050 m height h: 0.070 m thickness t: 0.030 m	$$s_{34} = R_z(\varphi_0) \cdot \begin{pmatrix} \frac{l_1}{2} cos\, \varphi_1 \\ 0.06075\ m \\ \frac{l_1}{2} sin\, \varphi_1 \end{pmatrix}$$ $$R_{34} = R_z(\varphi_0) \cdot R_y(-\varphi_1) \cdot E_3$$
link 2		thin-walled rectangular profile connect nodes: 5 and 6 length l_2: 0.150 m width b: 0.040 m height h: 0.060 m thickness t: 0.002 m	$$s_{56} = R_z(\varphi_0) \cdot$$ $$\begin{pmatrix} l_1 cos\, \varphi_1 + \frac{l_2}{2} cos\, \varphi_4 \\ 0 \\ l_1 sin\, \varphi_1 + \frac{l_2}{2} sin\, \varphi_4 \end{pmatrix}$$ $$R_{56} = R_z(\varphi_0) \cdot R_y(-\varphi_4) \cdot E_3$$
link k		thin-walled rectangular profile connect nodes: 6 and 7 length l_k-l_2: 0.3575 m width b: 0.040 m height h: 0.060 m thickness t: 0.002 m	$$s_{67} = R_z(\varphi_0) \cdot$$ $$\begin{pmatrix} l_1 cos\, \varphi_1 + \left(l_2 + \frac{l_k \cdot l_2 - l_{TCP}}{2}\right) cos\, \varphi_4 \\ 0 \\ l_1 sin\, \varphi_1 + \left(l_2 + \frac{l_k \cdot l_2 - l_{TCP}}{2}\right) sin\, \varphi_4 \end{pmatrix}$$ $$R_{67} = R_z(\varphi_0) \cdot R_y(-\varphi_4) \cdot E_3$$
link 3		thin-walled round profile connect nodes: 10 and 11 length l_3: 0.350 m diameter d: 0.013 m thickness t: 0.002 m	$$s_{1011}$$ $$= R_z(\varphi_0) \cdot \begin{pmatrix} \frac{l_3}{2} cos\, \varphi_1 + l_4 cos\, \varphi_4 \\ -0.03225\ m \\ \frac{l_3}{2} sin\, \varphi_1 + l_4 sin\, \varphi_4 \end{pmatrix}$$ $$R_{1011} = R_z(\varphi_0) \cdot R_y(-\varphi_1) \cdot E_3$$

element	coordinate system	properties	position and orientation
link 4		predefined stiffness element k_x: 1.5353 10^8 N/m k_y: 9.2065 10^6 N/m k_z: 2.5642 10^7 N/m connect nodes: 8 and 9 length l_4: 0,150 m	$\boldsymbol{s}_{89} = \boldsymbol{R}_z(\varphi_0) \cdot \begin{pmatrix} l_4\,cos\,\varphi_4 \\ -0.03225\,m \\ l_4\,sin\,\varphi_4 \end{pmatrix}$ $\boldsymbol{R}_{89} = \boldsymbol{R}_z(\varphi_0) \cdot \boldsymbol{R}_y(-\varphi_4) \cdot \boldsymbol{E}_3$
link 5		predefined stiffness element k_α: 1.2137 10^5 N/m k_β: 1.2137 10^5 N/m connect nodes: 1 and 2	$\boldsymbol{s}_{12} = \boldsymbol{R}_z(\varphi_0) \cdot \begin{pmatrix} 0 \\ 0 \\ -0.177\,m \end{pmatrix}$ $\boldsymbol{R}_{12} = \boldsymbol{R}_z(\varphi_0) \cdot \boldsymbol{E}_3$
drive D_0		predefined stiffness element k_α: 5.4462 10^4 Nm/rad k_β: 5.4462 10^4 Nm/rad k_γ: 7.6735 10^3 Nm/rad connect nodes: 0 and 1	$\boldsymbol{s}_{01} = \boldsymbol{R}_z(\varphi_0) \cdot \begin{pmatrix} 0 \\ 0 \\ -0.1885\,m \end{pmatrix}$ $\boldsymbol{R}_{01} = \boldsymbol{R}_z(\varphi_0) \cdot \boldsymbol{E}_3$
drive 1		predefined stiffness element k_γ: 7.0330 10^3 Nm/rad connect nodes: 2 and 3	$\boldsymbol{s}_{23M} = \boldsymbol{R}_z(\varphi_0) \cdot \begin{pmatrix} 0 \\ 0.06075\,m \\ 0 \end{pmatrix}$ $\boldsymbol{R}_{23M} = \boldsymbol{R}_z(\varphi_0) \cdot \boldsymbol{E}_3$

element	coordinate system	properties	position and orientation
drive 4		predefined stiffness element k_β: 8.4562 10^3 Nm/rad connect nodes: 2 and 8	$\boldsymbol{s}_{28M} = \boldsymbol{R}_z(\varphi_0) \cdot \begin{pmatrix} 0 \\ -0.03225\ m \\ 0 \end{pmatrix}$ $\boldsymbol{R}_{28M} = \boldsymbol{R}_z(\varphi_0) \cdot \boldsymbol{E}_3$
joint A_0		2x ball-bearings ID: 13807 connect nodes: 2 and 3	$\boldsymbol{s}_{23}{}' = \boldsymbol{R}_z(\varphi_0) \cdot \begin{pmatrix} 0 \\ 0.08075\ m \\ 0 \end{pmatrix}$ $\boldsymbol{s}_{23}{}'' = \boldsymbol{R}_z(\varphi_0) \cdot \begin{pmatrix} 0 \\ 0.04075\ m \\ 0 \end{pmatrix}$ $\boldsymbol{R}_{23} = \boldsymbol{R}_z(\varphi_0) \cdot \boldsymbol{R}_y(-\varphi_1) \cdot \boldsymbol{E}_3$
joint B_0		2x ball-bearing ID: 13807 connect nodes: 2 and 8	$\boldsymbol{s}_{28}{}' = \boldsymbol{R}_z(\varphi_0) \cdot \begin{pmatrix} 0 \\ -0.01225\ m \\ 0 \end{pmatrix}$ $\boldsymbol{s}_{28}{}'' = \boldsymbol{R}_z(\varphi_0) \cdot \begin{pmatrix} 0 \\ -0.05225 m \\ 0 \end{pmatrix}$ $\boldsymbol{R}_{28} = \boldsymbol{R}_z(\varphi_0) \cdot \boldsymbol{R}_y(-\varphi_4) \cdot \boldsymbol{E}_3$
joint A		2x ball-bearing ID: 13807 connecting nodes: 4 and 5	$\boldsymbol{s}_{45}{}' = \boldsymbol{R}_z(\varphi_0) \cdot \begin{pmatrix} l_1\ cos\ \varphi_1 \\ 0.08075\ m \\ l_1\ sin\ \varphi_1 \end{pmatrix}$ $\boldsymbol{s}_{45}{}'' = \boldsymbol{R}_z(\varphi_0) \cdot \begin{pmatrix} l_1\ cos\ \varphi_1 \\ 0.04075\ m \\ l_1\ sin\ \varphi_1 \end{pmatrix}$ $\boldsymbol{R}_{45} = \boldsymbol{R}_z(\varphi_0) \cdot \boldsymbol{R}_y(-\varphi_4) \cdot \boldsymbol{E}_3$
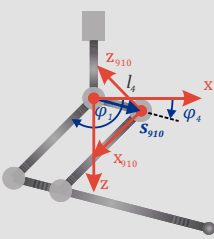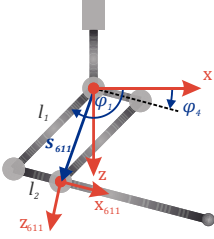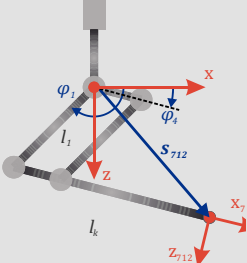
element	coordinate system	properties	position and orientation
Joint B		pivoting bearing ID: 11200 connect nodes: 9 and 10	$$s_{910} = R_z(\varphi_0) \cdot \begin{pmatrix} l_4 \cos \varphi_4 \\ -0.03225 \, m \\ l_4 \sin \varphi_4 \end{pmatrix}$$ $$R_{910} = R_z(\varphi_0) \cdot R_y(-\varphi_1) \cdot E_3$$
Joint C		pivoting bearing ID: 11200 connect nodes: 9 and 10	$$s_{611} = R_z(\varphi_0) \cdot$$ $$\begin{pmatrix} l_1 \cos \varphi_1 + l_2 \cos \varphi_4 \\ -0.03225 \, m \\ l_1 \sin \varphi_1 + l_2 \sin \varphi_4 \end{pmatrix}$$ $$R_{611} = R_z(\varphi_0) \cdot R_y(-\varphi_4) \cdot E_3$$
end-effector		vacuum end-effector connect nodes: 7 and 12	$$s_{712} = R_z(\varphi_0) \cdot$$ $$\begin{pmatrix} l_1 \cos \varphi_1 + l_k \cos \varphi_4 \\ -0.03225 \, m \\ l_1 \sin \varphi_1 + l_k \sin \varphi_4 \end{pmatrix}$$ $$R_{712} =$$ $$R_z(\varphi_0) \cdot R_y(-\varphi_4) \cdot R_x(\alpha_R) \cdot E_3$$

Table 9-4: Element types, connecting nodes, properties and coordinate systems for the PARAGRIP stiffness elements

9.6   Load Cases for the Identification of the PARAGRIP Stiffness Parameters

load case	φ_0	φ_1	φ_4	structure	load		displace-ment
1	0°	90°	-	link 3 removed, link 5 fixed	$F_{x\,joint\,A} =$	- 98.10 N	$\Delta x_{joint\,A}$
2	0°	90°	-	link 3 removed, drive 1 stopped	$F_{x\,joint\,A} =$	- 98.10 N	$\Delta x_{joint\,A}$
3	0°	-	0°	link 3 removed, link 5 fixed	$F_{z\,joint\,B} =$	98.10 N	$\Delta z_{joint\,B}$
4	0°	-	0°	link 3 removed, drive 1 stopped	$F_{z\,joint\,B} =$	98.10 N	$\Delta z_{joint\,B}$
5	0°	90°	0°	drive D0 fixed, drives 1,4 stopped	$F_{z\,TCP} =$	46.66 N	Δz_{TCP}
6	0°	90°	0°	drive D0 fixed, drives 1,4 stopped	$F_{x\,TCP} =$	46.66 N	Δx_{TCP}
7	0°	90°	0°	unmodified, drives active	$F_{y\,TCP} =$	- 11.53 N	Δy_{TCP}
8	0°	90°	0°	unmodified, drives active	$F_{y\,TCP} =$	11.53 N	Δy_{TCP}

Table 9-5: Measurement positions, displacements and loads for the identification of the stiffness parameters for the PARAGRIP stiffness model

9.7   Measurement and Model Data for the Identification of the PARAGRIP Stiffness Parameters

The measurements were performed with a dial indicator having a measurement resolution of 0.01 mm and repeated three times. The mean value and the band width of the measurement results are given.

load case	displacement	measured displacement	modeled displacement	$\Delta r_{abs\,e}$	$\Delta r_{rel\,e}$
1	$\Delta x_{joint\,A}$	- 1.90±0.03 mm	-1.870 mm	0.030 mm	0.016
2	$\Delta x_{joint\,A}$	- 2.36±0.01 mm	-2.333 mm	0.023 mm	0.013
3	$\Delta z_{joint\,B}$	0.16±0.01 mm	0.183 mm	0.022 mm	0.133
4	$\Delta z_{joint\,B}$	0.18±0.01 mm	0.210 mm	0.030 mm	0.166
5	Δz_{TCP}	2.82±0.02 mm	2.775 mm	0.045 mm	0.016
6	Δx_{TCP}	0.89±0.02 mm	0.956 mm	0.066 mm	0.074
7	Δy_{TCP}	-0.98±0.01 mm	-0.981 mm	0.001 mm	0.001
8	Δy_{TCP}	1.00±0.01 mm	0.981 mm	0.016 mm	0.016
mean				0.030 mm	0.055

Table 9-6: Measured and modeled displacement and the according deviations after the identification of the stiffness parameters for the PARAGRIP stiffness model

9.8   Load Cases for the Verification of the PARAGRIP Stiffness Model

The measurements were performed with an optical CMM with a minimum absolute accuracy of 0.15 mm.

e	φ_0	φ_1	φ_4	x_{TCP}	y_{TCP}	z_{TCP}	F_x	F_x	F_x
1	35.00°	45.00°	3.10°	0.7119 m	0.4985 m	0.2812 m	23.05 N	11.53 N	11.53 N
2	25.00°	47.85°	17.80°	0.7500 m	0.3497 m	0.4498 m	23.05 N	11.53 N	11.53 N
3	15.00°	57.70°	32.50°	0.6878 m	0.1843 m	0.6303 m	23.05 N	11.53 N	11.53 N
4	5.00°	91.29°	24.99°	0.5542 m	0.0485 m	0.6129 m	23.05 N	11.53 N	11.53 N
5	-5.00°	149.00°	45.99°	0.1320 m	-0.0115 m	0.6280 m	23.05 N	11.53 N	11.53 N
6	-15.00°	146.00°	26.51°	0.2578 m	-0.0691 m	0.4736 m	23.05 N	11.53 N	11.53 N
7	-25.00°	143.00°	6.99°	0.3066 m	-0.1430 m	0.2864 m	23.05 N	11.53 N	11.53 N
8	-35.00°	90.50°	5.05°	0.5054 m	-0.3539 m	0.4048 m	23.05 N	11.53 N	11.53 N

Table 9-7: Measurement positions and loads for the experimental verification of the PARAGRIP stiffness model

List of References

[ABB16]   ABB: *IRB 2400 Der beliebteste Industrieroboter*
            http://new.abb.com/products/robotics/de/industrieroboter/irb-2400 (last checked on
            14.10.2016).

[ABB17]   ABB: *IRC5 Controller*
            http://new.abb.com/products/en/3HAC020536-014/irc5-controller (last checked on 28.07.2017).

[ADI15]   Alff, S.; Detert, T.; Ingenlath, P.; Hüsing, M.; Corves, B.: *Aktive Verformung und Montage von flexi-
            blen Bauteilen mit einem Mehrarm-Robotersystem*
            In: Bertram, T. (Ed.), Fachtagung Mechatronik 2015, Dortmund, 2015, ISBN 978-3-00-048814-6, p.
            191–196.

[AEG08]   Albu-Schaffer, A.; Eiberger, O.; Grebenstein, M.; Haddadin, S.; Ott, C.; Wimbock, T.; Wolf, S.; Hir-
            zinger, G.: *Soft robotics*
            In: IEEE Robotics & Automation Magazine, 15 (2008) 3, p. 20–30, DOI 10.1109/MRA.2008.927979.

[AK16]   Almeida, D.; Karayiannidis, Y.: *Folding assembly by means of dual-arm robotic manipulation*
            In: IEEE (Ed.), Robotics and Automation (ICRA), 2016 IEEE International Conference, Stockholm,
            Sweden, 2016, ISBN 978-1-4673-8026-3, p. 3987–3993, DOI 10.1109/ICRA.2016.7487588.

[AN09]   Agheli, M. M.; Nategh, M. J.: *Identifying the kinematic parameters of hexapod machine tool*
            In: International Journal of Mechanical, Aerospace, Industrial, Mechatronic and Manufacturing En-
            gineering, 3 (2009) 4, p. 380–385.

[APA09]   Abtahi, M.; Pendar, H.; Alasty, A.; Vossoughi, G. R.: *Calibration of parallel kinematic machine tools
            using mobility constraint on the tool center point*
            In: The International Journal of Advanced Manufacturing Technology, 45 (2009) 5-6, p. 531–539,
            DOI 10.1007/s00170-009-1994-y.

[Arm91]   Armenàkas, A. E.: *Modern structural analysis,* The matrix method approach
            New York: McGraw-Hill, 1991, ISBN 9780070023482.

[AS05]   Alici, G.; Shirinzadeh, B.: *A systematic technique to estimate positioning errors for robot accuracy
            improvement using laser interferometry based sensing*
            In: Mechanism and Machine Theory, 40 (2005) 8, p. 879–906,
            DOI 10.1016/j.mechmachtheory.2004.12.012.

[ASG92]   Ananthanarayanan, S. P.; Szymczyk, C.; Goldenberg, A. A.: *Identification of kinematic parameters of
            multiple closed chain robotic manipulators working in coordination*
            In: IEEE (Ed.), Robotics and Automation (ICRA), IEEE 1992 International Conference, Nice, France,
            Oct. 1992, ISBN 0-8186-2720-4, p. 358–363, DOI 10.1109/ROBOT.1992.220313.

[BCB09]   Bonnemains, T.; Chanal, H.; Bouzgarrou, B.-C.; Ray, P.: *Stiffness Computation and Identification of
            Parallel Kinematic Machine Tools*
            In: Journal of Manufacturing Science and Engineering, 131 (2009) 4, p. 41013,
            DOI 10.1115/1.3160328.

[BDÜ17]   Bertelsmeier, F.; Detert, T.; Übelhör, T.; Schmitt, R.; Corves, B.: *Cooperating Robot Force Control
            for Positioning and Untwisting of large Components (submitted)*
            In: Journal of Robotics, (2017), DOI 10.1155/9140
            https://www.hindawi.com/journals/jr/.

[BH91]   Bennett, D.J.; Hollerbach, J. M.: *Autonomous calibration of single-loop closed kinematic chains
            formed by manipulators with passive endpoint constraints*
            In: IEEE Transactions on Robotics and Automation, 7 (1991) 5, p. 597–606, DOI 10.1109/70.97871.

[BH97]   Bonitz, R.G.; Hsia, T.C.: *Calibrating a multi-manipulator robotic system*
            In: Robotics & Automation Magazine, 4 (1997) 1, p. 18–22, DOI 10.1109/100.580975.

[BJB09]   Borgstrom, P.H.; Jordan, B.L.; Borgstrom, B.J.; Stealey, M.J.; Sukhatme, G. S.; Batalin, M.A.; Kaiser,
            W.J.: *NIMS-PL: A Cable-Driven Robot With Self-Calibration Capabilities*
            In: IEEE Transactions on Robotics, 25 (2009) 5, p. 1005–1015, DOI 10.1109/TRO.2009.2024792.

[BM89]   Borm, J.-H.; Menq, C.-H.: *Experimental study of observability of parameter errors in robot calibra-*
          tion
          In: IEEE (Ed.), Robotics and Automation (ICRA), IEEE 1989 International Conference, Scottsdale,
          1989, p. 587–592, DOI 10.1109/ROBOT.1989.100048.

[BM91]   Borm, J.-H.; Menq, C.-H.: *Determination of Optimal Measurement Configurations for Robot Calibra-*
          tion Based on Observability Measure
          In: The International Journal of Robotics Research, 10 (1991) 1, p. 51–63,
          DOI 10.1177/027836499101000106.

[BMH16]   Bai, P.; Mei, J.; Huang, T.; Chetwynd, D. G.: *Kinematic calibration of Delta robot using distance*
          measurements
          In: Proceedings of the Institution of Mechanical Engineers, Part C: Journal of Mechanical Engineer-
          ing Science, 230 (2016) 3, p. 414–424, DOI 10.1177/0954406215603739.

[BPB12]   Bondarenko, D.; Pashkevich, A.; Briot, S.; Ritou, M.; Furet, B.: *Elasto-Dynamic Model of Robotic*
          Milling Process Considering Interaction Between Tool and Workpiece
          In: ASME (Ed.), Engineering Systems Design and Analysis (ESDA), ASME 2012 11th Biennial Confer-
          ence on, Nantes, France, 2012, p. 217–226.

[BPC11]   Briot, S.; Pashkevich, A.; Chablat, D.: *Reduced Elastodynamic Modelling of Parallel Robots for the*
          Computation of their Natural Frequencies
          In: IFToMM (Ed.), 13th World Congress in Mechanism and Machine Science, Guanajuato, México,
          2011, ISBN 9781629930770, p. 1–8.

[Cab14 Dt] Cabezuelo, L.: *Validation of a stiffness model for the multi-arm robotic system PARAGRIP,* Master
          thesis, supervised by Detert, Tim, Aachen: RWTH Aachen University, Department of Mechanism
          Theory and Dynamics of Machines, 2014.

[Cam12]   Cammarata, A.: *On the Stiffness Analysis and Elastodynamics of Parallel Kinematic Machines*
          In: Kucuk, S. (Ed.), Serial and Parallel Robot Manipulators - Kinematics, Dynamics, Control and Op-
          timization, Online DOI: 10.5772/2301: InTech, 2012, ISBN 978-953-51-0437-7, DOI 10.5772/31891.

[CDM09]   Courteille, E.; Deblaise, D.; Maurine, P.: *Design optimization of a Delta-like parallel robot through*
          global stiffness performance evaluation
          In: IEEE/RSJ (Ed.), Intelligent Robots and Systems (IROS), 2009 IEEE/RSJ International Conference
          on, St. Louis Riverfront, 2009, p. 5159–5166, DOI 10.1109/IROS.2009.5353906.

[Che00]   Chen, S.-F.: *Conservative Congruence Transformation for Joint and Cartesian Stiffness Matrices of*
          Robotic Hands and Fingers
          In: The International Journal of Robotics Research, 19 (2000) 9, p. 835–847,
          DOI 10.1177/02783640022067201.

[CLC14]   Chen-Gang; Li-Tong; Chu-Ming; Xuan, J.-Q.; Xu, S.-H.: *Review on kinematics calibration technology*
          of serial robots
          In: International Journal of Precision Engineering and Manufacturing, 15 (2014) 8, p. 1759–1774,
          DOI 10.1007/s12541-014-0528-1.

[CLH11]   Chiang, M.-H.; Lin, H.-T.; Hou, C.-L.: *Development of a stereo vision measurement system for a 3D*
          three-axial pneumatic parallel mechanism robot arm
          In: Sensors, 11 (2011) 2, p. 2257–2281, DOI 10.3390/s110202257.

[CMR11]   Corves, B.; Mannheim, T.-P.; Riedel, M.: *Re-grasping : Improving Capability for Multi-Arm-Robot-*
          System by Dynamic Reconfiguration
          In: Hutchison, D. and others (Ed.), Intelligent Robotics and Applications (ICIRA), Proceedings 4th In-
          ternational Conference, Aachen, Germany, 2011, ISBN 978-3-642-25485-7, p. 132–141.

[CP04]   Chiu, Y.-J.; Perng, M.-H.: *Self-calibration of a general hexapod manipulator with enhanced precision*
          in 5-DOF motions
          In: Mechanism and Machine Theory, 39 (2004), p. 1–23, DOI 10.1016/S0094-114X(03)00101-0.

[CU16]   Caccavale, F.; Uchiyama, M.: *Cooperative Manipulation*
          In: Siciliano, B.; Khatib, O. (Ed.), Springer Handbook of Robotics, Cham: Springer International Pub-
          lishing, 2016, ISBN 978-3-319-32550-7, p. 989–1006, DOI 10.1007/978-3-319-32552-1_39.

[CWL14]   Chen, G.; Wang, H.; Lin, Z.: *Determination of the Identifiable Parameters in Robot Calibration Based on the POE Formula*
In: IEEE Transactions on Robotics, 30 (2014) 5, p. 1066–1077, DOI 10.1109/TRO.2014.2319560.

[CZW11]   Cheng, L.; Zhao, Y.; Wang, H.: *Dynamic measurement of the positioning accuracy of redundantly actuated parallel machine tool*
In: IEEE (Ed.), Intelligent Control and Information Processing (ICICIP), 2011 2nd International Conference, Harbin, China, 2011, ISBN 978-1-4577-0813-8, p. 634–639, DOI 10.1109/ICICIP.2011.6008327.

[DAC06]   Daney, D.; Andreff, N.; Chabert, G.; Papegay, Y.: *Interval method for calibration of parallel robots: Vision-based experiments*
In: Mechanism and Machine Theory, 41 (2006) 8, p. 929–944, DOI 10.1016/j.mechmachtheory.2006.03.014.

[Dah08]   Dahmen, W.: *Numerik für Ingenieure und Naturwissenschaftler*
Berlin, Heidelberg: Springer-Verlag Berlin Heidelberg, 2008, ISBN 978-3-540-76493-9.

[Dan99]   Daney, D.: *Self calibration of Gough platform using leg mobility constraints*
In: IFToMM (Ed.), World Congress on the Theory of Machines and Mechanisms, Oulu, Finland, 1999, p. 104–109.

[DC16]   Detert, T.; Corves, B.: *Extended procedure for stiffness modeling based on the Matrix Structure Analysis*
In: Corves, B. and others (Ed.), New Advances in Mechanisms, Mechanical Transmissions and Robotics, Proceedings of The Joint International Conference of the XII International Conference on Mechanisms and Mechanical Transmissions (MTM) and the XXIII International Conference on Robotics (Robotics '16), Aachen, 2016, ISBN 978-3-319-45450-4, p. 299–310, DOI 10.1007/978-3-319-45450-4_30.

[DCC10]   Dumas, C.; Caro, S.; Chérif, M.; Garnier, S.; Furet, B.: *A methodology for joint stiffness identification of serial robots*
In: IEEE/RSJ (Ed.), Intelligent Robots and Systems (IROS), 2010 IEEE/RSJ International Conference on, Taipei, 2010, ISBN 978-1-4244-6674-0, p. 464–469, DOI 10.1109/IROS.2010.5652140.

[DCG08]   Daidié, A.; Chaib, Z.; Ghosn, A.: *3D Simplified Finite Elements Analysis of Load and Contact Angle in a Slewing Ball Bearing*
In: Journal of Mechanical Design, 130 (2008) 8, p. 82601, DOI 10.1115/1.2918915.

[DDS05]   Dong, W.; Du, Z.; Sun, L.: *Stiffness influence atlases of a novel flexure hinge-based parallel mechanism with large workspace*
In: IEEE/RSJ (Ed.), Intelligent Robots and Systems (IROS), IEEE/RSJ 2005 International Conference, Edmonton, Alta., Canada, 2005, p. 856–861, DOI 10.1109/IROS.2005.1545078.

[DH55]   Denavit, J.; Hartenberg, R. S.: *A kinematic notation for lower-pair mechanisms based on matrices*
In: ASME Journal of Applied Mechanics, 22 (1955), p. 215–221.

[DHM06]   Deblaise, D.; Hernot, X.; Maurine, P.: *A systematic analytical method for PKM stiffness matrix calculation*
In: IEEE (Ed.), Robotics and Automation (ICRA), 2006 IEEE International Conference, Orlando, FL, USA, 2006, p. 4213–4219, DOI 10.1109/ROBOT.2006.1642350.

[Die05]   Dieker, S.: *Elementare Festigkeitslehre im Leichtbau*
Bremen: Donat, 2005, ISBN 978-3924444587.

[DMH14]   Detert, T.; Mannheim, T.-P.; Hüsing, M.; Corves, B.: *Improving the accuracy of a Multi-Arm-Robot-System by parameter identification of the single arms*
In: Key Engineering Materials, 613 (2014), p. 428–439.

[DP90]   Driels, M. R.; Pathre, U. S.: *Significance of observation strategy on the design of robot calibration experiments*
In: Journal of Robotic Systems, 7 (1990) 2, p. 197–223, DOI 10.1002/rob.4620070206.

[DPM05]   Daney, D.; Papegay, Y.; Madeline, B.: *Choosing Measurement Poses for Robot Calibration with the Local Convergence Method and Tabu Search*
In: The International Journal of Robotics Research, 24 (2005) 6, p. 501–518,
DOI 10.1177/0278364905053185.

[DPN04]   Daney, D.; Papegay, Y.; Neumaier, A.: *Interval methods for certification of the kinematic calibration of parallel robots*
In: IEEE (Ed.), Robotics and Automation (ICRA), IEEE 2004 International Conference, New Orleans, LA, USA, 2004, ISBN 0-7803-8232-3, 1913-1918 Vol.2, DOI 10.1109/ROBOT.2004.1308103.

[DTL12]   Dhatt, G.; Touzot, G.; Lefrançois, E.: *Finite Element Method*
Hoboken, NJ, USA: John Wiley & Sons, Inc, 2012, ISBN 9781118569764,
DOI 10.1002/9781118569764.

[DZ13]   Du, G.; Zhang, P.: *Online robot calibration based on vision measurement*
In: Robotics and Computer-Integrated Manufacturing, 29 (2013) 6, p. 484–492,
DOI 10.1016/j.rcim.2013.05.003
http://www.sciencedirect.com/science/article/pii/S0736584513000422.

[Eco10]   Ecorchard, G.: *Static accuracy enhancement of redundantly actuated parallel kinematic machine tools,* Doctoral Thesis, Chemnitz: Technische Universität Chemnitz, Institut für Werkzeugmaschinen und Produktionsprozesse, 2010.

[EF99]   El-Khasawneh, B. S.; Ferreira, P. M.: *Computation of stiffness and stiffness bounds for parallel link manipulators*
In: International Journal of Machine Tools and Manufacture, 39 (1999) 2, p. 321–342,
DOI 10.1016/S0890-6955(98)00039-X.

[EGZ04]   Elatta, A. Y.; Gen, L. P.; Zhi, F. L.; Daoyuan, Y.; Fei, L: *An Overview of Robot Calibration*
In: Information Technology Journal, 3 (2004), p. 74–78, DOI 10.1109/JRA.1987.1087124.

[EL88]   Everett, L. J.; Lin, C. Y.: *Kinematic calibration of manipulators with closed loop actuated joints*
In: IEEE (Ed.), Robotics and Automation (ICRA), 1988 IEEE International Conference, Philadelphia, PA, USA, 1988, ISBN 0-8186-0852-8, p. 792–797, DOI 10.1109/ROBOT.1988.12155.

[EM05]   Ecorchard, G.; Maurine, P.: *Self-calibration of delta parallel robots with elastic deformation compensation*
In: IEEE/RSJ (Ed.), Intelligent Robots and Systems (IROS), IEEE/RSJ 2005 International Conference, Edmonton, Alta., Canada, 2005, p. 1283–1288, DOI 10.1109/IROS.2005.1545024.

[Eur98]   European Committee for Standardization: *Manipulating industrial robots – Performance criteria and related test methods*
Standard: European Standard EN ISO 9283, 1998.

[Eve89]   Everett, L. J.: *Forward Calibration of Closed-Loop Jointed Manipulators*
In: The International Journal of Robotics Research, 8 (1989) 4, p. 85–91,
DOI 10.1177/027836498900800405.

[EVL14]   Elsayed, Y.; Vincensi, A.; Lekakou, C.; Geng, T.; Saaj, C. M.; Ranzani, T.; Cianchetti, M.; Menciassi, A.: *Finite Element Analysis and Design Optimization of a Pneumatically Actuating Silicone Module for Robotic Surgery Applications*
In: Soft Robotics, 1 (2014) 00, p. 255–262, DOI 10.1089/soro.2014.0016.

[GB93]   Goswami, A.; Bosnik, J. R.: *On a Relationship Between the Physical Features of Robotic Manipulators and the Kinematic Parameters Produced by Numerical Calibration*
In: Journal of Mechanical Design, 115 (1993) 4, p. 892–900, DOI 10.1115/1.2919284.

[GC08]   Gonçalves, R. S.; Carvalho, J. C. M.: *Stiffness Analysis of Parallel Manipulator Using Matrix Structural Analysis*
In: Ceccarelli, M. (Ed.), Proceedings of EUCOMES 08, The Second European Conference on Mechanism Science, Cassino, Italy, 2008, ISBN 978-1-4020-8914-5, p. 255–262, DOI 10.1007/978-1-4020-8915-2_31.

[GCH16]   Gao, C.; Cong, D.; Han, J.; Yang, Z.; Wang, X.: *Self-calibration of a 6-DOF redundantly actuated parallel mechanism*
          In: IEEE (Ed.), Mechatronics and Automation, 2016 IEEE International Conference, Harbin, Heilongjiang, China, 2016, ISBN 978-1-5090-2396-7, p. 128–132, DOI 10.1109/ICMA.2016.7558547.

[GDD14]   Gan, Y.; Dai, X.; Dong, D.: *Robot Calibration for Cooperative Process under Typical Installation*
          In: Journal of Applied Mathematics, 2014 (2014) 4, p. 1–12, DOI 10.1155/2014/576420.

[GEF10]   Ghasemi, A.; Eghtesad, M.; Farid, M.: *Neural Network Solution for Forward Kinematics Problem of Cable Robots*
          In: Journal of Intelligent & Robotic Systems, 60 (2010) 2, p. 201–215, DOI 10.1007/s10846-010-9421-z.

[GH88]   Goldberg, D. E.; Holland, J. H.: *Genetic Algorithms in Search, Optimization & Machine Learning*
          In: Machine Learning, 3 (1988) 2/3, p. 95–99, DOI 10.1023/A:1022602019183.

[GL07]   Gosselin, C.; Li, S.: *Stiffness Analysis of 3-RRR Planar Parallel Mechanisms Based on CCT*
          In: IFToMM (Ed.), 12th IFToMM World Congress, Proceedings, Besançon (France), 2007.

[GLW07]   Gatla, C. S.; Lumia, R.; Wood, J.; Starr, G.: *Calibration of industrial robots by magnifying errors on a distant plane*
          In: IEEE/RSJ (Ed.), Intelligent Robots and Systems (IROS), 2007 IEEE/RSJ International Conference, San Diego, CA, 2007, ISBN 978-1-4244-0912-9, p. 3834–3841, DOI 10.1109/IROS.2007.4398969.

[GM11]   Ginani, L. S.; Motta, M. S. T. J.: *Theoretical and practical aspects of robot calibration with experimental verification*
          In: Journal of the Brazilian Society of Mechanical Sciences and Engineering, 33 (2011), p. 15–21
          http://www.scielo.br/scielo.php?script=sci_arttext&pid=S1678-58782011000100003&nrm=iso.

[Gos90]   Gosselin, C.: *Stiffness mapping for parallel manipulators*
          In: IEEE Transactions on Robotics and Automation, 6 (1990) 3, p. 377–382, DOI 10.1109/70.56657.

[Got14]   Gottlieb, J.: *Non-parametric calibration of a stewart platform*
          In: Proceedings of 2014 Workshop on Fundamental Issues and Future Research Directions for Parallel Mechanisms and Manipulators, Tianjin, 2014.

[GP12]   Guo, Y.; Parker, R. G.: *Stiffness matrix calculation of rolling element bearings using a finite element/contact mechanics model*
          In: Mechanism and Machine Theory, 51 (2012), p. 32–45,
          DOI 10.1016/j.mechmachtheory.2011.12.006.

[Guo15 Dt] Guo, J.: *Simulation und Analyse erreichbarer Genauigkeiten bei der Objektintegration,* Bachelor Thesis, supervised by Detert, Tim, Aachen: RWTH Aachen University, Department of Mechanism Theory and Dynamics of Machines, 2015.

[GWS14]   Gross, D.; Wall, W. A.; Schröder, J.: *Technische Mechanik*
          Berlin: Springer, 12. Edition, 2014, ISBN 978-3642409653, DOI 10.1007/978-3-642-40966-0.

[HHK02]   Huang, C.; Hung, W.-H.; Kao, I.: *New conservative stiffness mapping for the Stewart-Gough platform*
          In: IEEE (Ed.), Robotics and Automation (ICRA), IEEE 2002 International Conference, Washington, DC, USA, 2002, p. 823–828, DOI 10.1109/ROBOT.2002.1013459.

[HKG16]   Hollerbach, J. M.; Khalil, W.; Gautier, M.: *Model Identification*
          In: Siciliano, B.; Khatib, O. (Ed.), Springer Handbook of Robotics, Cham: Springer International Publishing, 2016, ISBN 978-3-319-32550-7, p. 113–138, DOI 10.1007/978-3-319-32552-1_6.

[HL95]   Hollerbach, J. M.; Lokhorst, D. M.: *Closed-loop kinematic calibration of the RSI 6-DOF hand controller*
          In: IEEE Transactions on Robotics and Automation, 11 (1995) 3, p. 352–359,
          DOI 10.1109/70.388777.

[HLJ10]   Hernández Martínez, E. E.; López Cajún, C. S.; Jáuregui Correa, J. C.: *Calibration of Parallel Manipulators and their Application to Machine Tools - A State of the Art Survey*
          In: Ingeniería Investigación y Tecnología, XI (2010) 2, p. 141–154
          http://repositoriodigital.academica.mx/jspui/handle/987654321/12661.

[HLS14]   He, R.; Li, X.; Shi, T.; Wu, B.; Zhao, Y.; Han, F.; Yang, S.; Huang, S.; Yang, S.: *A kinematic calibration method based on the product of exponentials formula for serial robot using position measurements*
In: Robotica, (2014), p. 1–19, DOI 10.1017/S026357471400071X.

[HLZ09]   Huang, Z.; Liu, J.; Zeng, D.: *A general methodology for mobility analysis of mechanisms based on constraint screw theory*
In: Science in China Series E: Technological Science, (2009) 5, p. 1337–1347.

[HM85]   Hayati, S.; Mirmirani, M.: *Improving the absolute positioning accuracy of robot manipulators*
In: Journal of Robotic Systems, (1985) 2, p. 397–413, DOI 10.1002/rob.4620020406
http://onlinelibrary.wiley.com/doi/10.1002/rob.4620020406/abstract.

[HN09]   Horne, A.; Notash, L.: *Comparison of Pose Selection Criteria for Kinematic Calibration through Simulation*
In: Kecskeméthy, A.; Müller, A. (Ed.), Computational Kinematics, Berlin, Heidelberg: Springer Berlin Heidelberg, 2009, ISBN 978-3-642-01946-3, p. 291–298, DOI 10.1007/978-3-642-01947-0_36.

[HSG00]   Hernot, X.; Sartor, M.; Guillot, J.: *Calculation of the Stiffness Matrix of Angular Contact Ball Bearings by Using the Analytical Approach*
In: Journal of Mechanical Design, 122 (2000) 1, p. 83, DOI 10.1115/1.533548.

[HW96]   Hollerbach, J. M.; Wampler, C. W.: *The Calibration Index and Taxonomy for Robot Kinematic Calibration Methods*
In: The International Journal of Robotics Research, 15 (1996) 6, p. 573–591,
DOI 10.1177/027836499601500604.

[Int14]   International Organization for Standardization: *Test code for machine tools - Part 2: Determination of accuracy and repeatability of positioning of numerically controlled axes*
Standard: International Standard ISO 230-2, 2014.

[IP03]   Iuraşcu, C. C.; Park, F. C.: *Geometric Algorithms for Kinematic Calibration of Robots Containing Closed Loops*
In: Journal of Mechanical Design, 125 (2003), p. 23–32, DOI 10.1115/1.1539512.

[JB13]   Joubair, A.; Bonev, I. A.: *Comparison of the efficiency of five observability indices for robot calibration*
In: Mechanism and Machine Theory, 70 (2013), p. 254–265,
DOI 10.1016/j.mechmachtheory.2013.07.015.

[JB15]   Joubair, A.; Bonev, I. A.: *Kinematic calibration of a six-axis serial robot using distance and sphere constraints*
In: The International Journal of Advanced Manufacturing Technology, 77 (2015) 1-4, p. 515–523,
DOI 10.1007/s00170-014-6448-5.

[JSS09]   Jordt, A.; Siebel, N. T.; Sommer, G.: *Automatic high-precision self-calibration of camera-robot systems*
In: IEEE (Ed.), Robotics and Automation (ICRA), IEEE 2009 International Conference, Kobe, 2009, ISBN 1424427886, p. 1244–1249, DOI 10.1109/ROBOT.2009.5152570.

[JTB16]   Joubair, A.; Tahan, A. S.; Bonev, I. A.: *Performances of observability indices for industrial robot calibration*
In: IEEE/RSJ (Ed.), Intelligent Robots and Systems (IROS), 2016 IEEE/RSJ International Conference, Daejeon, South Korea, 2016, p. 2477–2484, DOI 10.1109/IROS.2016.7759386.

[JZB15]   Joubair, A.; Zhao, L. F.; Bigras, P.; Bonev, I. A.: *Absolute accuracy analysis and improvement of a hybrid 6-DOF medical robot*
In: Industrial Robot: An International Journal, 42 (2015) 1, p. 44–53, DOI 10.1108/IR-09-2014-0396.

[JZB16]   Joubair, A.; Zhao, L. F.; Bigras, P.; Bonev, I. A.: *Use of a Force-Torque Sensor for Self-Calibration of a 6-DOF Medical Robot*
In: Sensors, 16 (2016) 6, DOI 10.3390/s16060798.

[KB99]   Khalil, W.; Besnard, S.: *Self calibration of Stewart-Gough parallel robots without extra sensors*
In: IEEE Transactions on Robotics and Automation, 15 (1999) 6, p. 1116–1121,
DOI 10.1109/70.817674.

[KFC15]   Klimchik, A.; Furet, B.; Caro, S.; Pashkevich, A.: *Identification of the manipulator stiffness model parameters in industrial environment*
In: Mechanism and Machine Theory, 90 (2015), p. 1–22,
DOI 10.1016/j.mechmachtheory.2015.03.002.

[KHC15]   Kurtenbach, S.; Hüsing, M.; Corves, B.: *Modular System with Varying Contact Elements for a Reconfigurable Parallel Robot*
In: Bai, S.; Ceccarelli, M. (Ed.), Recent Advances in Mechanism Design for Robotics, Proceedings of the 3rd IFToMM Symposium on Mechanism Design for Robotics, Aalborg, Denmark, 2015, ISBN 978-3-319-18125-7, p. 307–315, DOI 10.1007/978-3-319-18126-4_29.

[KHL06]   Kang, Y.; Huang, C.-C.; Lin, C.-S.; Shen, P.-C.; Chang, Y.-P.: *Stiffness determination of angular-contact ball bearings by using neural network*
In: Tribology International, 39 (2006) 6, p. 461–469, DOI 10.1016/j.triboint.2005.02.005.

[KHO11]   Kotlarski, J.; Heimann, B.; Ortmaier, T.: *Experimental validation of the influence of kinematic redundancy on the pose accuracy of parallel kinematic machines*
In: IEEE (Ed.), Robotics and Automation (ICRA), 2011 IEEE International Conference, Shanghai, China, 2011, ISBN 978-1-61284-385-8, p. 1923–1929, DOI 10.1109/ICRA.2011.5980056.

[KL80]   Klema, V.; Laub, A.: *The singular value decomposition,* Its computation and some applications
In: IEEE Transactions on Automatic Control, 25 (1980) 2, p. 164–176,
DOI 10.1109/TAC.1980.1102314.

[Kle11]   Klein, B.: *Toleranzmanagement,* Dimensionelle und geometrische Produktspezifizierung
Kassel: Universität Kassel, 2011.

[Kle15]   Klein, B.: *FEM,* Grundlagen und Anwendungen der Finite-Element-Methode im Maschinen- und Fahrzeugbau
Wiesbaden: Springer Vieweg, 10. Edition, 2015, ISBN 3658060549.

[KMA16]   Klimchik, A.; Magid, E.; Afanasyev, I.; Pashkevich, A.: *Comparison of Serial and Quasi-Serial Industrial Robots for Isotropic Tasks*
In: Parenti-Castelli, V.; Schiehlen, W. (Ed.), ROMANSY 21 - Robot Design, Dynamics and Control, Proceedings of the 21st CISM-IFToMM Symposium, Udine, Italy, 2016, ISBN 978-3-319-33713-5, p. 421–429, DOI 10.1007/978-3-319-33714-2_47.

[KMC16]   Klimchik, A.; Magid, E.; Caro, S.; Waiyakan, K.; Pashkevich, A.; Sikora, A.; Choi, B.; Wang, S.: *Stiffness of serial and quasi-serial manipulators,* Comparison analysis
In: MATEC Web of Conferences, 75 (2016), p. 2003, DOI 10.1051/matecconf/20167502003.

[KPC13]   Klimchik, A.; Pashkevich, A.; Chablat, D.: *CAD-based approach for identification of elasto-static parameters of robotic manipulators*
In: Finite Elements in Analysis and Design, 75 (2013), p. 19–30, DOI 10.1016/j.finel.2013.06.008.

[KPL06]   Kim, T. S.; Park, K. W.; Lee, M. K.: *Study on observability of a parallel-typed machining center using a single planar table and digital indicators*
In: Mechanism and Machine Theory, 41 (2006) 10, p. 1147–1156,
DOI 10.1016/j.mechmachtheory.2005.12.005.

[KSS11]   Krüger, J.; Schreck, G.; Surdilovic, D.: *Dual arm robot for flexible and cooperative assembly*
In: CIRP Annals - Manufacturing Technology, 60 (2011) 1, p. 5–8, DOI 10.1016/j.cirp.2011.03.017.

[KUK16]   KUKA Systems Aerospace France: *Usine Agile 4.0: Cooperative Manipulation*
https://www.youtube.com/watch?v=yx1lJkPRAf4 (last checked on 28.07.2016).

[KUK17]   KUKA AG: *KR 40 PA*
https://www.kuka.com/en-de/products/robot-systems/industrial-robots/kr-40-pa (last checked on 31.07.2017).

[Kur16]   Kurtenbach, S.: *Modularer Handgelenkbaukasten zum flexiblen, rekonfigurierbaren Bauteilhandling mit einem Mehrarmrobotersystem,* = Modular system of wrist joints for flexible, reconfigurable object manipulation with a multi arm robot system
Aachen: Apprimus Verlag, 1. Edition, 2016, ISBN 978-3-86359-489-3.

[KWD13]   Klimchik, A.; Wu, Y.; Dumas, C.; Caro, S.; Furet, B.; Pashkevich, A.: *Identification of geometrical and elastostatic parameters of heavy industrial robots*
In: IEEE (Ed.), Robotics and Automation (ICRA), 2013 IEEE International Conference, Karlsruhe, Germany, 2013, p. 3707–3714, DOI 10.1109/ICRA.2013.6631098.

[KYH08]   Kurbanhusen Mustafa, S.; Yang, G.; Huat Yeo, S.; Lin, W.; Chen, I.-M.: *Self-Calibration of a Biologically Inspired 7 DOF Cable-Driven Robotic Arm*
In: Mechatronics, IEEE/ASME Transactions on, 13 (2008) 1, p. 66–75, DOI 10.1109/TMECH.2007.915024.

[LHS08]   Lightcap, C.; Hamner, S.; Schmitz, T.; Banks, S.: *Improved Positioning Accuracy of the PA10-6CE Robot with Geometric and Flexibility Calibration*
In: IEEE Transactions on Robotics, 24 (2008) 2, p. 452–456, DOI 10.1109/TRO.2007.914003.

[LL05]   Liew, H.-V.; Lim, T. C.: *Analysis of time-varying rolling element bearing characteristics*
In: Journal of Sound and Vibration, 283 (2005) 3-5, p. 1163–1179, DOI 10.1016/j.jsv.2004.06.022.

[LLN10]   Liu, Y.; Liu, H.; Ni, F.; Xu, W.; Han, F.: *Self-calibration of a Stewart Parallel Robot with a Laserranger*
In: Liu, H. and others (Ed.), Intelligent Robotics and Applications (ICIRA), Proceedings 3rd International Conference, Shanghai, China, 2010, ISBN 978-3-642-16583-2, p. 570–581, DOI 10.1007/978-3-642-16584-9_55.

[Lon87]   Loncaric, J.: *Normal forms of stiffness and compliance matrices*
In: IEEE Journal on Robotics and Automation, 3 (1987) 6, p. 567–572, DOI 10.1109/JRA.1987.1087148.

[LRH10]   Last, P.; Raatz, A.; Hesselbach, J.: *Calibration of Parallel Kinematic Structures – Overview, Classification and Comparison*
Berlin, Heidelberg: Springer, 2010, ISBN 978-3-642-16784-3, DOI 10.1007/978-3-642-16785-0_6.

[LRW98]   Lagarias, J. C.; Reeds, J. A.; Wright, M. H.; Wright, P. E.: *Convergence Properties of the Nelder-Mead Simplex Method in Low Dimensions*
In: SIAM Journal on Optimization, 9 (1998) 1, p. 112–147, DOI 10.1137/S1052623496303470.

[LSS15]   Lian, B.; Sun, T.; Song, Y.; Jin, Y.; Price, M.: *Stiffness analysis and experiment of a novel 5-DoF parallel kinematic machine considering gravitational effects*
In: International Journal of Machine Tools and Manufacture, 95 (2015), p. 82–96, DOI 10.1016/j.ijmachtools.2015.04.012.

[LSS16]   Lian, B.; Sun, T.; Song, Y.; Wang, X.: *Passive and active gravity compensation of horizontally-mounted 3-R P S parallel kinematic machine*
In: Mechanism and Machine Theory, 104 (2016), p. 190–201, DOI 10.1016/j.mechmachtheory.2016.05.021.

[LWW02]   Li, Y.-W.; Wang, J.-S.; Wang, L.-P.: *Stiffness analysis of a Stewart platform-based parallel kinematic machine*
In: IEEE (Ed.), Robotics and Automation (ICRA), IEEE 2002 International Conference, Washington, DC, USA, 2002, p. 3672–3677, DOI 10.1109/ROBOT.2002.1014280.

[Mar66]   Martin, H. C.: *Introduction to matrix methods of structural analysis*
New York [u.a.]: McGraw-Hill, 1966, ISBN 9780070406339.

[Mat16]   MathWorks, Inc.: *Generalized minimum residual method (with restarts)*
http://de.mathworks.com/help/matlab/ref/gmres.html (last checked on 31.07.2017).

[Mat17a]   MathWorks, Inc.: *How the Genetic Algorithm Works*
https://de.mathworks.com/help/gads/how-the-genetic-algorithm-works.html (last checked on 31.07.2017).

[Mat17b]   MathWorks, Inc.: *fminsearch Algorithm*
https://de.mathworks.com/help/matlab/math/optimizing-nonlinear-functions.html#bsgpq6p-11 (last checked on 31.07.2017).

[MCR05]   M'Barek, T.; Corves, B.; Riedel, M.; Nefzi, M.; Hüsing, M.: *Parallelkinematisches Greifsystem zum Greifen und Handhaben*
Patent DE 10 2005 059 349 A1, 16.06.2007, B25J 15/00.

[MdM01]   Motta, M. S. T. J.; de Carvalho, G. C.; McMaster, R. S.: *Robot calibration using a 3D vision-based measurement system with a single camera*
In: Robotics and Computer-Integrated Manufacturing, 17 (2001) 6, p. 487–497,
DOI 10.1016/S0736-5845(01)00024-2.

[Mer06]   Merlet, J.-P.: *Parallel robots*
Dordrecht: Springer, 2006, ISBN 978-1-4020-4133-4.

[Mer09]   Merlet, J.-P.: *Interval Analysis for Certified Numerical Solution of Problems in Robotics*
In: International Journal of Applied Mathematics and Computer Science, 19 (2009) 3,
DOI 10.2478/v10006-009-0033-3.

[Met06]   Metris: *K-Series Reference Manual,* 2006
http://www.nikonmetrology.com/en_US/Products/Portable-Measuring/Optical-CMM/K-Series-Optical-CMM (last checked on 13.12.2016).

[MGW07]   Majou, F.; Gosselin, C.; Wenger, P.; Chablat, D.: *Parametric stiffness analysis of the Orthoglide*
In: Mechanism and Machine Theory, 42 (2007) 3, p. 296–311,
DOI 10.1016/j.mechmachtheory.2006.03.018.

[MJZ96]   Masory, O.; Jiang, W.; Zhuang, H.: *Kinematic modeling and calibration of a Stewart platform*
In: Advanced Robotics, 11 (1996) 5, p. 519–539, DOI 10.1163/156855397X00191.

[MKA14]   Michalos, G.; Kaltsoukalas, K.; Aivaliotis, P.; Sipsas, P.; Sardelis, A.; Chryssolouris, G.: *Design and simulation of assembly systems with mobile robots*
In: CIRP Annals - Manufacturing Technology, 63 (2014) 1, p. 181–184,
DOI 10.1016/j.cirp.2014.03.102.

[MLS94]   Murray, R. M.; Li, Z.; Sastry, S. S.; Sastry, S. S.: *A mathematical introduction to robotic manipulation*
Berkeley: CRC press, 1994, ISBN 0849379814.

[MM08]   Marie, S.; Maurine, P.: *Elasto-geometrical modelling of closed-loop industrial robots used for machining applications*
In: IEEE (Ed.), Robotics and Automation (ICRA), IEEE 2008 International Conference, Pasadena, CA, USA, 2008, ISBN 978-1-4244-1646-2, p. 1294–1300, DOI 10.1109/ROBOT.2008.4543382.

[MME12]   Makris, S.; Michalos, G.; Eytan, A.; Chryssolouris, G.: *Cooperating Robots for Reconfigurable Assembly Operations,* Review and Challenges
In: Procedia CIRP, 3 (2012), p. 346–351, DOI 10.1016/j.procir.2012.07.060.

[MR12]   Müller, A.; Ruggiu, M.: *Self-Calibration of Redundantly Actuated PKM Based on Motion Reversal Points*
In: Latest Advances in Robot Kinematics, (2012), p. 75–82, DOI 10.1007/978-94-007-4620-6_10.

[MRD91]   Mooring, B.; Roth, Z. S.; Driels, M. R.: *Fundamentals of manipulator calibration*
New York: Wiley, 1991, ISBN 0471508640.

[MRH13]   Mannheim, T.-P.; Riedel, M.; Hüsing, M.; Corves, B.: *A New Way of Grasping: PARAGRIP—The Fusion of Gripper and Robot*
In: Carbone, G. (Ed.), Grasping in Robotics, London: Springer London, 2013, ISBN 978-1-4471-4664-3, p. 433–464, DOI 10.1007/978-1-4471-4664-3_17.

[MSF16]   Mirrazavi, S.; Seyed, S.; Figueroa, F.; Nadia, B.; Billard, A.: *Coordinated multi-arm motion planning: Reaching for moving objects in the face of uncertainty*
In: 2016 Robotics: Science and Systems Conference, Arbor, Michigan, USA, 2016.

[MSS10]   Majarena, A. C.; Santolaria, J.; Samper, D.; Aguilar, J. J.: *An Overview of Kinematic and Calibration Models Using Internal or External Sensors or Constraints to Improve the Behavior of Spatial Parallel Mechanisms*
In: Sensors, 10 (2010) 11, p. 10256–10297, DOI 10.3390/s101110256.

[MTW03]   Meng, G.; Tiemin, L.; Wensheng, Y.: *Calibration method and experiment of Stewart platform using a laser tracker*
In: IEEE Systems, Man and Cybernetics, 3 (2003), p. 2797–2802,
DOI 10.1109/ICSMC.2003.1244309.

[MWZ93]   Masory, O.; Wang, J.; Zhuang, H.: *On the accuracy of a Stewart platform. II. Kinematic calibration and compensation*
In: IEEE Journal on Robotics and Automation, - (1993), p. 725–731,
DOI 10.1109/ROBOT.1993.292064.

[NB13]   Nubiola, A.; Bonev, I. A.: *Absolute calibration of an ABB IRB 1600 robot using a laser tracker*
In: Robotics and Computer-Integrated Manufacturing, 29 (2013) 1, p. 236–245,
DOI 10.1016/j.rcim.2012.06.004.

[NBH00]   Newman, W. S.; Birkhimer, C. E.; Horning, R. J.; Wilkey, A. T.: *Calibration of a Motoman P8 robot based on laser tracking*
In: IEEE (Ed.), Robotics and Automation (ICRA), IEEE 2000 International Conference, San Francisco, CA, 2000, ISBN 0-7803-5886-4, p. 3597–3602, DOI 10.1109/ROBOT.2000.845292.

[NCH08]   Nefzi, M.; Corves, B.; Hüsing, M.; Renders, S.: *Kalibrierung eines Parallelroboters mit dem Freiheitsgrad fünf vor dem Einsatz in einer Nähanlage*
In: VDI/VDE (Ed.), VDI-Berichte 2032, Baden-Baden, 2008.

[NH96]   Nahvi, A.; Hollerbach, J. M.: *The noise amplification index for optimal pose selection in robot calibration*
In: IEEE (Ed.), Robotics and Automation (ICRA), Proceedings of the 1996 IEEE International Conference, Minneapolis, Minnesota, 1996, p. 647–654, DOI 10.1109/ROBOT.1996.503848.

[NHH94]   Nahvi, A.; Hollerbach, J. M.; Hayward, V.: *Calibration of a Parallel Robot Using Multiple Kinematics Closed Loops*
In: IEEE (Ed.), Robotics and Automation (ICRA), IEEE 1994 International Conference, San Diego, California, 1994, ISBN 0-8186-5330-2, p. 407–412, DOI 10.1109/ROBOT.1994.351262.

[NL07]   Nagai, K.; Liu, Z.: *A systematic approach to stiffness analysis of parallel mechanisms and its comparison with FEM*
In: SICE Annual Conference, Takamatsu, Japan, 2007, p. 1087–1094,
DOI 10.1109/SICE.2007.4421146.

[NL08]   Nagai, K.; Liu, Z.: *A systematic approach to stiffness analysis of parallel mechanisms*
In: IEEE Journal on Robotics and Automation, - (2008), p. 1543–1548,
DOI 10.1109/ROBOT.2008.4543421.

[NRF13]   Noel, D.; Ritou, M.; Furet, B.; Le Loch, S.: *Complete Analytical Expression of the Stiffness Matrix of Angular Contact Ball Bearings*
In: Journal of Tribology, 135 (2013) 4, p. 41101, DOI 10.1115/1.4024109.

[NSG10]   Norman, A. R.; Schönberg, A.; Gorlach, I. A.; Schmitt, R.: *Cooperation of Industrial Robots with Indoor-GPS*
In: Dimitrov, D. (Ed.), Proceedings of the International Conference on Competitive Manufacturing COMA 2010, Stellenbosch, Southafrica, 2010, p. 215–224.

[NSG12]   Norman, A. R.; Schönberg, A.; Gorlach, I. A.; Schmitt, R.: *Validation of iGPS as an external measurement system for cooperative robot positioning*
In: The International Journal of Advanced Manufacturing Technology, 64 (2012) 1-4, p. 427–446, DOI 10.1007/s00170-012-4004-8.

[NSJ14]   Nubiola, A.; Slamani, M.; Joubair, A.; Bonev, I. A.: *Comparison of two calibration methods for a small industrial robot based on an optical CMM and a laser tracker*
In: Robotica, 32 (2014) 03, p. 447–466, DOI 10.1017/S0263574713000714.

[NZG16]   Ni, Y.; Zhang, B.; Guo, W.; Shao, C.: *Kinematic calibration of parallel manipulator with full-circle rotation*
In: Industrial Robot: An International Journal, 43 (2016) 3, p. 296–307, DOI 10.1108/IR-08-2015-0161.

[OI14]   Oiwa, T.; Ikuma, H.: *A Calibration Method for a Six-Degree-of-Freedom Parallel Manipulator with a Redundant Passive Chain*
In: Petuya, V.; Pinto, C.; Lovasz, E.-C. (Ed.), New Advances in Mechanisms, Transmissions and Applications, Proceedings of the Second Conference MeTrApp 2013, University of the Basque Country, 2014, ISBN 978-94-007-7484-1, p. 349–356, DOI 10.1007/978-94-007-7485-8_43.

[OM95]   Oliviers, M. P.; Mayer, R. J. R.: *Global Kinematic Calibration of a Stewart Platform*
           In: Proceedings of the ASME Dynamic Systems Control Division, 57 (1995) 1, p. 129–136
           https://www.researchgate.net/profile/Rene_Mayer/publication/271525300_Global_kinematic_cal
           ibration_of_a_Stewart_platform/links/54cb8ff80cf2240c27e86aeb.pdf.

[OP96]   Okamura, K.; Park, F. C.: *Kinematic calibration using the product of exponentials formula*
           In: Robotica, 14 (1996) 04, p. 415–421, DOI 10.1017/S0263574700019810.

[Pal46]   Palmgren, A.: *Ball and roller bearing engineering*
           Philadelphia: S.H. Burbank, 1946.

[PCM05]   Piras, G.; Cleghorn, W. L.; Mills, J. K.: *Dynamic finite-element analysis of a planar high-speed, high-
           precision parallel manipulator with flexible links*
           In: Mechanism and Machine Theory, 40 (2005) 7, p. 849–862,
           DOI 10.1016/j.mechmachtheory.2004.12.007.

[PCW08]   Pashkevich, A.; Chablat, D.; Wenger, P.: *Stiffness Analysis Of Multi-Chain Parallel Robotic Systems*
           In: 9th IFAC Workshop on Intelligent Manufacturing Systems, France, 2008, p. 127–132.

[PCW09]   Pashkevich, A.; Chablat, D.; Wenger, P.: *Stiffness analysis of overconstrained parallel manipulators*
           In: Mechanism and Machine Theory, 44 (2009) 5, p. 966–982,
           DOI 10.1016/j.mechmachtheory.2008.05.017.

[PKB13]   Pastor, P.; Kalakrishnan, M.; Binney, J.; Kelly, J.; Righetti, L.; Sukhatme, G. S.; Schaal, S.: *Learning
           task error models for manipulation*
           In: IEEE (Ed.), Robotics and Automation (ICRA), 2013 IEEE International Conference, Karlsruhe,
           Germany, 2013, p. 2612–2618, DOI 10.1109/ICRA.2013.6630935.

[PKC09]   Pashkevich, A.; Klimchik, A.; Chablat, D.; Wenger, P.: *Accuracy Improvement for Stiffness Modeling
           of Parallel Manipulators*
           In: 42ème CIRP Conference on Manufacturing Systems, Grenoble, 2009, -.

[PKC11]   Pashkevich, A.; Klimchik, A.; Chablat, D.: *Enhanced stiffness modeling of manipulators with passive
           joints*
           In: Mechanism and Machine Theory, 46 (2011) 5, p. 662–679,
           DOI 10.1016/j.mechmachtheory.2010.12.008.

[PLC12]   Park, I.-W.; Lee, B.-J.; Cho, S.-H.; Hong, Y.-D.; Kim, J.-H.: *Laser-Based Kinematic Calibration of Robot
           Manipulator Using Differential Kinematics*
           In: IEEE/ASME Transactions on Mechatronics, 17 (2012) 6, p. 1059–1067,
           DOI 10.1109/TMECH.2011.2158234.

[RFS09]   Ren, X.-D.; Feng, Z.-R.; Su, C.-P.: *A new calibration method for parallel kinematics machine tools
           using orientation constraint*
           In: International Journal of Machine Tools and Manufacture, 49 (2009) 9, p. 708–721,
           DOI 10.1016/j.ijmachtools.2009.03.004.

[RFY13]   Ren, X.; Feng, Z.-R.; Yang, D.; Wang, X.; Gao, D.: *Calibration of parallel robots based on orientation
           constraint and total least squares approach*
           In: IEEE (Ed.), Information and Automation (ICIA), 2013 IEEE International Conference, Yinchuan,
           China, 2013, ISBN 978-1-4799-1334-3, p. 828–833, DOI 10.1109/ICInfA.2013.6720408.

[RHA14]   Rieg, F.; Hackenschmidt, R.; Alber-Laukant, B.: *Finite Element Analysis for Engineers*
           München: Carl Hanser Verlag GmbH & Co. KG, 2014, ISBN 978-1-56990-487-9,
           DOI 10.3139/9781569904886.

[Rie14]   Riedel, M.: *Flexible Bauteilhandhabung auf Basis einer rekonfigurierbaren parallelkinematischen
           Struktur,* Dissertation, Aachen: Aachen University, 2014.

[RMR87]   Roth, Z. S.; Mooring, B.; Ravani, B.: *An overview of robot calibration*
           In: IEEE Journal on Robotics and Automation, 3 (1987) 5, p. 377–385,
           DOI 10.1109/JRA.1987.1087124.

[Rob02]   Roberts, R. G.: *On the normal form of a spatial stiffness matrix*
           In: IEEE (Ed.), Robotics and Automation (ICRA), IEEE 2002 International Conference, Washington,
           DC, USA, 2002, p. 556–561, DOI 10.1109/ROBOT.2002.1013417.

[Rod14 Dt]   Rodilla, J.: *Kinematische Kalibrierung für das Mehrarm-Robotersystem PARAGRIP,* Bachelor thesis, supervised by Detert, Tim, Aachen: RWTH Aachen University, Department of Mechanism Theory and Dynamics of Machines, 2014.

[Rod16 Dt]   Rodilla, J.: *Auswertung von redundanten Antriebsinformationen zur Selbstkalibrierung des Mehrarm-Robotersystems PARAGRIP,* Master Thesis, supervised by Detert, Tim, Aachen: Aachen University, Department of Mechanism Theory and Dynamics of Machines, 2016.

[RPR06]   Rauf, A.; Pervez, A.; Ryu, J.: *Experimental results on kinematic calibration of parallel manipulators using a partial pose measurement device*
In: IEEE Transactions on Robotics, 22 (2006) 2, p. 379–384, DOI 10.1109/TRO.2006.862493.

[RR01]   Rauf, A.; Ryu, J.: *Fully autonomous calibration of parallel manipulators by imposing position constraint*
In: IEEE (Ed.), Robotics and Automation (ICRA), IEEE 2001 International Conference, COEX, Seoul, Korea, 2001, ISBN 0-7803-6576-3, p. 2389–2394, DOI 10.1109/ROBOT.2001.932979.

[RT15]   Rus, D.; Tolley, M. T.: *Design, fabrication and control of soft robots*
In: Nature, 521 (2015) 7553, p. 467–475, DOI 10.1038/nature14543.

[RVA06]   Renaud, P.; Vivas, A.; Andreff, N.; Poignet, P.; Martinet, P.; Pierrot, F.; Company, O.: *Kinematic and dynamic identification of parallel mechanisms*
In: Control Engineering Practice, 14 (2006) 9, p. 1099–1109, DOI 10.1016/j.conengprac.2005.06.011.

[SAG97]   Schröer, K.; Albright, S. L.; Grethlein, M.: *Complete, minimal and model-continuous kinematic models for robot calibration*
In: Robotics and Computer-Integrated Manufacturing, 13 (1997) 1, p. 73–85, DOI 10.1016/S0736-5845(96)00025-7.

[Sal80]   Salisbury, J.: *Active stiffness control of a manipulator in cartesian coordinates*
In: IEEE (Ed.), Decision and Control, 1980 19th IEEE Conference, Albuquerque, New Mexiko, 1980, p. 95–100, DOI 10.1109/CDC.1980.272026.

[SAL97]   Schroer, K.; Albright, S. L.; Lisounkin, A.: *Modeling closed-loop mechanisms in robots for purposes of calibration*
In: IEEE Transactions on Robotics and Automation, 13 (1997) 2, p. 218–229, DOI 10.1109/70.563644.

[Sch12]   Schaeffler Technologies AG & Co. KG: *Bearinx®-online Wellenberechnung*
http://www.schaeffler.com/remotemedien/media/_shared_media/08_media_library/01_publicati ons/schaeffler_2/brochure/downloads_1/pbo_de_de.pdf (last checked on 01.08.2017).

[SCH16]   Schmidt, R.; Corves, B.; Hüsing, M.; Bertelsmeier, F.; Detert, T.; Haag, S.; Hoffmann, M.; Holters, M.; Kurtenbach, S.; Permin, E.; Prochnau, M.; Storm, C.: *Cognition-enhanced, Self-optimizing Assembly Systems*
In: Brecher, C. (Ed.), Integrative Production Technology for High-Wage Countries, Berlin: Springer Berlin Heidelberg, 2016, p. 877–992.

[SDG13]   Sandretto, J. A.; Daney, D.; Gouttefarde, M.: *Calibration of a Fully-Constrained Parallel Cable-Driven Robot*
In: Padois, V.; Bidaud, P.; Khatib, O. (Ed.), Romansy 19 - Robot Design, Dynamics and Control, Proceedings of the 19th CISM-Iftomm Symposium, Paris, 2013, ISBN 978-3-7091-1378-3, p. 77–84, DOI 10.1007/978-3-7091-1379-0_10.

[Sei14 Dt]   Seiedardeshir, S.: *Herleitung und Implementierung von Steifigkeitsmodellen für 3-DOF Parallelmanipulatoren und Validierung der Modelle mittels MATLAB SimMechanics,* Masterarbeit, supervised by Prause, Isabel; Detert, Tim, Aachen: RWTH Aachen University, Institut für Getriebetechnik und Maschinendynamik, 2014.

[SG13]   Santolaria, J.; Ginés, M.: *Uncertainty estimation in robot kinematic calibration*
In: Robotics and Computer-Integrated Manufacturing, 29 (2013) 2, p. 370–384, DOI 10.1016/j.rcim.2012.09.007.

[SH08]   Sun, Y.; Hollerbach, J. M.: *Observability index selection for robot calibration*
           In: IEEE Journal on Robotics and Automation, - (2008), p. 831–836,
           DOI 10.1109/ROBOT.2008.4543308.

[SK16]   Siciliano, B.; Khatib, O. (Ed.), *Springer Handbook of Robotics*
           Cham: Springer International Publishing, 2016, ISBN 978-3-319-32550-7, DOI 10.1007/978-3-319-
           32552-1.

[SS86]   Saad, Y.; Schultz, M. H.: *GMRES: A Generalized Minimal Residual Algorithm for Solving Nonsym-
           metric Linear Systems*
           In: SIAM Journal on Scientific and Statistical Computing, 7 (1986) 3, p. 856–869,
           DOI 10.1137/0907058.

[SS88]   Stone, H. W.; Sanderson, A. C.: *Statistical performance evaluation of the S-model arm signature
           identification technique*
           In: IEEE (Ed.), Robotics and Automation (ICRA), IEEE 1988 International Conference, Philadelphia,
           PA, USA, 1988, p. 939–946, DOI 10.1109/ROBOT.1988.12180.

[ŠŠŠ14]   Švaco, M.; Šekoranja, B.; Šuligoj, F.; Jerbić, B.: *Calibration of an Industrial Robot Using a Stereo
           Vision System*
           In: Procedia Engineering, 69 (2014), p. 459–463, DOI 10.1016/j.proeng.2014.03.012.

[SV12]   Spiller, A.; Verl, A.: *Force controlled handling with cooperating industrial robots*
           In: VDE (Ed.), Proceedings of ROBOTIK 2012, 7th German Conference on Robotics, Munich, Germa-
           ny, 2012, ISBN 978-3-8007-3418-4, p. 496–501.

[TAL12]   Taghvaeipour, A.; Angeles, J.; Lessard, L.: *On the elastostatic analysis of mechanical systems*
           In: Mechanism and Machine Theory, 58 (2012), p. 202–216,
           DOI 10.1016/j.mechmachtheory.2012.07.011.

[Tho12]   Thomas Lens: *Physical Human-Robot Interaction with a Lightweight, Elastic Tendon Driven Robotic
           Arm,* Dissertation, Darmstadt: Technische Universität Darmstadt, 2012
           http://tuprints.ulb.tu-darmstadt.de/3493/.

[TMM14]   Tsarouchi, P.; Makris, S.; Michalos, G.; Stefos, M.; Fourtakas, K.; Kaltsoukalas, K.; Kontrovrakis, D.;
           Chryssolouris, G.: *Robotized Assembly Process Using Dual Arm Robot*
           In: Procedia CIRP, 23 (2014), p. 47–52, DOI 10.1016/j.procir.2014.10.078.

[TST13]   Traslosheros, A.; Sebastian, J. M.; Torrijos, J.; Carelli, R.; Castillo, E.: *An inexpensive method for
           kinematic calibration of a parallel robot by using one hand-held camera as main sensor*
           In: Sensors, 13 (2013) 8, p. 9941–9965, DOI 10.3390/s130809941.

[TW12]   To, M.; Webb, P.: *An improved kinematic model for calibration of serial robots having closed-chain
           mechanisms*
           In: Robotica, 30 (2012) 06, p. 963–971, DOI 10.1017/S0263574711001184.

[TZZ14]   Tian, W.; Zeng, Y.; Zhou, W.; Liao, W.: *Calibration of robotic drilling systems with a moving rail*
           In: Chinese Journal of Aeronautics, 27 (2014) 6, p. 1598–1604, DOI 10.1016/j.cja.2014.10.028.

[VC00]   Vischer, P.; Clavel, R.: *Kinematic calibration of the parallel Argos mechanism*
           In: Robotica, (2000) 18, p. 589–899.

[WA92]   Wampler, C. W.; Arai, T.: *Calibration of robots having kinematic closed loops using nonlinear
           leastsquares estimation*
           In: IFToMM-jc (Ed.), International Symposium on Theory of Machines and Mechanisms, Nagoya,
           Japan, 1992, p. 153–158.

[WBZ12]   Wang, D.; Bai, Y.; Zhao, J.: *Robot manipulator calibration using neural network and a camera-based
           measurement system*
           In: Transactions of the Institute of Measurement and Control, 34 (2012) 1, p. 105–121,
           DOI 10.1177/0142331210377350.

[WHA95]   Wampler, C. W.; Hollerbach, J. M.; Arai, T.: *An implicit loop method for kinematic calibration and
           its application to closed-chain mechanisms*
           In: IEEE Transactions on Robotics and Automation, 11 (1995) 5, p. 710–724,
           DOI 10.1109/70.466613.

[WLY15]   Wang, W.; Liu, F.; Yun, C.: *Calibration method of robot base frame using unit quaternion form*
            In: Precision Engineering, 41 (2015), p. 47–54, DOI 10.1016/j.precisioneng.2015.01.005.

[WWY10]   Wu, J.; Wang, J.; You, Z.: *An overview of dynamic parameter identification of robots*
            In: Robotics and Computer-Integrated Manufacturing, 26 (2010) 5, p. 414–419,
            DOI 10.1016/j.rcim.2010.03.013.

[YB02]   Young, W. C.; Budynas, R. G.: *Roark's formulas for stress and strain,* Warren C. Young; Richard G.
            Budynas
            New York: McGraw-Hill, 7. ed., 2002, ISBN 9780070725423.

[YL08]   Yun, Y.; Li, Y.: *Comparison of Two Kinds of Large Displacement Precision Parallel Mechanisms for
            Micro/nano Positioning Applications*
            In: IEEE (Ed.), Robotics, Automation and Mechatronics (RAM), IEEE Conference, Chengdu, China,
            2008, p. 284–289, DOI 10.1109/RAMECH.2008.4681430.

[Yu08]   Yu, D.-Y.: *Parallel robots pose accuracy compensation using artificial neural networks*
            In: IEEE (Ed.), Mechatronics and Automation (ICMA), IEEE International Conference, Takamatsu,
            Japan, 2008, ISBN 978-1-4244-2631-7, p. 750–754, DOI 10.1109/ICMA.2008.4798850.

[YWL14]   Yang, X.; Wu, L.; Li, J.; Chen, K.: *A minimal kinematic model for serial robot calibration using POE
            formula*
            In: Robotics and Computer-Integrated Manufacturing, 30 (2014) 3, p. 326–334,
            DOI 10.1016/j.rcim.2013.11.002.

[YWR06]   Ye, S. H.; Wang, Y.; Ren, Y. J.; Li, D. K.: *Robot Calibration Using Iteration and Differential Kinematics*
            In: Journal of Physics: Conference Series, 48 (2006) 1, p. 1
            http://stacks.iop.org/1742-6596/48/i=1/a=001.

[YZR03]   Ying Bai; Zhuang, H.; Roth, Z. S.: *Experiment study of PUMA robot calibration using a laser tracking
            system*
            In: IEEE Soft Computing in Industrial Applications, 03 (2003), p. 139–144,
            DOI 10.1109/SMCIA.2003.1231359.

[ZDT16]   Zhang, G.; Du, J.; To, S.: *Calibration of a small size hexapod machine tool using coordinate measur-
            ing machine*
            In: Proceedings of the Institution of Mechanical Engineers, Part E: Journal of Process Mechanical
            Engineering, 230 (2016) 3, p. 183–197, DOI 10.1177/0954408914544203.

[Zhu97]   Zhuang, H.: *Self-calibration of parallel mechanisms with a case study on Stewart platforms*
            In: IEEE Transactions on Robotics and Automation, 13 (1997) 3, p. 387–397,
            DOI 10.1109/70.585901.

[ZLD15]   Zhang, P.; Liu, X.; Du, G.: *Online robot auto-calibration using IMU with CMAC and EKF*
            In: IEEE (Ed.), Cyber Technology in Automation, Control, and Intelligent Systems (CYBER), 2015 IEEE
            International Conference, Shenyang, China, 2015, ISBN 978-1-4799-8728-3, p. 896–901,
            DOI 10.1109/CYBER.2015.7288063.

[ZRH92]   Zhuang, H.; Roth, Z. S.; Hamano, F.: *A complete and parametrically continuous kinematic model for
            robot manipulators*
            In: IEEE Transactions on Robotics and Automation, 8 (1992) 4, p. 451–463,
            DOI 10.1109/70.149944.

[ZTL16]   Zeng, Y.; Tian, W.; Liao, W.: *Positional error similarity analysis for error compensation of industrial
            robots*
            In: Robotics and Computer-Integrated Manufacturing, 42 (2016), p. 113–120,
            DOI 10.1016/j.rcim.2016.05.011.

[ZWZ05]   Zhang, H.; Wang, J.; Zhang, G.; Gan, Z.; Pan, Z.; Cui, H.; Zhu, Z.: *Machining with flexible manipula-
            tor: toward improving robotic machining performance*
            In: IEEE/ASME (Ed.), Advanced Intelligent Mechatronics, International Conference, Monterey, CA,
            2005, ISBN 0-7803-9047-4, p. 1127–1132, DOI 10.1109/AIM.2005.1511161.

[ZXM04]   Zhang, D.; Xi, F.; Mechefske, C. M.; Lang, S. Y.T.: *Analysis of parallel kinematic machine with kineto-static modelling method*
In: Robotics and Computer-Integrated Manufacturing, 20 (2004) 2, p. 151–165,
DOI 10.1016/j.rcim.2003.08.005.

[ZYM98]   Zhuang, H.; Yan, J.; Masory, O.: *Calibration of stewart platforms and other parallel manipulators by minimizing inverse kinematic residuals*
In: Journal of Robotic Systems, 15 (1998) 7, p. 395–405, DOI 10.1002/(SICI)1097-4563(199807)15:7<395::AID-ROB2>3.0.CO;2-H
http://onlinelibrary.wiley.com/doi/10.1002/(SICI)1097-4563(199807)15:7%3C395::AID-ROB2%3E3.0.CO;2-H/abstract.

List of Figures

List of Tables